FATIGUE CRACK GROWTH IN AIRCRAFT ALUMINIUM ALLOYS

by

David Rhodes, BSc(Eng), ACGI, AMRAeS

Thesis submitted in fulfilment of
the requirements for the
Doctor of Philosophy (PhD) degree
of the University of London, and for the
Diploma of Membership of Imperial College (DIC)

July 1981

Department of Mechanical Engineering
Imperial College of Science & Technology
London SW7 2BX

TO POLLY.....

....and AMY

ABSTRACT

An experimental study was carried out to examine the fatigue crack growth characteristics of some high-strength aluminium alloys used in the civil aircraft industry. The materials were studied in a range of thicknesses, from 0.9 mm to 15 mm. In all cases, the thickness was significantly less than that required for plane strain fracture analysis at failure. Compact tension specimens were used of the minimum dimensions for which linear elastic fracture mechanics could be considered valid, and the results were compared with existing data from large centre-cracked panel tests. The effects of specimen thickness, and of positive and negative stress ratios, were examined and some fractographic studies were undertaken.

Satisfactory results were obtained from the small specimens, provided that general yielding did not occur, and that due account was taken of variations in the non-singular stress component parallel to the crack when comparing tests on different specimen types. Data were obtained for DTD.5120 (7010-T7651), BS.L97 (2024-T3) and BS.L109 (2024-T3 Al clad) alloys. Compressive minimum loads were found to be detrimental to fatigue crack growth performance, but prolonged constant-amplitude tension-compression testing led to crack retardation, or arrest in some cases.

Fractography showed that for crack growth rates above about 10^{-5} mm/cycle, the crack extension process consisted of both ductile striation formation and micro-void coalescence. An energy balance method was used to derive a "crack resistance addition model" by which the two processes could be superimposed, and this was found to account for observed stress ratio effects. At high stress intensities, the crack growth rate was influenced by the maximum load toughness value, and

methods were discussed whereby a convenient toughness parameter could be derived from the R-curve or, alternatively, from maximum load toughness data for a range of geometries.

Finally, a semi-empirical equation was derived from the crack resistance addition model which may be useful in structural analysis, i.e.

$$\frac{da}{dN} = \frac{A\ (\Delta K)^n}{(1-R)^{n-2}\ [1 - (K_{max}/K_{eng_c})^m]}$$

in which A and n are empirical constants from fatigue data, m and K_{eng_c} are constants from R-curve or maximum load toughness data, da/dN is the crack growth rate, R is the load ratio, and ΔK and K_{max} are the stress intensity range and maximum stress intensity factor, respectively.

ACKNOWLEDGEMENTS

The author wishes to acknowledge the invaluable assistance and advice which has been forthcoming from so many people. In particular, he wishes to thank the following:

Dr J.C. Radon and *Dr L.E. Culver* of the Department of Mechanical Engineering, Imperial College, for their supervision and their great interest in this work; and other academic and technical staff within the department for their assistance.

Dr K.J. Nix, formerly of the Department of Metallurgy & Materials Science, Imperial College (now with the Central Electricity Research Laboratories, Leatherhead), for his cooperation with the fractography and for many useful exchanges of ideas.

Mr J.A.B. Lambert of the Structures Department, British Aerospace (Aircraft Group), Hatfield, for his interest and support, and to many others at British Aerospace for their help and advice.

Mr C. Wheeler of the Materials Department, Royal Aircraft Establishment, Farnborough, for discussions on test techniques.

Dr J.M. Krafft of the Naval Research Laboratory, Washington, D.C., USA, for his time and the use of the TLIM77 computer program.

Mrs E.A. Hall for typing the thesis, and many other reports and papers.

British Aerospace (Aircraft Group), Hatfield-Chester Division, and the *Science Research Council* for financial support.

CONTENTS

		Page
Abstract		2
Acknowledgements		4
Contents		5
Notation		8
CHAPTER 1:	INTRODUCTION	13
1.1	Fatigue in Aircraft Structures	13
1.2	Applications of Fracture Mechanics	14
1.3	Objectives of the Project	16
CHAPTER 2:	FRACTURE MECHANICS	19
2.1	Theory	19
2.2	Current Practice in the Civil Aircraft Industry	25
2.3	The Validity of Linear Elastic Fracture Mechanics	26
CHAPTER 3:	CRACK PROPAGATION MECHANISMS	29
3.1	Slip-Controlled Mechanisms	29
3.2	Micro-Void Coalescence	34
3.3	Cleavage, and Brittle Striations	37
3.4	Effect of Frequency, and Environmental Influences	38
3.5	Plane Strain Fracture Toughness	40
3.6	Some Notes on Metallurgy of Aluminium Alloys	40
3.7	Some Crack Propagation Models	44
3.8	Crack Closure, and Stress Ratio Effects	47
CHAPTER 4:	TESTING	58
4.1	Review of Test Techniques	58

		Page
4.2	Specimen Selection and Design	59
4.3	Thin Sheet Testing	64
4.4	Crack Length Measurement	67
4.5	Fatigue Test Programme	69
4.6	*R*-Curve Determination	74
4.7	Cyclic Stress-Strain Measurement	75
4.8	Fractography	75
CHAPTER 5:	RESULTS	92
5.1	Fatigue Crack Growth Rates	92
5.2	Striation Spacing Measurements	93
5.3	Crack Growth Resistance	94
5.4	Mode Transition Observations	94
5.5	Fracture Toughness	95
5.6	Batch Effects in 2024-T3	97
5.7	Cyclic Stress-Strain Data	97
5.8	Error Analysis	97
CHAPTER 6:	DISCUSSION	113
6.1	Combination of Cyclic and Monotonic Data	117
6.2	The Dual Mechanism Concept	120
6.3	Striation Behaviour at Low Stress Intensities	127
6.4	Tearing Below K_{Ic} - A Stochastic Approach	131
6.5	Tensile Ligament Instability Model (TLIM)	133
6.6	The Geometry Dependence of K_c	135
6.7	Fracture Mode Transition and Specimen Compliance	139
6.8	The Effect of Frequency and Environment	142
6.9	The Effect of Specimen Thickness	143

Page

6.10 Negative Stress Ratios 144

6.11 Comparison with CCT Test Results 145

CHAPTER 7: APPLICATIONS 189

7.1 Combined Fatigue and Residual Strength Data 189

7.2 Analysis of an Engineering Component 192

7.3 Applications of Fractography in Failure Analysis 196

7.4 Stress Ratio and Random Loading Effects 196

7.5 Crack Propagation Life Predictions 199

CHAPTER 8: CONCLUSIONS 211

CHAPTER 9: RECOMMENDATIONS FOR FURTHER WORK 214

Bibliography 217

Appendix I: Stress Intensity and Compliance Relationships for CT and CCT Test Specimens 234

Appendix II: Nominal Stress Distribution for CT Specimens in Tension and Compression 240

Appendix III: Pre-Cracking and "Stepping Down" in Fatigue Test Specimens 245

Appendix IV: Crack Resistance Model - Numerical Evaluation 250

NOTATION

a	:	crack length
a'	:	effective crack length
Δa	:	crack extension
$\Delta a'$	:	effective crack extension
a_o	:	initial crack length
a_c	:	critical crack length
d	:	distance between intermetallic particles
$\bar{d}$	:	mean value of d
d_T	:	process zone size (TLIM)
f	:	geometry function
k	:	buckling coefficient
m	:	empirical index
n	:	(i) work-hardening exponent (ii) empirical index
n'	:	cyclic work-hardening exponent
p	:	empirical index
r	:	distance from crack tip
r_c	:	critical distance from crack tip
r_p	:	plastic zone radius
Δr_p	:	cyclic plastic zone radius
r_T , Δr_T	:	ligament radii (TLIM)
$\bar{s}$	:	mean striation spacing
v_f	:	volume fraction of inclusion phase
x	:	proportion of crack growth due to a specified mechanism
A	:	(i) empirical coefficient (ii) cross-sectional area
B	:	thickness

C : (i) empirical coefficient
(ii) total compliance

C_o : machine compliance

C_s : specimen compliance

E : elastic modulus

E' $\equiv$ $E/(1-\nu^2)$

F : material function

$\mathcal{F}$: normal distribution function

G : strain energy release rate

H : specimen dimension

I : second moment of area

K : stress intensity factor

ΔK : stress intensity range

ΔK_{eff} : effective stress intensity range

K_m : mean stress intensity factor

K_{op} : value of K at crack opening

K_R : crack growth resistance in units of K

K_I : opening mode stress intensity factor

K_{Ic} : plane strain fracture toughness

K_{Ii} : value of K_I for void initiation

K_{It} : value of K_I for 5% probability of tearing

K_{Iv} : value of K_I for void coalescence

K_{II} : in-plane shear mode stress intensity factor

K_{III} : out-of-plane shear mode stress intensity factor

K_{eng} : engineering stress intensity factor

ΔK_{eng} : range of K_{eng} in fatigue

K_{eng_c} : critical value of K_{eng}

K_t : elastic stress concentration factor

L : loading parameter

ΔL : range of L in fatigue

L_m : mean value of L

M : (i) bending moment
(ii) empirical coefficient

N : number of cycles

P : load

Q $\equiv$ $2^{n'+1}/4(\sigma_y/\sigma_y')^2$

R : (i) stress ratio
(ii) crack growth resistance

R_p : load ratio

S : standard deviation

U : strain energy

W : specimen dimension

Y $\equiv$ $K/\sigma\sqrt{\pi a}$

Z : empirical coefficient

γ : geometry sensitivity

δ : load point displacement

ε : strain

ε_i : instability strain

$\Delta\varepsilon_p$: plastic strain range

ε_v : void initiation strain

ε_{yy} : strain component normal to crack plane

η : stress ratio dependence

θ : (i) orientation with respect to crack direction
(ii) variation in crack front orientation

λ : stress biaxiality factor

λ_o : inherent stress biaxiality

ν : Poisson's ratio

σ : stress

σ_{nom} : nominal stress

σ_v : void initiation stress

σ_y	:	yield stress
σ'_y	:	cyclic yield stress
σ_{xx} , σ_{yy} , σ_{zz}	:	components of direct stress
τ	:	shear stress
τ_{xy} , τ_{yz} , τ_{zx}	:	components of shear stress
ϕ	:	empirical coefficient
ψ	:	variation of crack plane orientation
Γ	:	geometry characteristic
ACFM	:	alternating current field measurement
ACPD	:	alternating current potential drop
ASTM	:	American Society for Testing and Materials
BAe	:	British Aerospace
BCC	:	body centre cubic
BS	:	British Standards
CCT	:	centre-cracked tension
CPH	:	close packed hexagonal
CT	:	compact tension
CTAD	:	crack tip advance displacement
CTOD	:	crack tip opening displacement
DCB	:	double cantilever beam
DCPD	:	direct current potential drop
DENT	:	double edge notch, tension
DTD	:	Directorate of Technical Development (UK Ministry of Defence)
ESDU	:	Engineering Sciences Data Unit
FCC	:	face centre cubic
LEFM	:	linear elastic fracture mechanics
NDT	:	non-destructive testing

RAE	:	Royal Aircraft Establishment
SEM	:	scanning electron microscope
SENB3	:	single edge notch, three-point bend
SENT	:	single edge notch, tension
TLIM	:	tensile ligament instability model

CHAPTER 1

INTRODUCTION

1.1 FATIGUE OF AIRCRAFT STRUCTURES

Fatigue in aircraft structures was first recognised as a serious problem during the early 1950s as designers gained confidence in the use of stressed skin metal airframes and aircraft were built to operate with ever higher stress levels. At the same time, higher aircraft weights and performance, the introduction of pressurised cabins, and the tendency towards more flexible structures all served to increase the number of components subjected to severe fluctuations in load during their lives. The loss of a number of aircraft - most notably the early de Havilland Comet airliners - as a result of catastrophic fatigue failures led to the introduction of mandatory airworthiness requirements for "safe life" structures. This implied that the probability of a fatigue failure at the end of an aircraft's life would not exceed a specified level; typically, 10^{-7} per flying hour. When that limit was reached, the aircraft had to be retired. In the late 1950s, many civil aircraft designers adopted an alternative "fail-safe" approach for major structural components. This enables a higher probability of local failure to be tolerated, provided that the probability of a major structural collapse is not increased. In order to achieve this, it is necessary to locate the local damage before it becomes dangerous. In general, this was verified at the design stage by assuming (or simulating on test) the total failure of each principal structural member in turn, and demonstrating the static strength of the remaining structure.

The problems of predicting fatigue lives involve the analysis of aerodynamic and inertial loads, operating conditions, structural dynamics, and other factors, as well as the accepted fatigue parameters of quasi-

static stress analysis and material behaviour. These wide ranging aspects of the subject have been reviewed extensively by Payne [1].

A number of recent cases of fatigue cracking in fail-safe airliner structures [2] have served to highlight the importance of inspection standards laid down through the airworthiness authorities, by the manufacturer, and the way in which they are implemented by the operator. Fatigue prone areas must be identified, either by analysis or by testing, and techniques must be developed whereby damage may be located in service before the load carrying capacity of the structure is reduced to an unacceptable level [3,4].

1.2 APPLICATIONS OF FRACTURE MECHANICS

The techniques of fracture mechanics may be applied to aircraft fatigue problems to help to provide the following essential information:

(i) The relationship between the size of any defect, as located and measured by an appropriate technique, and the load carrying capacity of the structure (i.e. the residual strength).

(ii) The rate at which the defect size will increase under the loading sequence expected in service (i.e. the crack propagation).

There are five principal areas in which this information may then be applied to civil aircraft structures:

1.2.1 Materials Selection

Basic residual strength and crack propagation data may be used to characterise materials and may then contribute to the procedure for

selecting materials for specific components. This is particularly straightforward where single parameters, such as the plane strain fracture toughness, are relevant.

1.2.2 Damage Tolerant Design

Design codes based on fracture mechanics may be used in relation to fatigue sensitive areas to obtain high residual strengths or low crack propagation rates by virtue of local geometric effects. For example, optimisation of positions of reinforcements, stiffeners, or crack-stoppers may be effected at an early stage.

1.2.3 Structure Assessment

Traditionally, fail-safe structures have been assessed by assuming the total failure of each component in turn. The application of fracture mechanics may enable progressive failure of a component to be analysed. It may also be possible to assess the gradual redistribution of the load in a redundant structure in which one member is cracked.

1.2.4 Structure Re-Assessment

Re-assessment of old aircraft structures may be necessary as airworthiness requirements become more stringent, or as high costs of new aircraft make life extension modifications economically attractive. The application of fracture mechanics, in conjunction with non-destructive test methods, may improve confidence in such structures.

1.2.5 Inspection Scheduling

This is the most important application of fracture mechanics to civil aircraft at present. From a knowledge of the residual strength and the crack propagation rate, it is possible to determine the length of

time for which a defect is detectable (taking into account the inspection method) while remaining safe. With a suitable safety factor, this time may be used as a basis for recommendations to certification authorities and to aircraft operators for routine structural inspections.

1.3 OBJECTIVES OF THE PROJECT

The overall objective was to advance the state of the art in the acquisition, analysis and interpretation of crack growth data for aluminium alloys, in which the section thickness was significantly less than that required for plane strain conditions to dominate. Some more specific items were as follows:

1.3.1 To increase confidence in the use of small specimens for the generation of useful crack growth data for design purposes.

1.3.2 To compare the behaviour of a new alloy, DTD.5120 (7010-T7651), with a conventional material, BS.L97 (2024-T3).

1.3.3 To examine the influence of compressive minimum loads during fatigue cycling, and to discuss the application of any results to fracture analysis and predictions.

1.3.4 To examine the influence of specimen thickness on crack propagation in a region where mode transition (from 'square' to 'slant' fracture) is expected.

1.3.5 To carry out some fractographic analyses and to use these to assist in the extrapolation of crack growth data. Also, to comment on the use of fractography in the analysis of service and test failures.

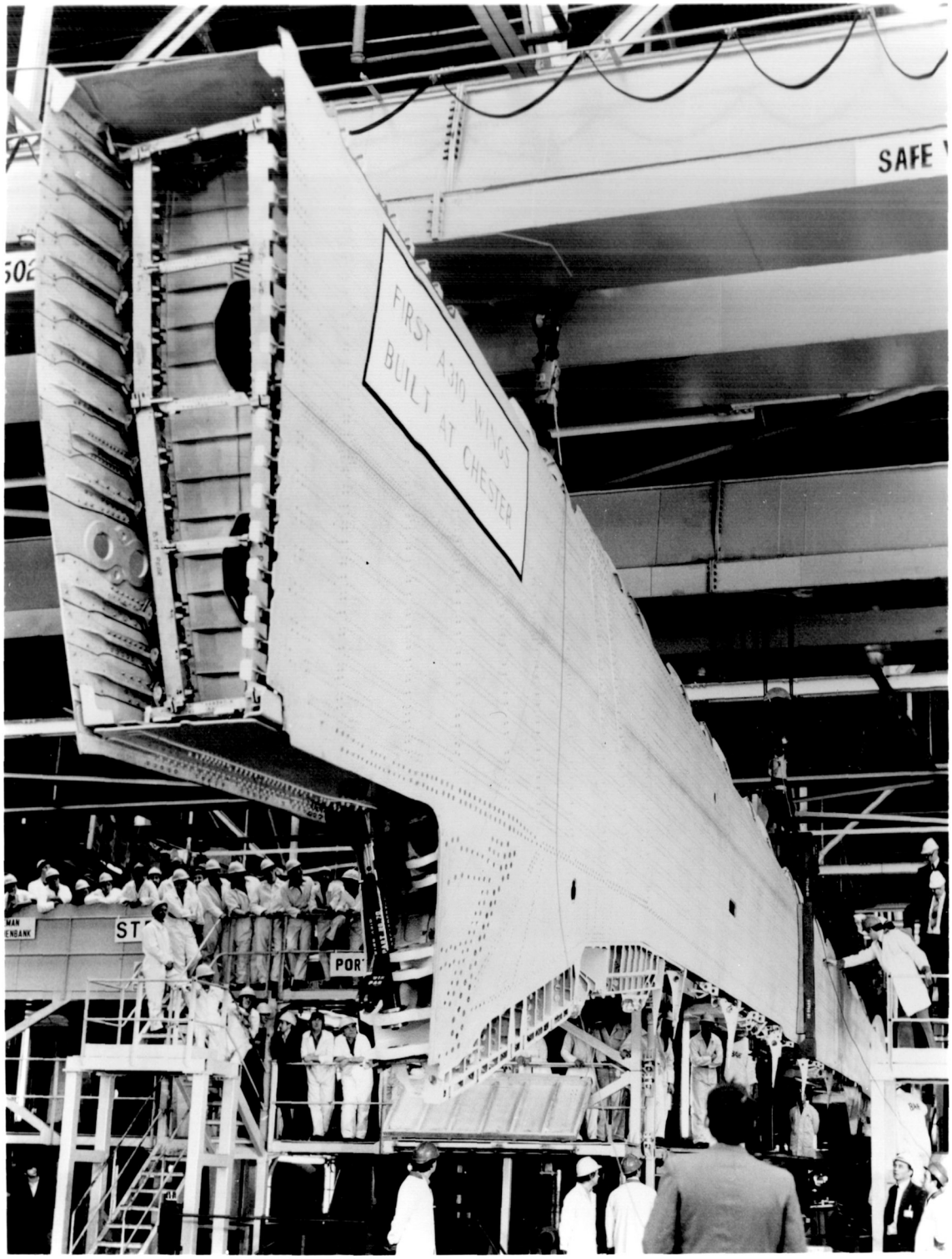


Figure 1.1: The spars, ribs and many of the attachment fittings on the wing of the Airbus A310 airliner are made from 7010-T76 and 7010-T7651 aluminium alloys.
[Photo: Courtesy of British Aerospace]

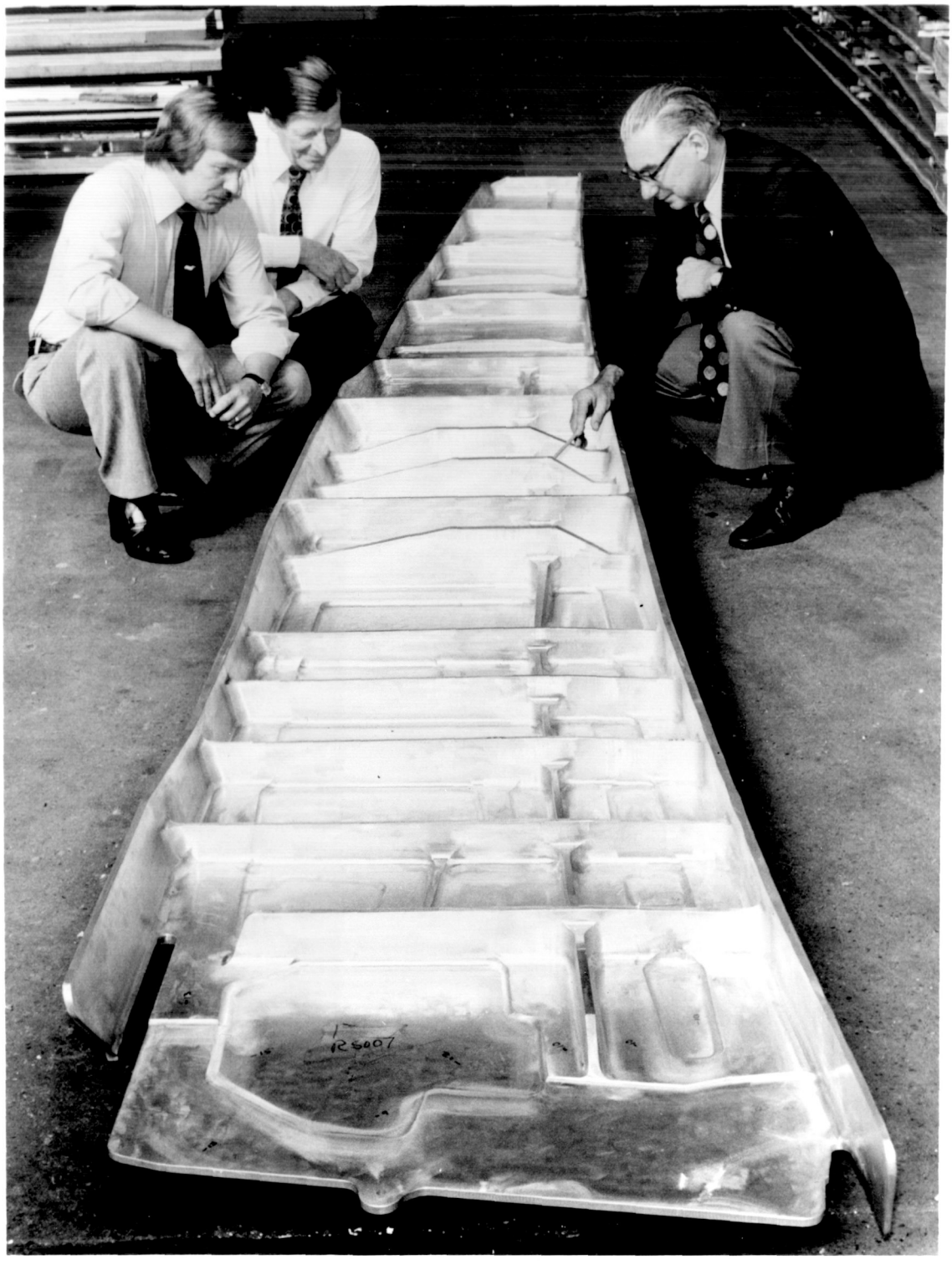


Figure 1.2: The inner rear spar of an Airbus A310 wing, which is machined from a single forged billet of 7010-T76 aluminium alloy. [Photo: Courtesy of British Aerospace]

CHAPTER 2

FRACTURE MECHANICS

2.1 THEORY

Any reader who is not familiar with the fundamental principles of linear elastic fracture mechanics is referred to any of the recent text-books on the subject (for example, [5,6]). A brief resumé follows:

The term "fracture mechanics" has been adopted to describe aspects of applied mechanics relating to bodies which contain cracks or other crack-like defects. There are two independent approaches to the problem:

2.1.1 Energy Balance Approach

Historically, this was the first rigorous means of analysis of cracked bodies. If it is assumed that all significant deformations are linear and elastic, then the energy available for crack propagation is equal to the reduction in strain energy. Thus, one may define the strain energy release rate (or crack extension force), G, in a body of unit thickness by:

$$G \equiv \frac{\partial U}{\partial a} \tag{2.1}$$

in which U is the strain energy, and a is the crack length. If the overall load point displacement for the body is δ under an applied load, P, then:

$$U = \tfrac{1}{2} P \delta \tag{2.2}$$

Putting the compliance C_s equal to δ/P:

$$U = \tfrac{1}{2} P^2 C_s \tag{2.3}$$

and:

$$G = \frac{P^2}{2}\frac{\partial C_s}{\partial a} \tag{2.4}$$

This method is not valid if large scale yielding occurs, when it must be modified [7] to account for plastic work absorbed.

2.1.2 Stress Analysis Approach

An alternative method involves the analysis of the stress distribution close to the crack tip, normally by complex stress function methods. Once again, linear elastic behaviour is assumed. This leads to an expression for the stress field, in which (r,θ) are polar coordinates, with their origin at the crack tip, and $\theta = 0$, an extension of the crack line:

$$\begin{bmatrix}\sigma_{xx}\\ \sigma_{yy}\\ \tau_{xy}\end{bmatrix} \simeq \frac{K_I \cos\theta/2}{\sqrt{2\pi\, r}}\begin{bmatrix}1-\sin\frac{\theta}{2}\sin\frac{3\theta}{2}\\ 1+\sin\frac{\theta}{2}\sin\frac{3\theta}{2}\\ \sin\frac{\theta}{2}\cos\frac{3\theta}{2}\end{bmatrix} + \frac{K_{II}\sin\theta/2}{\sqrt{2\pi\, r}}\begin{bmatrix}2+\cos\frac{\theta}{2}\cos\frac{3\theta}{2}\\ \cos\frac{\theta}{2}\cos\frac{3\theta}{2}\\ \cos\frac{\theta}{2}-\sin\frac{3\theta}{2}\end{bmatrix}$$

$$\begin{bmatrix}\tau_{xz}\\ \tau_{yz}\end{bmatrix} \simeq \frac{K_{III}}{\sqrt{2\pi\, r}}\begin{bmatrix}\sin\frac{\theta}{2}\\ \cos\frac{\theta}{2}\end{bmatrix} \tag{2.5}$$

K_I, K_{II} and K_{III} are known as the stress intensity factors associated with the 'opening' (Mode I), in-plane shear (Mode II) and out-of-plane shear (Mode III) cracking modes, respectively.

2.1.3 Linear Elastic Fracture Mechanics (LEFM)

It may be shown that the energy balance and stress analysis approaches are compatible by virtue of the relationship:

$$K_I^2 = E' G \tag{2.6}$$

where E' = E (Young's modulus) under plane stress conditions, i.e. when $\sigma_{zz} = 0$

and $E' = E/(1-\nu^2)$, where ν = Poisson's ratio, under plane strain conditions, i.e. when $\epsilon_{zz} = 0$

The terms K_I, K_{II} and K_{III} are dependent on local geometry, crack size, and applied loading. Standard tables of stress intensity factors are available [8]. A general expression would be of the form:

$$K = L\, f(a) \tag{2.7}$$

where f is a function depending on geometry

L is a "loading parameter" proportional to the applied load or stress, for example

and a is the crack length

By the use of von Mises yield criterion, in conjunction with equations (2.5), it may be shown that yielding occurs along the line $\theta = 0$ for $r \leq r_p$, the "plastic zone size", such that, for plane stress:

$$r_p = \frac{1}{2\pi} \left(\frac{K_I}{\sigma_y}\right)^2 \tag{2.8}$$

and, for plane strain (depending on the value of ν), then:

$$r_p \simeq \frac{1}{6\pi} \left(\frac{K_I}{\sigma_y}\right)^2 \tag{2.9}$$

where σ_y is the material's yield stress in simple tension.

Strictly speaking, the assumption of linear elasticity does not apply if any yielding occurs. In practice (see Section 2.3), a small plastic zone has little effect on the stress analysis, although it plays an important part in determining material behaviour.

2.1.4 Crack Growth Resistance, and Fracture Toughness [9]

If a body containing a crack of length a_o is loaded, the crack may extend by an amount Δa. This extension is normally accompanied by plastic blunting of the crack tip, and, possibly, shear lip formation. The rate at which energy becomes available for crack growth is given by G in equation (2.1), dependent on load and geometry. The rate at which energy is absorbed is referred to as the crack growth resistance, R. It is assumed, generally, that the relationship between R and Δa is dependent only on the material and thickness, and is independent of geometry and initial crack length. This relationship was described by Krafft et al [10] in 1961, and is supported by many subsequent empirical studies where suitable corrections are made for local plasticity [9-12].

For convenience, in the predominantly linear elastic case, one may define (c.f. equation (2.6)):

$$K_R^2 \equiv E' R \qquad (2.10)$$

Referring to Figure 2.1 [9,10], a load of P_1 may result in energy being available at a rate given by the "G-curve" or "driving force curve" shown. If this energy is absorbed by the crack extension process, the resulting crack growth, Δa, is defined by the intersection of the "G-curve" and the "R-curve", or "resistance curve", at X. If the load is increased further, the crack continues to extend until the curves become

tangential at the point C. From this point, unstable crack growth may occur at constant load. The stress intensity factor associated with this condition is referred to as the "fracture toughness", K_c.

In many engineering materials, the crack growth may be zero or negligible until some initiation value of stress intensity is achieved. In addition, when the plastic zone is very small compared with the specimen thickness, blunting and shear lip formation are inhibited and the increase in resistance after initiation may be correspondingly small. This combination gives a sharp 'corner' in the R-curve, and the toughness becomes insensitive to the shape of the G-curve and consequently independent of the geometry. This toughness is the "plane strain fracture toughness", denoted by K_{Ic}, and is essentially a material property.

Historically, the concept of a critical stress intensity, K_{Ic}, for unstable crack growth pre-dates the R-curve concept [5,6] and it has been used for thick section and brittle materials as a design parameter. Its relevance will be discussed with reference to the micro-mechanisms of crack growth in Section 3.2. As a special case of the R-curve tangency condition, K_{Ic} may be considered as the minimum possible stress intensity for unstable crack growth.

2.1.5 Fracture Mechanics and Fatigue Crack Growth

As the stress intensity factor characterises the crack tip stress-strain field, it is reasonable to expect some correlation between any crack growth process and K_I. In traditional fatigue analysis, the time to failure is normally related to the stress range, $\Delta\sigma$ (or alternating stress, $\sigma_a = \frac{1}{2}\Delta\sigma$), and the mean stress, σ_m. For crack propagation analyses, the corresponding parameters would be the stress intensity range (c.f. equation (2.7)):

$$\Delta K \equiv \Delta L\, f(a) \qquad (2.11)$$

and some mean value of K. If K_m (= $L_m f(a)$) is used, then it is a function of crack length, as is ΔK. If the stress ratio, R, is used, there is no dependence on crack length.

Rigorously:

$$R \equiv \frac{\sigma_{min}}{\sigma_{max}} \tag{2.12}$$

For $R \geq 0$, there is no ambiguity in:

$$R = \frac{\sigma_{min}}{\sigma_{max}} = \frac{L_{min}}{L_{max}} = \frac{K_{min}}{K_{max}} \tag{2.13}$$

The case of $R < 0$ will be discussed in Section 3.1.1 and in Appendix II.

Paris [13] showed that for a wide range of values of ΔK, the crack advance in each loading cycle, da/dN, is related to the stress intensity range by a simple power law. At constant R:

$$\frac{da}{dN} = A\ (\Delta K)^n \tag{2.14}$$

In fact, a similar expression was proposed by Frost [14] some years earlier. From dimensional analysis, he had concluded that:

$$\frac{da}{dN} \propto \sigma^3\ a \tag{2.15}$$

Intuitively, as the maximum stress intensity in each cycle approaches the critical value, K_c, the crack growth rate should increase towards infinity. A variety of empirical relationships have been derived. For thin section aluminium alloys, that due to Forman et al [15] is widely used:

$$\frac{da}{dN} = \frac{A\ (\Delta K)^n}{(1-R)\ K_c - \Delta K} \tag{2.16}$$

Pearson [16] modified this for thicker sections, by taking the square root of the bottom line.

The presence of the term K_c may cause some difficulty as it has been demonstrated that this is sensitive to the geometry and crack length (Section 2.1.4). This may not be true of the stress ratio dependence in general. Omitting the high growth rate region altogether, Walker [17] suggested:

$$\frac{da}{dN} = f\,[K_{max}\,(1-R)^p] \tag{2.17}$$

and Boeing [18] use: $$\frac{da}{dN} = \alpha\,\left(\frac{K_{max}\,Z}{M}\right)^p \tag{2.18}$$

where α, p and M are constants, and $Z = (1-R)^q$, q being a further constant. The use of K_{max} rather than ΔK is not significant as both (2.17) and (2.18) reduce to equations of the form:

$$\frac{da}{dN} = \frac{A\,(\Delta K)^n}{(1-R)^r} \tag{2.19}$$

At very low stress intensities, there is evidence of a threshold value, ΔK_{th}, below which crack growth is negligible. Some empirical equations include such a term, but these are not widely used.

2.2 CURRENT PRACTICE IN THE CIVIL AIRCRAFT INDUSTRY [19-21]

The principal areas of application of fracture mechanics were discussed in Section 1.2. In most cases, civil aircraft structures are designed to operate with net section stresses well below the yield stress in fatigue critical areas. There are, however, three factors which are of particular importance in aircraft fracture analyses:

i) The majority of aircraft structural components are constructed from ductile materials with fairly thin sections. For this reason, one cannot assume that failure will occur by mode I (plane strain) fracture. Mode transition, transverse strains, and slow stable crack growth may affect behaviour to a significant extent.

ii) The development of fail-safe and damage tolerant structures has led to designs in which cracks may exist which are large in comparison with local geometric features. For this reason, standard stress intensity solutions [8] must be extended by means of compounding and superposition techniques [22]. There is also the possibility of a redistribution of load when one member of a redundant structure contains a growing crack [23]. These factors may become serious problems when the iterative crack growth calculations associated with fatigue or *R*-curve analyses are considered. They may also make more complicated analytical methods, such as those of yielding fracture mechanics, undesirable unless a substantial improvement in reliability can be demonstrated.

iii) The loading applied to aircraft structures is rarely of constant amplitude. Indeed, many areas of the structure are subjected to a very broad band random loading. Fatigue life and crack propagation predictions are normally based on an expected load spectrum for an aeroplane in "normal service". The residual strength, however, must be sufficient to withstand a much higher load with a suitable safety margin at any time. Thus, the final failure must be considered for any crack length or prior loading history, and not simply as the final cycle of a fatigue test.

2.3 THE VALIDITY OF LINEAR ELASTIC FRACTURE MECHANICS

It was indicated in Section 2.1.3 that LEFM may become inaccurate if

the plastic zone size, r_p, is too large. For many cases, simple "corrections" may be applied to account for some degree of contained plasticity. Two methods are widely accepted and involve modifications to the crack length, a.

2.3.1 Compliance Derived Crack Length

Using equations (2.4) and (2.6), it is possible to relate the stress intensity factor to the specimen compliance for a specified geometry without precise knowledge of the crack length. The apparent crack length may subsequently be calculated from equation (2.7). This will, in fact, be the equivalent crack length for a perfectly elastic body. The application of this method to the current test programme is described in Sections 4.2 and 4.4.3.

2.3.2 Plastic Zone Correction

An alternative method of correcting for plasticity [7] is by adding the plastic zone size to the crack length. i.e.

$$a' = a + r_p \tag{2.20}$$

In either case, LEFM only remains valid if the plastic zone size is significantly less than the uncracked ligament width. Once again, this aspect is discussed in some detail in Chapter 4, where the test specimen design is described.

The compliance derived crack length is most readily used for fracture testing of simple specimens. The plastic zone correction is more easily applied in design studies and in the assessment of engineering structures.

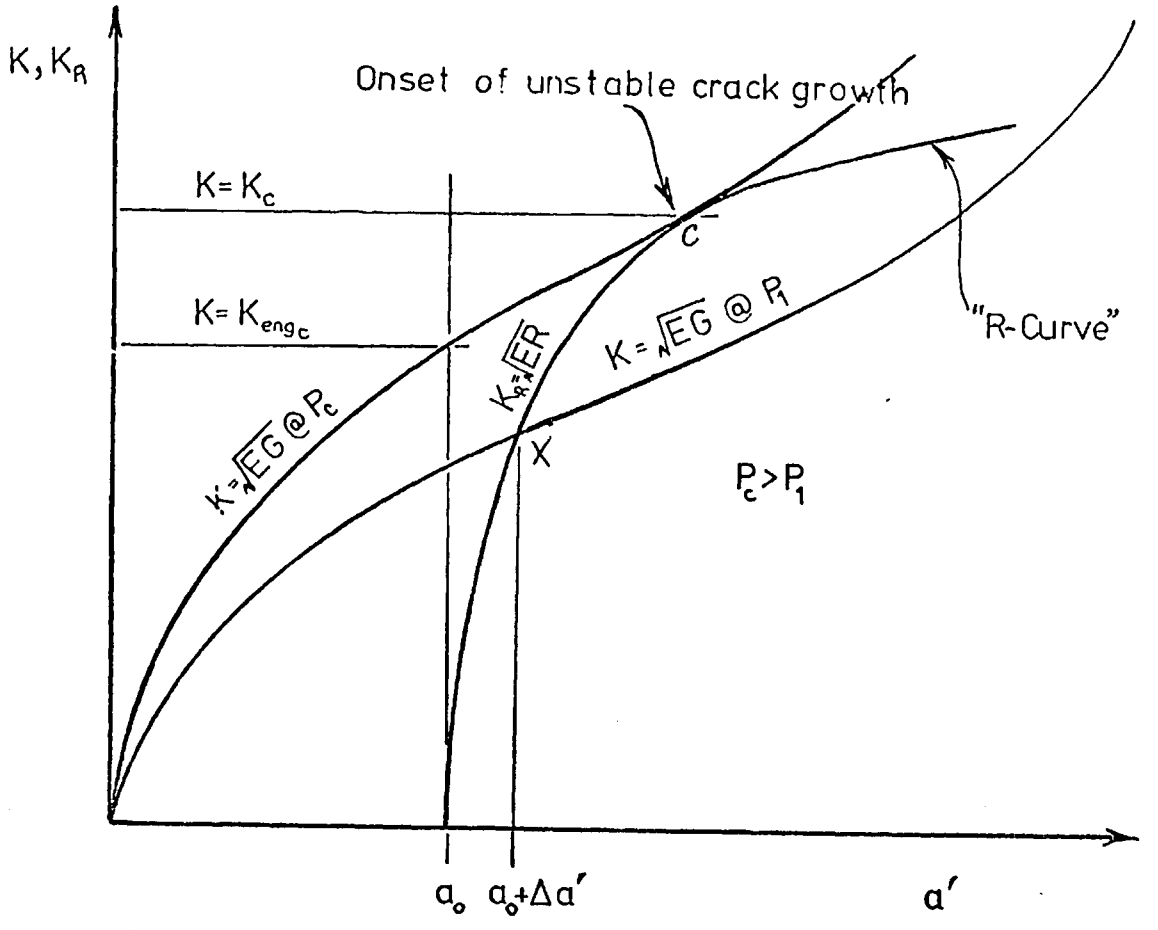


Figure 2.1: Crack growth resistance curve ("*R*-curve")

CHAPTER 3

CRACK PROPAGATION MECHANISMS

Fatigue crack propagation in ductile alloys is influenced by a number of processes. In particular, slip-controlled mechanisms of striation formation, and micro-void coalescence, may be important. Some consideration will also be given to brittle (cleavage) and environmental processes.

3.1 SLIP-CONTROLLED MECHANISMS

In the early stages of fatigue crack growth from a notch or from a smooth surface, the crack may extend on the principal shear plane as imperfect reversal of the slip results in the formation of "intrusions" and "extrusions" where slip bands meet the free surface [24].

Once the defect has reached a sufficient size, the crack turns from the principal shear plane ("stage I" growth) to a plane normal to the applied tensile stress. Fracture surfaces in stage II growth frequently exhibit lines running (approximately) parallel to the crack front at intervals similar to the crack advance in one cycle. Observation of these markings after programmed-load variable amplitude testing shows that each marking is the result of the action of a single load cycle [25,26]. There are a number of theories of this "striation formation" in ductile materials [25-28], all of which depend on slip occurring on at least two planes passing through the crack front. Figure 3.1 shows a generalised process of crack blunting and re-sharpening [27,28] typical of these models. On loading, the maximum shear stress occurs on two planes at $\theta = \pm cos^{-1}(1/3)$ through the crack front. In an homogeneous material, slip first occurs on these planes. The crack becomes blunt, and Rice [29] has shown that the profile may be represented by calculation of the crack

tip opening displacement (CTOD) and the crack tip advance displacement (CTAD) which are each directly proportional to the reversed plastic zone size, Δr_p (q.v.). On unloading, slip on the planes through the crack tip is restricted by oxide formation and local hardening. The CTOD is reduced by slipping on other planes, but the CTAD is not (Figure 3.1) and permanent crack extension results.

3.1.1 Reversed Plastic Zone Size

The plastic zone size may be estimated by assuming that the strain distribution is given by equation (2.5), regardless of local yielding, i.e.

$$\varepsilon_{yy} \simeq \frac{K_I \cos \theta/2}{E\sqrt{2\pi r}} \left(1 - \sin\frac{\theta}{2}\cos\frac{3\theta}{2}\right) \quad , \quad \text{etc.} \tag{3.1}$$

This is a reasonable assumption when the plastic zone is entirely embedded in an elastic region of the material. The stress and strain distributions associated with a load, L_{max}, and $\theta = 0$ are shown in Figure 3.2a for a perfectly elastic-perfectly plastic material [29]. On unloading (i.e. $L \to 0$), it is then assumed that the strain returns to zero for all values of r and $\theta = 0$. Referring to Figure 3.2b, the first loading cycle causes the stress/strain to change from O to A and back to B, resulting in the stress distribution of Figure 3.2c. During subsequent cycles, the strain varies between zero and ε_{max}, as shown in Figure 3.2b, so that fully reversed plastic straining only occurs very close to the crack tip. If this "reversed plastic zone size" is Δr_p, Rice [29] showed that for a perfectly elastic-perfectly plastic material in plane stress (c.f. equation (2.8)):

$$\Delta r_p = \frac{1}{\pi}\left(\frac{\Delta K}{2\sigma_y}\right)^2 \tag{3.2}$$

and in plane strain (c.f. equation (2.9)):

$$\Delta r_p \approx \frac{1}{3\pi} \left(\frac{\Delta K}{2\sigma_y}\right)^2 \tag{3.3}$$

Schwalbe [28] has carried out the same analysis for a material with a work-hardening exponent, n', measured after plastic strain cycling to saturation. He obtained:

$$\frac{\Delta r_p}{r_p} = \frac{2^{n'+1}}{4} \left(\frac{\sigma_y}{\sigma'_y}\right)^2 \tag{3.4}$$

in both plane strain and plane stress. σ_y and σ'_y are the tensile yield stress before and after cycling to saturation.

Notice that if the minimum stress is compressive, the strain energy distribution at the minimum load may be taken as:

$$\varepsilon_{yy} = \frac{\sigma_{min}}{E} \tag{3.5}$$

where σ_{min} is the section stress, ignoring the existence of the crack. Now, following Rice's method for fully reversed plastic straining, where $\Delta\varepsilon_{yy} \geq 2\sigma_y/E$, we have:

$$\Delta\varepsilon_{yy} = \frac{K_{Imax}}{E\sqrt{2\pi r}} + \frac{\sigma_{min}}{E} \tag{3.6}$$

Thus:

$$\Delta r_p = \frac{1}{\pi} \left(\frac{K_{Imax}}{2\sigma_y - \sigma_{min}}\right)^2 \tag{3.7}$$

which is identical to (3.2), except that the term ΔK is replaced by:

$$K_{Imax} \left(\frac{2}{2 - \sigma_{min}/\sigma_y}\right) \tag{3.8}$$

The equations (3.2) to (3.8) are independent of the stress ratio, R.

3.1.2 Striation Spacing

From the foregoing argument, one expects the crack growth rate to be equal to the striation spacing, which is equal to the CTAD. As this is directly proportional to Δr_p, we have (for $R \geq 0$):

$$\frac{da}{dN} = \bar{s} \propto (\Delta K)^2 \tag{3.9}$$

where $\bar{s}$ is the mean striation spacing.

Another method [30,31] is to relate the crack advance by striation formation directly to the maximum CTOD, giving:

$$\frac{da}{dN} \propto \frac{K_{max}}{E\,\sigma_y} = \frac{(\Delta K)^2}{(1-R)^2\,E\,\sigma_y} \tag{3.10}$$

Tomkins [31] goes on to show that at low growth rates, the mean striation spacing, $\bar{s}$, is very much larger than the growth rate in an alloy steel, but that at high stress intensities, $da/dN > \bar{s}$. This is confirmed by Broek [25], Kirby & Beevers [32] and Yokobori [33] and others for both aluminium alloys and steels.

Under a monotonically increasing load, crack extension by slip controlled mechanisms is likely to be small, but may be present in the form of a "stretch zone" at the onset of crack growth [25,34].

3.1.3 Crystallographic Effects [35]

Figure 3.3 shows the arrangement of atoms in a single unit of each of three crystallographic structures which are found in engineering alloys. They are the face-centre cubic (FCC) structure, found in

aluminium alloys and austenitic steels; the body-centre cubic (BCC) structure common to most other steels; and the close-packed hexagonal (CPH) structure, found in titanium and zinc. The most common form of plastic deformation occurs when layers of atoms within the crystal move over one another (i.e. 'slip') so that each atom takes up a position where another atom had been before and the lattice structure is not changed. (In practice, residual imperfections - dislocations - remain after any such deformation. These may inhibit further slip and influence the mechanical properties and behaviour during heat treatments.)

Slip will usually occur as the planes with the closest packing move over each other. The most densely packed planes are also the most widely separated, and this particular deformation process requires the least shear stress. In addition, the direction of slip will always be in the direction of closest packing within the plane, as the energy required to move an atom from one position to the next (the dislocation strain energy) is the least in that direction. Thus, slip planes and slip directions are defined for any particular crystal structure. One slip direction on one slip plane is referred to as a slip system.

The FCC structure contains the most dense overall packing possible. This gives four close-packed planes, each having three close-packed directions (Figure 3.4) so that there are twelve slip systems, all requiring the minimum possible strain energy. This is particularly important during slip-controlled crack extension processes, where it gives a high probability of two slip systems lying closely to the two planes of maximum shear stress ($\theta = \pm cos^{-1} 1/3$).

In the BCC structure are three "families" of four slip planes, but none close-packed. In each plane, there is a single close-packed direction (the cube diagonal). This also gives a total of twelve slip systems, but slip is generally more restricted than in the FCC system.

The CPH structure has only one close-packed plane with three slip directions, giving only three slip systems. The precise deformation behaviour is influenced by the spacing between the close-packed planes but, in general, CPH materials have very restricted slip behaviour.

3.2 MICRO-VOID COALESCENCE

In engineering alloys, crystallographic slip cannot continue to failure because of the behaviour of the material in the vicinity of second phase particles or impurities. In the late 1940s, Tipper [36] observed the formation of voids around inclusions in mild steel subjected to very high strains. Improved microscopy techniques showed this to be the most common cause of ductile failure in many materials [37].

Essentially, the void forms by decohesion of non-deformable particles within the matrix, such as oxides and sulphides in steels, and iron- or silicon-rich particles in Al-Zn-Mg alloys (see Section 3.6). It has been shown that the applied stress required to nucleate a void is given by [38]:

$$\sigma_v \propto \sqrt{\frac{E\gamma}{p}} \tag{3.11}$$

where γ is the free surface energy, and p is the diameter of the particle. For convenience, this may be expressed in terms of the volume fraction, v_f, of the relevant inclusion phase and the distance between particles, $\bar{d}$. Thus:

$$p^3 = v_f \bar{d}^3 \tag{3.12}$$

and the void nucleation strain, ε_v, is given by:

$$\varepsilon_v = \frac{\sigma_v}{E} \propto \sqrt{\frac{\gamma}{E p}} \tag{3.13}$$

The constant proportionality in equations (3.11) and (3.13) depends on the shape and relative rigidity of the particle within the matrix. As γ is a material constant, it may be included in the proportionality. Thus, substituting from equation (3.12), we have:

$$\varepsilon_v \propto v_f^{-1/6}\, \bar{d}^{-1/2} \tag{3.14}$$

From equation (3.1), with $\theta = 0$:

$$\varepsilon_v = \frac{K_{Iv}}{E\sqrt{2\pi\, r}} \tag{3.15}$$

in which r is the distance from the crack tip to the void nucleation site. If tearing is the only crack extension mechanism available, then the crack tip must always advance from one such particle to the next, so that $r = \bar{d}$. Thus, combining equations (3.14) and (3.15), the stress intensity factor required for void nucleation is:

$$K_{Iv} \propto v_f^{-1/6}\, \sqrt{2\pi/E} \tag{3.16}$$

Failure of the ligament between the crack tip and the void is assumed to depend on tensile instability ("necking") [39]. For this to occur, a constant load condition is required. i.e.

$$\frac{dP}{P} = 0 \quad \Rightarrow \quad \frac{\partial\sigma}{\partial\varepsilon} = 0 \tag{3.17}$$

For a power law strain hardening material with $\sigma = K\varepsilon^n$, the ligament instability strain, ε_i, may be derived, assuming a constant volume process ($\nu = 0.5$) at the instability point. This gives:

$$\varepsilon_i = n \tag{3.18}$$

Once again, using equation (3.1) with $\theta = 0$, the stress intensity factor for ligament instability becomes:

$$K_{Ii} = E\,\varepsilon_i \sqrt{2\pi\, r} = E\, n \sqrt{2\pi\, r} \tag{3.19}$$

By the same argument as that preceding equation (3.16), where tearing is the only mechanism available, the distance from the crack tip to the next void must be $r = \bar{d}$ for sustained crack growth. Thus:

$$K_{Ii} = E\, n \sqrt{2\pi\, \bar{d}} \tag{3.20}$$

The overall condition for crack growth by void coalescence alone is achieved when the stress intensity factor exceeds both K_{Ii} and K_{Iv} simultaneously. This is illustrated in Figure 3.5. The point $\bar{d}_1$ is typical of an inclusion phase in an engineering alloy, where the void initiates readily, and final failure is controlled by the ligament instability condition. Notice that increasing the particle size (i.e. increasing v_f at constant $\bar{d}$) does not influence the toughness. This is observed in practice for particles between 1 μm and as much as 200 μm in diameter [38]. Indeed, large particles are beneficial for a given volume fraction as this implies a large $\bar{d}$.

The point $\bar{d}_2$ is representative of a finely dispersed phase in which the nucleation stress intensity is greater than that required for ligament instability. The fine strengthening phases in aluminium alloys do not, in fact, behave in quite this way as they are capable of some deformation and may be partially coherent with the matrix, so that the constant of

proportionality in equation (3.11) is correspondingly high. Their primary contribution is in inhibiting dislocation movement, and thereby increasing the work hardening exponent, n. This increases K_{Ii} in equation (3.20).

3.3 CLEAVAGE, AND BRITTLE STRIATIONS

Failure by cleavage implies the separation, rather than the relative slip, of crystallographic planes. It is not a likely mode of failure in homogeneous FCC crystals, as it requires very much more energy than slip. In more restrictive lattice structures, and especially at low temperatures, cleavage may occur. This is apparent in the ductile-brittle transition of many steels at low temperatures and accounts for the use of aluminium alloys and austenitic steels in cryogenic process plant. Cleavage may also be induced by the absorption of damaging chemical species into the metal, as occurs with hydrogen embrittlement, for example.

There has been a number of reports of cleavage facets formed at low stress intensity ranges during fatigue cracking of aluminium alloys [40] and a distinction has been drawn between ductile and brittle striations [24]. Recent developments in high-resolution electron microscopy have demonstrated that cleavage does not, in fact, occur under these conditions and that variations in the appearance of striation profiles are due, primarily, to variations in the relative orientation of the crystallographic slip systems and the maximum shear stress planes ahead of the crack [26,41]. This is discussed in some detail in Section 3.1.

There may be some cleavage failure at the beginning of each loading half-cycle in fatigue if an appropriate chemical species has been absorbed (e.g. hydrogen or oxygen). This may account for the alternate bands of high deformation and relatively low dislocation density associated with the very marked striations found on aluminium alloy fracture surfaces, resulting

from fatigue failures in normal air environments [26]. If this is the case, the striation markings are each, in fact, part "brittle" and part "ductile".

3.4 EFFECT OF CYCLING FREQUENCY, AND ENVIRONMENTAL INFLUENCES

It is well known that in corrosive environments, the rate of crack propagation under fatigue loads is dependent on the frequency of load cycling [42,43]. This is easily understood, qualitatively at least, if it is assumed that crack propagation combines a fatigue mechanism, which is dependent on the number of cycles experienced, and a corrosion mechanism, which is dependent on the elapsed time. Any interaction between these two is influenced both by the number of cycles and by the elapsed time, and thus by the frequency.

Variations in fatigue crack growth rates in non-corrosive environments have been observed, often in 'control' experiments for corrosion fatigue test experiments [44-46], although there is some recent literature reporting tests aimed specifically at investigation of frequency effects in air.

Bradshaw & Wheeler [45] identified two types of frequency dependence. In creep resistant alloys, including RR58 Al clad sheet to DTD.5070A (2618-T6), there was no variation in crack growth rate with frequency in a vacuum, whereas in air lower crack growth rates - da/dN - were observed at 100 Hz than at 1 Hz or 1/60 Hz. However, in DTD.683 (7075-T6) Al clad sheet, which is known to be more prone to creep, a general trend towards lower growth rates at higher frequencies was noted both in air and *in vacuo*. To quote their paper, "the immediate conclusion is that frequency effects *in vacuo* depend on the alloy, and that in air frequency effects can sometimes be caused solely by the environment." The results show greatest sensitivity at around ΔK = 12 $MN/m^{3/2}$, which was the highest

stress intensity tested, with little or no effect at 5 $MN/m^{3/2}$ in DTD.5070A in air.

Hartman & Schijve [46] carried out very similar tests to those of Bradshaw & Wheeler using 2024-T3 Al clad and 7075-T6 Al clad aluminium alloy sheets in the frequency range 0.4 Hz $\leq f \leq$ 60 Hz in dry and "wet" air. A decrease in crack growth rate with increasing frequency was noted throughout the range, being most marked in 2024-T3 in dry air. The minimum stress intensity range tested was around 10 $MN/m^{3/2}$, and frequency dependence decreased as stress intensities increased from that level to K_c.

Results throughout the range of stress intensity, from threshold to K_c, in RR58 aluminium alloy specimens [44] show little frequency effect at the extremes of this range, but significant differences in crack growth rate between tests at 0.15 Hz and 35 Hz at intermediate levels.

Two recent papers offer empirical relationships between frequency and crack growth rate. Yokobori & Sato [33] tested 2024-T3 aluminium alloy and SM-50 steel, and measured both crack growth rates and striation spacing. They suggest a relationship of the form:

$$\frac{da}{dN} = A\ (\Delta K)^{3\cdot 5}\ f^{-\lambda} \qquad (3.21)$$

where f is the frequency, and $0.08 < \lambda < 0.09$.

A Russian investigation [47] of D16AT ($\simeq$ 2024-T3) and V95 ($\simeq$ 7075-T6) aluminium alloys showed no dependence on frequency for $f \leq$ 10 Hz. Revising their notation, an approximate relationship was found as follows:

$$\left(\frac{da}{dN}\right)_{f=f} = \phi\ \left(\frac{da}{dN}\right)_{f=10\ \mathrm{Hz}} \qquad (3.22)$$

where, for $f \leq$ 10 Hz, $\phi = 1$, and for $f >$ 10 Hz, $\phi = (1.07 - 0.07\, f^*)\, F\,(\Delta K, f^*)$, in which $f^* = f/10$, and F may be obtained by linear interpolation in the

following table:

	$\Delta K = 0$	$\Delta K = 30$ MN/m$^{3/2}$
$f^* = 1$	1	1.07
$f^* = 10$	1	2.40

3.5 PLANE STRAIN FRACTURE TOUGHNESS

The concept of plane strain fracture toughness was introduced in Section 2.1.4. In terms of the micro-mechanisms involved, K_{Ic} must be the minimum stress intensity factor for which a monotonic loading mechanism can cause sustained crack growth. For ductile materials, this is normally the minimum value of K_I for crack growth by void coalescence, given by equation (3.20), i.e.

$$K_{Ic} = K_{Ii} = E\, n \sqrt{2\pi\, \bar{d}} \tag{3.23}$$

3.6 SOME NOTES ON THE METALLURGY OF ALUMINIUM ALLOYS [48-50]

Aluminium is extracted from alumina-rich minerals, known collectively as bauxite, by a two-stage process. The alumina is first prepared by the Bayer process, in which it is dissolved out of bauxite in hot caustic soda. The alumina is then reduced, electrolytically between carbon electrodes, in solution in molten cryolite. This second process, known as smelting, requires a very heavy current, low voltage electricity supply. For this reason, no commercial production of aluminium was possible until the late nineteenth century. Modern smelting plants are usually sited close to hydro-electric power stations and may consume as much as 60 MW continuously.

Bauxite contains, typically, 40%-60% alumina (Al_2O_3) and 12%-30% water. In addition, Fe_2O_3 (5%-30%), SiO_2 (1%-8%) and TiO_2 (2%-4%) are usually present. As a result, commercial grades of "pure" aluminium are expected to contain around 0.1% silicon and 0.12% iron as the principal impurities.

Although commercially pure aluminium finds some applications, it is normally used in alloy form. The addition of up to 1.25% manganese or 7% magnesium may be used to form a useful range of lightweight, corrosion resistant alloys of up to ≈ 300 MN/m^2 UTS after work hardening. They are classified by the Aluminium Association as '3000 series' and '5000 series' alloys, respectively.

Casting alloys are usually produced with a high silicon content - typically 11% - to improve flow properties.

The most significant ranges of aluminium alloys in the aerospace industry are the heat-treatable, wrought alloys [51-54]. The original alloy in this category was developed by Wilm in 1906. He found that an alloy of Al-4.5% Cu-1.5% Mg was softened by quenching, but then hardened at room temperature to give strength as high as 400 MN/m^2 (UTS) after a few days. The alloys used in modern aircraft structures fall into two categories: those based on the aluminium-copper system ('2000 series'), and those based on the aluminium-zinc-magnesium system ('7000 series').

Figure 3.6 shows the relevant portion of the Al-Cu binary phase diagram, in which the α-phase has an FCC structure and θ is a tetragonal intermetallic phase of approximate composition $CuAl_2$. Alloys containing less than 5.7% copper are heated to around 550°C and then quenched to form a super-saturated α solution. On ageing at room temperature (e.g. T3 and T4 tempers), sub-microscopic copper-rich zones form which are coherent with the matrix. These are known as Guinier-Preston zones and they subsequently form into larger coherent platelets of the θ″ phase. These

cause strengthening by interaction with dislocations, but the alloy retains a high toughness.

Artificial ageing at temperatures of around 190°C (e.g. T6 and T8 tempers) leads to the formation of semi-coherent θ′ and incoherent θ particles, especially at grain boundaries and dislocations. These increase the proof strength significantly, but reduce the fracture toughness as they provide preferential crack paths.

Commercial 2000 series alloys also contain magnesium which forms GP-B zones of CuMg on room temperature ageing, and a partially coherent *S* phase, Al_2CuMg, during artificial ageing. Plastic deformation between quenching and ageing (e.g. TX51 tempers) leads to a finer distribution of θ′ and *S*, which both nucleate at dislocations. Manganese is also added to improve tensile properties and some alloys, such as 2014, contain silicon to improve artificial ageing. Weldability improves with decreasing magnesium content (e.g. 2014 and 2219 alloys) and stability of the grain structure at elevated temperatures may be improved by adding iron and nickel to form an insoluble $FeNiAl_9$ phase, as in the RR58 alloy series (e.g. 2618).

Strengthening mechanisms in 7000 series alloys are similar, but here the relevant precipitates are the η ($MgZn_2$) and *T* (Mg_3Zn_3Al) phases. In general, very much higher strength may be achieved compared with 2000 series alloys, but often at much lower toughness and with poor stress corrosion resistance. The low toughness is attributed to the presence of iron and silicon impurities mentioned earlier in this chapter [55]. Iron may form massive particles of Al_7Cu_2Fe, which have little effect on strength but which reduce the toughness severely. Silicon normally forms Mg_2Si. This depletes the matrix of magnesium, and hence of the η and *T* phases, and thus reduces the strength. Theoretically, there is a corresponding increase in toughness. However, if the alloy is aged to the specification strength, the final toughness may, in fact, be reduced.

Conventional alloys, such as 7075, have maximum permitted impurity levels of around 0.5% Fe and 0.4% Si. Recognition of the detrimental effects of these elements has led to reductions of levels in alloys, such as 7175 and 7475, in order to raise the toughness. Improved quality control may allow guaranteed maximum iron and silicon levels down to 0.12% Fe and 0.1% Si for production alloys, using conventional smelting processes. Super purity aluminium (e.g. 0.0005% Fe and 0.0003% Si) may be obtained by using an electrolytic refining process, but this increases the material cost and is unlikely to be economically viable, even though further toughness improvements are possible [55].

Reductions in iron and silicon levels also improve fatigue crack propagation performance under constant amplitude loading at high stress intensities [56]. There has been some recent debate on the effects of iron and silicon content under variable amplitude loading. Schulte et al [57] have shown that higher purity alloys exhibit less retardation of the crack, following severe overload. This issue is further complicated by some work [58,59] on - nominally - 7075-T7351 and 7010-T7651, showing lower crack growth rates for the 7075 alloy under spectrum loading. In fact, the "7075" used had the same Fe/Si content as the 7010, and the heat treatment had resulted in a higher toughness and lower strength, so that the improved crack propagation life is not surprising.

There is some danger of re-crystallisation during heat treatment of 7000 series alloys. Chromium, manganese or zirconium may be added to the material to form intermetallic particles which pin the grain boundaries and prevent reversion to an equiaxed structure. Chromium, and to a lesser extent manganese, makes the alloy very sensitive to quench rate, particularly with reference to its fracture toughness. Thus, zirconium is preferred for high toughness materials, where thick sections are to be solution treated (e.g. 7010 and 7050).

The level of copper in 7000 series alloys is also very important. A low copper content improves weldability (e.g. 7039, 7079) and castability, but a high copper content improves stress corrosion resistance. There is some evidence [60] that copper is detrimental to fatigue and fracture properties, presumably because of its part in forming Al_7Cu_2Fe, mentioned above. In more aggressive environments, the improved stress corrosion resistance offsets this effect and the overall effect in damp air is for copper to improve the fatigue crack propagation life slightly.

Further improvements to stress corrosion resistance may be obtained by ageing 7000 series alloys beyond their peak strength (e.g. T76, T736, T73 tempers).

Tables 3.1 and 3.2 list some common wrought, heat-treatable alloys used in aircraft structures.

3.7 SOME CRACK PROPAGATION MODELS

There have been many attempts to model fatigue crack propagation and it is not the author's intention to present an exhaustive survey. Five models are described briefly, and these are representative of five somewhat different approaches to the problem.

3.7.1 Tensile Ligament Instability Model (After Krafft [39,61,62])

This is one of the earliest models, based on the assumption that equations of the form of (3.20) may be applied to the entire fatigue crack propagation régime. This model has been developed into a sophisticated "normalising procedure for organising fatigue crack growth rate data with a minimum parameter system", which is successful in fitting a very wide range of fatigue and corrosion fatigue data.

Conditions for ligament instability below K_{Ic} are derived as follows. In the tensile ligament, stability is enhanced by strain

hardening but reduced by Poisson contraction, as discussed in Section 3.2. In addition, stress relaxation may occur during the dwell time of cyclic loading and this influences dP/P in equation (3.17). Thus, stability is reduced. Finally, Krafft introduces a surface corrosion rate, dependent on stress, to account for environmental effects. A set of "TLIM maps" are drawn up using the materials cyclic stress-strain curve. A value of $\overline{d}$ is chosen to fit the curves through the threshold condition and a maximum of four other parameters are used to fit data for variations in frequency, stress ratio, and environment. Krafft makes it clear [62] that this "is not a rigorous analysis of the elastic-plastic crack tip field, or of the micro-separation processes which reside in it. It is rather a refined dimensional analysis ..."

3.7.2 Plastic Strain Range Method (After Duggan [63])

A modification of Neuber's [64] theory for strains around blunt notches may be used to estimate the plastic strain distribution close to the tip of the fatigue crack. Once this is established, it is possible to calculate the plastic strain range, $\Delta\varepsilon_p$, within a notional process zone ahead of the crack. If a smooth specimen is subjected to plastic strain cycling, the number of cycles to failure, N_f, is given by the empirical relationship [65]:

$$\Delta\varepsilon_p \propto \frac{1}{\sqrt{N_f}} \tag{3.24}$$

If the process zone size, r_x, is proportional to the reversed plastic zone size, Δr_p, then:

$$\frac{da}{dN} = \frac{r_x}{N_f} \tag{3.25}$$

Using the strain distribution of equation (3.1):

$$\frac{da}{dN} \propto (\Delta K)^2 \tag{3.26}$$

The difficulty of this method lies in the derivation of a process zone size and in avoiding the prediction of infinite plastic strains (with the implication of zero life) at the tip of a sharp crack. The relationship between Coffin's equation, (3.24), and fatigue crack growth behaviour is not surprising, as low cycle fatigue lives are in any case dominated by crack propagation.

3.7.3 Super-Dislocation Analysis (After Kanninen & Atkinson [66])

Small scale yielding is treated as symmetrical pairs of super-dislocations on the principal shear planes ($\theta = \pm cos^{-1}(1/3)$) ahead of the crack tip. One pair of dislocations represents the strain due to the current cycle and the other represents residual strain from preceding cycles. This gives a final equation:

$$\frac{da}{dN} \propto \frac{A}{E\,\sigma_y} (K_{max} - K_r)^2 \left(1 - \frac{\sigma_{max}}{\sigma_y}\right)^{-1} \tag{3.27}$$

in which A is a constant, and K_r is the "residual plasticity stress intensity factor". This model is related closely to the striation formation process described in Section 3.1.

3.7.4 "Fatigue Toughness" Method (After Turner [67])

Turner has proposed an energy balance method, whereby the fatigue toughness, R_f, is related to the plastic work done, and the strain energy release rate. The work done is integrated between limits, r_o and $\bar{r}$, assuming a similar strain energy distribution to that known for monotonic

loading cases. These limits represent the process zone dimensions; if $\bar{r}$ is assumed proportional to Δr_p, and r_o is replaced by:

$$r_o \equiv \left(\frac{\Delta K_{th}}{\sigma_y}\right)^2 \tag{3.28}$$

one obtains:

$$\frac{da}{dN} = \frac{C\,(\Delta K)^2\,(\Delta K_f^2 - \Delta K_{th}^2)}{\sigma_y^2\,(K_f^2 - K_m^2)} \tag{3.29}$$

in which $(\Delta K_f/\sigma_y)^2 \propto \bar{r}$ and $K_f^2 = E R_f$, assumed constant. K_m is the mean stress intensity factor.

3.7.5 Dual Mechanism Model (After Schwalbe [28])

Schwalbe's modification of Rice's equation for crack advance by blunting was described in Section 3.1. For crack growth by void coalescence, he obtains a condition for the crack tip strain to exceed the true fracture strain, ε_f. It is then assumed that, for $R = 0$:

(a) Striation formation is responsible for all crack growth below a value $K = K_1$, i.e. $da/dN = (da/dN)_s$.

(b) Void coalescence is responsible for all crack growth above a value $K = K_2$, i.e. $da/dN = (da/dN)_v$.

(c) In the transition region, $K_1 < K < K_2$:

$$\frac{da}{dN} = \left(\frac{K - K_1}{K_2 - K_1}\right)\left(\frac{da}{dN}\right)_s + \left(1 - \frac{K - K_1}{K_2 - K_1}\right)\left(\frac{da}{dN}\right)_v \tag{3.30}$$

This provides a smooth curve between the two theoretical models, but the terms K_1 and K_2 are purely empirical.

3.8 CRACK CLOSURE, AND STRESS RATIO EFFECTS

At any point just behind the advancing crack tip, some permanent

deformation will remain in the 'wake' of the plastic zone. When the crack is open, the tensile stress across the crack must be zero, and when the crack is closed, by symmetry the strain (ε_{yy}) must be zero. Immediately prior to the crack passing a particular point, the material is cycled according to a stress-strain diagram, such as Figure 3.2. The zero strain condition (point B) is not changed as the crack tip passes the position in question but, on loading, the strain increases elastically only as far as the zero stress condition, point C. During subsequent load cycles, the material at the crack sides continues to undergo elastic cycling between $\varepsilon_{min} = 0$ and $\sigma_{max} = 0$, so that for a part of each cycle, the faces are in contact and support a compressive stress.

Elber [68] argued that if a stress is supported across the crack near to the tip, no singularity occurs and that if, during any part of the cycle, the crack is closed, the stress intensity factor is meaningless and no damage can occur. If the nominal stress intensity factor at the point of crack opening is given by K_{op}, then Elber suggests that:

$$\frac{da}{dN} = f(\Delta K_{eff}) \tag{3.31}$$

where:

$$\Delta K_{eff} \equiv K_{max} - K_{op} \tag{3.32}$$

It has been shown that as the stress ratio increases, the opening stress changes so that equation (3.31) may be independent of stress ratio, R [68]. In practice, this is only true for fairly low values of R. If it is high, $K_{op} \rightarrow K_{min}$ and thus $\Delta K_{eff} \rightarrow \Delta K$. However, stress ratio continues to influence crack propagation rates [69-71].

The crack closure model also claims considerable success in explaining the effect of overloads during fatigue crack propagation tests, which tend to retard subsequent crack growth [72] but this can only be successful as

one component of a more complicated model [73,74].

Some further discussion of the crack closure approach is included in Section 7.4.

TABLE 3.1: "2000 Series" Aluminium Alloys

AA Designation	Temper	L-T Properties			Composition (%wt) Al-Rem.							Corresponding British Standards	Corresponding UK Ministry of Defence Standards	Corresponding Proprietary Standards	Remarks
		$K_{I\sigma}$ ($MN/m^{3/2}$)	σ_y* (MN/m^2)	UTS (MN/m^2)	Cu	Mg	Mn	Zn	Fe	Ni	Si				
2014	T451	44	250	400	4.5	0.5	0.8	0.25	0.7	-	0.8	L64 (Bar) L72 (Clad sheet) L89 (Clad sheet)			
2014	T651	27	405	460	4.5	0.5	0.8	0.25	0.7	-	0.8	L65 (Bar) L73 (Clad sheet) L90 (Clad sheet)			
2618	T651	30	370	420	2.6	1.5	-	-	1.15	1.15	0.25		DTD.731 (Plate) DTD.5070A (Sheet)	Hiduminium RR58	Developed for high temperature use
2219	T62	55	245	370	6.3	0.02	0.3	0.10	0.3	-	0.2		DTD.5004A (Forging)	Hiduminium RR57	Weldable alloy
2024	T3	49	310	430	4.4	1.5	0.6	0.25	0.5	-	0.5	L97 (Plate) L109 (Clad sheet)		Alcan GB24S	Used where very good fatigue properties are required
2024	T651	30	360	440	4.4	1.5	0.6	0.25	0.5	-	0.5	L93 (Plate)	DTD.5100 (Plate)	Alcan GB24S-WP	

* 0.2% proof stress

TABLE 3.2: "7000 Series" Aluminium Alloys

AA Designation	Temper	L-T Properties			Composition (%wt) Al-Rem.								Corresponding British Standards	Corresponding UK Ministry of Defence Standards	Remarks
		K_{Ic} ($MN/m^{3/2}$)	σ_y* (MN/m^2)	UTS (MN/m^2)	Zn	Mg	Cu	Cr	Mn	Zr	Fe (max)	Si (max)			
7010	"T7351"	41	420	500	6.2	2.5	1.7	<0.05	<0.03	0.14	0.15	0.10		DTD.5130	Alcan proprietary thermo-mechanical treatment
7010	"T7651"	36	440	530	6.2	2.5	1.7	<0.05	<0.03	0.14	0.15	0.10		DTD.5120	Alcan proprietary thermo-mechanical treatment
7039	T64	>44	330	390	4.0	2.8	0.1	0.2	0.25	-	0.4	0.3			
7049	T73	35	420	490	7.7	2.45	1.6	0.16	0.20	-	0.35	0.25			
7050	T73651	34	450	520	6.2	2.25	2.4	<0.04	<0.10	0.11	0.15	0.12			
7075	T6	30	450	520	5.6	2.5	1.6	0.21	0.30	-	0.5	0.4	L88 (Clad sheet) L95 (Plate)	DTD.683 (Clad sheet) DTD.5110 (Plate)	
7075	T73	32	365	440	5.6	2.5	1.6	0.21	0.30	-	0.5	0.4			
7175	"T736"	37	430	500	5.6	2.5	1.6	0.24	0.10	-	0.2	0.15			Alcan proprietary thermo-mechanical treatment. High purity forging material
7475	T73651	52	400	480	6.0	2.35	1.55	0.21	0.06	-	0.12	0.10			High purity sheet material
7178	T651	25	500	575	6.8	2.75	2.0	0.21	0.30	-	0.5	0.4			
7079	T6	29	435	495	4.3	3.3	0.6	0.18	0.20	-	0.4	0.3		DTD.5054A (Plate)	

* 0.2% proof stress

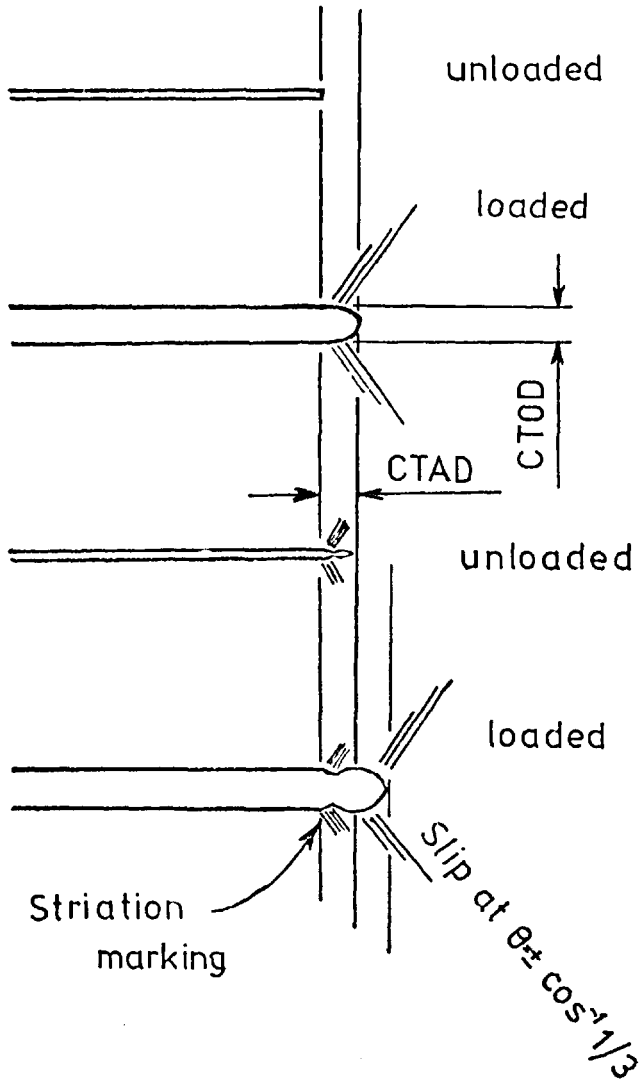


Figure 3.1: Blunting/resharpening model for fatigue crack growth

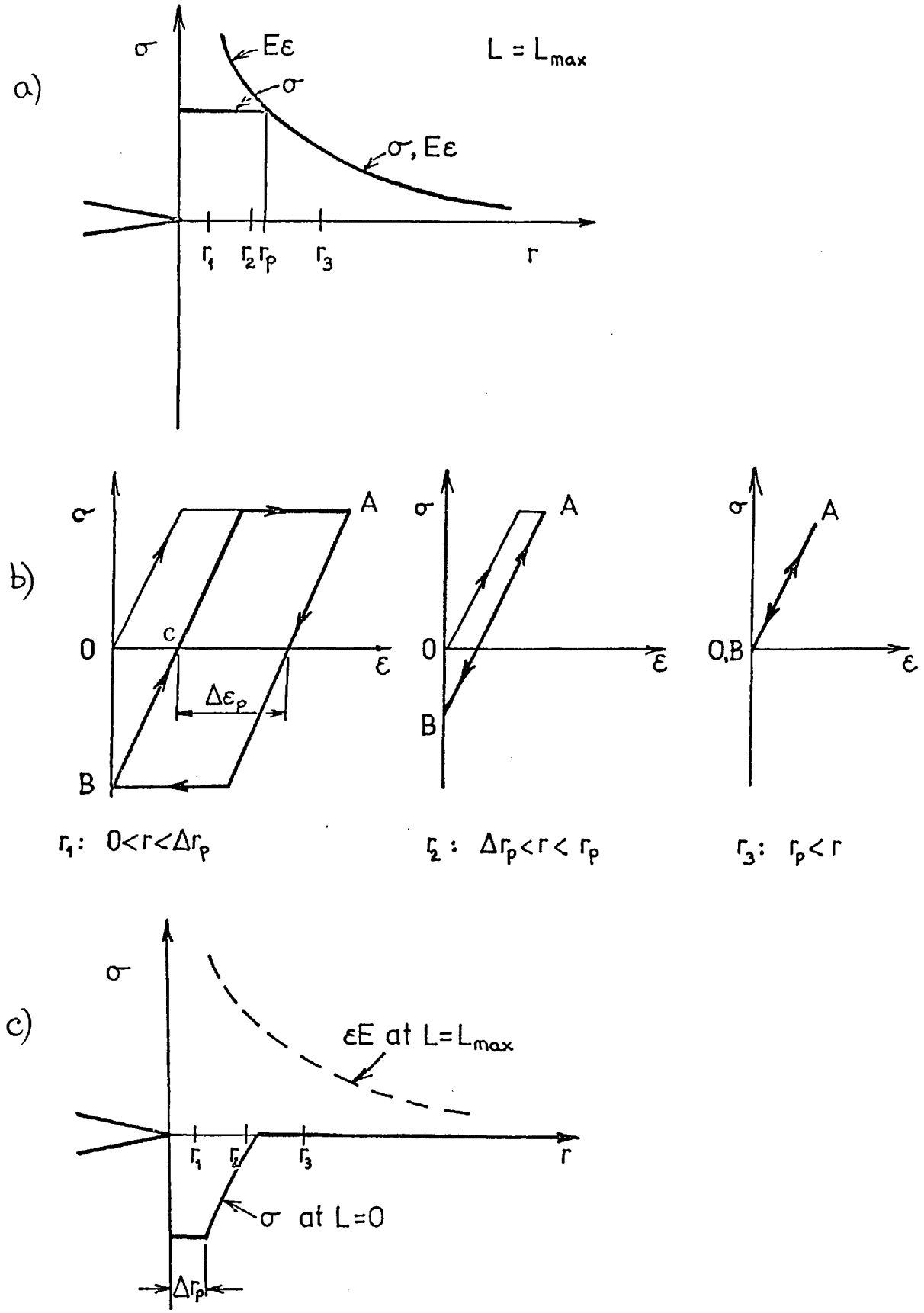
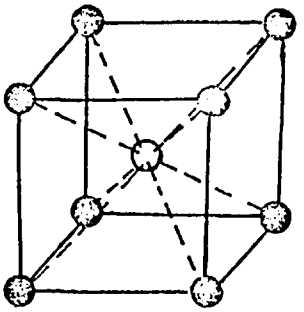
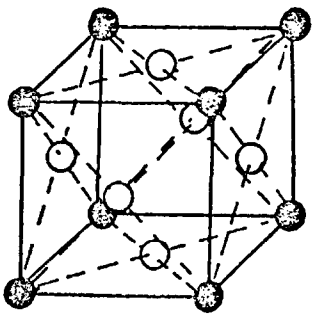


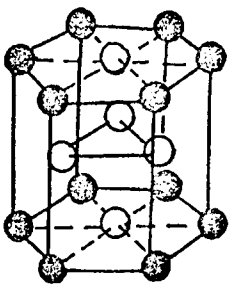
Figure 3.2: Monotonic and cyclic plastic zone sizes



BODY CENTRED CUBIC (B.C.C.)

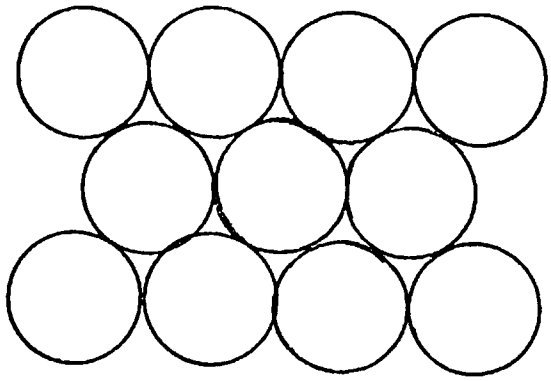
FACE CENTRED CUBIC
(F.C.C.)



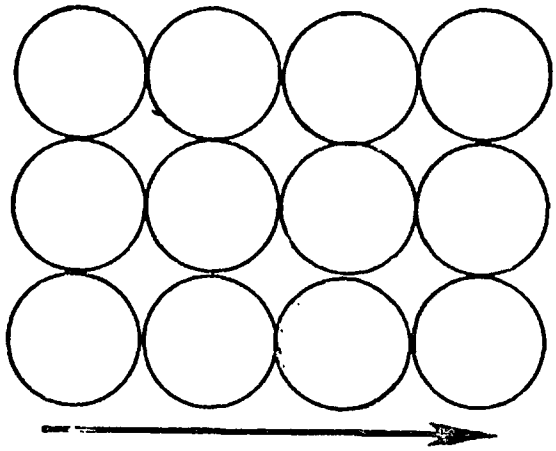


CLOSE PACKED HEXAGONAL
(C.P.H.)

Figure 3.3: Unit cells of crystal structures in engineering alloys



CLOSE - PACKED PLANE



CLOSE-PACKED DIRECTION

Figure 3.4: Close packing

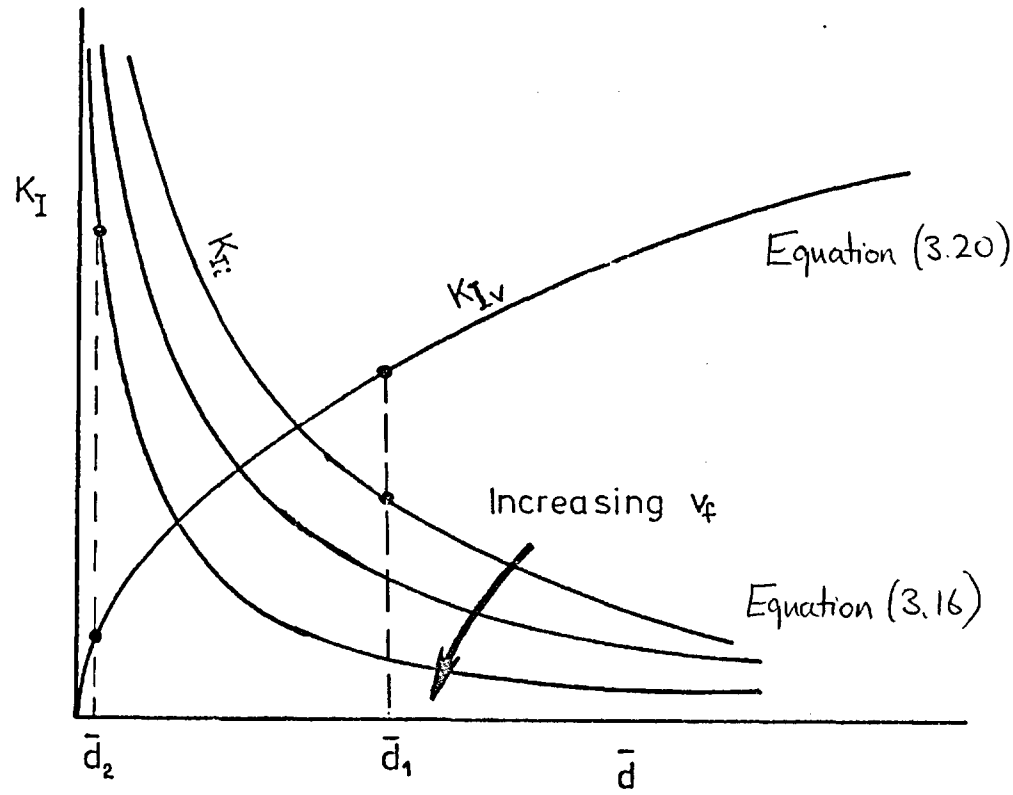


Figure 3.5: Void initiation and ligament instability conditions

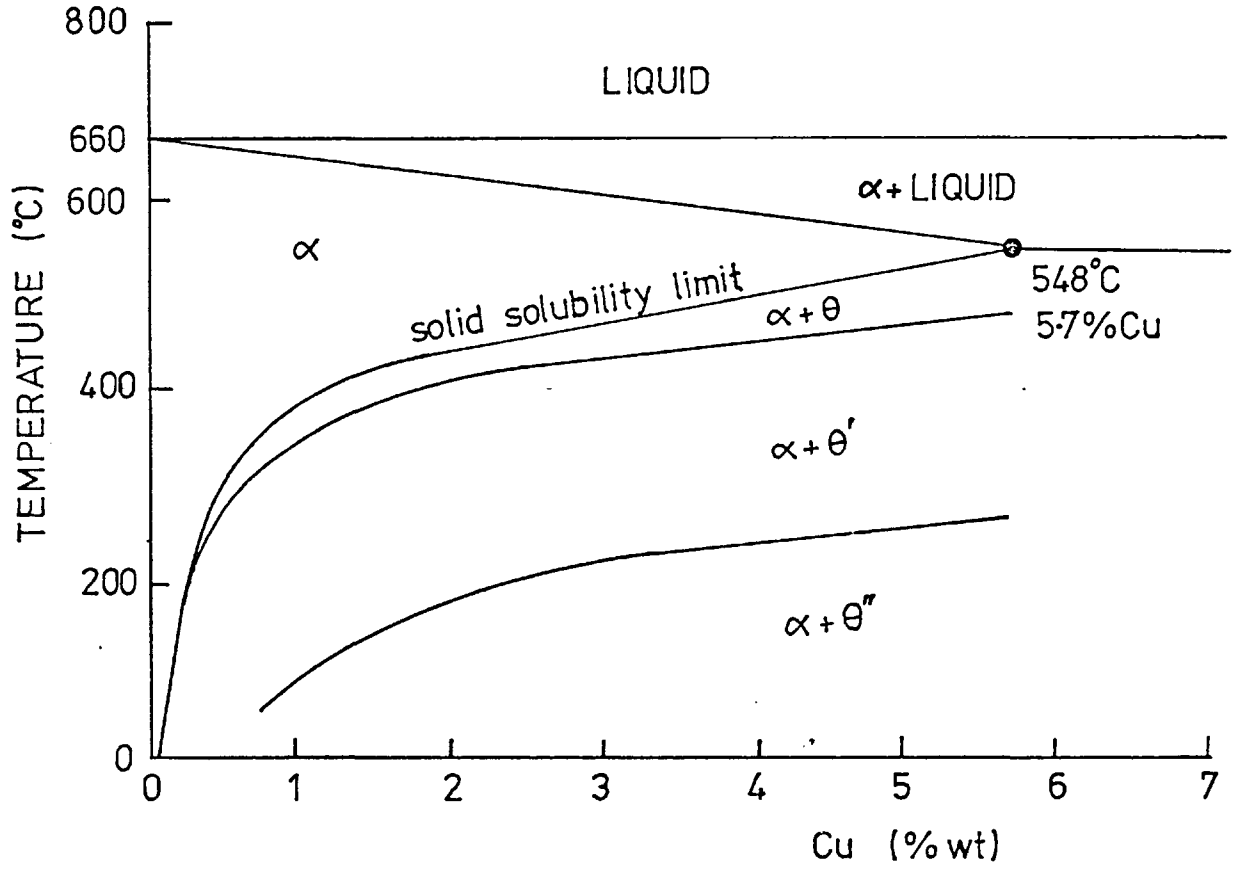


Figure 3.6: Binary phase diagram for aluminium and copper

CHAPTER 4

TESTING

4.1 REVIEW OF TEST TECHNIQUES

A number of standard test techniques exist, or are under development, for the measurement of fracture parameters. Plane strain fracture toughness (K_{Ic}) measurements are now well-defined [75-77], the validity of the result being dependent on the thickness being well in excess of the plastic zone size. Predictions of failure according to the critical CTOD [78], K_R-curves [79] and maximum load toughness [80] parameters are still the subject of some debate, as is the tentative standard for fatigue crack growth rate measurement [81].

Two specimen types are generally approved for fatigue crack propagation testing. These are the compact tension (CT) and centre-cracked tension (CCT) specimens, which are illustrated in Figure 4.1. The CT specimens make use of local bending stresses in order to increase the local crack tip loading without increasing the external load applied.

There are many other fracture specimens in widespread use. Some of these are indicated in Figure 4.2. The single-edge notch three-point bend (SENB3) specimen is widely used for fracture toughness testing and for stable crack growth measurements [75,76,78,82], but offers insufficient crack extension to be economic for fatigue studies. The single- and double-edge notch tension (SENT and DENT) specimens make no use of bending components, and are preferred for small scale testing of polymers and composites [83]. Double cantilever beam (DCB) tests [84] are well-suited to sub-critical crack growth studies and have been used successfully for fatigue [44], stress corrosion [54] and creep [85] crack growth measurements. The contoured DCB specimens are designed so that the bending stiffness of the arm increases as its length increases (i.e. as

the crack grows) and the stress intensity factor becomes independent of the crack length [44,84].

4.2 SPECIMEN SELECTION AND DESIGN

Fracture testing may be carried out for various reasons and optimum selection of test methods must depend on the intended application of the results. Testing may be put into three broad categories:

i) Research; investigating fracture processes and material behaviour.
ii) Collection of data for design purposes.
iii) Assessment of life or damage tolerance of engineering components or structures.

For the purposes of fracture research, the fundamental requirement is for a specimen in which the stress distribution is understood well, so that material response may be related to parameters which are known with some accuracy. For design data collection, some attention must be paid to the method of application of the data to other geometries and, for structural assessment, faithful representation of real features may be more important than a true understanding of the stress distribution.

In this project, it was intended to fulfil requirements relating to (i) and (ii) (see Section 1.3). A specimen was required which would give representative data for design application and which would enable analysis to be made of fundamental material behaviour. It was also desirable that requirements for material and test machine capacity be as small as possible. Specimens considered in detail included the contoured DCB specimen, and CT and CCT designs. The DCB specimen was finally discarded on the basis of crack path stability criteria.

4.2.1 Crack Path Stability

Cottrell [86] has shown that if there is a tensile stress parallel to the crack, σ_{xx}, which is greater than the nominal stress normal to the crack, σ_{yy}, the crack may deviate from its path normal to the applied load. This is not a problem in CCT specimens as σ_{xx} is compressive [87]. For a CT or DCB specimen, the relevant stresses are:

$$\sigma_{xx} \simeq \frac{6P\,a}{B\,H^2} \tag{4.1}$$

and:

$$\sigma_{yy} = \sigma_{nom} \simeq \frac{2P\,(2W+a)}{B\,(W-a)^2} \tag{4.2}$$

σ_{xx} and σ_{yy} are obtained from simple bending theory in the "arms" and "back" of the specimen, respectively, as in Appendix I.

The condition $\sigma_{xx} > \sigma_{yy}$ is thus given by:

$$\left(\frac{2H}{W}\right)^2 < \frac{12(a/W)\,(1-a/W)^2}{(2+a/W)} \tag{4.3}$$

which gives rise to an unstable crack path.

Thus, the maximum crack length for which the crack path is stable increases as the ratio $(2H/W)$ increases. In DCB specimens, $(2H/W)$ is small and it becomes necessary to machine side grooves in the specimen to guide the crack. Although this has little effect on the stress intensity factor (provided that the net thickness is used in the analysis [88]), it may influence the way in which behaviour varies with specimen thickness. In general, conditions closer to those of plane strain are achieved for a given specimen thickness by adding side grooves. As the thickness effect was to be investigated in the present study, side grooves were considered unacceptable, precluding the use of DCB specimens.

Bradshaw & Wheeler found that the problem of path stability

became more serious in thin specimens [89] and at high loads [90], and some problems were, indeed, encountered in the present study where slanting (mixed mode I/III) cracks existed. For this reason, CT specimens with the ASTM profile [79-81], having $(2H/W)$ = 1.2, were considered for "plate" thickness ($B \geqslant 6$ mm) and the RAE recommendation [89] with $(2H/W)$ = 1.9 used for thin sheet specimens. Further problems in path stability may arise with unfavourable grain orientation of the specimen with respect to the rolling direction [91]. This is thought to be related to the variations in shear and tensile properties with orientation.

4.2.2 Net Section Stresses

The specimen size was determined by a decision to use linear elastic fracture mechanics (albeit with a plasticity correction) as far as possible, so that widespread yielding could not be tolerated. By the method of Brown & Srawley [92], LEFM is applicable provided that the nominal net section stress is less than the yield stress when the stress intensification at the crack tip is neglected. In analysing their R-curve data for thin sheet aluminium alloys, Schwalbe & Setz [12] demonstrated that a limit of 90% of the 0.2% proof stress was suitable, provided that a plasticity correction was used. This philosophy is also supported by Turner [93] for "contained yield" situations.

In a CCT specimen, the nominal stress is given by the applied load divided by the net section area:

$$\sigma_{nom} = \frac{P}{B\,(W - 2a)} \tag{4.4}$$

where B is the thickness, W is the overall width, and a is the semi-crack length. P is the applied load.

For a CT specimen, the nominal stress may be estimated by

simple bending theory (see Appendix I). Thus:

$$\sigma_{nom} = \frac{2P\ (2W+a)}{B\ (W-a)^2} \tag{4.2}$$

The stress intensity factor is given by:

$$K = \frac{P}{B\sqrt{W}} f(\frac{a}{W}) \tag{4.5}$$

for each specimen design. If the nominal stress at a specified value of K, K_{max}, must not exceed some value σ_{max}, then for CCT specimens:

$$\sigma_{max} \leqslant \frac{K_{max}\sqrt{W}}{f_{CCT}(a/W)\ (W-2a)} \tag{4.6}$$

and for CT specimens:

$$\sigma_{max} \leqslant \frac{2K_{max}\sqrt{W}\ (2W+a)}{f_{CT}(a/W)\ (W-a)^2} \tag{4.7}$$

Taking typical values of $2a/W = 0.33$ for a CCT specimen and $a/W = 0.5$ for a CT specimen, then:

$$\sqrt{W_{CCT}} \geqslant \frac{K_{max}}{\sigma_{max}} \frac{1}{f_{CCT}(0.16)(0.67)} = 1.96\ (\frac{K_{max}}{\sigma_{max}}) \tag{4.8}$$

and:
$$\sqrt{W_{CT}} \geqslant \frac{K_{max}}{\sigma_{max}} \frac{1}{f_{CT}(0.5)(1-0.5)^2} = 2.07\ (\frac{K_{max}}{\sigma_{max}}) \tag{4.9}$$

The required load capacity for the test machine is then given by equation (4.5), thus:

$$P_{max,CCT} \geqslant 2.57\ B\ (\frac{K_{max}}{\sigma_{max}})^2 \tag{4.10}$$

and:
$$P_{max,CT} \geqslant 0.214\ B\ (\frac{K_{max}}{\sigma_{max}})^2 \tag{4.11}$$

The material required for a CCT specimen is of area $3W^2$, and that for a CT specimen is $1.5W^2$ (see Figure 4.1). Also, the usable semi-crack length for fatigue testing is about $W/6$ for a CCT specimen, and $W/2$ for a CT specimen, so that the compact tension specimen is more economical in terms of both machine capacity and material requirements. This behaviour of the CT specimen, in terms of both stress intensity and nominal stress, is summarised in Figure 4.3.

For the materials tested, σ_{max} was taken as an estimated 0.2% proof stress after cycling, and K_{max} as an estimated value of K_c. These estimates were amended subsequently, but the final result was not affected greatly:

for DTD.5120: $\left(\frac{K_{max}}{\sigma_{max}}\right) = \left(\frac{75}{500}\right) = 0.15\ \sqrt{\text{in}}$

for BS.L97: $\left(\frac{K_{max}}{\sigma_{max}}\right) = \left(\frac{75}{400}\right) = 0.1875\ \sqrt{\text{in}}$

Substituting these into equations (4.8) and (4.9) gave:

for DTD.5120: $W_{CCT} \geq 91$ mm , $W_{CT} \geq 96$ mm

for BS.L97: $W_{CCT} \geq 142$ mm , $W_{CT} \geq 150$ mm

Two "families" of specimens were drawn up. The first, designated CT'A' has $(2H/W) = 1.2$ and the second, CT'B', has $(2H/W) = 1.9$. Although the ASTM [81] and RAE [89] profiles were used, the size and position of the loading holes were altered to enable all specimens to be tested using existing shackles and pins (Figure 4.4). DTD.5120 specimens were made initially to CT'A'/105 dimensions and BS.L97 specimens to CT'A'/150. At a later stage, specimens of both materials were made to

CT'A'/90 dimensions to economise on material and to ease comparison of data. It was also anticipated that modifications to shackles would be necessary for tension-compression testing, and the CT'A'/90 size would enable common shackles to be used for this work and a parallel project on steel specimens [94].

BS.L109 thin sheet specimens were made to CT'B'/120. This size was chosen to aid comparison with published *R*-curve data [89].

4.3 THIN SHEET TESTING

Testing of very thin specimens is complicated further by the possibility of local buckling. In both the CCT and CT specimens, areas of compressive stress occur under nominal tension loading, as indicated in Figure 4.5. Dixon & Strannigan [87] have estimated the compressive stresses in CCT specimens to be of the same order as the net section stresses. Those in CT specimens may be deduced from the stress distribution estimated in Appendix I. Calculation of critical loads for instability is difficult because the constraining effect of the tensile areas of the specimen is not well defined.

Taking the relatively straightforward case of the "back edge" of a CT specimen, approximated to a rectangular beam under combined end load and bending, Appendix I gives a compressive stress of:

$$\sigma_{min} = -\frac{2P}{BW(1-a/W)^2}(1+2a/W) \qquad (4.12)$$

For the simple beam case, Timoshenko [95] predicts buckling instability when:

$$\sigma = \frac{Ek\pi^2 B^2/W^2}{12(1-\nu)^2\ (1-a/W)^2} \qquad (4.13)$$

where k is a numerical factor, dependent on edge constraints and buckling

modes. Values of k vary between about 0.5 for end load cases with one side simply supported and one free, to about 40 for a pure bending case with both sides built in. Unfortunately, bending cases with little constraint are the most difficult to calculate and no reliable values of k are known to the author.

In an attempt to solve this problem, a CT'B'/120 specimen was loaded, unsupported, in tension with three different lengths of saw cut to simulate cracks. The out-of-plane deflection of the back edge was measured by the simple device of an elastic band, stretched lightly over the specimens as indicated in Figure 4.6a. The maximum deflection of the plate from the band was measured and plotted against the applied load (Figure 4.6b). The critical load was estimated by extrapolating back to a condition for zero deflection. These values of load were then substituted back into equations (4.12) and (4.13) to give values of k. It is seen that as the crack grows, the constraint is reduced and k decreases.

In extending this information to thicker specimens, one may expect a relationship between buckling loads and the term $(B/W)^2$ for given crack lengths, (a/W). For the specimens tested, the following values are predicted:

a/W	0.277	0.396	0.488
k (from experiment)	2.2	0.93	0.74
Critical loads (kN)			
CT'B'/120, B = 0.9 mm (experimental)	0.388	0.136	≈0.1
CT'A'/90, B = 6.0 mm	30.6	10.7	7.9
CT'A'/90, B = 9.5 mm	76.9	26.9	19.8
CT'A'/90, B = 15.0 mm	192.2	67.4	49.5
CT'A'/105, B = 9.5 mm	56.4	19.8	14.5
CT'A'/150, B = 9.5 mm	27.6	9.7	7.1

In practice, loads greater than 20 kN were applied in all of the cases above. No back edge buckling was observed for $B > 6$ mm. In CT'A'/105 and /150 cases, some out-of-plane deflection was noticed at the other edge (the end of the slot), albeit less than 0.5 mm in all instances. Observation of the buckling behaviour of the CT'B'/120 specimen suggests that this may have been the first indication of back edge buckling. The discrepancy in the predicted buckling loads is probably due to the restriction on out-of-plane rotation of the specimen arms when the thickness is large compared with the pin clearance in the hole.

As a very rough guide, a simple linear interpolation would give:

$$P_{CRIT} \simeq (1400 + 350B) \left(\frac{B}{W}\right)^2 \qquad (4.14)$$

with P in kN, and B and W in mm, and $a/W \simeq 0.5$. It is suggested that this may be a conservative guide to buckling conditions for use when designing CT specimens in aluminium alloys.

4.3.1 Anti-Buckling Plates

In most crack propagation testing, significant degrees of specimen buckling cannot be tolerated. If buckling occurs, an unwanted K_{III} component occurs at the crack tip and the crack growth rate increases. Although some buckling may occur in real structures, it is not modelled readily in small specimen tests. In order to obtain reproducible results, buckling should be prevented as far as possible. In the case of CCT specimens, this may be achieved by clamping stiff bars lightly across the specimen parallel to and close to the crack. If optical crack length measurements are required (see Section 4.4), it is necessary to leave some gap between the bars and this may reduce their effect. Some recent tests [96] have been carried out with no "window" for crack tip observation,

using electrical or compliance methods for crack measurement.

For the CT specimens, this problem does not arise as the areas prone to buckling are away from the crack tip. The 0.9 mm thick specimens tested in this study were held between plates (Figure 4.7) of 6.3 mm thick mild steel to prevent buckling. These plates were lubricated with molybdenum disulphide grease before each test.

4.4 CRACK LENGTH MEASUREMENT

Fracture mechanics testing relies necessarily on reliable measurement of crack length. It is particularly important to record small changes in crack length. Several methods of measurement are in current use:

4.4.1 Direct Optical Methods

Under some circumstances, it is possible to locate the crack tip visually and measure the crack length directly, or against a grid drawn on the specimen. This becomes very difficult at low stress intensities where crack tip deformations are small, so that a good surface finish is required. The situation is improved by using a low power travelling microscope, and identification of the crack tip is enhanced further by polishing the specimen and by the use of oblique lighting. When testing thick section specimens, crack length measurements may be required on both sides of the specimen. These may be taken separately, or using a single travelling microscope and a system of mirrors. Even so, crack front curvature cannot be detected.

4.4.2 Fracture Surface Inspection

The crack length may be determined by measurements made on the fracture surface after breaking the specimen open. The crack front position may be marked by use of an ink or oil drawn into the crack by

capillary action or by "heat-tinting" before breaking the specimen. When ductile steels are tested, it is common practice to make the final break at liquid nitrogen temperature. During variable amplitude fatigue tests, "marker loads" may be used to identify crack front positions during subsequent fractography.

4.4.3 Specimen Compliance Measurements

From equations (2.4) and (2.6), it is seen that the specimen compliance, C_s, is dependent on the length of the crack. Consequently, measurement of the compliance and a knowledge of the specimen geometry may be used to calculate the crack length. The method will always give an equivalent linear elastic crack length as plasticity is ignored in deriving the compliance equations (in Appendix II), but the difference is small at low stress intensities. This method is especially useful when the crack tip is inaccessible as it may be during corrosion fatigue, or controlled temperature tests, or when automatic monitoring is required.

4.4.4 "Brittle Wire" Techniques

Discrete increases in crack length may be detected by fixing low ductility electrical conductors across the crack path. The loss of conductivity as the wire breaks may be recorded and this is taken as an indication of crack growth. Wires may be used singly or in arrays known as "crack propagation gauges". Although less accurate than many methods of crack length measurement, brittle wire techniques are very convenient for monitoring crack growth on major structural tests.

4.4.5 Electrical Methods

It is possible to calculate the crack length from measurement of the electrical properties of the specimen itself. Common methods

include both alternating and direct current potential drop techniques (ACPD or DCPD), by which the net section area is calculated from the electrical impedance or alternating current field measurement (ACFM) techniques, which use variations in the surface electric field to estimate crack face area. Electrical methods provide a way of measuring the average physical crack length over the specimen thickness and, once again, may be used for automatic monitoring.

4.4.6 In-Service NDT Methods

A survey of non-destructive test (NDT) methods for structures in service is beyond the scope of this thesis. It is worth mentioning, however, that most of the methods in use are designed to detect cracks and that crack length measurement is a secondary function. X-ray, visual and enhanced visual (e.g. dye penetrant or magnetic particle) methods may be used to measure large cracks. The most reliable means of measuring small defects currently in widespread use is the high frequency eddy current technique, which can measure cracks between about 0.5 mm and 3 mm in depth, by comparing the signal with that generated by a known crack in a calibration block. Most other NDT methods (low frequency eddy current, ultrasonic, acoustic emission, etc.) have some crack length measurement capability, but it is important to recognise that, at present, crack length measurements such as these are much less accurate than those achieved in the laboratory.

4.5 FATIGUE TEST PROGRAMME

An experimental programme was carried out to determine the fatigue and static crack growth characteristics of two aluminium alloys. The study was centred on an investigation of 7010-T7651, a high-purity Al-Zn-Mg-Cu-Zr alloy which has been adopted recently for use in the

primary structure of civil transport aircraft. All of the material supplied was from a single batch of 50 mm thick plate, conforming to Ministry of Defence specification DTD.5120 (the plate also met the requirements of British Aerospace specification SO7-1213). A proprietary heat treatment, developed by Alcan-Booth [52], involves solution treatment, controlled stretching and then heating at a controlled rate of 20 K per hour to the final ageing temperature of 172°C.

To provide a comparison material, many of the tests were repeated on a conventional naturally aged Al-Cu-Mg alloy, 2024-T3, which is widely used in those areas of aircraft primary structure where fatigue is a major consideration. Several pieces of material were supplied - two pieces of 50 mm thick plate and one of 25 mm thick plate, all to BS.L97 and from three separate batches - and specimens from three batches of 0.9 mm thick Al clad sheet, to BS.L109. One of the batches of L109 was cut from centre-cracked tension specimens tested at British Aerospace, Hatfield, in 1977-78, so that reliable da/dN versus ΔK data were available.

The location of specimens taken from the material as supplied is shown in Figure 4.8. The outline of the experimental programme was as follows:

i) Specimens 1-16: To establish test techniques and basic data. This included six specimens of 9.5 mm thick DTD.5120, six specimens of 9.5 mm thick BS.L97, and four specimens of 0.9 mm thick BS.L109.

ii) Specimens 17-19: Further evaluation of test techniques. Three specimens of 9.5 mm thick DTD.5120 used to indicate the likely effect of frequency and to establish test methods for negative load ratios.

iii) Specimens 20-28: Crack growth in 6 mm thick DTD.5120. These

tests were run for comparison with data from CCT tests at $R = 0.1$ at British Aerospace, Manchester, in the same thickness [97].

iv) Specimens 29-30: Two DTD.5120 specimens, 15 mm thick, tested to obtain information on mode transition in thicker material.

v) Specimens 31-36: Six specimens, 9.5 mm thick, to study stress ratio effects in BS.L97.

vi) Specimens 37-42: Six specimens, 9.5 mm thick, to study stress ratio and frequency effects in DTD.5120.

vii) Specimens 43-44: Two specimens, 9.5 mm thick, from the same plate as specimens K-R to indicate batch effects.

viii) Specimens 45-54: 0.9 mm thick BS.L109 to extend data from earlier specimens, and to examine variations between batches.

ix) Specimens A - R: "Hourglass specimens" (Figure 4.9) for measurement of the cyclic stress-strain behaviour of (A-J) DTD.5120 and (K-R) BS.L97.

Nominal properties of these alloys are given in Table 4.1.

Most of the fatigue testing was carried out using a Dowty servo-hydraulic test machine of 60 kN load capacity, operating in load control at a frequency of 10 Hz. Some of the other tests were carried out in a 50 kN Instron machine in displacement control with a crosshead displacement rate of 0.4 mm/s, resulting in a typical frequency of 0.2 Hz, the precise value depending upon the compliance.

The crack length was measured periodically using a travelling microscope of about ×40 magnification. At 10 Hz and at higher frequencies, it was necessary to stop the test to take each reading. This was usually done with a load applied equal to about 80% of the maximum load in the fatigue cycle. Cracks were initiated at a "chevron" notch, as shown in

Figure 4.10. Previous experience [44,98] with aluminium alloys had shown that this provided a more reliable straight crack front than a straight notch, where the crack may initiate at either corner. The specimens were pre-cracked with a maximum load equal to the maximum load to to be applied in the fatigue test with a load ratio $R = 0.1$. If a reduction in K_{max} was necessary, it was limited to steps of 10% and crack growth measurements were ignored until a steady-state was reached. It was not expected that changes in ΔK with constant K_{max} would cause significant load interaction effects (e.g. crack retardation) [99]. Crack initiation and step down times are discussed in detail in Appendix III.

During the crack propagation test, readings were taken at intervals of crack growth of, typically, 0.5 mm. The crack growth rate was calculated in two ways:

(i) Mean values of stress intensity factor and crack length were recorded for each pair of consecutive readings, and the crack growth was recorded as:

$$\frac{da}{dN} = \frac{a_{i+1} - a_i}{N_{i+1} - N_i} \qquad (4.15)$$

and:

$$\Delta K = \Delta L \left[f(a_{i+1}) - f(a_i) \right]$$

This is shown in Figure 4.11. In general, this result was only used for monitoring tests in progress and was not used in the final processing of the results.

(ii) The crack length was plotted against the number of cycles, N, for the entire test and a smooth curve drawn by eye. Values of crack length, a, were estimated for a number of specific values of ΔK, and these were marked

off on the curve of a versus N. A line was constructed normal to the curve at each specified point and the slope measured. The reciprocal of this slope was recorded as da/dN. The values of ΔK were chosen as whole numbers or simple fractions when measured in $MN/m^{3/2}$. Intervals of ΔK were, typically, as follows:

$da/dN \leqslant 10^{-4}$ mm/cycle ; interval of ΔK, 0.5 $MN/m^{3/2}$

$10^{-4} \leqslant da/dN \leqslant 10^{-3}$ mm/cycle ; interval of ΔK, 1.0 $MN/m^{3/2}$

$10^{-3} \leqslant da/dN \leqslant 10^{-2}$ mm/cycle ; interval of ΔK, 2.0 $MN/m^{3/2}$

$10^{-2} \leqslant da/dN$ mm/cycle ; interval of ΔK, 5.0 $MN/m^{3/2}$

A typical curve of a versus N is shown in Figure 4.12.

Some testing was carried out with tension-compression cycles. The first such test was run with guides attached to the shackles to prevent rotation of the specimen. These were originally designed for steel specimens [94] and some problems were encountered with the aluminium test pieces. As the loads were somewhat lower than those used for testing steel, the guide friction became a significant part of the applied load, so that the load cell output was not a reliable indication of the specimen load. However, as the aluminium specimens were lighter than the steel test pieces, rotation was easily resisted by the heavy steel shackle design on the Dowty machine. After the first test, no guides were used and no problems were encountered other than some noise and vibration due to the clearance of the pins in the loading holes of the specimen. This did not appear to affect the performance of the test.

Figure 4.13 shows a CT'A'/150 specimen of BS.L97 during a fatigue test in the Instron machine.

4.6 *R*-CURVE DETERMINATION

In order to determine the stable crack growth characteristics of the materials under monotonic loading, pre-cracked specimens were loaded in the 50 kN Instron machine using a constant crosshead displacement rate of 4.2×10^{-3} mm/s. The crack length was measured periodically using a travelling microscope and a record of load versus crosshead displacement was kept using the recording equipment built into the machine.

The remote compliance, C, was derived from the crosshead displacement, δ, and the load, P, so that:

$$C \equiv \frac{\delta}{P}$$

At low values of P, it was assumed that the crack length, a, measured by means of a travelling microscope was identical to the effective crack length, a', derived from the specimen compliance, C_s. The relationship between C_s and a' is known for a perfectly elastic specimen (Appendix II) so that the assumption $a' = a$ implies a negligible plastic zone size.

The machine/instrumentation compliance, C_o, was calculated from:

$$C_o = C - C_s \tag{4.17}$$

As the load was increased, the subsequent values of effective crack length, a', were derived from the updated values of specimen compliance, where:

$$C_s = \frac{\delta}{P} - C_o \tag{4.18}$$

During some low frequency tests in the Instron machine, periodic compliance measurements were made with small loads applied to demonstrate the independence of C_o on crack length. These values are shown in Appendix II.

4.7 CYCLIC STRESS-STRAIN MEASUREMENT

The cyclic stress-strain curves for the two alloys were measured by carrying out incremental step tests [100] on waisted specimens of the type shown in Figure 4.9. A standard clip gauge was modified to measure the minimum specimen diameter from which the diametral strain could be deduced. Each specimen was loaded, cycling between displacement limits, in the 50 kN Instron machine, until the stress-strain curve settled to a saturated condition. The maximum stress and strain were then recorded and the displacement limits increased. This was repeated a number of times to obtain a full cyclic stress-strain curve. The maximum strain range was limited by specimens buckling when reversing the load.

The method has been used with considerable success using identical specimens of BS.4360 grade 50D alloy steel [101], where it has been demonstrated to give results identical to those obtained by more conventional methods [102].

4.8 FRACTOGRAPHY

Close examination of fracture surface topography may assist in the interpretation of fatigue crack growth testing and may provide useful data for comparison with service failures.

Samples were cut from the fracture surfaces of compact tension specimens and examined using a Cambridge Stereoscan 600 scanning electron microscope. This enabled pictures to be taken at magnifications of up to ×10000.

Further samples were passed to the Department of Metallurgy and Materials Science for examination under a Jeol C120X Temscan high resolution transmission/scanning/analytical microscope so that features could be examined at ×100000 magnification, and X-ray analyses of second phase particles could be carried out.

Although due account was taken of tilt angle (where tilting was used), surface measurements were not corrected for facet angle. Such a correction would involve analysis of stereoscopic pairs of fractographs and the improvement in accuracy is not great enough to justify the complications involved [103].

Striation spacing measurements were only quoted where a mean value over at least five - and usually more than ten - consecutive striae could be calculated.

TABLE 4.1

Nominal Composition of Aluminium Alloys

Element	Zn	Mg	Cu	Zr	Mn	Cr	Fe	Si
7010 (%wt)	6.20	2.50	1.70	0.14	<0.03	<0.05	<0.15	<0.10
2024 (%wt)	0.25	1.50	4.40	-	0.60	-	<0.50	<0.50

Mechanical Properties (Typical Measured Values)

	DTD.5120 (7010-T7651*)	BS.L97 (2024-T3)	BS.L109 (2024-T3 Al clad)
0.2% proof stress (MN/m^2)	484	310	320
Ultimate tensile stress (MN/m^2)	544	430	450
Elongation (%)	12.1	>8	19
Tensile modulus, E (GN/m^2)	74.3	72.0	74.0

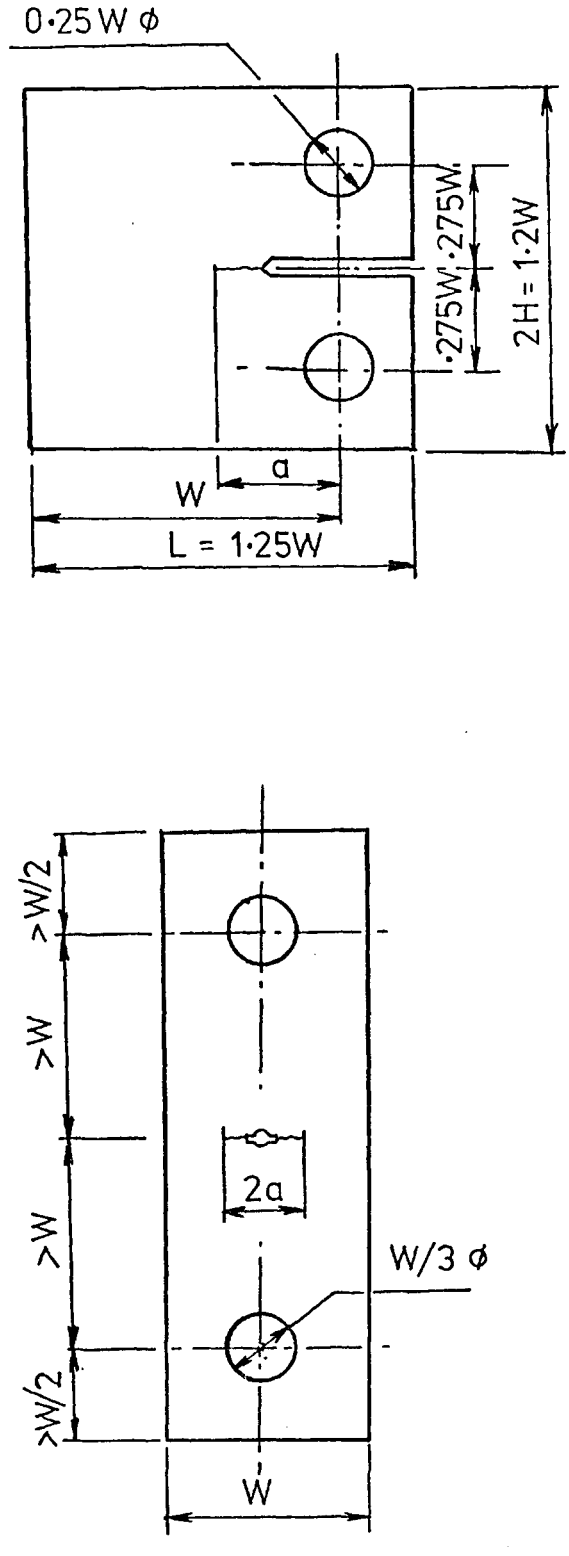


Figure 4.1: ASTM [81] standard test specimens, CT (top) and CCT (bottom)

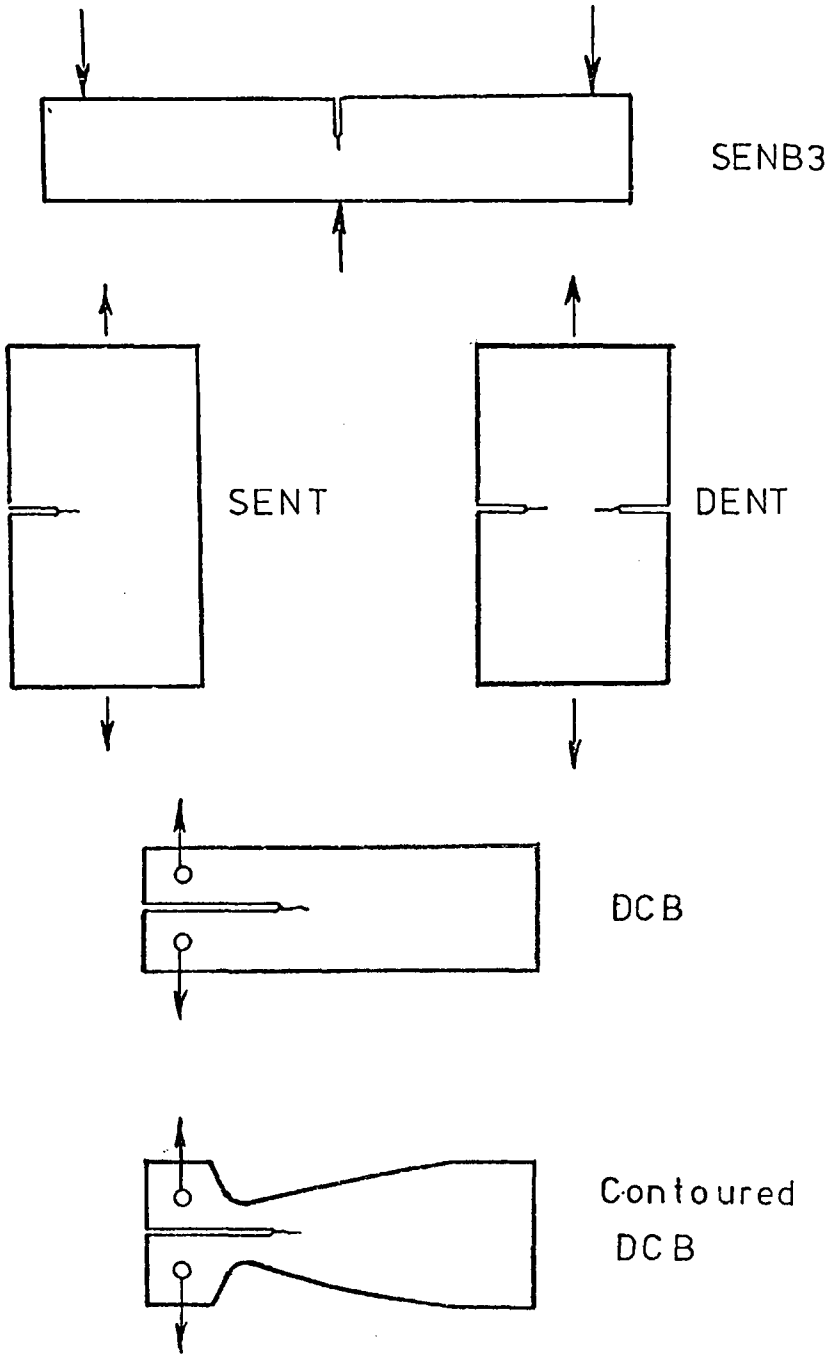


Figure 4.2: Fracture test specimens

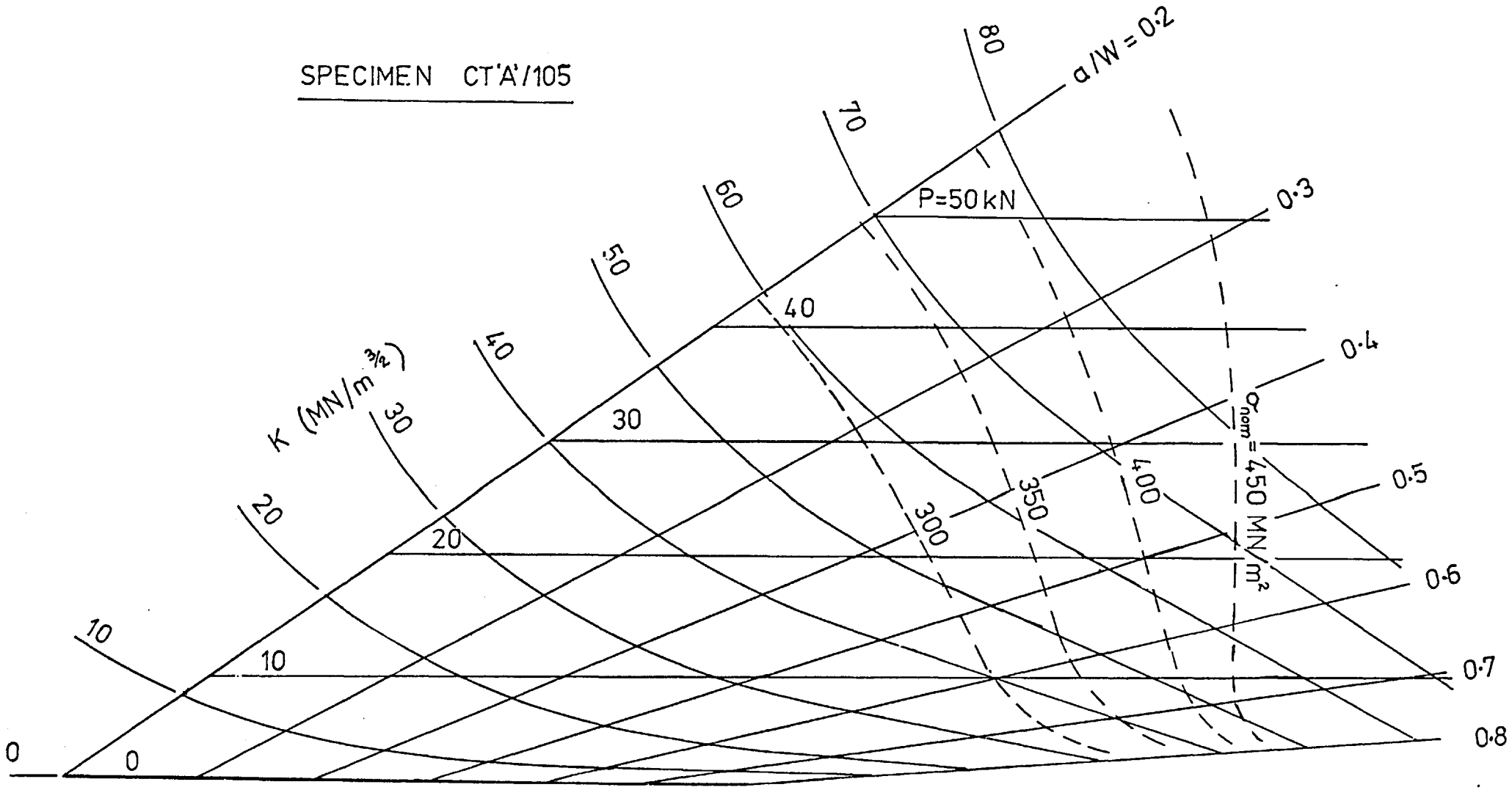


Figure 4.3: Stress intensity factor and nominal stress in a CT specimen

	W	X	2H	h
CTA/90	91	114	110	20
CTA/105	107	133	128	25
CTA/150	152	190	183	25

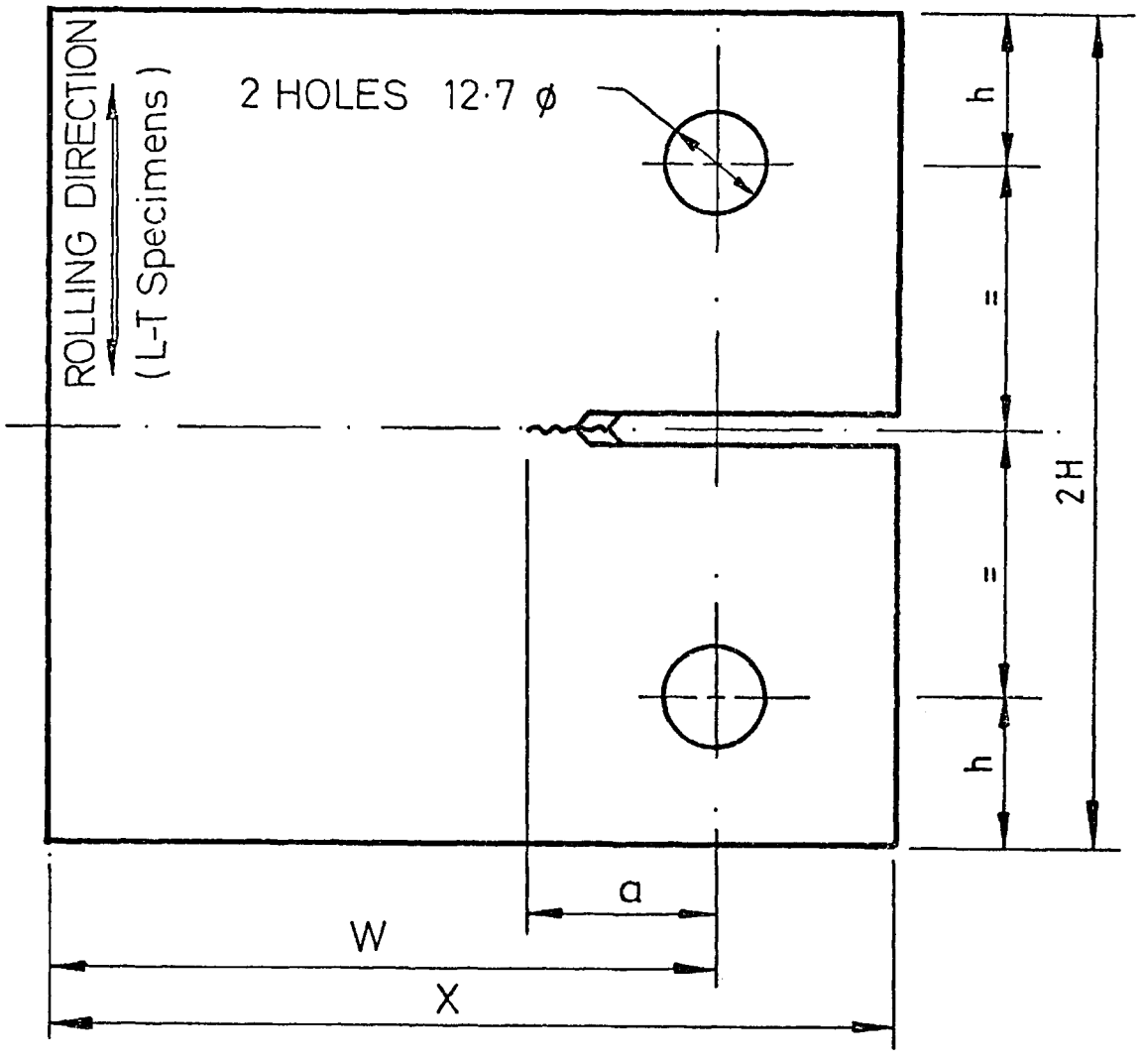


Figure 4.4a: Compact specimen, CT'A'

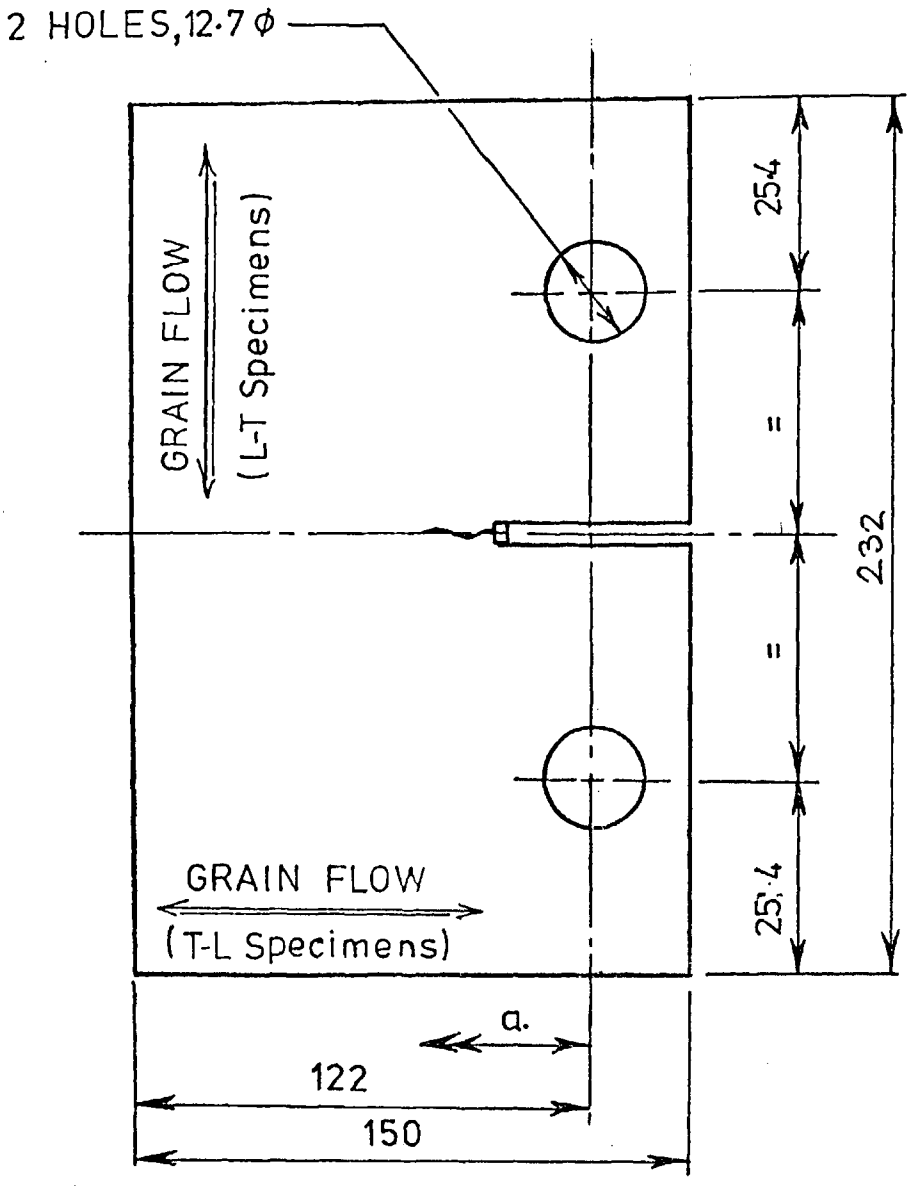


Figure 4.4b: Compact specimen, CT'B'/120

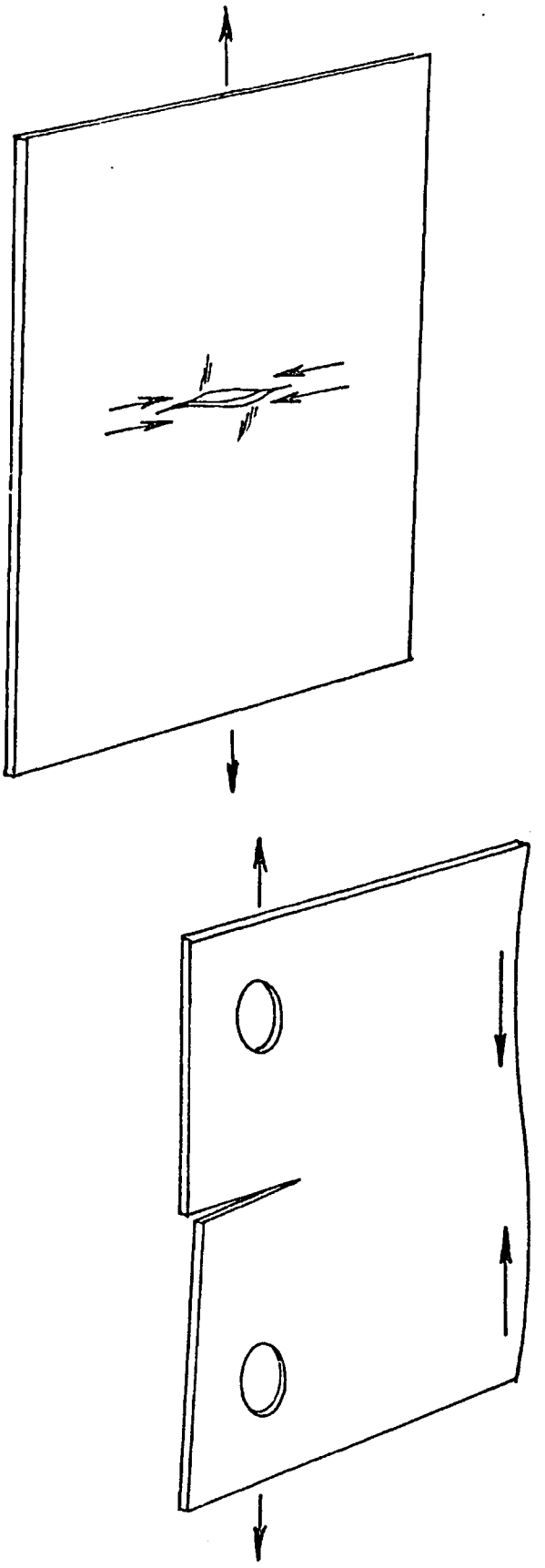
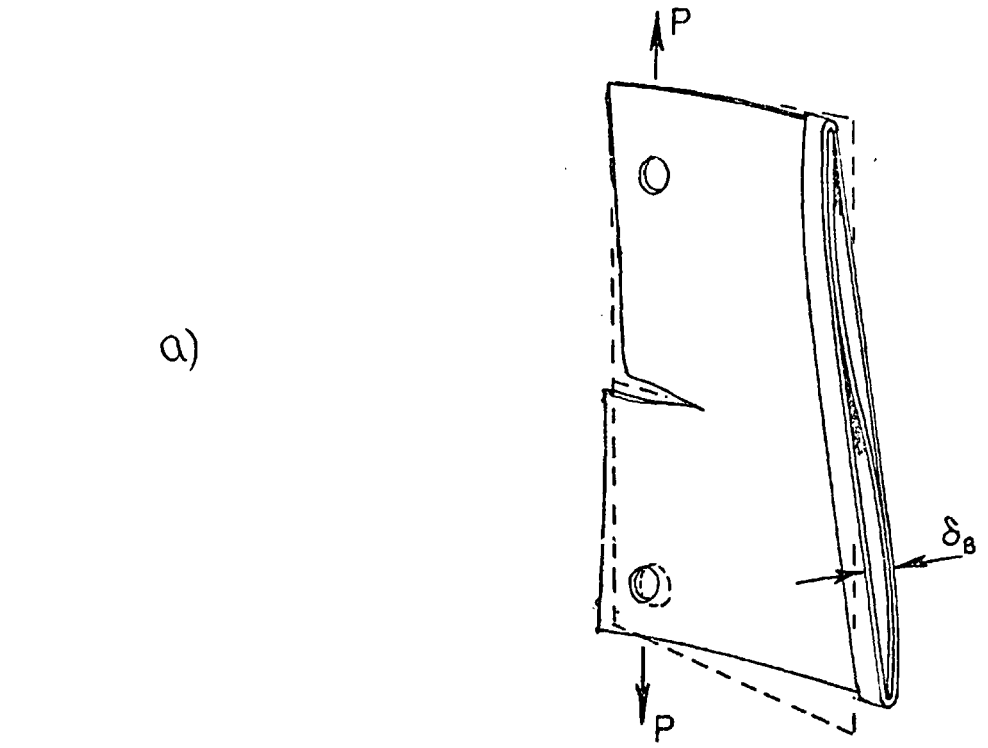


Figure 4.5: Buckling behaviour of unsupported CCT and CT specimens



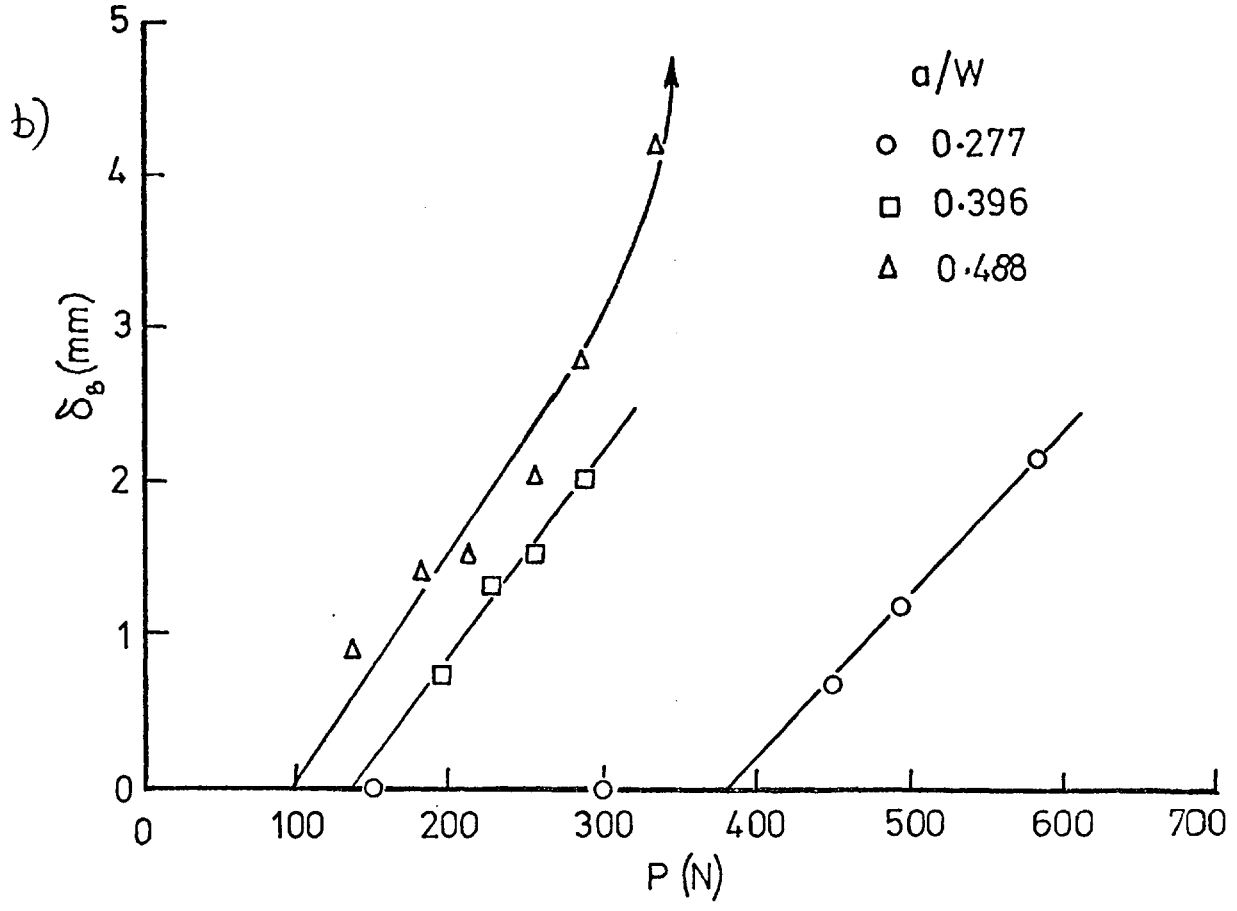


Figure 4.6: Buckling measurements on an unsupported CT'B'/120 specimen

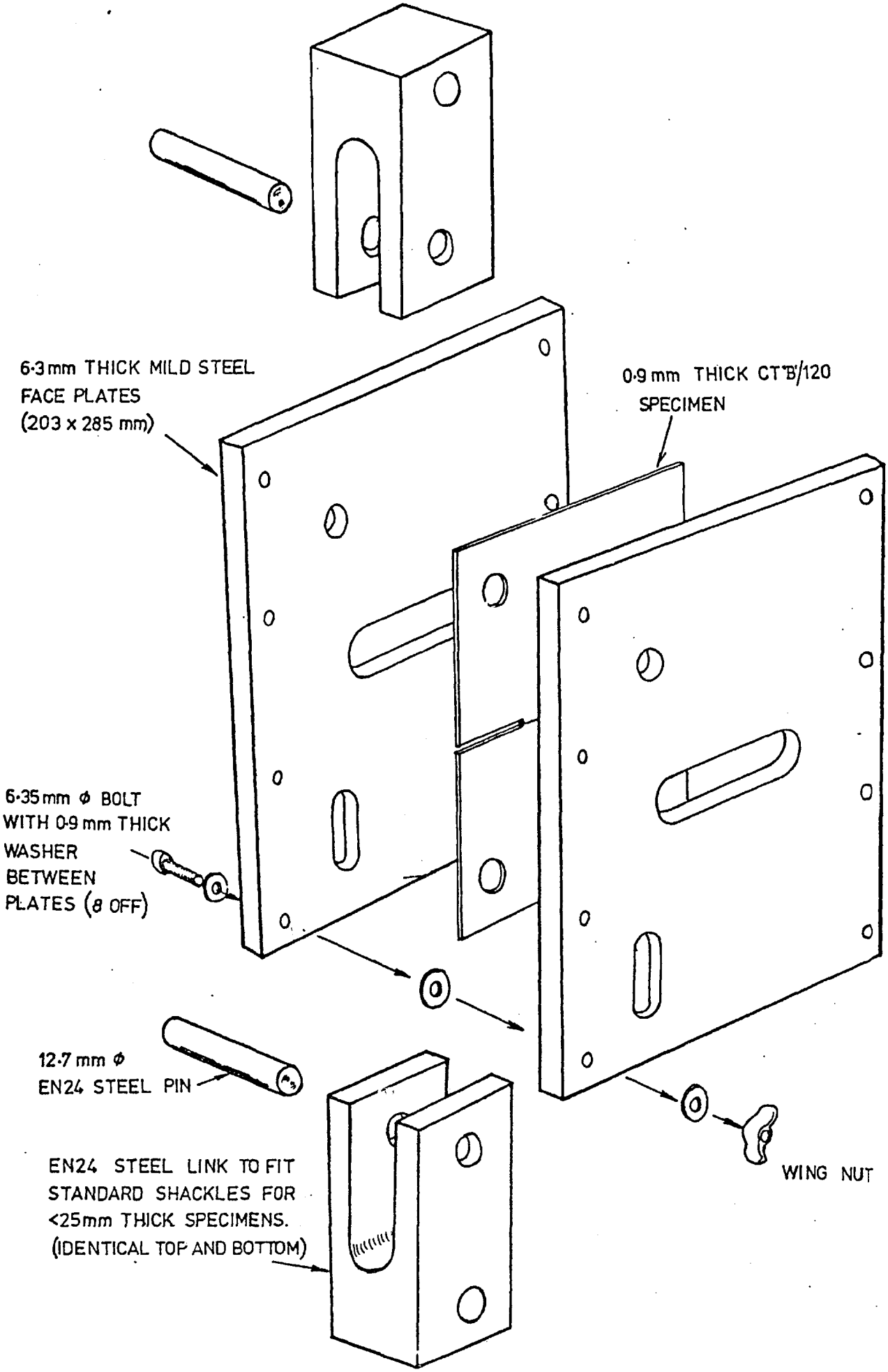


Figure 4.7: Anti-buckling plates for CT'B'/120 specimens

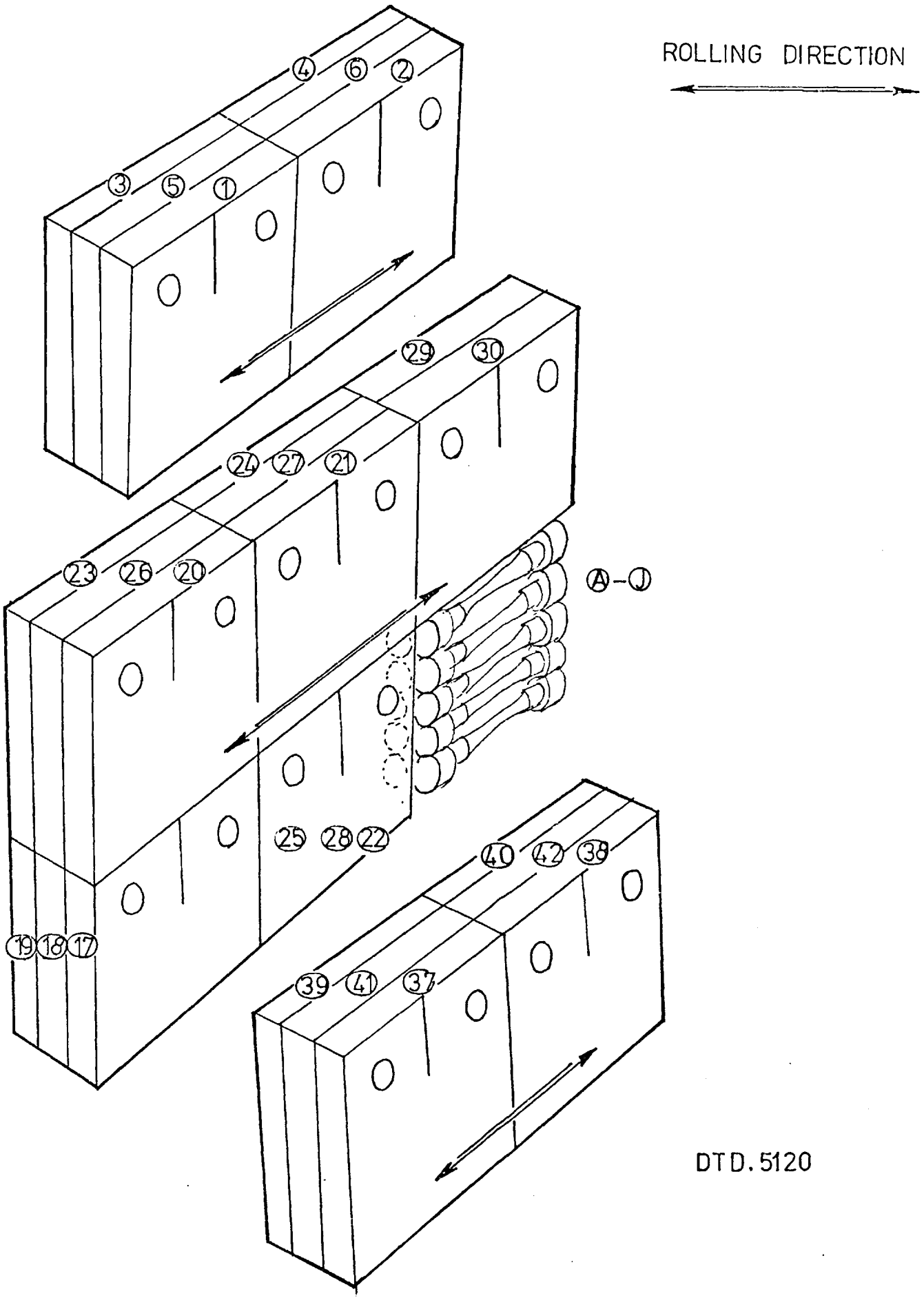


Figure 4.8a: Location of specimens in DTD.5120 plate

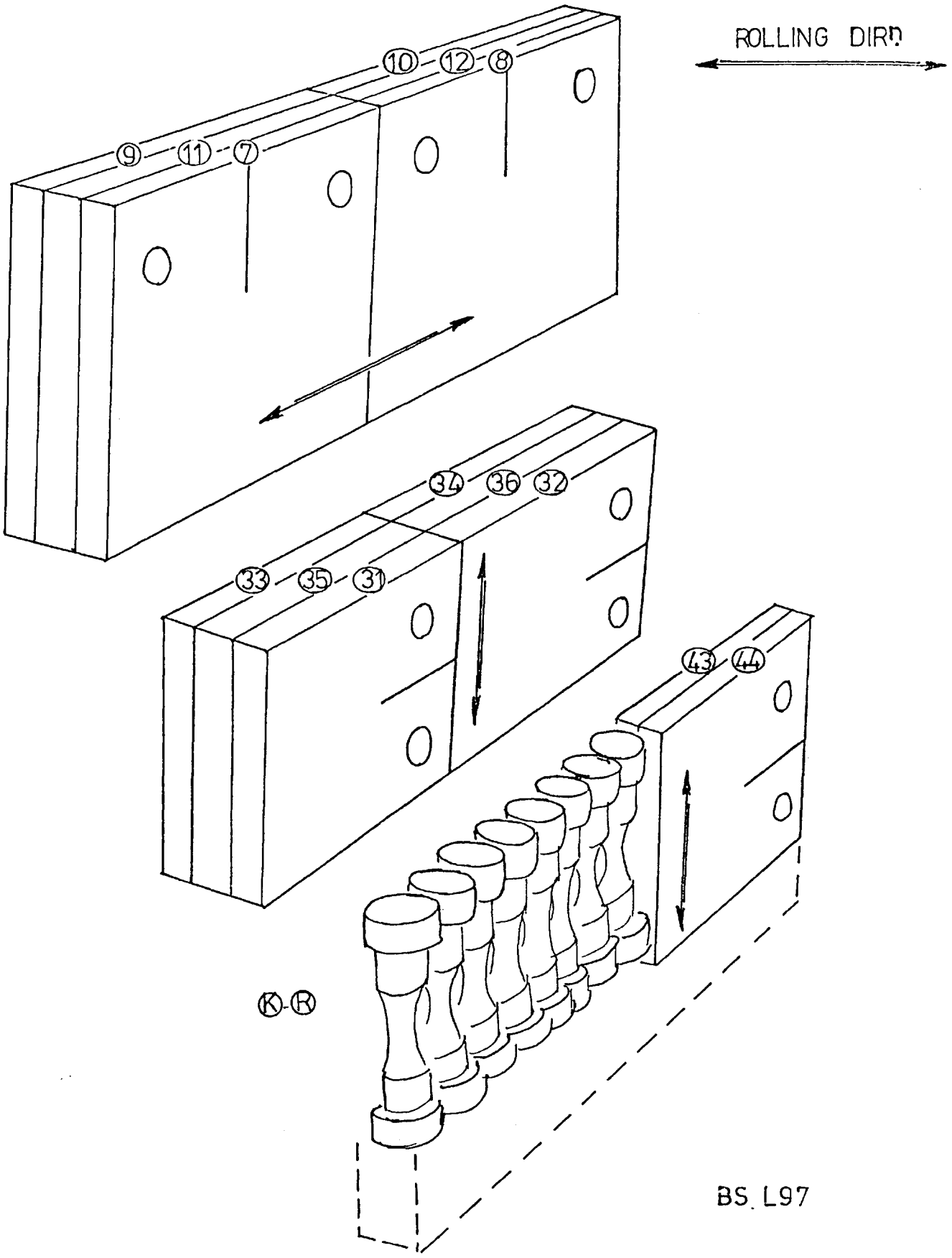


Figure 4.8b: Location of specimens in BS.L97 plate

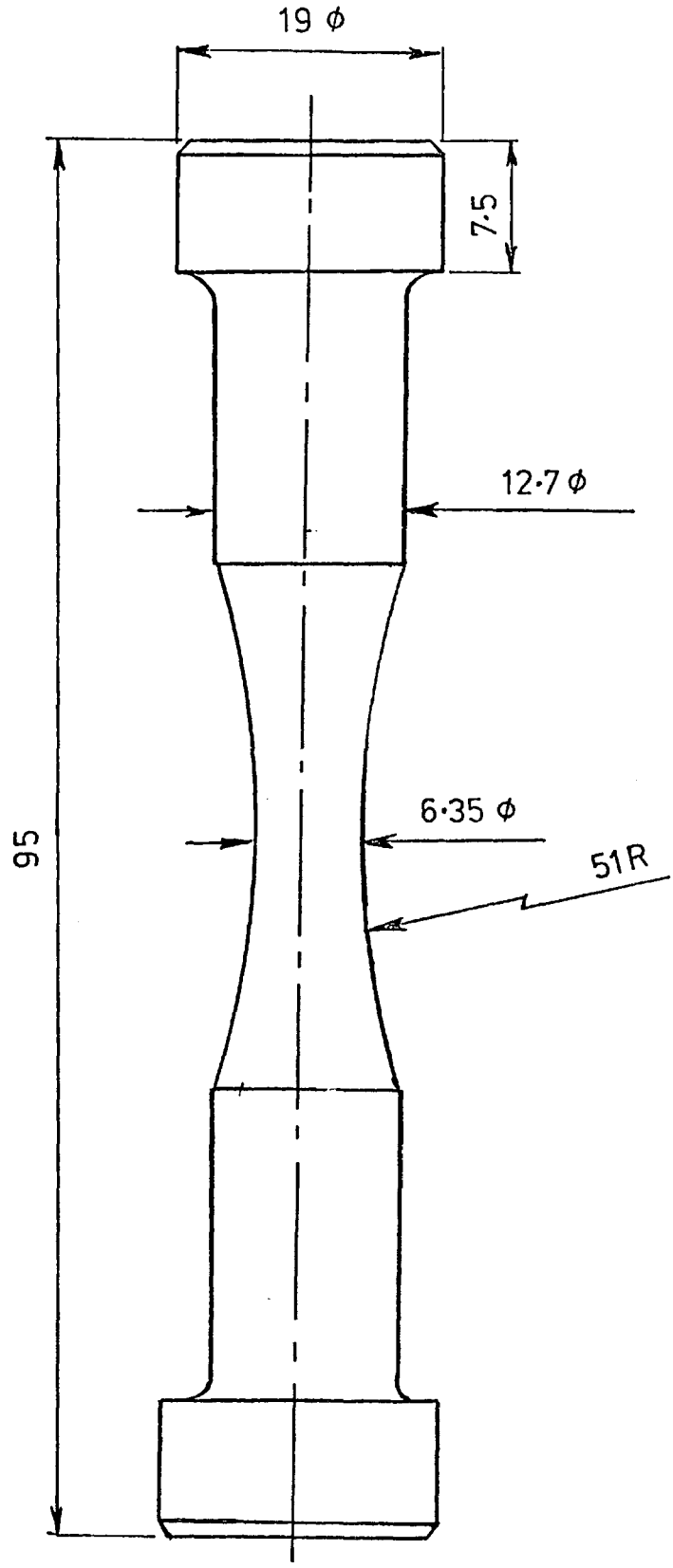


Figure 4.9: 'Hourglass' specimen for determination of cyclic stress-strain curve

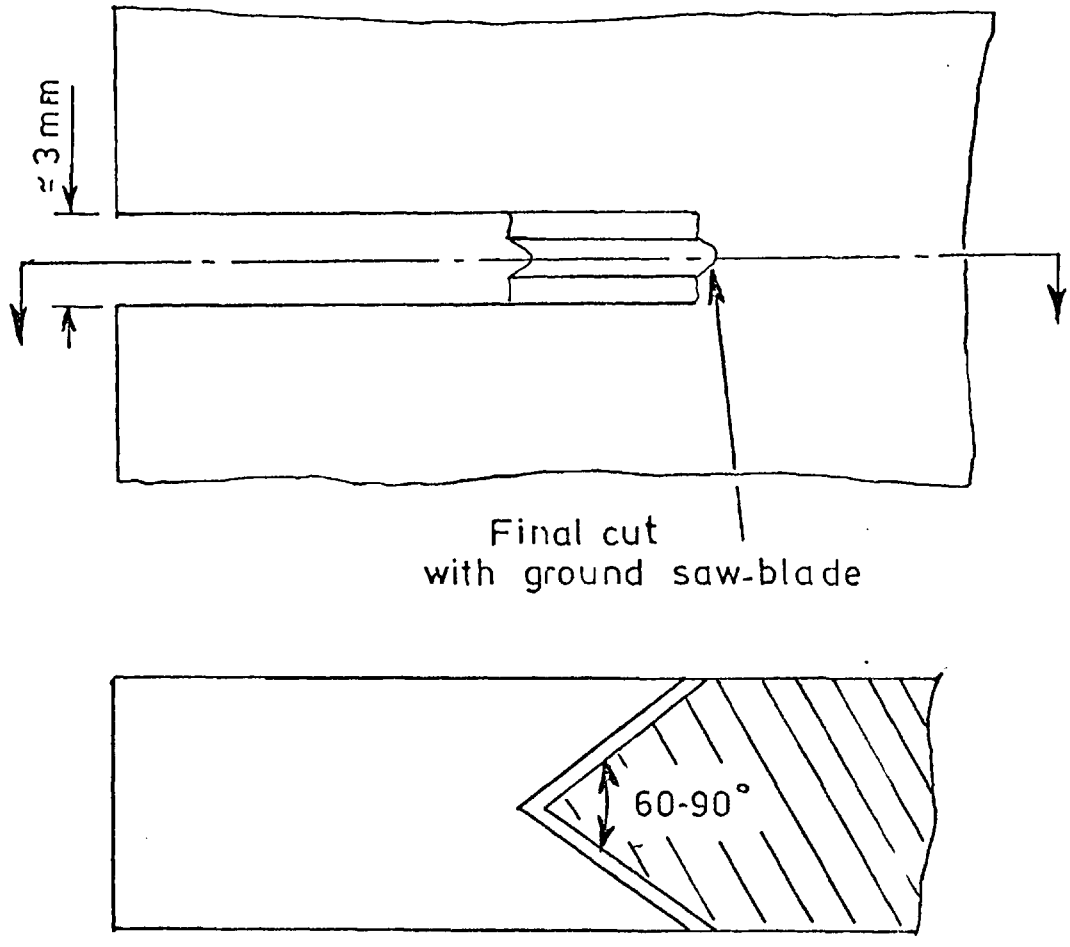
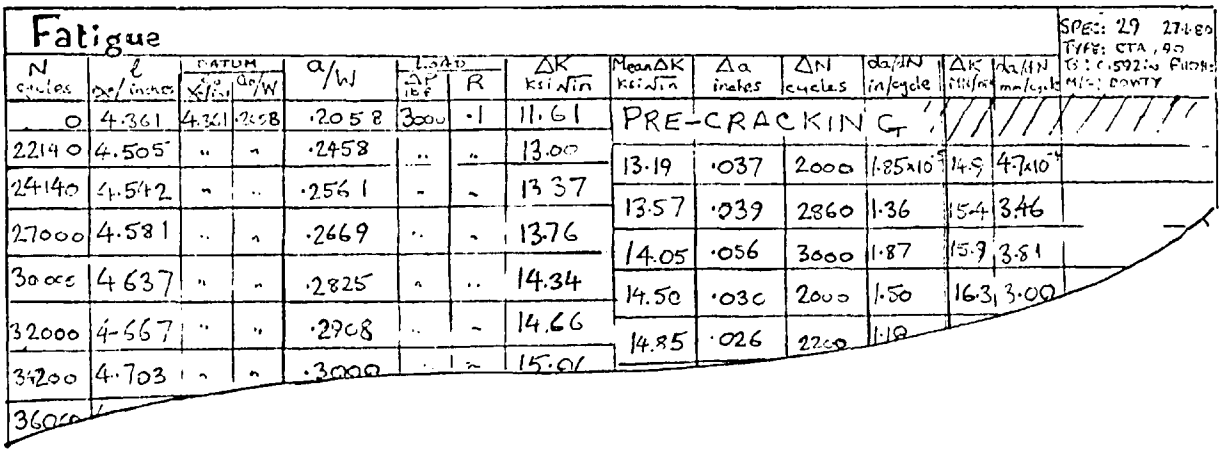


Figure 4.10: Crack starter notch in a CT specimen



Fatigue

SPEC: 29 27-80
TYPE: CTA, 90
G: 0.592in PLATE:
M/C: DOWTY

N cycles	ℓ ins	DATUM x_0 ins	DATUM a_0/W	a/W	LOAD ΔP lbf	LOAD R	ΔK ksi$\sqrt{in}$	Mean ΔK ksi$\sqrt{in}$	Δa ins	ΔN cycles	da/dN in/cycle	ΔK MN/m$^{3/2}$	da/dN m/cycle
0	4.361	4.361	.2058	.2058	3000	.1	11.61	PRE-CRACKING					
22140	4.505	"	"	.2458	"	"	13.00						
24140	4.542	"	"	.2561	"	"	13.37	13.19	.037	2000	1.85×10^{-5}	14.5	4.7×10^{-4}
27000	4.581	"	"	.2669	"	"	13.76	13.57	.039	2860	1.36	15.4	3.46
30000	4.637	"	"	.2825	"	"	14.34	14.05	.056	3000	1.87	15.9	3.81
32000	4.667	"	"	.2908	"	"	14.66	14.50	.030	2000	1.50	16.3	3.00
34200	4.703	"	"	.3000	"	"	15.01	14.85	.026	2200	1.18		
36000													

Figure 4.11: Typical laboratory log sheet

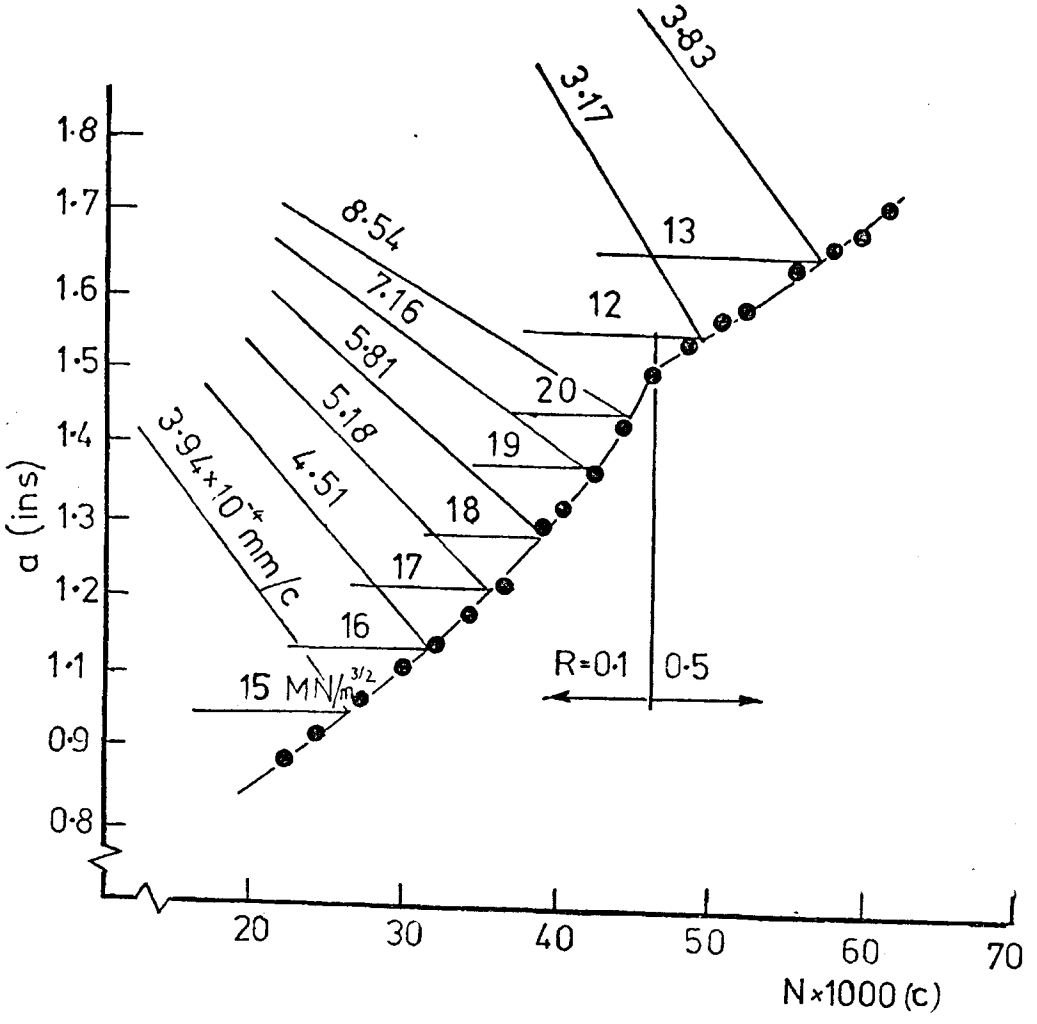


Figure 4.12: Graphical determination of da/dN for curve of a versus N

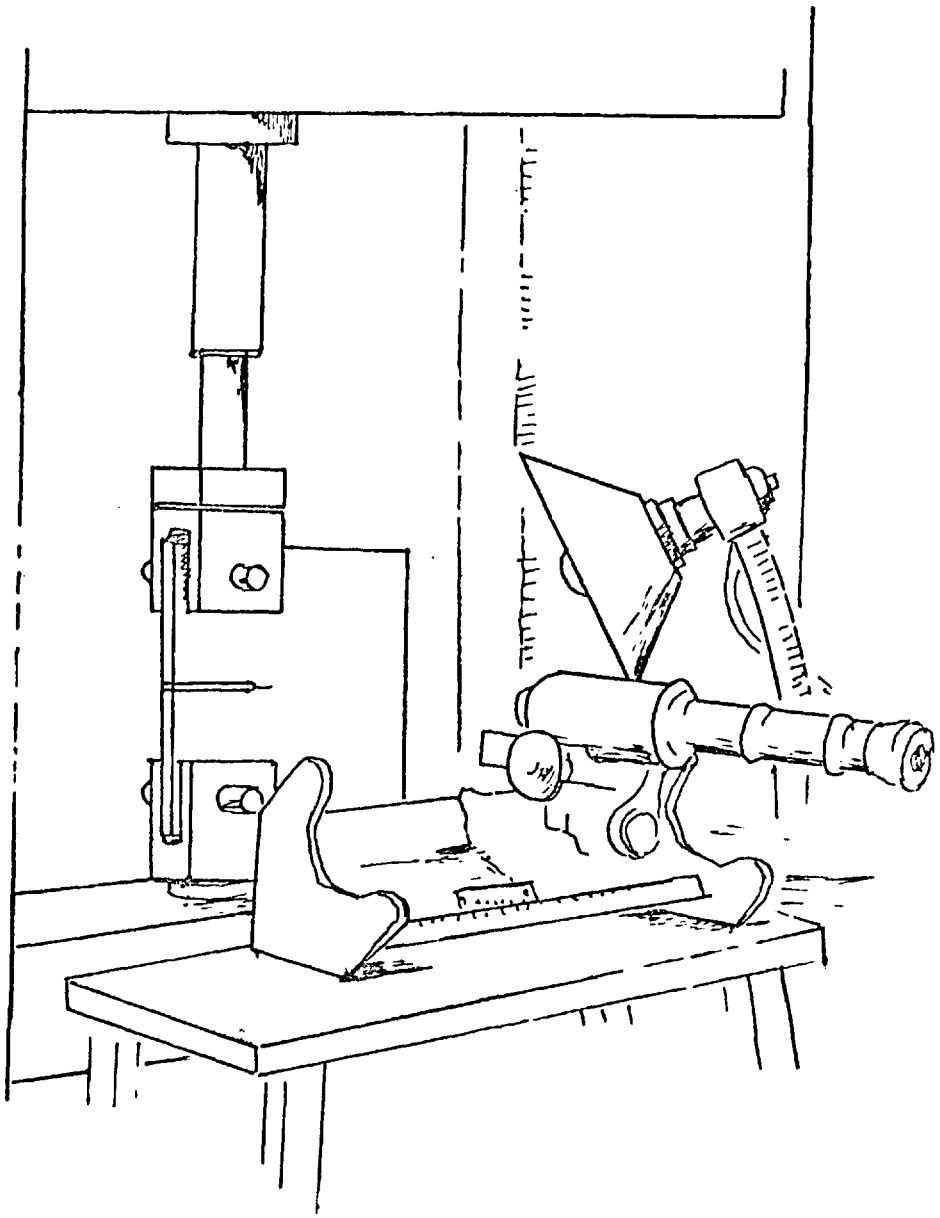


Figure 4.13: Typical fatigue test arrangement (CT'A'/150 specimen in Instron machine)

CHAPTER 5

RESULTS

5.1 FATIGUE CRACK GROWTH RATES

Using the method of Section 4.5, results were obtained for fatigue crack propagation rates in DTD.5120 and BS.L97 materials at load ratios of -2, -1, -2/3, -1/3, 0.1 and 0.5 at frequencies of ≈0.2 Hz, 10 Hz and 50 Hz. BS.L109 specimens were tested at R = 0.1 and 0.5, and at 1 Hz.

5.1.1 DTD.5120 at Positive Stress Ratio

Figures 5.1 and 5.2 show points obtained from a versus N data which had been smoothed, graphically. The reference line on both figures is simply a "best fit" line through data for R = 0.1 and f = 10 Hz. Data for both 6 mm and 9.5 mm thick specimens are included, as there was no systematic difference between these. Data for 15 mm thick specimens are shown in Figure 5.3 with the same reference line.

5.1.2 BS.L97 at Positive Stress Ratio

Figures 5.4 and 5.5 correspond to Figures 5.1 and 5.2, but they were obtained by testing 9.5 mm thick specimens of BS.L97. A further variable is introduced as there appears to be some consistent effect of specimen position in the original plate. Referring back to Figure 4.8b, specimens 11, 12, 35 and 36 are referred to as "core" specimens, and the remainder as "surface" specimens. Variations between batches and locations are discussed in Section 5.6. Once again, a reference line for R = 0.1 and f = 10 Hz is drawn on both graphs.

5.1.3 BS.L109 at Positive Stress Ratio

Unfortunately, considerable problems were encountered with

fatigue tests on thin sheets. The anti-buckling plates were found to move (in an out-of-plane sense) at high frequencies and at low loads. Enough data were obtained, cycling at 1 Hz in the Dowty machine, to establish a da/dN versus ΔK curve for $R = 0.1$ and $da/dN > 10^{-4}$ mm/cycle (Figure 5.6), so that a comparison may be made between CT and CCT test results discussed in Section 6.11. Some means of improving the test technique are discussed in Section 9.1.

5.1.4 DTD.5120 at Negative Stress Ratio

Figure 5.7 shows negative stress ratio data for DTD.5120 specimens, 6 mm and 9.5 mm thick, tested at 10 Hz. The reference line for $R = 0$ was estimated from $R = 0.1$ and $R = 0.5$ data using equation (7.6). Values of R_p, quoted in Figure 5.7, are the load ratio, P_{min}/P_{max}. The stress intensity term is derived from equation (3.8).

5.1.5 BS.L97 at Negative Stress Ratio

Figure 5.8 shows negative stress ratio data for BS.L97 specimens, 9.5 mm thick, tested at 10 Hz. During this testing, there was a tendency for the crack to arrest during tension-compression cycling, but crack growth resumed when the load ratio was changed to $R = 0.1$ with the same K_{max} (Figure 5.9). Although one DTD.5120 specimen did show some signs of this behaviour, it was most noticeable in the lower strength material.

5.2 STRIATION SPACING MEASUREMENTS

A total of six specimens were examined under the 'Stereoscan' microscope, and a further six under the 'Temscan' microscope. Where sufficient consecutive striae were found, striation spacing, $\bar{s}$, was recorded and plotted against ΔK calculated from the position of the sample

on the fracture surface and the original test records. The results are summarised in Figure 5.10 which also shows some data from other sources [25,28,33,104]. There is much scatter in the data as local variations in striation spacing may be very large indeed. Some fractographs are included in Figures 6.13 and 6.14.

5.3 CRACK GROWTH RESISTANCE (*R*-CURVES)

R-curves obtained by the method described in Section 4.6 are shown in Figure 5.11. For the slower tests ($\dot{\delta}$ = 0.004 mm/s), both optical and compliance crack length measurements were made but during the fast tests, remote compliance measurements alone were possible.

During one of the tests on a CTA/150 specimen of BS.L97, the specimen was unloaded three times to about one tenth of the maximum applied load and the set of *R*-curves of Figure 6.3 were derived. There was very little change in K_R versus $\Delta a'$ but when physical crack extensions were measured, a reduction in crack extension after cycling was noted. This effect will be discussed in some detail in Chapter 6.

5.4 MODE TRANSITION OBSERVATIONS

5.4.1 Mode Transition in Fatigue Tests

During fatigue tests at high stress ratios, the crack plane gradually "rotated" to a slanting ($\simeq$ 45°) plane. The onset of this rotation appeared to depend on the material thickness and crack growth rate and was independent of stress ratio or frequency. The behaviour is summarised in the following table:

Material	Thickness, B (mm)	da/dN at Onset of Mode Transition (mm/cycle)
DTD.5120	6.0	5.5×10^{-4}
DTD.5120	9.5	9.0×10^{-4}
DTD.5120	15.0	$>2.0 \times 10^{-3}$
BS.L97	9.5	5.5×10^{-4}

5.4.2 Mode Transition Under Monotonic Loading

During monotonic load increases on DTD.5120 specimens with "square" fatigue cracks, mode transition occurred by the progressive build up of shear lips, leaving a triangular region of flat fracture ahead of the fatigue crack front. At the higher loading rate, the length of specimen over which transition occurred was significantly shorter - about 10 mm at $\dot{\delta}$ = 0.4 mm/s, compared with 18 mm at 0.004 mm/s.

In the L97 specimens, mode transition did not occur but there was a tendency for the crack to "tunnel", i.e. for the crack tip to extend more rapidly away from the specimen surface.

These different types of transition behaviour are discussed in Section 6.7.

5.5 FRACTURE TOUGHNESS

Maximum load fracture toughness values were recorded for all specimen failures, during both fatigue and R-curve testing. In some other cases, specimens were loaded monotonically in load control to failure. The data is tabulated below. The terms K_{eng_c} and Γ are defined in Section 6.6, and the types of test are indicated in the table.

Maximum Load Toughness Data

Specimen	Material	B (mm)	Type	Test to Failure	a/W	Γ (mm)	K_{eng_c} (MN/m$^{3/2}$)
1	DTD.5120	9.5	CTA/105	SR	0.448	37.9	86.3
2	DTD.5120	9.5	CTA/105	SF	0.681	21.1	59.0
4	DTD.5120	9.5	CTA/105	SR	0.507	34.1	82.6
6	DTD.5120	9.5	CTA/105	FR	0.513	33.5	73.1
7a	BS.L97	9.5	CTA/150	SR	0.457	54.3	88.0
7b	BS.L97	9.5	CTA/150	CR	0.497	49.4	95.1
7c	BS.L97	9.5	CTA/150	CR	0.529	45.1	85.6
8	BS.L97	9.5	CTA/150	SR	0.629	35.8	72.0
9	BS.L97	9.5	CTA/150	SF	0.806	17.5	≈60
11	BS.L97	9.5	CTA/150	FR	0.513	47.8	81.3
12	BS.L97	9.5	CTA/150	FF	0.742	24.2	≈66
13	BS.L109	0.9	CTB/120	MLC	0.405	40.2	93.4
14	BS.L109	0.9	CTB/120	MLC	0.601	27.9	≈103
15	BS.L109	0.9	CTB/120	MLC	0.590	31.6	79.1
16	BS.L109	0.9	CTB/120	MLC	0.215	41.3	80.0
18	DTD.5120	9.5	CTA/90	SR	0.513	28.7	74.9
19	DTD.5120	9.5	CTA/90	FF	≈0.64	20.7	>54
21	DTD.5120	6.0	CTA/90	FF	0.76	13.6	>60
22	DTD.5120	6.0	CTA/90	MLC	0.63	21.3	67.4
23	DTD.5120	6.0	CTA/90	SR	0.48	30.8	71.1
24	DTD.5120	6.0	CTA/90	FF	≈0.7	17.0	>52
25	DTD.5120	6.0	CTA/90	MLC	0.667	19.4	54
26	DTD.5120	6.0	CTA/90	MLC	0.542	27.1	75.5
27	DTD.5120	6.0	CTA/90	MLC	0.647	20.1	65.9
29	DTD.5120	15.0	CTA/90	SR	0.453	32.4	71.6
30	DTD.5120	15.0	CTA/90	SR	0.730	13.7	46.8
31	BS.L97	9.5	CTA/90	FF	0.69	17.6	57.6
32	BS.L97	9.5	CTA/90	FF	0.67	18.6	48.9
33	BS.L97	9.5	CTA/90	FF	0.62	21.9	>47
36	BS.L97	9.5	CTA/90	MLC	0.68	18.2	53.7
37	DTD.5120	9.5	CTA/90	MLC	0.722	15.8	52.2
38	DTD.5120	9.5	CTA/90	MLC	0.697	17.0	63.4
42	DTD.5120	9.5	CTA/90	MLC	0.733	15.1	56.5
43	BS.L97	9.5	CTA/90	MLC	0.65	20.1	52.4
44	BS.L97	9.5	CTA/90	MLC	0.606	20.6	57.1
45	BS.L109	0.9	CTB.120	MLC	0.24	42.1	72

SR : slow R-curve ($\dot{\delta}$ = 0.004 mm/s)

FR : fast R-curve ($\dot{\delta}$ = 0.4 mm/s)

SF : slow fatigue test ($f \simeq 0.2$ Hz, displacement control)

FF : fast fatigue test (f = 10 Hz, load control)

MLC : monotonic test, load control

5.6 BATCH EFFECTS IN 2024-T3

Although the BS.L97 and BS.L109 specimens came from several batches of material, there was no discernible difference between the fatigue crack growth or toughness data for the specimens.

One exception appears to be the "through-thickness" variations in one batch of L97, as specimens 11 and 12 both gave consistently low crack growth rates. The effect was not seen in the other 50 mm thick plate. This may have been due to an uneven distribution of precipitates in one particular plate.

5.7 CYCLIC STRESS-STRAIN DATA

Hysteresis loops and plastic strain versus stress data for the two plate materials are shown in Figures 5.12 to 5.15. The DTD.5120 specimens were found to cyclically strain soften a little, and BS.L97 specimens hardened considerably. Following cycling to saturation, and conversion to longitudinal strains, the following properties were measured.

	DTD.5120	BS.L97
0.2% proof stress (MN/m^2)	460	360
Work-hardening exponent, n'	0.05	0.12

The low value of n' for DTD.5120 is due mainly to the very high elongation at failure with some 12% plastic strain.

5.8 ERROR ANALYSIS

5.8.1 Fatigue Crack Growth Measurements

Errors may arise in both load and crack length measurement. The accuracy of load measurement on the 50 kN Instron machine is ±45N, giving

rise to errors of the order of ±1% in ΔK. An additional error of similar order occurs due to fluctuations in load reversal points. Crack length measured on the specimen surface could be measured using a travelling microscope to within ±0.01 mm, but the true error is somewhat greater as the crack length varies through the thickness of the specimen. Overall accuracy of the order ±4% is expected for ΔK.

When using the 60 kN Dowty machine, the accuracy of load measurement is improved, but this has little effect on the accuracy of ΔK.

Crack growth rates obtained from graphically smoothed a versus N curves are expected to be correct within ±10%, although it is important to recognise that the crack extension in any given cycle may be vastly different from this mean value.

Final da/dN data lies within a scatter band of, typically, ±50% on crack growth rates (i.e. ±12% on ΔK), which implies a true scatter in material response of around ±30%.

5.8.2 *R*-Curve Determination

Errors in load are the same as for fatigue crack growth measurements (Section 5.8.1). Load point deflection measurements are within ±0.01 mm. The specimen compliance, C_s, is obtained by graphical measurement of the load-deflection curve, and the total error is expected to be ±2%.

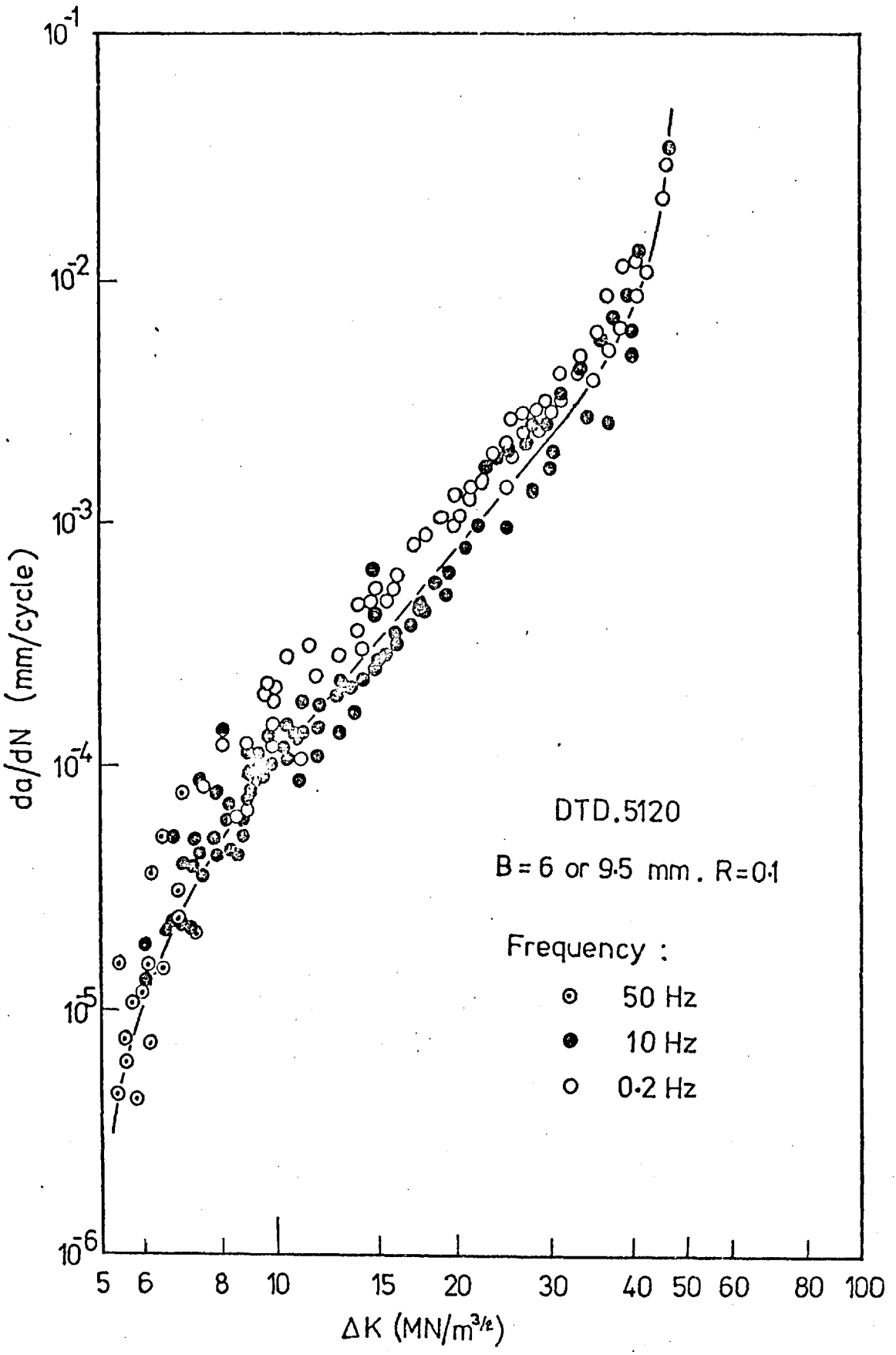


Figure 5.1: Fatigue crack growth in DTD.5120

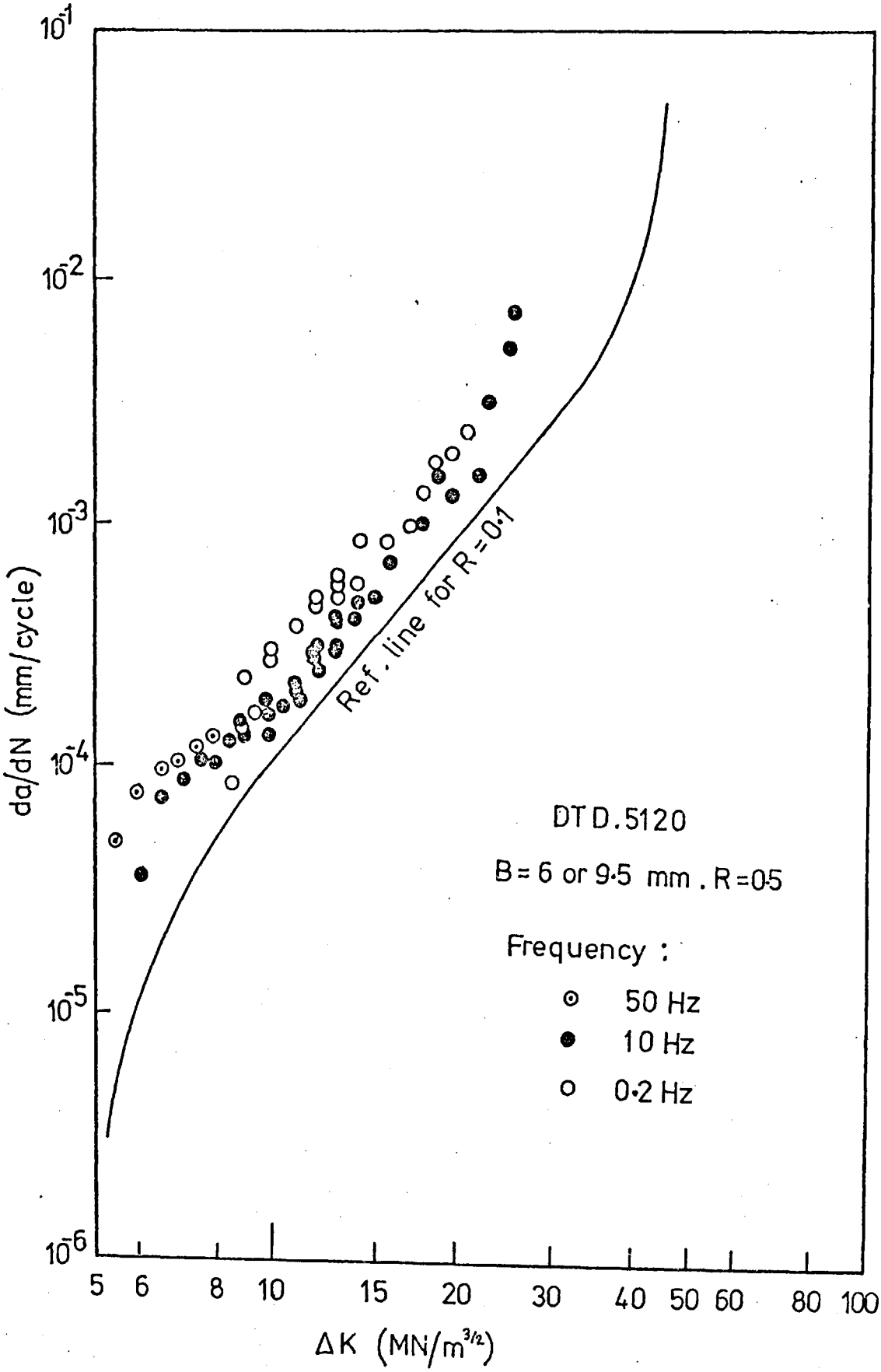


Figure 5.2: Fatigue crack growth in DTD.5120

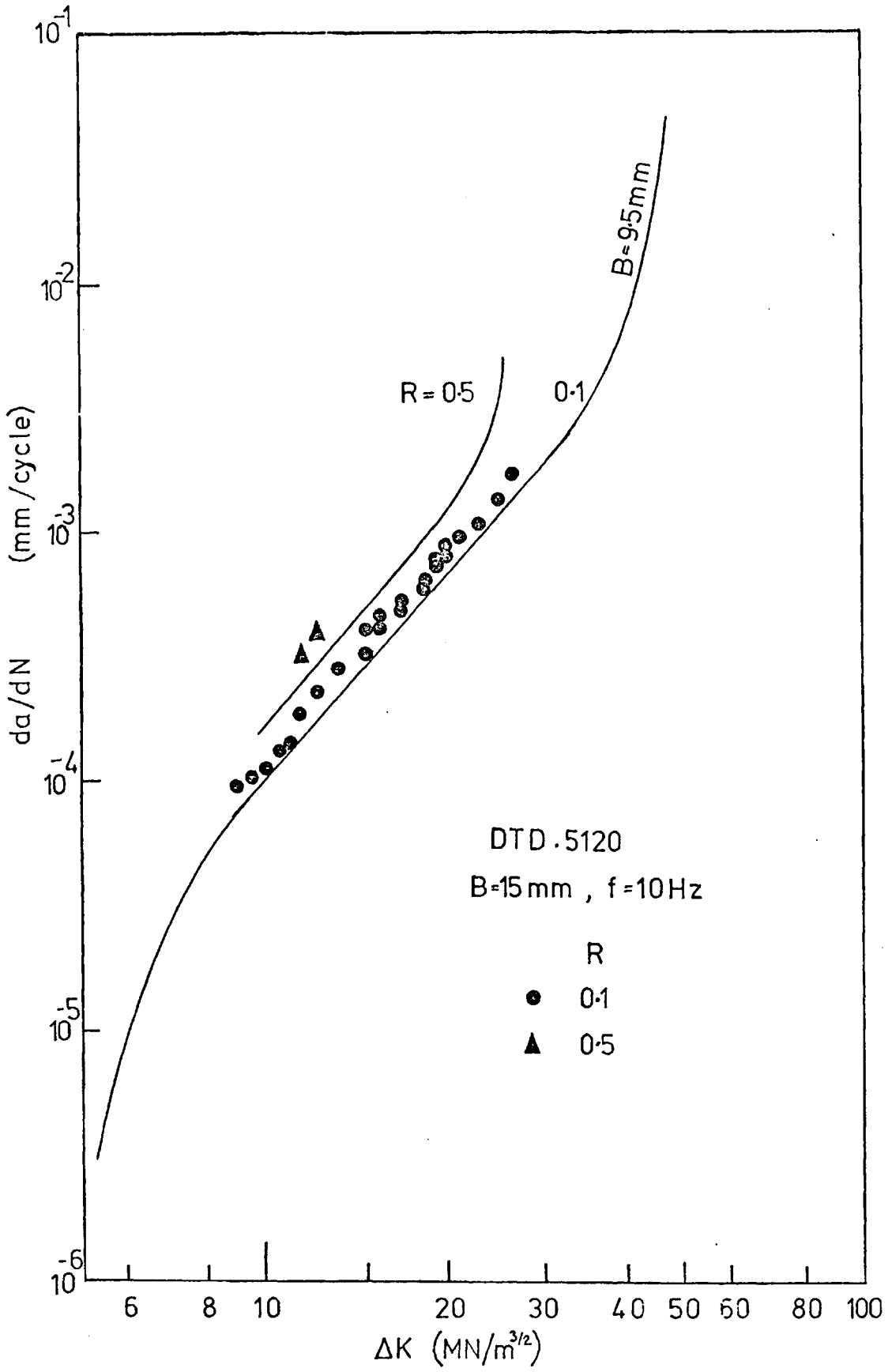


Figure 5.3: Fatigue crack growth in DTD.5120

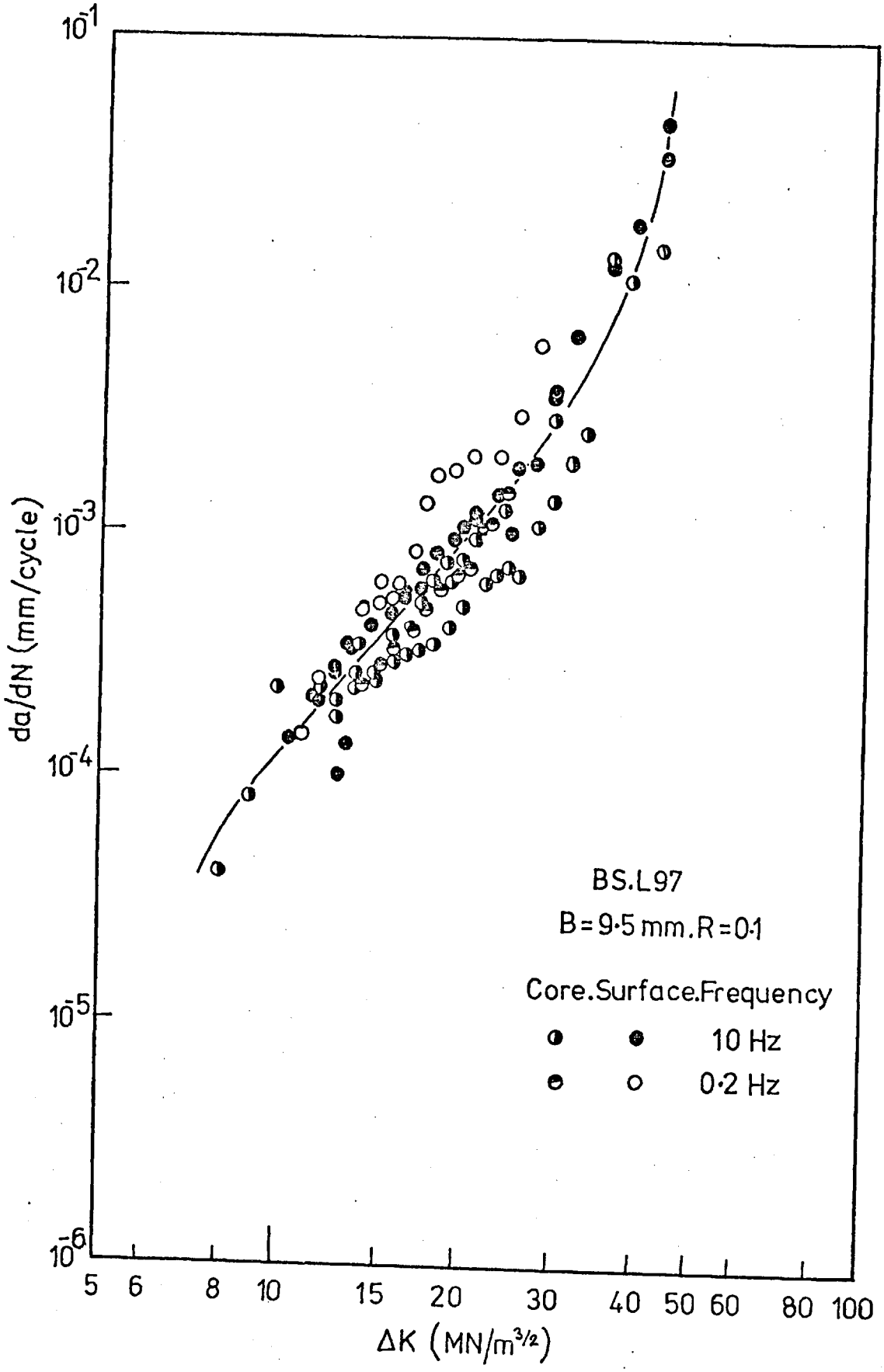


Figure 5.4: Fatigue crack growth in BS.L97

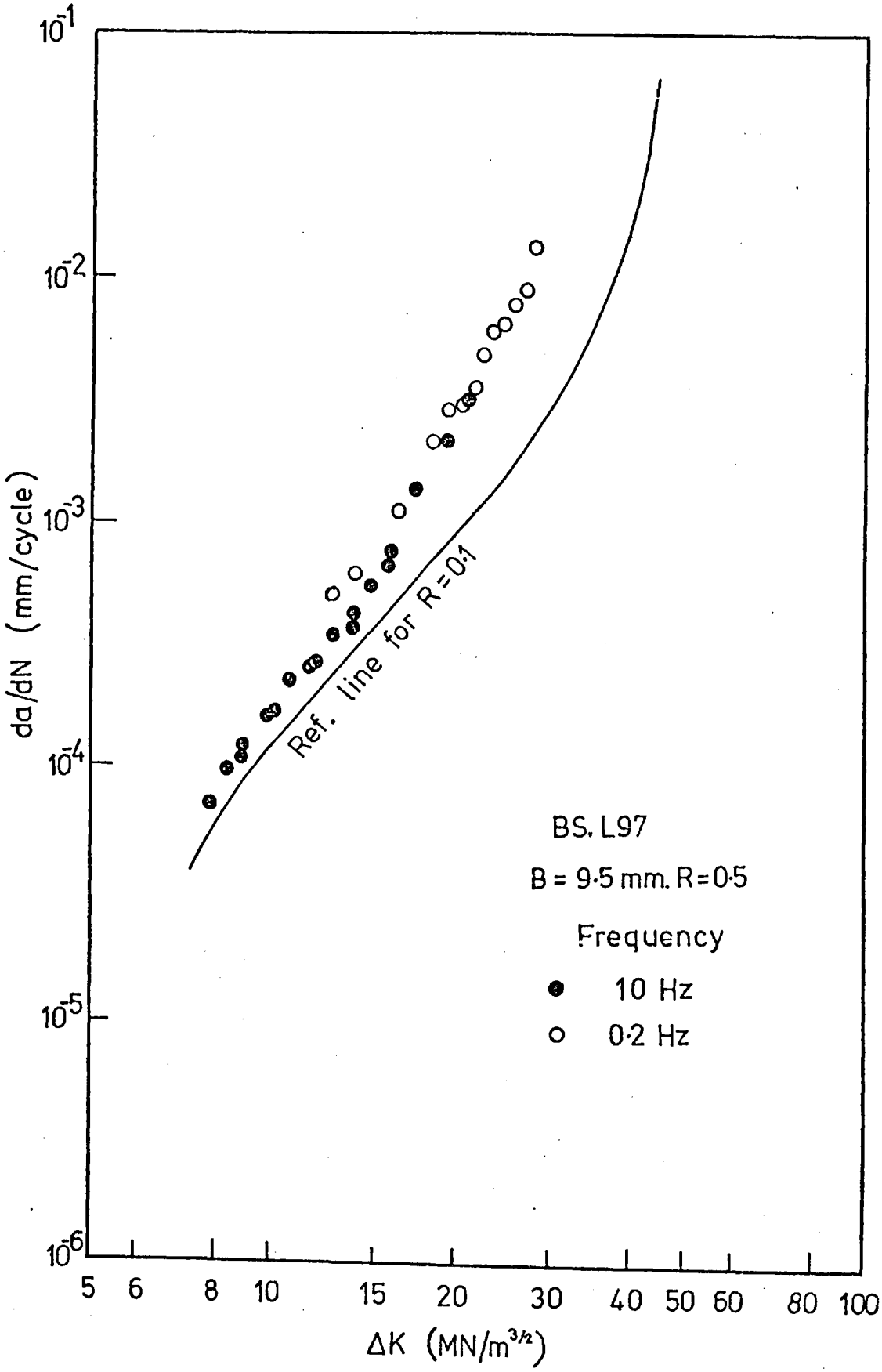


Figure 5.5: Fatigue crack growth in BS.L97

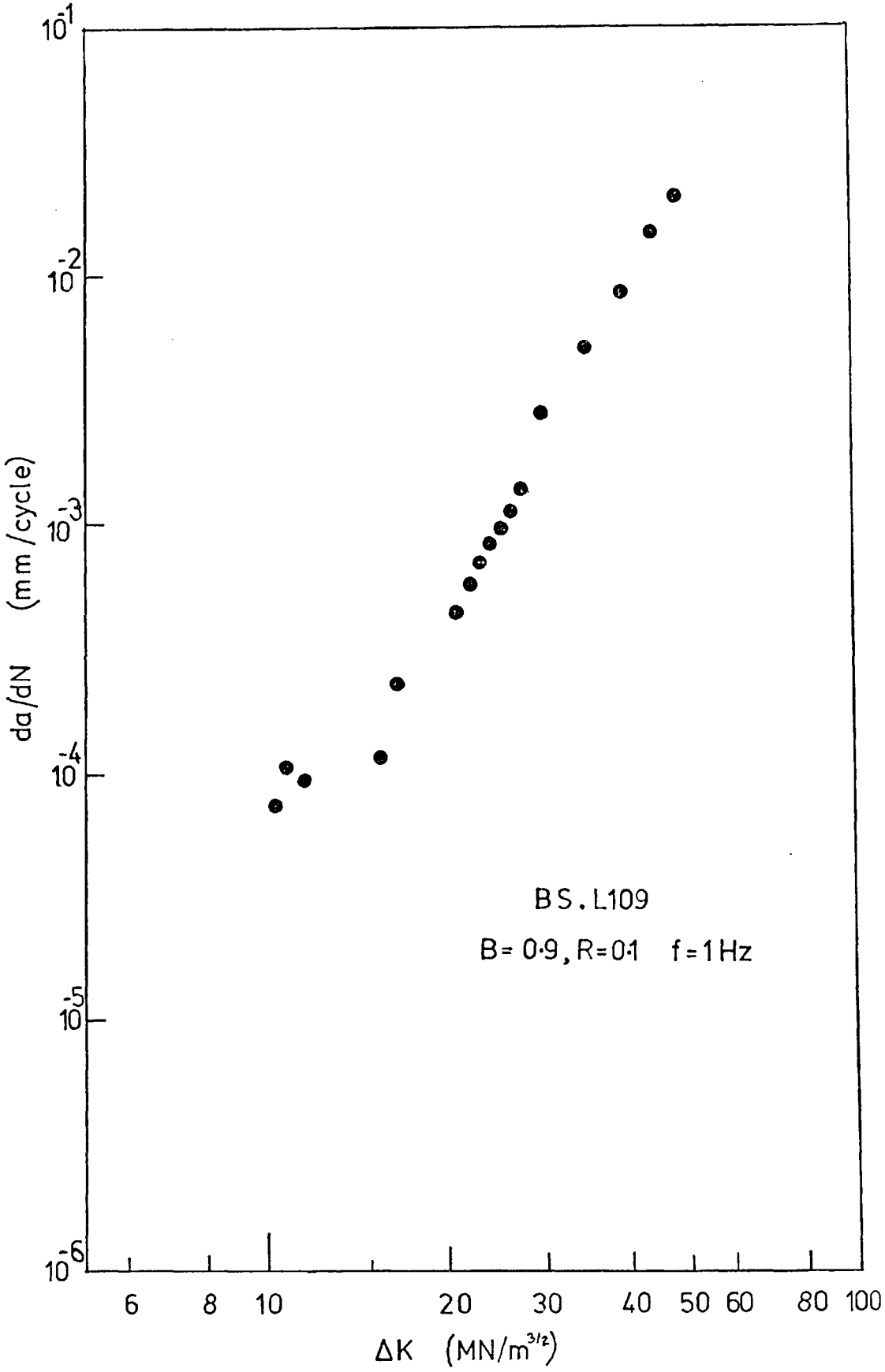


Figure 5.6: Fatigue crack growth in BS.L109

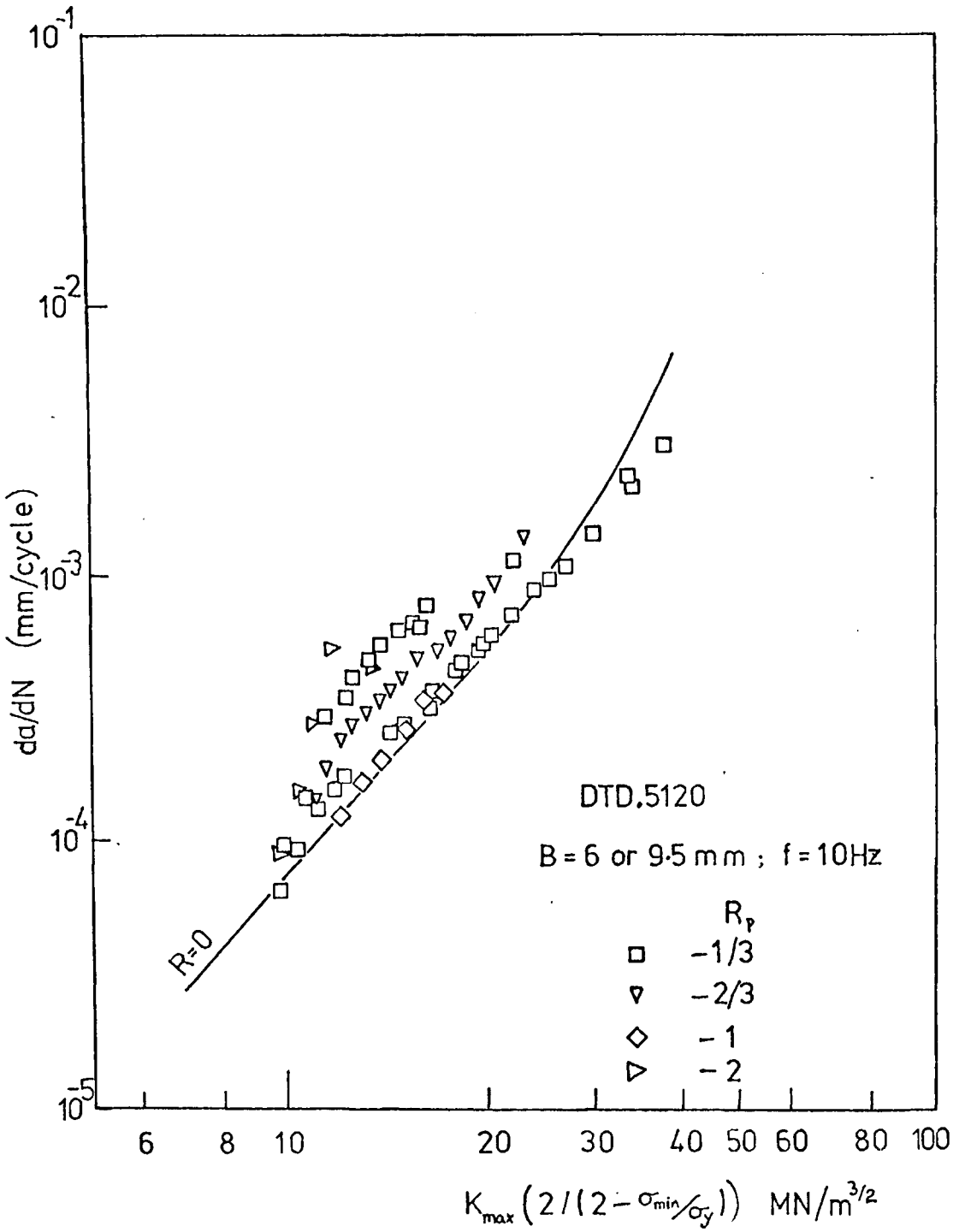


Figure 5.7: Fatigue crack growth in DTD.5120 at negative load ratios

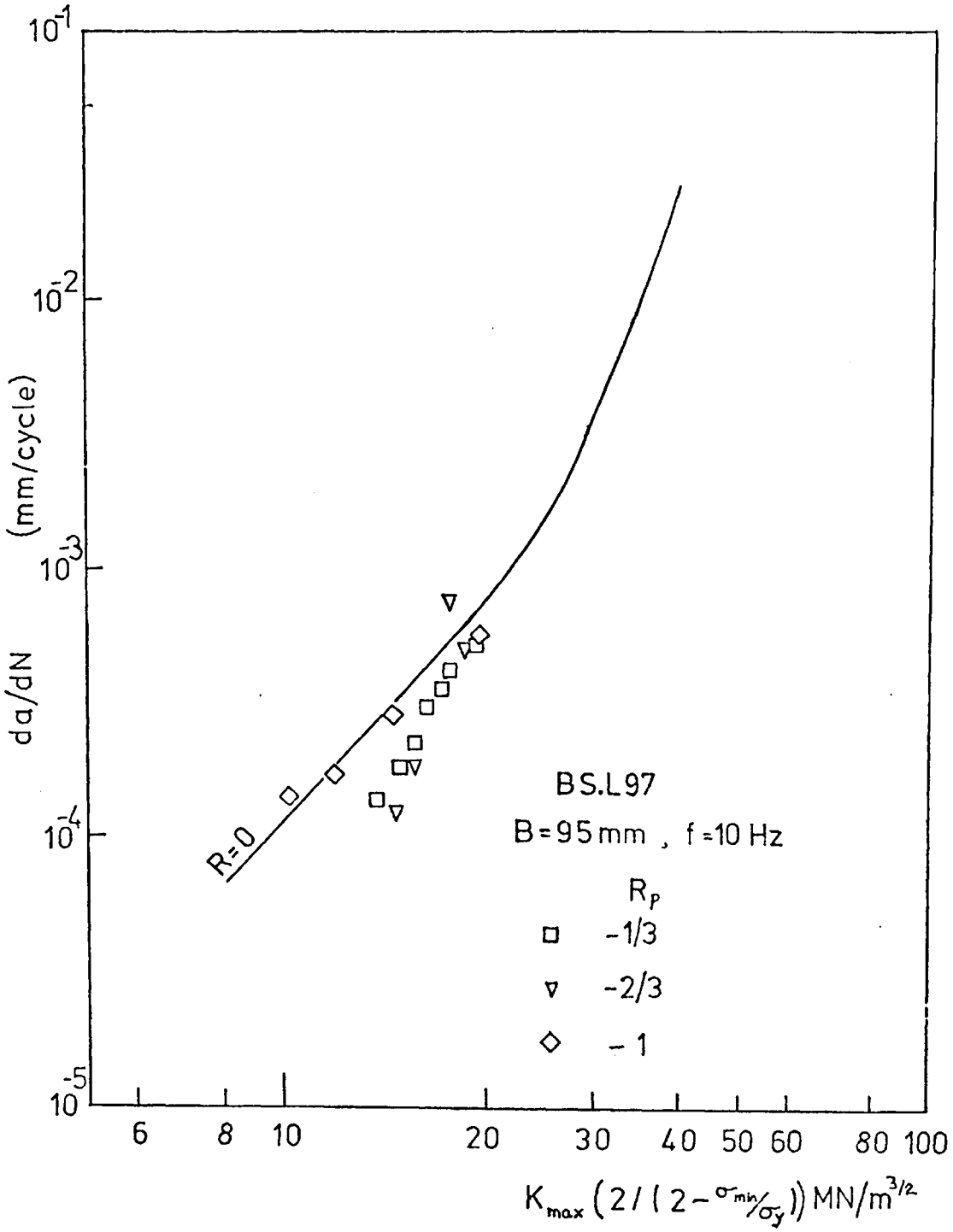


Figure 5.8: Fatigue crack growth in BS.L97 at negative load ratios

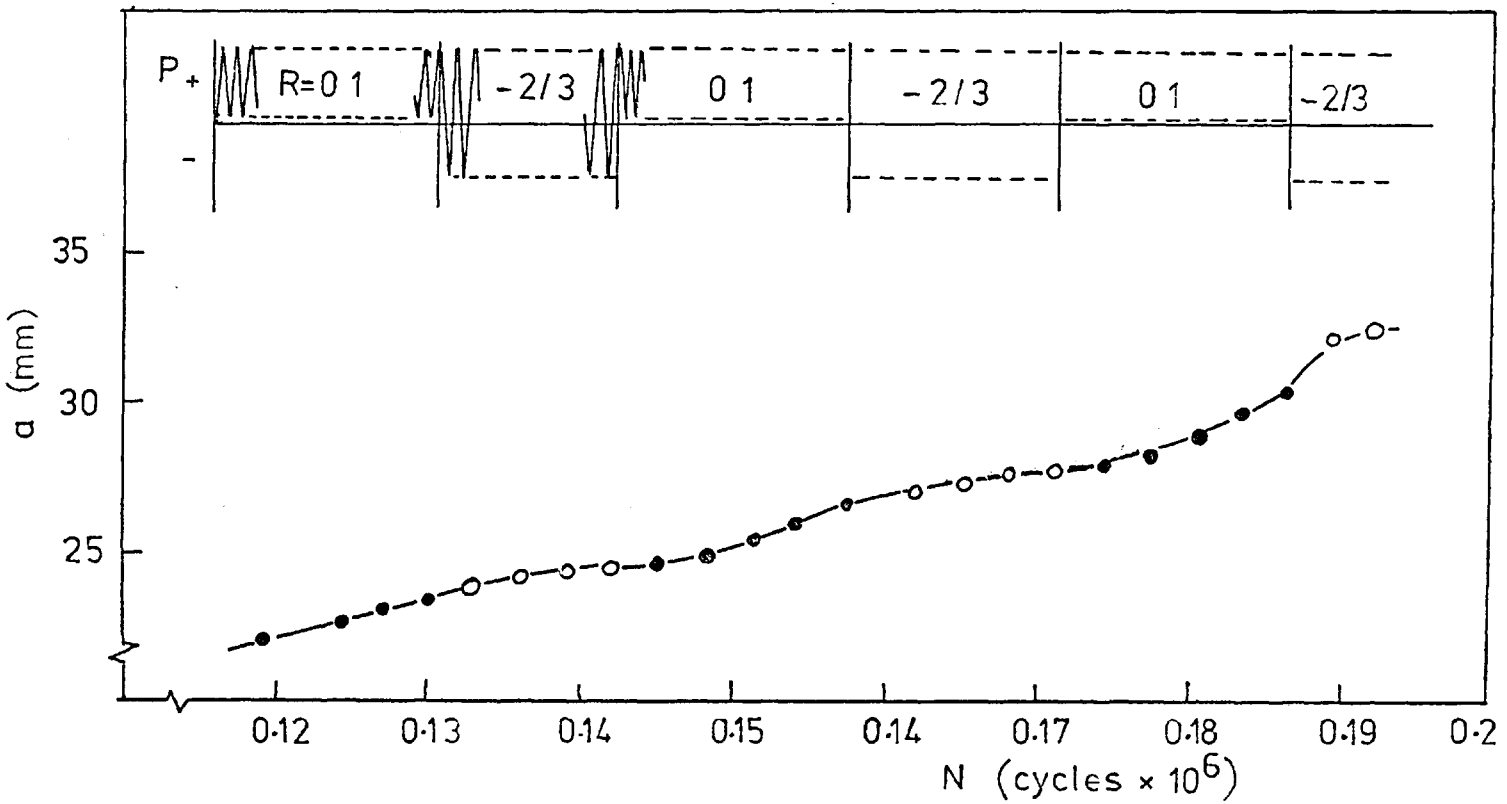


Figure 5.9: Crack retardation at negative load ratios in BS.L97

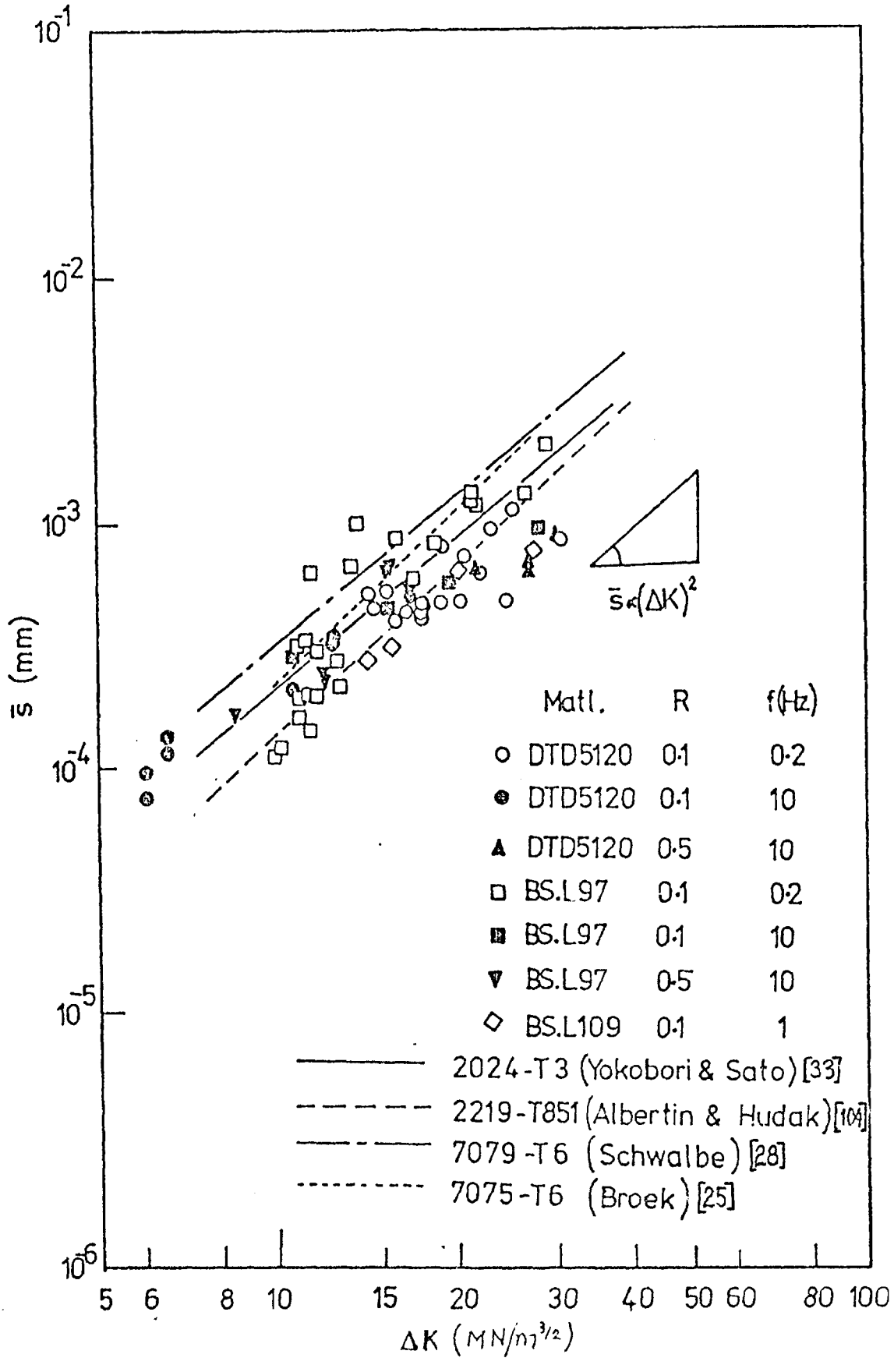


Figure 5.10: Striation spacing measurements in aluminium alloys

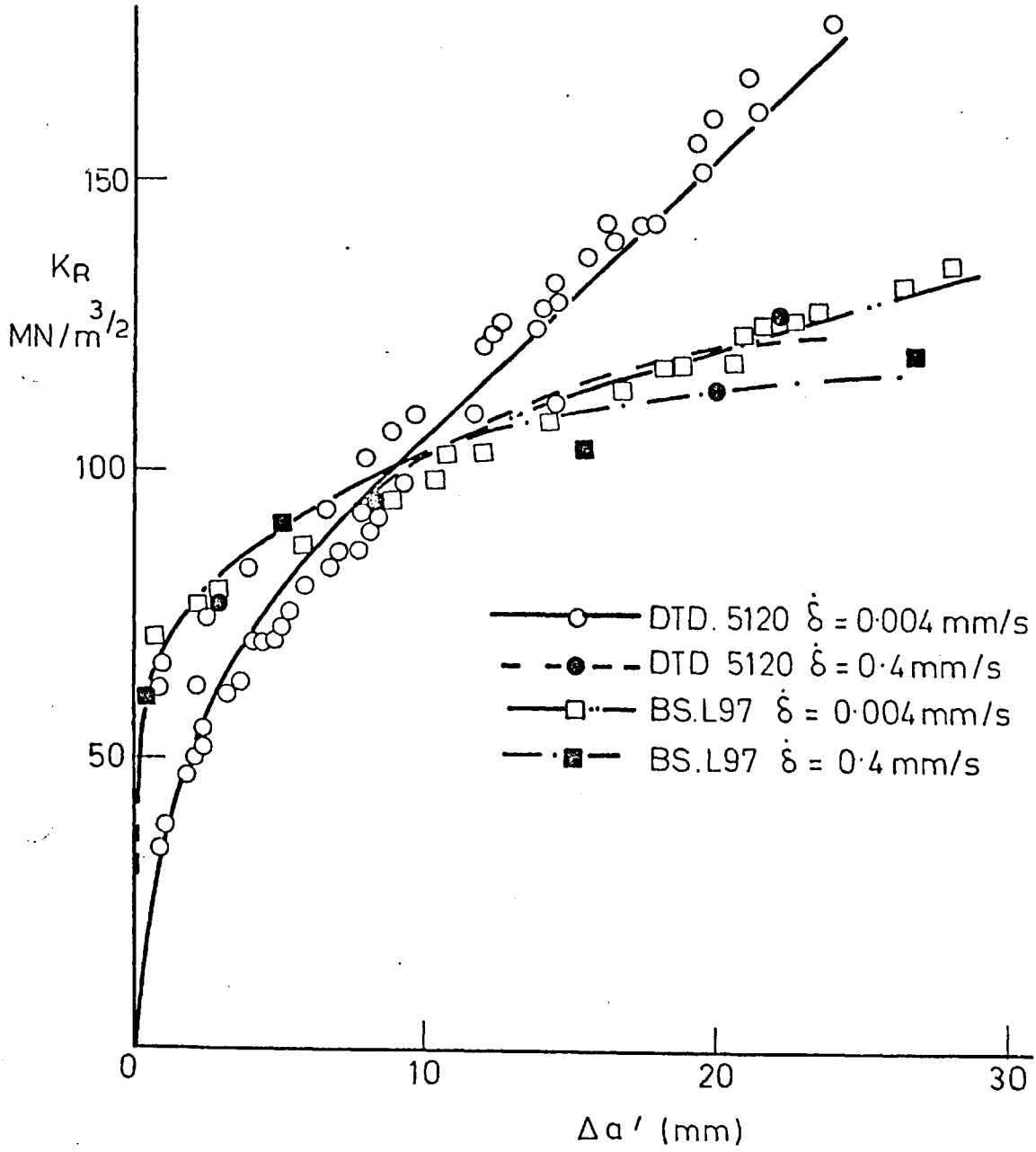


Figure 5.11: Resistance curves for DTD.5120 and BS.L97

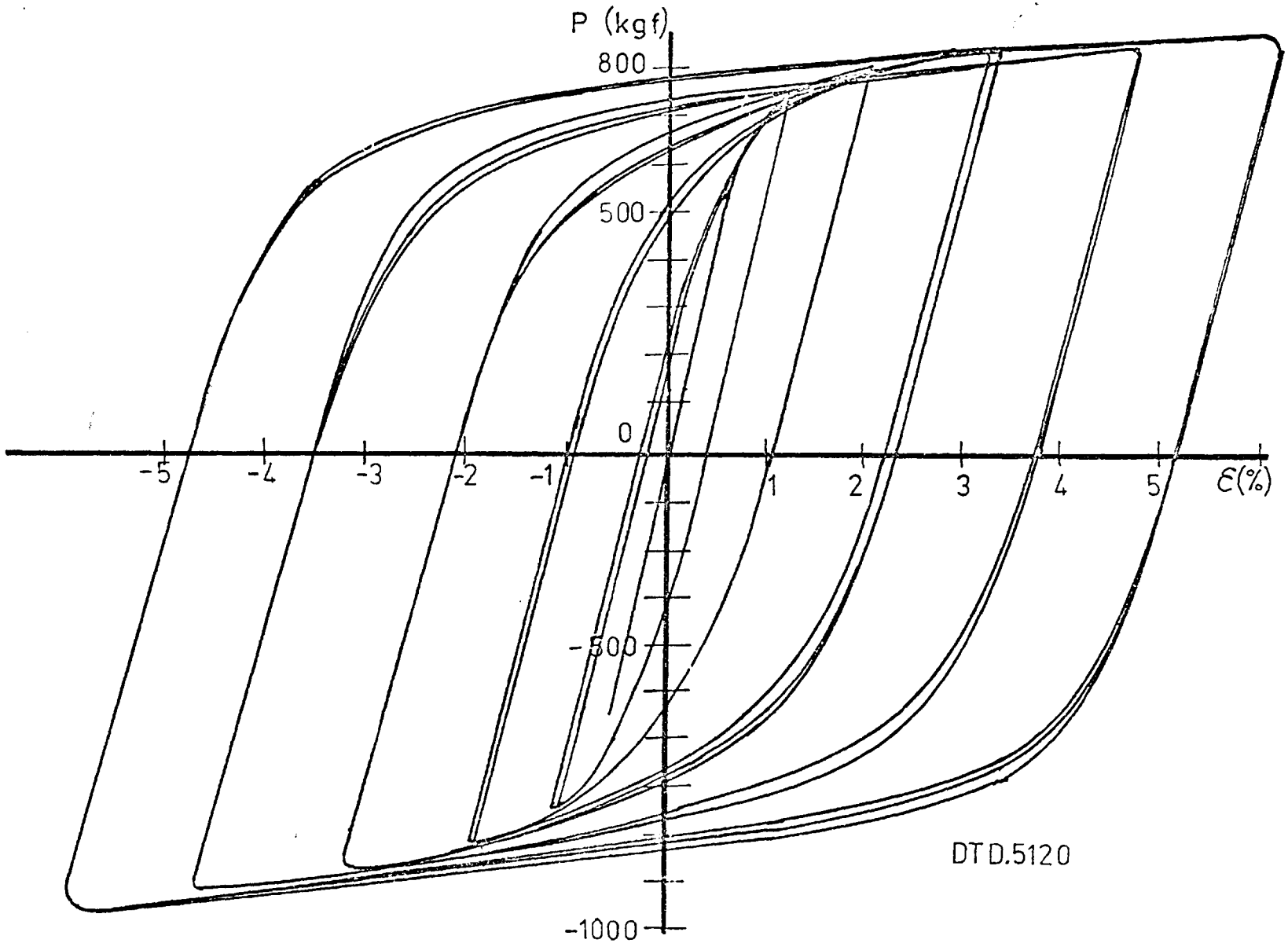


Figure 5.12: Cyclic load-diametral strain results for DTD.5120

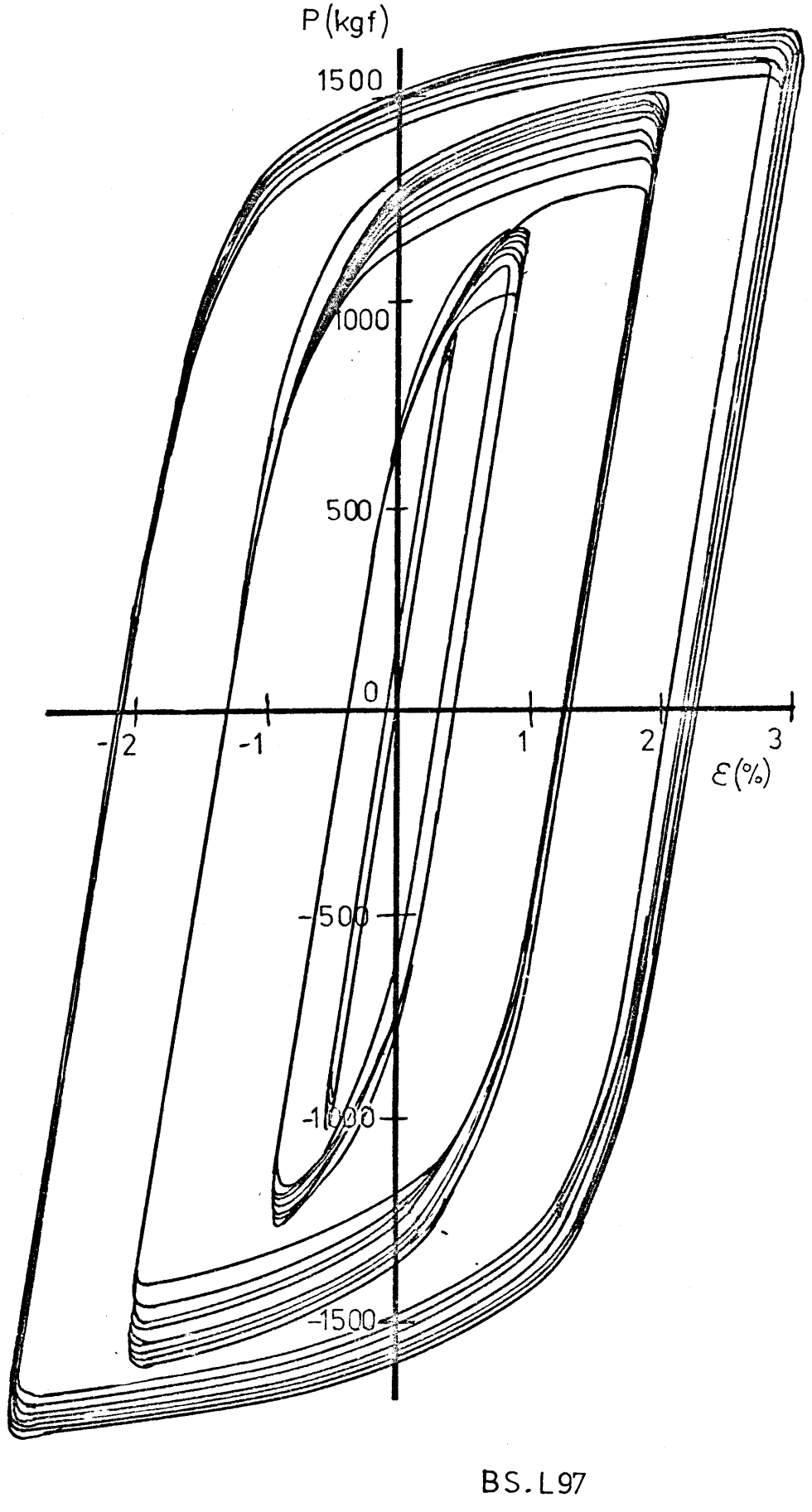


Figure 5.13: Cyclic load-diametral strain results for BS.L97

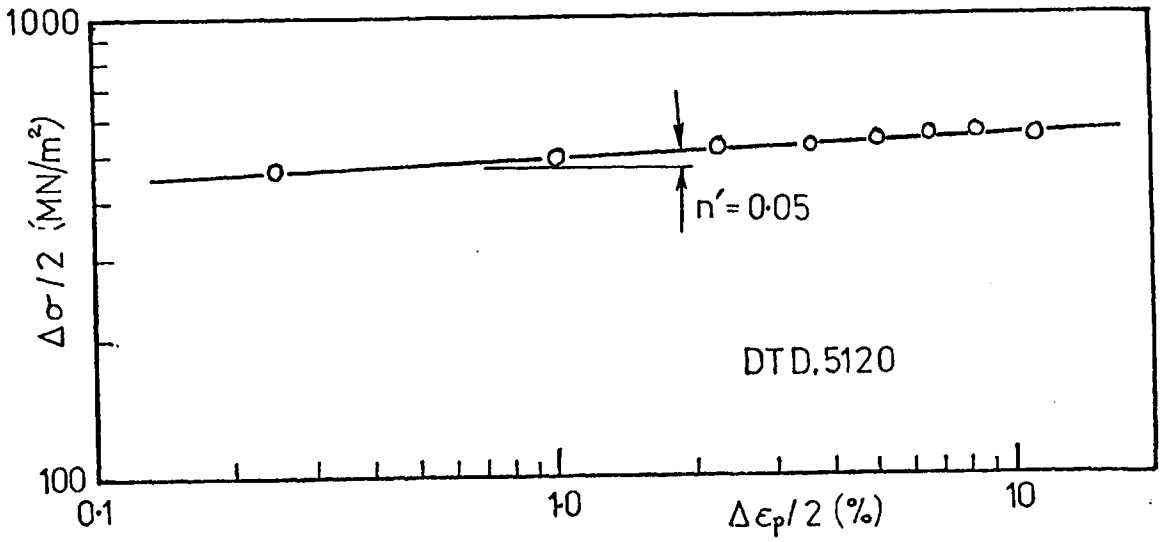


Figure 5.14: Plastic strain range for DTD.5120

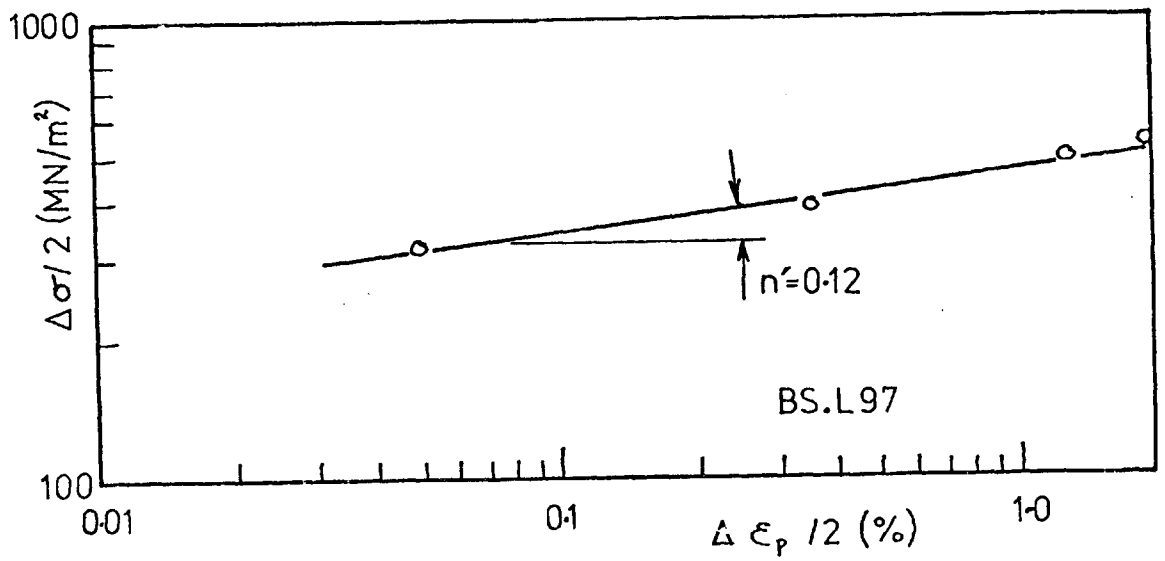


Figure 5.15: Plastic strain range for BS.L97

CHAPTER 6

DISCUSSION

Much of the analysis in this section is based on a simple hypothesis:

Consider a body containing a straight crack with a load applied normal to the crack. An increase in load from zero to L_{max} is accompanied by an increase in crack length from a_o to $(a_o + \Delta a_{o \to max})$ and a corresponding increase in crack growth resistance from zero to K_{Rmax}. Similarly, an increase from a_o to $(a_o + \Delta a_{o \to min})$ would be associated with an increase in resistance from zero to K_{Rmin}.

Now, the increase from zero to L_{max} must give the same crack extension and the same overall increase in crack resistance, as an increase from zero to L_{min} followed immediately by an increase from L_{min} to L_{max}. i.e.

$$\Delta a_{o \to max} = \Delta a_{o \to min} + \Delta a_{min \to max} \tag{6.1}$$

If there is some functional relationship, F, between crack extension and crack growth resistance, e.g.

$$\Delta a_{o \to max} = F(K_{Rmax}) \quad , \quad \text{etc.} \tag{6.2}$$

then:
$$F(K_{Rmax}) = F(K_{Rmin}) + \Delta a_{min \to max} \tag{6.3}$$

i.e.
$$\Delta a_{min \to max} = F(K_{Rmax}) - F(K_{Rmin}) \tag{6.4}$$

Such a relationship is usually assumed to exist when using R-curve methods for analyses of crack growth under monotonic loading, and the relationship, F, is then dependent on the material and thickness (see Section 2.1.4).

During stable crack growth, the resistance must be equal to the stress intensity factor, which may be expressed in general terms, as in Section 2.1.3, by:

$$K = L\, f(a) \tag{6.5}$$

The relationship, F, is found to be most reliable when the equivalent linear elastic crack length, a', measured by compliance methods is used. i.e.

$$a' = a + \phi = a_o + \Delta a + \phi \tag{6.6}$$

where ϕ is a plasticity correction factor, approximating to the plastic zone size (see Section 6.7).

Substituting equations (6.5) and (6.6) into equation (6.4) and dropping the subscript from Δa, we have:

$$\Delta a' = F\left[L_{max}\, f(a'_{max})\right] - F\left[L_{min}\, f(a'_{min})\right] \tag{6.7}$$

If the initial crack length is a_o, and ϕ is negligible at the minimum load, then:

$$\Delta a' = F\left[L_{max}\, f(a_o + \Delta a')\right] - F\left[L_{min}\, f(a_o)\right] \tag{6.8}$$

By conventional fatigue notation, the stress ratio or load ratio, R, is given by:

$$R = \frac{L_{min}}{L_{max}} \tag{6.9}$$

and the range by: $$\Delta L = L_{max} - L_{min} \tag{6.10}$$

Thus: $$\Delta a' = F\left[\frac{\Delta L}{(1-R)}\, f(a_o + \Delta a')\right] - F\left[\frac{R\ \Delta L}{(1-R)}\, f(a_o)\right] \tag{6.11}$$

In order to make use of this equation, four additional steps are required:

i) Identification of a suitable function, F

ii) Evaluation of the crack length dependence, f

iii) Extraction of $\Delta a'$ as an explicit term in the equation

iv) Recognition of the relationship between $\Delta a'$ and Δa

Initially, a simple logarithmic function, F, will be assumed and the function, f, left as a general term. For most geometries, f is, in fact, a known function [8]. On this basis, some attempt will be made to solve the algebraic problem of extracting $\Delta a'$ from the equation. At this stage, reference will be made to observed experimental behaviour to relate Δa to $\Delta a'$, and to improve upon the simple function, F.

Throughout the analysis, reference will be made to the stress intensity factor, as given by:

$$K \equiv L\, f(a') \tag{6.12}$$

and to the "engineering stress intensity factor", given by:

$$K_{eng} \equiv L\, f(a_o) \tag{6.13}$$

Thus, as a starting point, we have:

$$F[K_R] = C\, K_R^{\,m} \tag{6.14}$$

Substituting this into equation (6.11) gives:

$$\Delta a' = C \left\{ \left[\frac{\Delta L}{(1-R)} f(a_o + a') \right]^m - \left[\frac{R\ \Delta L}{(1-R)} f(a_o) \right]^m \right\} \tag{6.15}$$

As a first approximation, assume that $\Delta a' << a_o$ (and hence that $K \simeq K_{eng}$). Thus:

$$\Delta a' = C \left[\Delta L\ f(a_o) \right]^m \frac{(1-R^m)}{(1-R)^m} \tag{6.16}$$

i.e.
$$\Delta a' = C\ (\Delta K)^m \frac{(1-R^m)}{(1-R)^m} \tag{6.17}$$

For $R = 0$, a simple algebraic analysis is also feasible for the assumption that $(\Delta a')^2 << a_o^2$, i.e. equation (6.15) becomes:

$$\Delta a' = C \left[\Delta L\ f(a_o + \Delta a') \right]^m \tag{6.18}$$

By Taylor's expansion:

$$f(a_o + \Delta a') \simeq f(a_o) + \Delta a'\ f'(a_o) + \text{terms in } (\Delta a')^2 \text{ , etc.} \tag{6.19}$$

where:
$$f'(a) = \frac{d}{da} f(a) \tag{6.20}$$

or:
$$f'(a) = \frac{\partial K}{\partial a} \tag{6.21}$$

Ignoring terms in $(\Delta a')^2$, etc., in equation (6.19), and making $\Delta a'$ the subject of the equation:

$$\Delta a' \simeq C \left\{ \Delta L \left[f(a_o) + \Delta a'\ f'(a_o) \right] \right\}^m \tag{6.22}$$

Hence:
$$\Delta a' \simeq C \left\{ \Delta K_{eng} \left[1 + \Delta a' \frac{f'(a_o)}{f(a_o)} \right] \right\}^m \tag{6.23}$$

By binomial expansion, once again ignoring terms in $(\Delta a')^2$, etc.

$$\Delta a' \simeq C\,(\Delta K_{eng})^m\,(1 + m\,\Delta a'\,\frac{f'(a_o)}{f(a_o)}) \tag{6.24}$$

i.e.
$$\Delta a' \simeq \frac{C\,(\Delta K_{eng})^m}{1 - m\,C\,(\Delta K_{eng})^m\,(f'(a_o)/f(a_o))} \tag{6.25}$$

6.1 COMBINATION OF CYCLIC AND MONOTONIC DATA

The preceding analysis - equations (6.1) to (6.25) - is expressed in terms of crack growth under monotonic loading, and is perfectly general, provided that equation (6.14) is a reasonable approximation to the material behaviour.

Under cyclic loading at $R = 0$, Schwalbe [28] has suggested that the physical crack extension is reduced in the ratio of the reversed plastic zone size to the total plastic zone size, as compared with monotonic loading (Section 3.1.1). The limitations of this statement will be discussed below, but it is important to examine the implications of this method for non-zero positive stress ratios.

The crack extension is related to the increase in the distance r ($\theta = 0$), within which tensile yielding takes place on loading. Under cyclic loading, this is clearly Δr_p (from equations (3.2) to (3.4)) and for monotonic loading it is the increase in r_p from that associated with K_{min} to that associated with K_{max}. i.e.

$$\frac{da/dN}{\Delta a'} = \frac{\Delta r_p}{r_{p_{max}} - r_{p_{min}}} \tag{6.26}$$

$$\frac{da/dN}{\Delta a'} = \frac{2^{n'+1}}{4}\,(\frac{\sigma_y}{\sigma'_y})^2\,\frac{(K_{max} - K_{min})^2}{(K_{max}^2 - K_{min}^2)} \tag{6.27}$$

in which n' is the cyclic work hardening exponent, and σ_y and σ'_y are the

yield stress before and after cycling to saturation, respectively.

Dividing the top and bottom lines of equation (6.27) by K_{max}^2 gives:

$$\frac{da/dN}{\Delta a'} = Q \frac{(1-R)^2}{(1-R^2)} \tag{6.28}$$

For fatigue crack growth, the crack extension due to any one loading event is likely to be very much less than the crack length. Thus, equation (6.17) is appropriate which, combined with equation (6.28), gives:

$$\frac{da}{dN} = \frac{(1-R)^2}{(1-R^2)} \frac{(1-R^m)}{(1-R)^m} Q\, C\, (\Delta K)^m \tag{6.29}$$

Figures 6.1 and 6.2 show positive stress ratio fatigue crack growth curves for DTD.5120 and BS.L97, plotted with their R-curves, after applying the factor, Q. Fig. 6.3 shows slow cyclic data (Section 5.3) for BS.L97, similarly.

Although, logically, the preceding argument should only apply to slip controlled mechanisms, the alignment of these results and the consistency of Schwalbe's own data [28] suggest a wider - albeit empirical - application. The major discrepancies lie in the prediction of stress ratio effects (especially in L97) which are over-estimated and in the obvious difference in the slope of static and fatigue curves. There is also some difficulty in extracting physical crack extension data from the monotonic R-curves, in which mode transition may have occurred. Indeed, it is likely that the stated relationship between $\Delta a'$ and da/dN would <u>not</u> apply where a preceding load history had resulted in the formation of macroscopic shear lips. The R-curves shown in Figures 6.1 to 6.3 are all actual values of Δa, measured with a travelling microscope, plotted against true values of K derived from $\Delta a'$. Although this is satisfactory for qualitative comparisons, it will be modified when numerical results are

required at a later stage in the analysis.

The method has some interesting implications with regard to the standard practice [79] of partial unloading during monotonic R-curve tests to check for buckling, etc. Consider, for example, a test in which a specimen is loaded from $L = 0$ to $L = L_1$, unloaded to $L = L_2$, and then reloaded to $L = L_3 \geq L_1$.

The crack extension associated with the first loading is:

$$(\Delta a')_1 = F(K_R)_1 \tag{6.30}$$

For the unloading, there is assumed to be no change in crack length. As the specimen is reloaded to $L = L_1$, there is no change in plastic zone size, compared with the previous condition at L_1, but crack extension is expected, given by:

$$(\Delta a')_2 = Q\,[F(K_R)_1 - F(K_R)_2 - \phi] \tag{6.31}$$

Continuing to load to L_3:

$$(\Delta a')_3 = F(K_R)_3 - F(K_R)_1 \tag{6.32}$$

Thus (Figure 6.4), if the crack growth during unloading is ignored, an error, e, in total crack growth is introduced, given by:

$$e = \frac{(\Delta a')_2}{\{(\Delta a')_1 + (\Delta a')_2 + (\Delta a')_3\}} \tag{6.33}$$

If ϕ is small compared with the crack growth, this gives:

$$e = \frac{Q\,[F(K_R)_1 - F(K_R)_2]}{Q\,[F(K_R)_1 - F(K_R)_2] + F(K_R)_3} \tag{6.34}$$

In Table 6.1, equation (6.34) has been evaluated for $(K_R)_3 = (K_R)_1$, $\Delta a = C\, K_R^m$, and $Q = 0.54$. Unloading to 80% of the applied load, which is a typical figure in practice, gives rise to errors of around 4% which may be acceptable. Further unloading may cause significant errors in the results.

TABLE 6.1

Error, e, Due to Unloading During an R-Curve Test

$(K_R)_1/(K_R)_2$ \ m	3	4	5
0.95	0.004	0.005	0.006
0.9	0.007	0.010	0.011
0.8	0.029	0.035	0.040
0.7	0.062	0.072	0.079
0.5	0.292	0.312	0.323
0	0.54	0.54	0.54

6.2 THE DUAL MECHANISM CONCEPT

It is clear from the most elementary fractography of aluminium alloys that at least two distinct micromechanisms contribute to crack propagation. A simple extension of Schwalbe's [28] dual mechanism approach (see Section 3.7.5) to non-zero stress ratios would seem to solve the problem of changing the power-law index, m, between fatigue and static crack growth with some physical meaning, but this requires the identification of a transition range, $K_1 < K < K_2$. As both theoretical and experimental data for crack growth by a slip mechanism (Sections 3.1 and 5.2) indicate values of m somewhat less than that for the macroscopic crack growth rate curve, da/dN versus ΔK, K_1 would seem to be below the lowest values

considered, and the model becomes very sensitive to the somewhat arbitrary choice of K_1 and K_2. In order to improve this, it is necessary to isolate the two mechanisms.

For the striation formation mechanism, this is quite straightforward as the observed spacing, $\bar{s}$, is closely approximated by equation (6.14) with suitable constants. Following this through to equation (6.29), one obtains:

$$\left(\frac{da}{dN}\right)_1 \simeq \bar{s} = \frac{(1-R)^2}{(1-R^2)} \frac{(1-R^{m_1})}{(1-R)^{m_1}} Q\, C_1\, (\Delta K)^{m_1} \qquad (6.35)$$

In practice, $m_1 \simeq 2$ and the stress ratio dependence is not significant, i.e. equation (6.35) becomes:

$$\left(\frac{da}{dN}\right)_1 \simeq Q\, C_1\, (\Delta K)^2 \qquad (6.36)$$

Isolation of the tearing mechanism is rather more difficult, as a relationship between physical crack extension, Δa, and K_R is required, rather than one involving $\Delta a'$, and this introduces all of the problems of evaluating ϕ. These problems are compounded by the difficulty in measuring "pure tearing" in the fatigue régime. It may be measured reliably during a monotonic test at comparatively high loads, but the backward extrapolation of such data implies many assumptions about the validity of the factor Q and about the micro-mechanisms of sub-critical tearing (see Section 6.4).

If a power-law relationship is assumed, then:

$$\left(\frac{da}{dN}\right)_2 \simeq \frac{(1-R)^2}{(1-R^2)} \frac{(1-R^{m_2})}{(1-R)^{m_2}} Q\, C_2\, (\Delta K)^{m_2} \qquad (6.37)$$

which may, at least, give some insight into the mathematical behaviour of a dual mechanism approach.

[Note that, as $m_1 = 2$, there is no ambiguity in dropping the subscript, so that $m_2 = m$.]

6.2.1 Crack Extension Addition

Having isolated the two processes, and assuming that values may be assigned to the constants C_1, C_2 and m, it is necessary to find some means of combining equations (6.36) and (6.37). The simplest means is, of course, linear addition. This assumes that the crack growth by each mechanism is limited by the imposed stress intensity factor, and that the processes do not interact in any way. Thus:

$$\frac{da}{dN} = \left(\frac{da}{dN}\right)_1 + \left(\frac{da}{dN}\right)_2 = Q\left[\frac{(1-R)^2}{(1-R^2)}\,\frac{(1-R^m)}{(1-R)^m}\,C_2\,(\Delta K)^m + C_1\,(\Delta K)^2\right] \qquad (6.38)$$

This is shown in Figures 6.5 and 6.6 and has also been used by Musuva [94] for a ductile alloy steel at constant stress ratio. The figures show that the problem of discontinuity in the slope has been solved, but that of predicting the sensitivity to stress ratio has not.

6.2.2 Crack Resistance Addition

Another method of combining the two mechanisms is suggested by considerations of energy exchange. As indicated in Section 2.1.5, the justification for the term ΔK as a characterising parameter in fatigue is largely empirical and a corresponding term, ΔG, is not readily interpreted in terms of energy availability. However, if the crack resistance argument is extended to fatigue crack growth, one would expect the rate at which energy becomes available to be related to $(\Delta K)^2$, as in equation (2.6), although this must include, for example, hysteresis losses due to repeated plastic deformation in the cyclic plastic zone. Similarly, the resistance to fatigue crack growth will be represented by a term

corresponding to $(\Delta K_R)^2$.

If, for each mechanism acting alone, $\Delta K_R = \Delta K$, then for a number of mechanisms acting together, the total of all the associated resistance terms must be equal to the rate of energy input, represented by $(\Delta K)^2$. i.e.

$$(\Delta K)^2 = \sum (\Delta K_R)^2 \tag{6.39}$$

Substituting from equation (6.14) for each of the two processes, one obtains:

$$(\Delta K_R)_1 = \left[\frac{\Delta a'}{C_1}\right]^{1/m_1} \quad \text{and} \quad (\Delta K_R)_2 = \left[\frac{\Delta a'}{C_2}\right]^{1/m_2} \tag{6.40}$$

If the total crack extension consists of a fraction, x, due to "mechanism 1", and a fraction, $(1-x)$, due to "mechanism 2", then equations (6.39) and (6.40) become:

$$(\Delta K)^2 = (\Delta K_R)_1^2 + (\Delta K_R)_2^2 = \left[\frac{x\ \Delta a'}{C_1}\right]^{2/m_1} + \left[\frac{(1-x)\ \Delta a'}{C_2}\right]^{2/m_2} \tag{6.41}$$

From this, the value of ΔK required for a given crack extension may be plotted as a function of x for any two mechanisms, as shown in Figure 6.7. In this case, nominal values of m_1 and m_2 equal to 2 and 4, respectively, have been used for illustration. The stress intensity factor and crack extensions have been normalised against the values at the intersection point, i.e. where:

$$(\Delta K)_{ref} = \left(\frac{C_2}{C_1}\right)^{m_2-m_1}$$

and:
$$(\Delta a')_{ref} = C_1 \left(\frac{C_2}{C_1}\right)^{m_1/(m_1-m_2)} \tag{6.42}$$

By logarithmic interpolation, the curve of ΔK versus x may be cross-plotted as $\Delta a'$ versus x, as shown in Figure 6.8.

It is seen that a maximum value of $\Delta a'$ occurs when $x = 0$ for $(\Delta K)_{ref} > \Delta K$, and when $x = 1$ for $(\Delta K)_{ref} < \Delta K$. There is also a minimum value of $\Delta a'$ which may be calculated:

Differentiating equation (6.41) with respect to x at constant ΔK, one obtains:

$$\frac{\partial}{\partial x}\left[\frac{x\ \Delta a'}{C_1}\right]^{2/m_1} + \frac{\partial}{\partial x}\left[\frac{(1-x)\ \Delta a'}{C_2}\right]^{2/m_2} = 0 \tag{6.43}$$

i.e. $$\frac{2}{m_1}\left(\frac{\Delta a'}{C_1}\right)^{(2/m_1-1)} + \frac{2}{m_1}\left(\frac{x}{C_1}\right)^{(2/m_1-1)} \Delta a'^{\,2/m_1}\ \frac{\partial}{\partial x}(\Delta a')$$

$$= \frac{2}{m_2}\left(\frac{\Delta a'}{C_2}\right)^{2/m_2} x^{(2/m_2-1)} - \frac{2}{m_2}\left(\frac{1-x}{C_2}\right)^{2/m_2} \Delta a'^{\,(2/m_2-1)}\ \frac{\partial}{\partial x}(\Delta a') \tag{6.44}$$

The minimum crack extension occurs when $\partial(\Delta a')/\partial x = 0$:

$$\frac{2}{m_1}\left(\frac{\Delta a'}{C_1}\right)^{2/m_1} x^{(2/m_1-1)} = \frac{2}{m_2}\left(\frac{\Delta a'}{C_2}\right)^{2/m_2} (1-x)^{(2/m_2-1)} \tag{6.45}$$

If, for a given crack extension:

$$\begin{aligned} (\Delta K)_1 &\equiv \left(\frac{\Delta a'}{C_1}\right)^{1/m_1} \\ (\Delta K)_2 &\equiv \left(\frac{\Delta a'}{C_2}\right)^{1/m_2} \end{aligned} \tag{6.46}$$

then equation (6.45) becomes:

$$\left[\frac{(\Delta K)_1^{1/m_1}}{(\Delta K)_2^{1/m_2}}\right]^2 = \frac{x^{(1-2/m_1)}}{(1-x)^{(1-2/m_2)}} \tag{6.47}$$

for the minimum crack extension.

For stress ratio $R = 0$, the two mechanisms give identical crack growth rates at the intersection point specified by equations (6.42). If the crack extension at a stress ratio $R > 0$ is η times greater than that at $R = 0$, then the intersection moves to:

$$\Delta a_R = \eta_1 C_1 \left(\frac{\eta_2 C_2}{\eta_1 C_1}\right)^{m_1/(m_1-m_2)}$$

and:
$$\Delta K_R = \left(\frac{\eta_2 C_2}{\eta_1 C_1}\right)^{1/(m_1-m_2)} \qquad (6.48)$$

From equation (6.29):

$$\eta = \frac{(1-R)^2}{(1-R^2)} \frac{(1-R^m)}{(1-R)^m} \qquad (6.49)$$

Within the range of interest, the locus of the intersection point $(\Delta a_R, \Delta K_R)$ is found to be a straight line on the log-log plot with a slope of 2. Increasing R moves the intersection back down this line. The complete Δa versus ΔK curve moves in the same way, as illustrated in Figure 6.9.

In Appendix IV, equations (6.40), (6.41), (6.48) and (6.49) have been used to model fatigue crack growth behaviour in the alloys tested, using striation measurements and monotonic R-curve data. The resulting curves are shown in Figures 6.10 to 6.12 compared with experimental results at different positive stress ratios.

6.2.3 Multi-Mechanism Processes

Theoretically, the crack resistance addition model may be extended to more than two micro-mechanisms, using a correspondingly increased number of empirical constants. For example, under corrosion fatigue conditions, the coefficients of the mechanical fatigue crack growth

terms may be changed by environmental influences, and at the same time a new process, such as active path dissolution, may be introduced [43]. In this case, the total rate at which energy becomes available is increased by an amount due to chemical energy release which is proportional to the CTOD [105]. As this, in turn, is proportional to K^2 (Section 3.1), one obtains an expression of the form:

$$(\Delta K)^2 \ (1 + Z) \ = \ \sum_{i=1}^{3} \ (\frac{x_i}{C_i} \frac{da}{dN})^{1/m_i} \tag{6.50}$$

where process i = 1 is active path dissolution

i = 2 is ductile striation formation

i = 3 is micro-void coalescence

and it is assumed that no other process operates, i.e.

$$\sum_{i=1}^{3} x_i \ = \ 1 \tag{6.51}$$

In practice, the corrosion process is likely to be time-dependent and not cycle-dependent, although cyclic variations in crack opening do influence process zone mass transfer kinetics. It is likely, then, that:

$$Z \ \propto \ \frac{1}{[f \ x_1 \ (da/dN)]} \tag{6.52}$$

where f is the cyclic frequency. Putting z as the constant of proportionality in equation (6.52) and substituting into equation (6.50), one obtains:

$$(\Delta K)^2 \left[1 + \frac{z}{f \ x_1 \ (da/dN)}\right] \ = \ \sum_{i=1}^{3} \ (\frac{x_i}{C_i} \frac{da}{dN})^{1/m_i} \tag{6.53}$$

In order to make full use of any crack resistance addition model, some means must be found by which the proportion, x, due to each mechanism may be estimated. Before this may be attempted, some more detailed attention must be paid to the behaviour of each process.

6.3 STRIATION BEHAVIOUR AT LOW STRESS INTENSITIES

At low stress intensities, the fractography shows quite clearly that the ductile striation formation process is the dominant crack growth mechanism (Figure 6.13). The upper limit of the process is represented by an increasing contribution of the tearing mechanism (Figure 6.14), but the behaviour at the lower limit is unclear. Two observations are reported widely in the literature:

i) That at very low stress intensities, striation markings are not found [32,40,106].

ii) That at their least spacing, the striation markings are further apart than the macroscopic crack growth rate would suggest [25,32,33].

In the present study, tests were not carried out at very low propagation rates, but Figure 6.15 shows Kirby & Beevers data for 7075-T7351 which coincides with the DTD.5120 data at 10^{-5} mm/cycle < da/dN < 10^{-4} mm/cycle, and gives some indication of the expected threshold behaviour.

It is very difficult to devise a model for any threshold in the striation formation mechanism. None of the models in Section 3.1 appear to have a lower limiting condition in terms of continuum mechanics. The results are in good agreement with the theoretical prediction $\overline{s} \propto \Delta K^2$ (equation (3.9)), although any yield stress dependence (c.f. equation

(3.10)) is a little doubtful. Several tentative explanations may be offered for the apparent reduction in da/dN below $\bar{s}$.

6.3.1 Effect of Microscope Resolution Limit

In the present study, the Cambridge "Stereoscan" microscope was used with magnifications up to ×10000, and the Jeol "Temscan" at ×100000, giving resolution limits of about 500 Å (5×10^{-5} mm) and 50 Å (5×10^{-6} mm), respectively. At low stress intensities, striations may be in the form of gentle shallow ridges or shallow slots [26,41] and cannot be identified reliably unless their spacing is substantially greater than the resolution limit. This gave a practical lower limit for the measurement of striation spacing at around 5×10^{-5} mm. By using shadowing techniques on two-stage replicas in a transmission electron microscope, Broek [25] claims to have measured striations 1.4×10^{-5} mm apart, but this seems to be exceptional.

In order to identify a change in micro-mechanism at the low crack growth rate extreme of the striation observations, it is necessary to achieve better resolution or to show differences in the fracture appearance at lower magnification. Several papers in the literature report "quasi-cleavage" fracture appearance for $da/dN \simeq 10^{-6}$ mm/cycle [40,106] without fulfilling either of these requirements. Kirby & Beevers [32] have shown, however, that there is a change in the appearance of the surface at "low" magnifications for crack growth rates below 10^{-7} mm/cycle.

A further difficulty arises in interpreting the statistical significance of striation spacing measurements in this region. If the resolution limit lies within the scatter band for $\bar{s}$, the sample of striation markings observed will be biassed in favour of the higher crack growth rates. In contrast, the quoted macroscopic data, da/dN, at a

corresponding value of ΔK would be based on a crack advance of, say, 0.1 mm, which implies an average over tens or even hundreds of thousands of cycles. This is unlikely, however, to explain the differences of an order of magnitude between $\bar{s}$ and da/dN.

6.3.2 Local In-Plane Variations in Crack Front Orientation

The precise orientation of any small element of the crack front may be influenced by local microstructural features, for example, and may differ significantly from the macroscopic crack front orientation (Figure 6.16). If this difference were an angle θ, then one would expect, locally:

$$\frac{da}{dN} = \bar{s} \cos \theta \tag{6.54}$$

The angle θ is likely to be close to zero for much of the time, i.e. one would expect the local crack front orientation to be similar to that of macroscopic crack front. Considering the worst case, however, one may evaluate a mean value of da/dN for θ varying in a totally random way between ±90°:

$$\frac{da}{dN} = \bar{s} \frac{1}{\pi/2 - 0} \int_0^{\pi/2} \cos \theta \, d\theta \tag{6.55}$$

i.e.

$$\frac{da}{dN} \simeq 0.637 \, \bar{s} \tag{6.56}$$

6.3.3 Local Out-of-Plane Variations in Crack Tip Orientation

In a similar way, one may consider variations in crack growth direction out of the macroscopic crack plane. If the angle of the deviation is ψ, then:

$$\frac{da}{dN} = \bar{s} \frac{1}{\psi_{max}} \int_{o}^{\psi_{max}} \cos \psi \, d\psi \tag{6.57}$$

If ψ_{max} is taken as the maximum possible deviation from the nearest slip system in an FCC crystal (i.e. 30°), then:

$$\frac{da}{dN} \simeq 0.955 \, \bar{s} \tag{6.58}$$

Notice that in this case, the resolved stress is reduced by a factor, $\cos \psi$. If $\bar{s} = C_1 (\Delta K)^2$, then the striation spacing will be reduced by $\cos^2 \psi$. This gives a mean value of:

$$\frac{\bar{s}}{C_1 (\Delta K)^2} = \frac{65}{\pi} \int_{o}^{\pi/6} \cos^2 \psi \, d\psi \tag{6.59}$$

$$\frac{\bar{s}}{C_1 (\Delta K)^2} \simeq 0.913 \tag{6.60}$$

6.3.4 Non-Contributing Cycles

As Sections 6.3.1 to 6.3.3 do not seem to provide a sufficiently powerful process to reduce da/dN below $\bar{s}$, one must conclude that some load cycles produce no striations. This may mean that some cycles do not contribute at all to local crack growth or that several cycles may be needed to produce a single striation. The second argument is unlikely for two reasons: firstly, the correlation between striation spacings and the "once-per-cycle" argument of equation (3.9) is excellent. Secondly, it would imply damage on a scale less than the lattice spacing.

The author prefers the view that some cycles do not contribute at all to crack growth. This could be due, for example, to interactions between the crack front and microstructural features. Any quantitative

assessment of this behaviour would involve modelling a non-continuum stochastic process which is beyond the scope of the present study.

6.4 TEARING BELOW K_{Ic} - A STOCHASTIC APPROACH

Following the arguments of Section 3.2, tearing is not possible when the maximum stress intensity factor is less than K_{Ic} (equation (3.23)). This statement is modified a little if one assumes the potential void nucleation sites to be distributed at random with some mean spacing, $\bar{d}$. For example, the probability that the spacing, d, is less than a critical radius, r_c, may be given by:

$$P\{d; d \leq r_c\} = \mathcal{F}(d) \tag{6.61}$$

where $\mathcal{F}(d)$ is a normal distribution function:

$$\mathcal{F}(d) = \frac{1}{S\sqrt{2\pi}} \int_{-\infty}^{b} exp\left[-\frac{1}{2}\left(\frac{d-\bar{d}}{S}\right)^2\right] dd \tag{6.62}$$

in which S is the standard deviation. Of course, negative values of $\mathcal{F}$ are meaningless but, if $\bar{d} \geq 3S$, the negative part of the distribution curve is less than 0.1% of the total. This curve is shown in Figure 6.17. If K_{Ic} is now defined as the stress intensity factor for which the probability of tearing at any point on the crack front exceeds, say, 0.95, then for a standard deviation of 10%, one has:

$$K_{Ic} \simeq 1.11\, E\, n \sqrt{2\pi\, \bar{d}} \tag{6.63}$$

Although this applies to crack growth by tearing alone, it is not sufficient when two mechanisms may contribute. In Section 3.2, $\bar{d}$ was used in place of r, which is the distance from the crack tip to the next

void nucleation site. If the alternative mechanism may also influence the position of the crack tip in relation to the next void, then r may be any distance less than d. Consider the probability of tearing if d is normally distributed about $\bar{d}$, and b is uniformly distributed, such that $0 \leqslant b \leqslant d$. The probability density function, illustrated in Figure 6.18, is now given by:

$$P\{d,b\,;\,(d-b) \leqslant r_c\} = \iint_X f_{bd}(b,d)\, db\, dd \qquad (6.64)$$

This may be evaluated by modifying the standard normal distribution tables for the domain $0 \leqslant b \leqslant d|_o^\infty$, and subtracting that for $0 \leqslant b \leqslant d|_{r_c}^\infty$. This results in the curves of Figure 6.19.

If the tearing threshold stress intensity, K_{It}, is defined as the point at which the probability of tearing at any position on the crack front is 0.05, then for tearing alone and $S = 0.1$:

$$K_{It} \simeq 0.8\, K_{Ic} \simeq 0.9\, E\, n \sqrt{2\pi\, \bar{d}} \qquad (6.65)$$

but, for a two-mechanism process:

$$K_{It} \simeq 0.2\, K_{Ic} \simeq 0.22\, E n \sqrt{2\pi\, \bar{d}} \qquad (6.66)$$

This information may now be put back into the crack resistance addition model of Section 6.2.2 in order to estimate the fraction of the crack growth due to tearing, i.e. $(1-x)$.

Consider three possibilities:

i) That all values of x - and thus of $(1-x)$ - are equally likely.

ii) That all values of $(1-x) \leqslant P\{tearing\}$ are equally likely.

iii) That the mean value of $(1-x)$ is equal to $P\{tearing\}$.

Once again, numerical evaluation of these expressions is carried out in Appendix IV.

The crack growth rate is a mean value for the appropriate values of x at a given value of ΔK. The percentage of the surface covered by striations is derived from the mean value of $(x\,Q\,\Delta a)$ divided by the crack growth rate. This is seen to decrease as ΔK increases or as R increases. Figures 6.20 to 6.22 indicate this behaviour.

6.5 TENSILE LIGAMENT INSTABILITY MODEL (TLIM)

As an alternative to the stochastic approach to tearing below K_{Ic}, an attempt was made to adapt Krafft's tensile ligament instability model, described in Section 3.7.1. Although this proved unsuccessful, the method is described briefly:

In its usual form, a ligament instability criterion is supposed to apply to all fatigue crack growth. It should be possible, however, to apply the method to the tearing component alone. Data on DTD.5120, BS.L97 and RR58 [44] have been used by the Naval Research Laboratory in conjunction with their "TLIM77" computer program, and the results [107] are presented in Figures 6.23 to 6.25. Some difficulties were encountered when using TLIM77 for $K_{max} > K_{Ic}$, so that complete curves are not available for the alloys in the present study. There is, however, a general trend to underestimate da/dN in the high growth rate régime, and to underestimate stress ratio effects. This is particularly noticeable for RR58 and is consistent with similar analyses on data for 2124-T851 and 2219-T851 aluminium alloys [62].

There are two curve fitting parameters which are quoted. The "process zone size", d_T, is said to correspond to the dimple size or

inclusion spacing in steels and titanium alloys [61]. Secondly, the term M is defined by:

$$z^M \equiv \frac{\Delta r_T / r_T}{\Delta \varepsilon_p} \qquad (6.67)$$

in which $\Delta r_T / r_T$ is the proportional reduction in ligament size due to surface annihilation by a corrosion process, and $\Delta \varepsilon_p$ is the plastic strain range experienced close to the crack tip. (N.B. This notation is consistent with the TLIM77 program. In earlier versions [31], this term would be represented by a function proportional to z^{M-N}.) If there is no corrosion, one expects $M \to -\infty$, but this, in practice, underestimates the slope of the da/dN versus ΔK curve in region II. The "best fit" results obtained are summarised by the following data:

Material	d_T (μm)	M
DTD.5120 (L-T)	3.2	-5
BS.L97 (L-T)	6.3	-4
RR58 (S-L)	7.0	-7

It is a little surprising that d_T has the smallest value for the high purity material, and that M has the least value (implying the least corrosion effect) for a material and orientation known to be susceptible to stress corrosion cracking. Furthermore, if these values of d_T are substituted for $\overline{d}$ in equation (3.23), along with the values of n that were used in the TLIM analysis, the following values of K_{Ic} were obtained.

Although the calculated value for DTD.5120 appears to be very close to the actual value, there is not obvious correlation between calculated and measured values of K_{Ic}. In general, both K_{Ic} and d_T are larger than expected.

Material	d_T (μm)	n	K_{Ic} (Calculated) ($MN/m^{3/2}$)	K_{Ic} (Typical Value) ($MN/m^{3/2}$)
DTD.5120 (L-T)	3.2	0.11	36.6	36
BS.L97 (L-T)	6.3	0.18	62.5	49
RR58 (S-L)	7.0	0.08	37.7	23
2124-T851 [62]	6.5	0.055	25.0	20

If the TLIM results are used to interpret only the tearing component of crack growth, the physical process considered is matched much more closely by the theoretical background to TLIM. However, the only curves which may be taken from the TLIM77 computer output to fit the tearing data require that both d_T and M be increased to account for the elevated threshold and steeper slope, respectively. This implies that both K_{Ic} and the corrosion sensitivity are increased compared with the earlier fit, neither of which is acceptable (Figures 6.26 and 6.27).

6.6 THE GEOMETRY DEPENDENCE OF K_c

From the description of crack growth resistance behaviour in Section 2.1.4, it has been shown that unstable crack growth occurs under load control when the curve of strain energy release rate (the "G-curve") is tangential to that of crack growth resistance (the "R-curve").

This implies that:

$$K = K_R \quad \text{and} \quad \frac{\partial K}{\partial a} = \frac{\partial K_R}{\partial a} \tag{6.68}$$

If equations (6.5) and (6.14) apply - i.e. $\Delta a = C\, K_R^{\,m}$ and $K = L\, f(a)$, then:

$$\frac{\partial}{\partial a}\left(\frac{\Delta a}{C}\right)^{1/m} = \frac{\partial L}{\partial a} f(a) + L\, f'(a) \tag{6.69}$$

For instability, the load reaches a maximum so that $\partial L/\partial a = 0$, giving:

$$\frac{1}{m\,C}\left(\frac{\Delta a}{C}\right)^{(1/m)-1} = L\,f'(a) \tag{6.70}$$

Now, substituting $K_c = L\,f(a') = K_R$ at the instability point:

$$\frac{1}{m\,C} = K_c^{\,m}\,\frac{f'(a)}{f(a)} \tag{6.71}$$

The term $f'(a)/f(a)$ is dependent on the geometric properties (e.g. shape, size and crack length) and is independent of loading. It may be considered as a geometry characterising parameter denoted by Γ thus:

$$K_c = \left(\frac{\Gamma}{m\,C}\right)^{1/m} \tag{6.72}$$

Values of Γ for CT and CCT specimens are given in Appendix I.

Calculation of the load at failure involves calculation of the crack growth prior to instability, i.e.

$$L_{max} = \frac{K_c}{f(a_c)} \tag{6.73}$$

This procedure may be avoided by evaluating the term K_{eng_c}, such that:

$$\text{as } K_c = L_{max}\,f(a_c) \quad , \quad \text{then } K_{eng_c} \equiv L_{max}\,f(a_o) \tag{6.74}$$

Now, for small crack extensions:

$$K_{eng_c} \simeq K_c - \Delta a_c\left(\frac{\partial K}{\partial a}\right) \tag{6.75}$$

$$= K_c - C\,K_c^{\,m}\left(\frac{\partial K}{\partial a}\right) \tag{6.76}$$

Substituting from equation (6.71) for K_c^m:

$$K_{eng_c} \simeq K_c - C \frac{f(a)}{f'(a)} \frac{1}{m\,C} \left(\frac{\partial K}{\partial a}\right) \tag{6.77}$$

$$= K_c - C \frac{K_c}{\partial K/\partial a\big|_c} \frac{1}{m\,C} \left(\frac{\partial K}{\partial a}\right) \tag{6.78}$$

$$= K_c \left(1 - \frac{1}{m}\right) \tag{6.79}$$

Thus: $$K_{eng_c} \simeq \left(1 - \frac{1}{m}\right) \left(\frac{\Gamma}{m\,C}\right)^{1/m} \tag{6.80}$$

Although several approximations are involved in deriving this function, the form of the final equation may be used as a basis for an empirical function, such as:

$$K_{eng_c} = K_{c_{ref}} \left(\frac{\Gamma}{\Gamma_{ref}}\right)^{\gamma} \tag{6.81}$$

where γ is a measure of the "geometry sensitivity". Maximum load toughness values have been obtained for a number of materials and geometries, and the correlation is demonstrated in Figure 6.28.

Comparing equations (6.72) and (6.81), it can be shown that the parameters m and C and the parameters γ and $\{K_{c_{ref}}/\Gamma_{ref}^{\gamma}\}$ are related, so that the equation:

$$\Delta a' = C\,K_R^m$$

may be rewritten as:

$$K_R = \frac{K_{eng_c}}{1-\gamma} \left(\frac{\Delta a}{\gamma\,\Gamma_{ref}}\right)^{\gamma} \tag{6.82}$$

Thus, a curve of $K_{eng_c}/(1-\gamma)$ against $\gamma\Gamma$ is identical to a curve of

K_R versus $\Delta a'$ - the conventional R-curve - provided that $\Delta a'_c$ is small. Figures 6.29a and 6.29b show R-curve and K_{eng_c} data plotted together, which demonstrates that this is the case.

Notice that in equation (6.25), an infinite crack growth rate is predicted when:

$$m\,C\,(\Delta K_{eng})^m \frac{f'(a_o)}{f(a_o)} \simeq 1 \tag{6.83}$$

$$\Rightarrow K_{eng_c} \simeq \left[\frac{1}{m\,C}\frac{f'(a_o)}{f(a_o)}\right] \tag{6.84}$$

which is of the same form as the present case.

Some recent NASA research [108-110] has been aimed at deriving R-curves from existing residual strength data (e.g. K_c). Using their notation, a sensitivity factor, γ, is identified, defined by:

$$\gamma \equiv \frac{(1 + 2\alpha)}{\lambda} \tag{6.85}$$

in which $\lambda = a/W$ and $\alpha = \lambda/Y\ (dY/d\lambda)$, where $Y = K/(\sigma\sqrt{\pi a})$.

The expression for α has certain elements in common with the definition of Γ above. It is important to recognise the significance of the dimensions of Γ (i.e. length) absent from equation (6.85). The non-dimensional form can only account for the influence of specimen shape, whereas the geometry characteristic Γ incorporates size effects as well.

Figures 6.30 and 6.31 show some residual strength data from the literature, which has been re-calculated to enable K_{eng_c} versus Γ to be derived. In each case, data were calculated from basic maximum load and crack length results, and not from authors' calculated values of K_c, so that consistent stress intensity and Γ/W solutions were used.

Figure 6.30 shows data on DTD.5014 (an RR58 aluminium alloy) pin-lug specimens tested at RAE Farnborough [111]. It had been thought that SENT

toughness tests were unreliable as they did not always give conservative K_c values for predicting fracture behaviour of the more representative lug specimens. It is seen that the low toughness values, which occurred with either long or short cracks, all coincide with very low values of Γ.

Figure 6.31 shows some data for thin section 18% Ni maraging steel specimens [112]. For each specimen size, there is a tendency for K_{eng_c} to be reduced at the highest values of Γ. These cases are representative of long cracks in CCT specimens, where buckling may have occurred.

Data on other aluminium alloys from various sources [89,113-115] also confirm a general trend for increasing K_{eng_c} with increasing Γ. For design purposes, it seems that K_{eng_c} versus Γ data are more reliable than conventional K_c data, but not as reliable as complete R-curve analyses. It may, however, provide a useful method of residual strength analysis when data is limited.

6.7 FRACTURE MODE TRANSITION AND SPECIMEN COMPLIANCE

The results of Section 5.4 show that, although K_R versus Δa may be affected by mode transition, there is very little effect on "effective" R-curve, K_R versus $\Delta a'$.

In order to match the R-curve to the top of the da/dN versus ΔK curve, the two must be expressed in terms of the same parameters. Any term da'/dN is rather ambiguous as it is not clear whether one should consider cyclic or total plastic zone sizes, or whether one should consider loading half-cycles or complete cycles. It is, therefore, desirable that the R-curve should be expressed as K_R versus Δa, the physical crack extension.

As a first approach, it was decided that this could be achieved by subtracting the theoretical plastic zone size (c.f. Section 2.3.2) from compliance-derived crack extensions. In support of this method, use was made of the R-curve results to measure the difference between compliance-

derived and physical crack extensions.

Defining $\phi \equiv (a' - a)$, one expects:

$$\phi = r_p = \frac{1}{2\pi} \left(\frac{K}{\sigma_y}\right)^2 \quad \text{or} \quad \frac{1}{6\pi} \left(\frac{K}{\sigma_y}\right)^2 \tag{6.86}$$

for plane stress and plane strain, respectively.

For convenience (initially, at least), a non-dimensional graph may be plotted showing:

$$\frac{\phi}{B} \quad \text{versus} \quad \frac{1}{B} \left(\frac{K}{\sigma_y}\right)^2 \tag{6.87}$$

The following trends were observed:

i) The theoretical plane stress plastic zone size represents an upper limit for values of ϕ.

ii) The value of ϕ cannot exceed the specimen thickness, B, unless transition to a fully developed 45° plane is complete.

iii) During monotonic loading, the value of ϕ may remain constant, equal to the specimen thickness, while the mode transition occurs, but the transition may commence long before this condition is reached.

In order to extend this data to very large values of ϕ/B, it is necessary to consider thin sections for which fully developed slant fracture is expected throughout the test. Detailed R-curve tests were not carried out on the L109 sheet specimens, but some data are available from the literature (Figure 6.32). At RAE, Farnborough [89,116], centre-cracked tension (CCT) specimens were used, as well as CT specimens. Their CT2/30, CT2/120 and CT2/240 specimens correspond to the CTB/30, CTB/120 and CTB/240 specimens in the present study, apart from minor details.

Heyer & McCabe [117] used crack line wedge loaded specimens (CLWL). The results are shown in Figure 6.32a. Moving from the large CCT specimens through progressively smaller CT specimens to the CLWL tests, the loading and buckling constraints become more severe and the value of ϕ decreases. Even in the CCT case, it is only about two-thirds of the theoretical plane stress value.

These results may now be considered in comparison with the results on 6 mm and 9.5 mm thick specimens (Chapter 5) shown in Figure 6.32b. For plane strain conditions [75,76], standards require $B > 2.5\ (K/\sigma_y)^2$ (and, in some cases, much more than this [77]) which is indicated in the figure. Most points lying just above this condition have ϕ close to the theoretical plane stress value. As the crack extends and mode transition commences, the slope gradually decreases as described above.

The dependence of transition characteristics on loading rate and loading constraint is not entirely clear, but there are some consistent trends. Mode transition normally occurs by the progressive development of shear lips (Figure 6.34) which eventually meet so that they cover the entire specimen width. During fatigue crack propagation, the transition more usually occurs by gradual "rotation" of the crack front from square to a 45° slant fracture. In every case, an increase in loading rate causes a reduction in the amount of crack extension required to complete the transition. The early completion of transition at high loading rates is thought to account for the reduction in K_R at long crack extensions for the fast R-curve in Figure 5.11.

A comparison of fatigue crack surfaces formed at 0.2 Hz with those obtained at 10 Hz confirms this trend. Despite this, the mode transition always began at a crack growth rate of about 9×10^{-4} mm/cycle in 9.5 mm thick DTD.5120 and 5.5×10^{-4} mm/cycle in BS.L97, regardless of stress ratio or frequency. This observation is in agreement with the early work

of Broek & Schijve [118].

6.8 EFFECT OF FREQUENCY AND ENVIRONMENT

Observations of frequency effects in the present study confirmed the general trends discussed in Section 3.4. Increasing the frequency from 0.2 Hz to 10 Hz caused a reduction in crack growth rates of no more than one half at $R = 0.1$ in both DTD.5120 and BS.L97, although this is rather less than the general scatter of data. At $R = 0.5$, the effect is less noticeable and a further increase from 10 Hz to 50 Hz did not appear to make any difference.

Yokobori's formula (equation (3.21)) implies a reduction of about 30% over the same frequency range and a further 6% changing from 10 Hz to 50 Hz. Equation (3.22) predicts no difference between 0.2 Hz and 10 Hz, and about 15% reduction for $\Delta K < 10$ MN/m$^{3/2}$ increasing from 10 Hz to 50 Hz. Evidently, in all cases, the reduction in crack growth rate with increasing frequency is a small effect in the range of interest, but serves as a warning against accelerated tests at very high frequencies, which may not give conservative results.

There is considerable evidence in support of environment controlled processes causing frequency effects, but the concept of a simple time-dependence/cycle-dependence interaction may be misleading. Under stress corrosion conditions, corrosion fatigue crack growth rates become more sensitive to frequency as the frequency decreases. In the limit, the crack growth is simply time-dependent and becomes "stress corrosion cracking" [43]. For aluminium alloys in air, the situation is reversed. The sensitivity to frequency is less at very high frequencies. The environmental influence is more likely to be related to dislocation transport of hydrogen [26], for example, which is a rate sensitive process, rather than any active path corrosion.

6.9 EFFECT OF SPECIMEN THICKNESS

The variations in fatigue crack growth rate and stable crack growth behaviour are indicated in Figures 5.3 and 6.33. It is noticeable that the two 15 mm thick specimens of DTD.5120 showed higher crack growth rates than 9.5 mm or 6 mm specimens under the same conditions, and had lower crack growth resistance under static loading. The reduction in K_{eng_c} (Figure 6.28a) was relatively small - rather less than 10% - for given values of Γ. There was no significant difference between 6 mm and 9.5 mm thick specimens.

The effect of the reduction in K_{eng_c} upon fatigue crack growth rates may be estimated by substituting from equation (6.71) into equation (6.25), giving a crack growth equation with the denominator:

$$1 - (K_{max}/K_{eng_c})^m \qquad (6.88)$$

where m is the slope of log $\Delta a'$ versus log K_R. (This is developed further in Section 7.1.) Taking a typical case of Γ = 20 mm, K_{eng_c} at B = 9.5 mm is about 60 MN/m$^{3/2}$, and that at B = 15 mm is 54 MN/m$^{3/2}$. Using m = 2.04 from Figure 6.28a, this gives the following changes in da/dN:

ΔK (MN/m$^{3/2}$)	10	20	30	40	50
$\frac{da/dN\ (B = 15\ mm)}{da/dN\ (B = 9.5\ mm)}$	1.247	1.276	1.343	1.523	2.65

These figures are of the same order as the increases in growth rate observed, implying that the reduced fatigue crack propagation lives of thicker sections are entirely due to their reduced toughness. The

reasons for the reductions in toughness of thicker sections are well documented [5,6]. The increased constraint in the "through-thickness" (z) direction causes a reduction in total plastic zone size until the ideal plane strain condition is reached. At this point, the toughness is of a minimum value equal to K_{Ic}.

6.10 NEGATIVE STRESS RATIOS

It is clear from Figures 5.7 to 5.9 that the cyclic plastic zone correction to the stress intensity range (Section 3.1.1) is not sufficient to account for the effects observed at negative stress ratios. Indeed, neither K_{max} nor $K_{max}/(1-R)$ nor $2K_{max}/(2-\sigma_{min}/\sigma_y)$ provide a good correlation with experimental data. Two certain conclusions may be drawn:

i) That the compressive portion of the cycle may be detrimental.

ii) That constant amplitude tension-compression cycling may cause crack retardation after some time.

Data on 2219 aluminium alloy [104] suggest that there is little effect on striation spacing, so that any crack extension or retardation in compression must be due to some other process. Detailed fractography is not very informative as considerable impact and fretting damage may occur during subsequent testing which obscures any features of the crack growth mechanism.

It is suggested that any acceleration in fatigue crack growth is due to changes in tearing behaviour caused by damage occurring during prior compression cycles. In this way, there is no crack growth in compression but the occurrence of negative loads does cause an acceleration in crack growth rates.

Any retardation seems almost certain to be the result of branching or turning of the crack tip. Travelling microscope observations during testing indicated a more irregular crack path at negative load ratios than at positive ones.

6.11 COMPARISON WITH CCT TEST RESULTS

Both the 6 mm thick DTD.5120 and the 0.9 mm thick BS.L109 results may be compared directly with data obtained using centre-cracked tension specimens [91,97]. These results are shown in Figures 6.35 and 6.36. In general, the CCT results show higher crack growth rates than the CT tests. There are three major differences to be considered:

6.11.1 Inherent Stress Biaxiality

The differences in the non-singular stress component parallel to the crack in CT and CCT specimens were discussed in qualitative terms in Section 4.3. Although this does not affect the stress intensity factor, there is considerable evidence to suggest that the non-singular component does affect the fatigue crack growth rate in aluminium alloys [119,120], steels [121] and polymers [122]. This is attributed to changes in the plastic zone shape under biaxial conditions.

If the applied load parallel to the crack is denoted by P_x and that normal to the crack by P_y, then one may define a biaxiality ratio, λ, by:

$$\lambda \equiv \frac{P_x}{P_y} \tag{6.89}$$

Some data are available for thin section RR58 aluminium alloy: using CCT data at $\lambda = 0$ as a base line, Anstee et al [119] showed an increase in crack propagation life by a factor 1.5 at $\lambda = 0.5$ and 2.2 at $\lambda = 1$. Hopper and Miller [120] studied the same material and showed

little effect at low crack growth rates (e.g. 5×10^{-5} mm/cycle) but a factor of 1.4 at $\lambda = 1$ and 0.85 at $\lambda = -1$ at higher da/dN. These results are quite consistent as Anstee's tests were carried out with high mean crack propagation rates. Qualitatively, these results are the same as those on steels [121] and polymers [122], showing a decrease in da/dN with increasing λ.

Leevers [122] has used a computational technique to derive expressions for an inherent biaxiality ratio, λ_o, for various test specimens which have finite non-singular stresses, σ_{xx}, even under uniaxial external loading ($\lambda = 0$). These are illustrated in Figure 6.37 and show typical values of $0 < \lambda_o < 0.6$ in a CT specimen and $\lambda_o \simeq -1$ in a CCT specimen. By simple superposition, one would expect a CCT specimen with an externally applied $\lambda = 1$ and inherent $\lambda_o = -1$ to give the same results as a CT specimen containing a short crack ($\lambda_o \simeq \lambda = 0$). If it is assumed that the behaviour of RR58 is typical of other high-strength aluminium alloys, one would expect no difference between CT and CCT results at low crack growth rates, but for CT tests to give about one half of the crack growth rate for CCT tests at high crack growth rates.

6.11.2 Buckling Constraint

As indicated in Section 4.3, it is more difficult to provide anti-buckling devices in a CCT test than in a CT test. If the CCT anti-buckling bars are only clamped at the ends, wide panels with bars of insufficient stiffness may show a tendency to buckle. Similarly, if a gap is left between the bars for crack tip observation, buckling may occur. This may introduce an unwanted K_{III} component and accelerate crack growth. (Note that no buckling constraint was applied in either CT or CCT tests on 6 mm thick alloys.)

6.11.3 Geometry Characteristic

At very high stress intensities, the difference in the geometry characteristic, Γ (see Section 6.6), may be significant. It is shown in Appendix I that the non-dimensional term, Γ/W, increases with a/W for the normal working range of a CCT specimen, but decreases for a CT specimen. This would tend to decrease crack propagation rates at very high stress intensities in CCT specimens.

In conclusion, it appears that the difference between compact tension test results and centre-cracked tension results is no greater than one would expect in view of the difference between the test specimens. As the trends are the same for 0.9 mm thick and 6 mm thick materials, and very high crack growth rates cannot be compared in detail, the differences are most likely to be due to differences in the inherent stress biaxiality in the two designs.

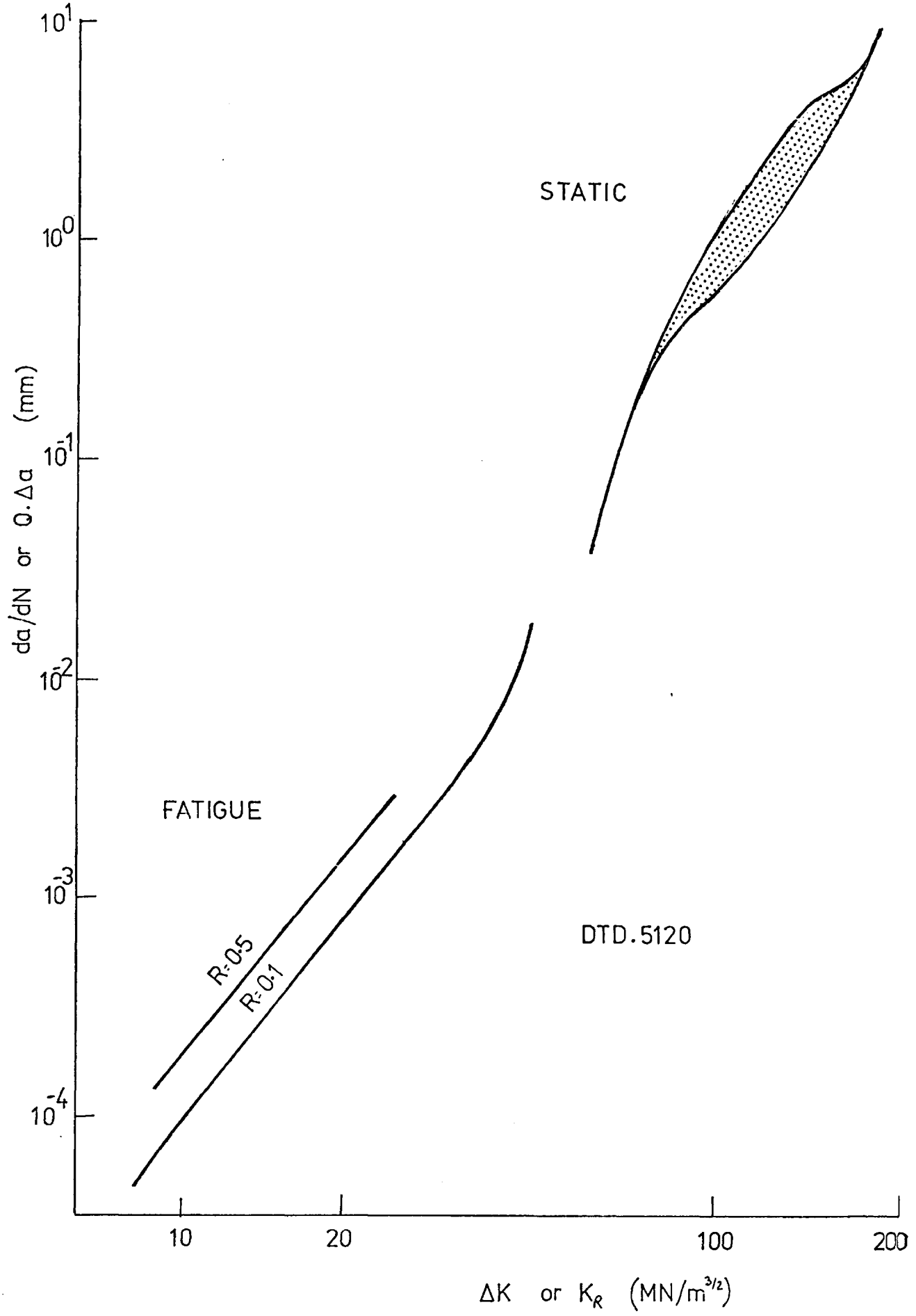


Figure 6.1: Static and monotonic data for DTD.5120

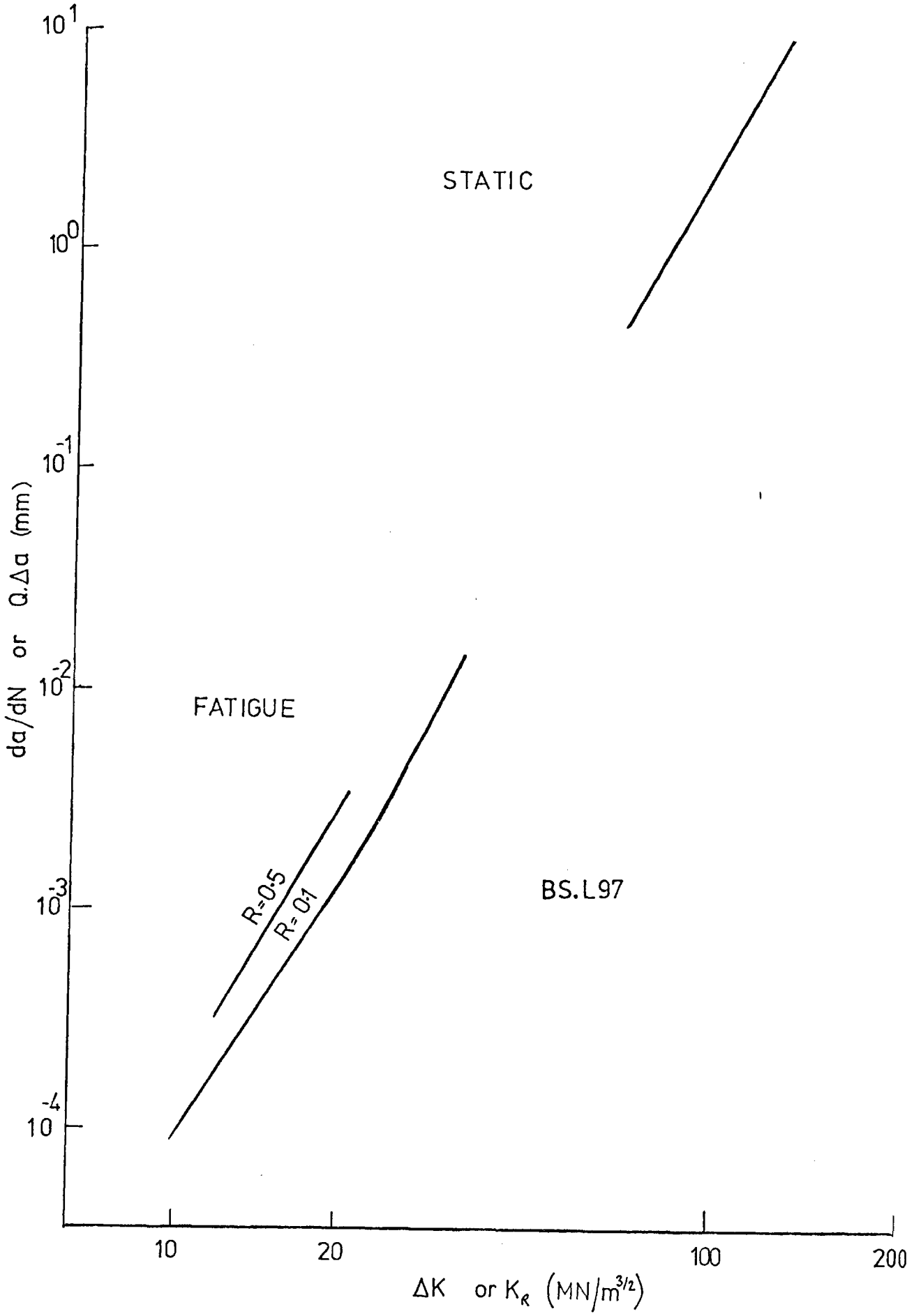


Figure 6.2: Static and monotonic data for BS.L97

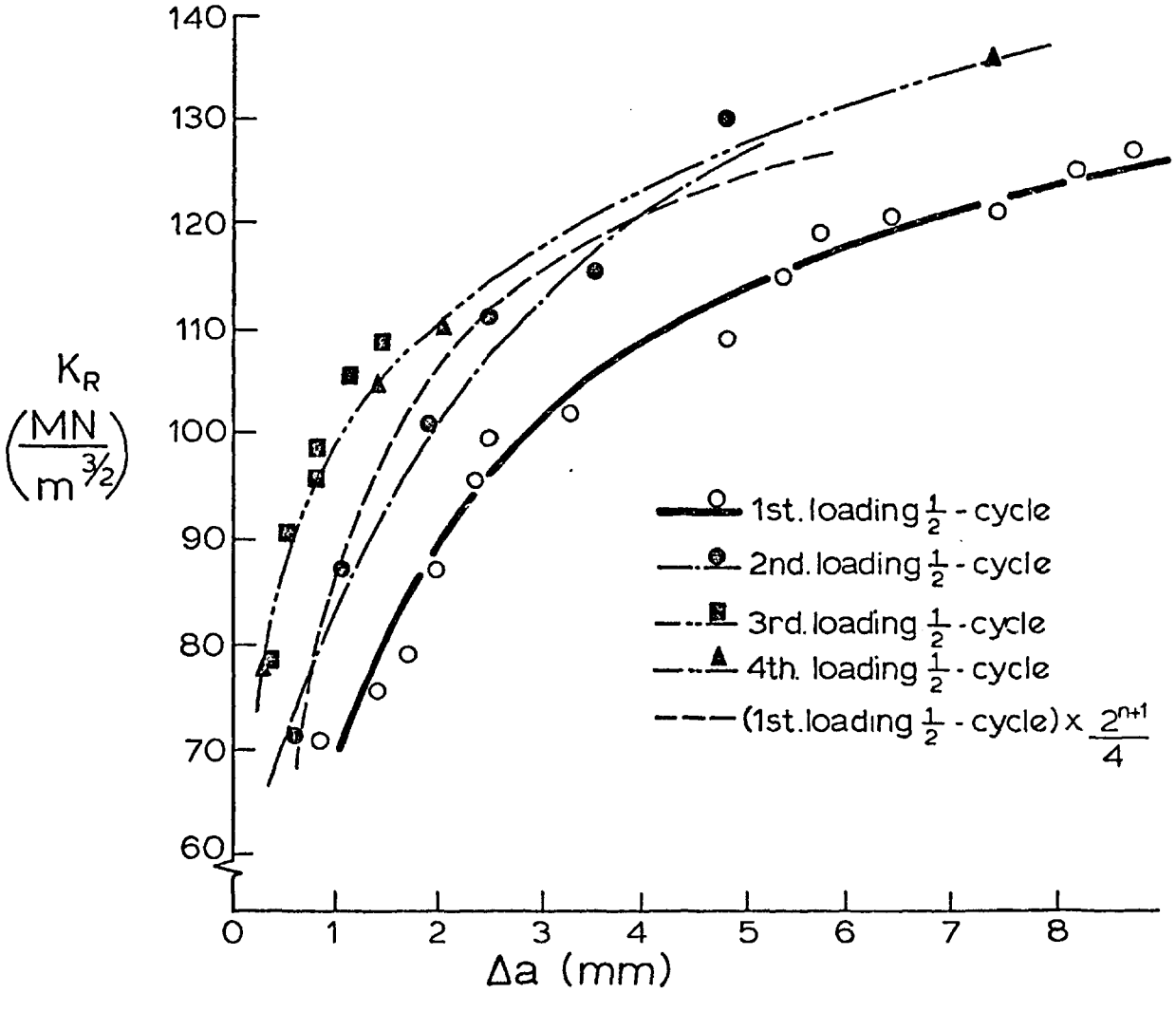


Figure 6.3: Cyclic *R*-curve data for BS.L97

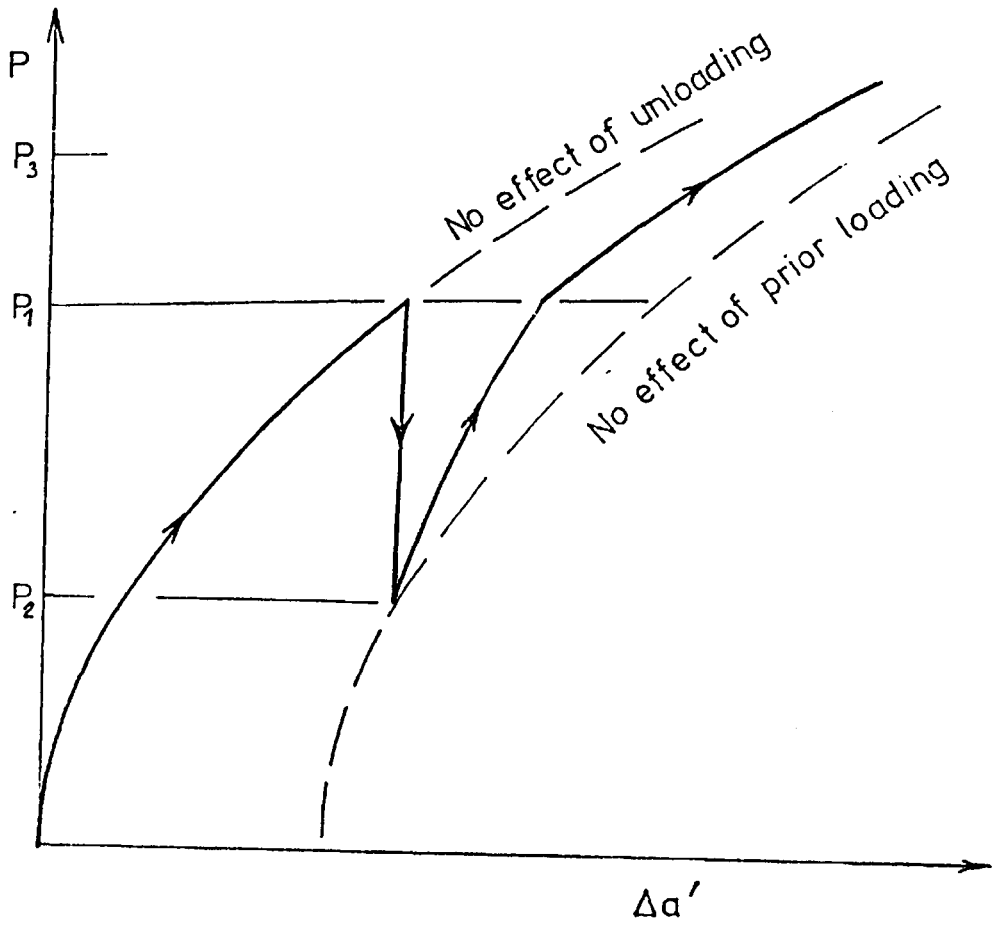


Figure 6.4: Effect of unloading during *R*-curve testing

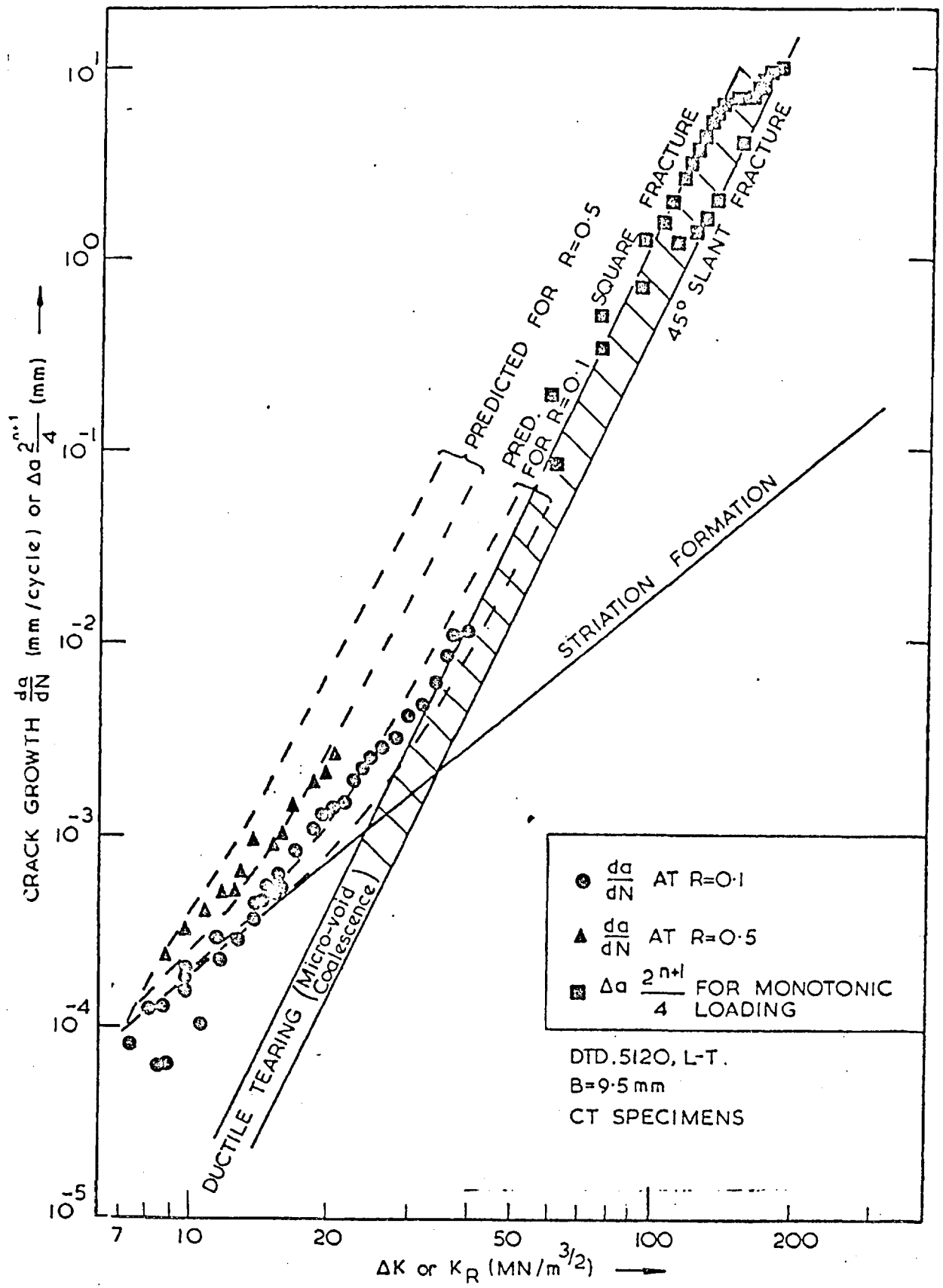


Figure 6.5: Crack extension addition model for DTD.5120

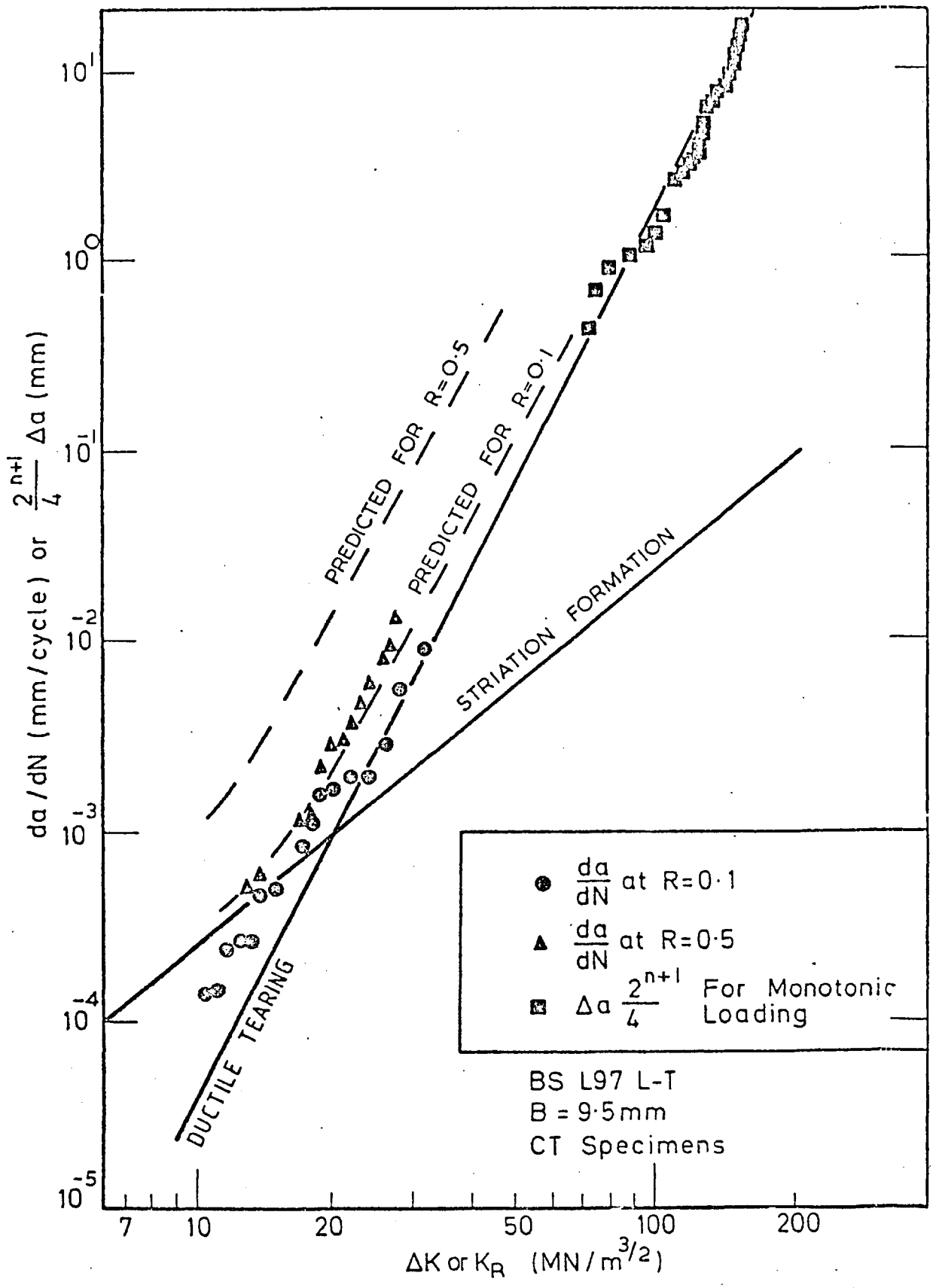


Figure 6.6: Crack extension addition model for BS.L97

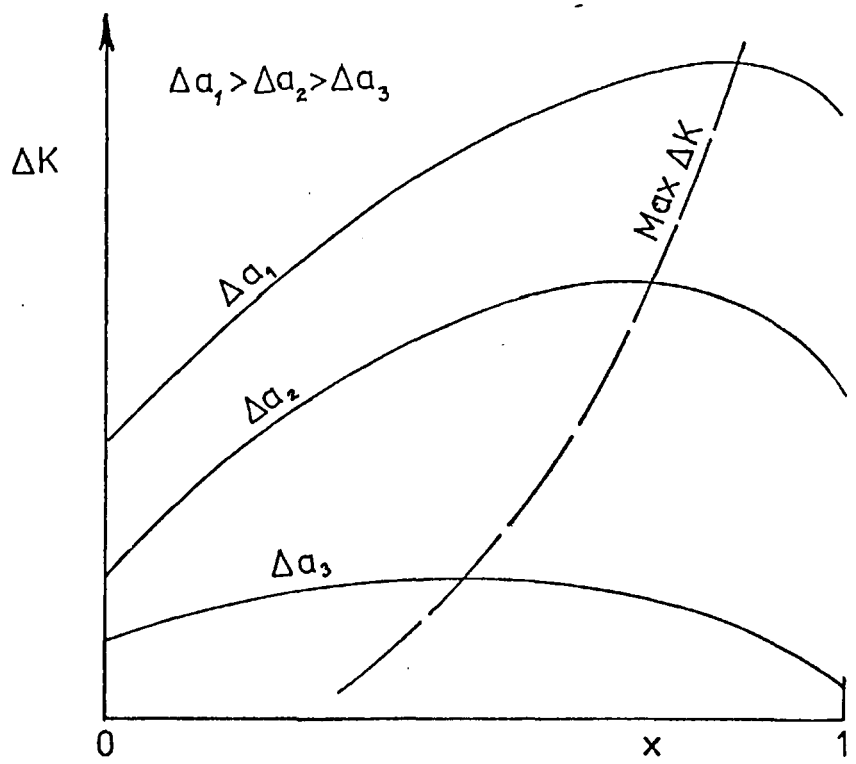


Figure 6.7: Variation of ΔK with x at constant Δa

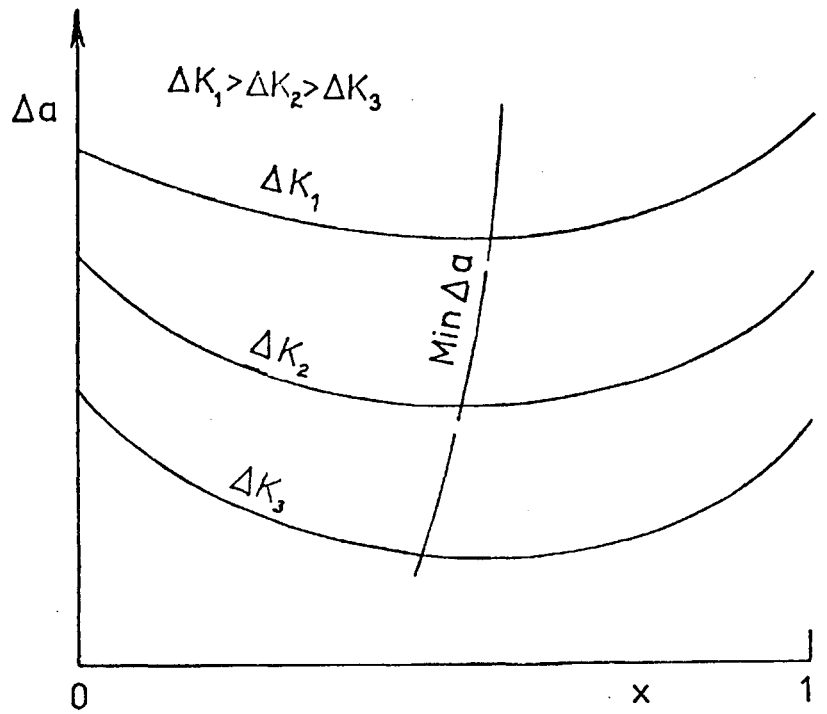


Figure 6.8: Variation of Δa with x at constant ΔK

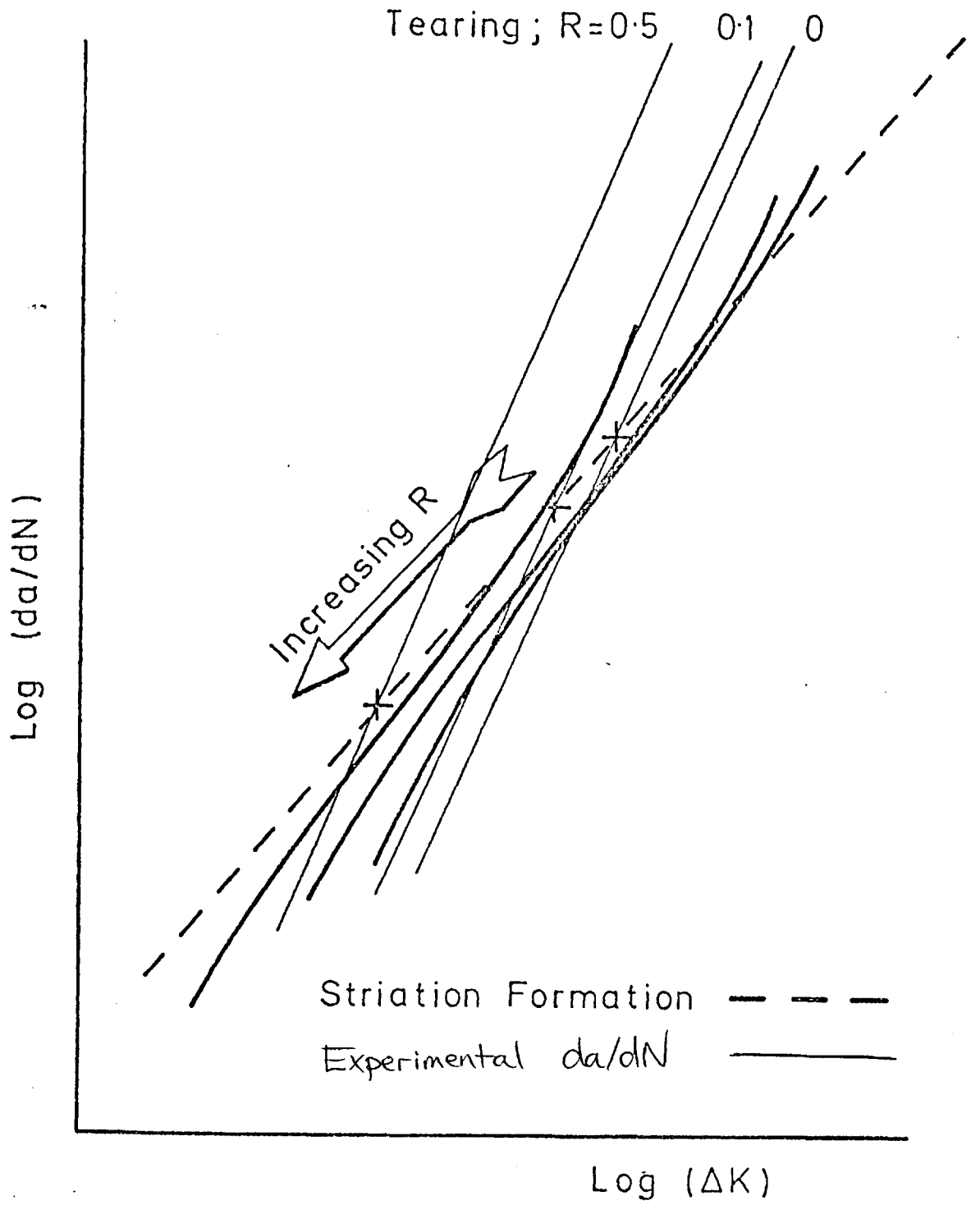


Figure 6.9: Effect of stress ratio, R, on crack growth rate

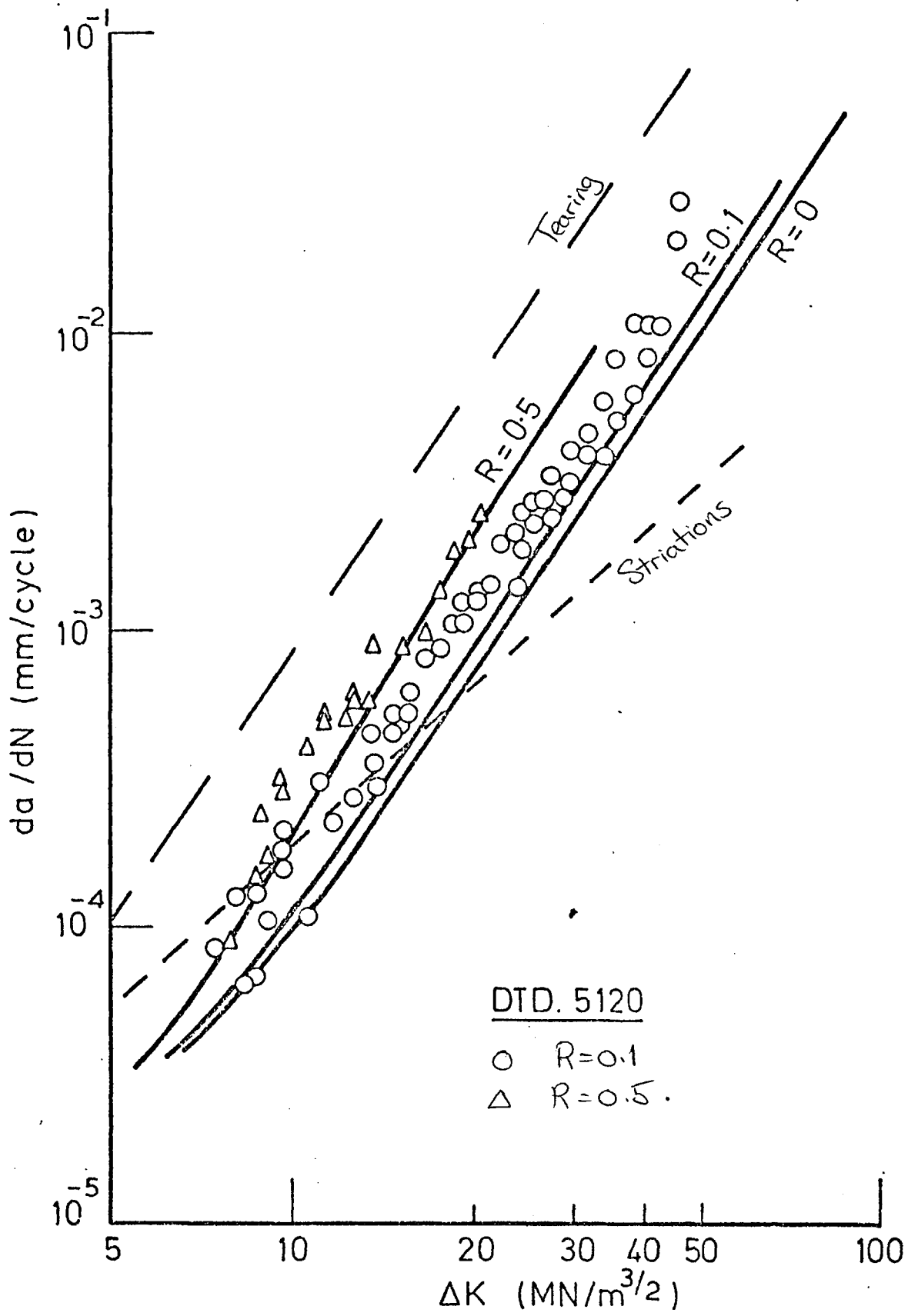


Figure 6.10: Crack resistance addition model for DTD.5120

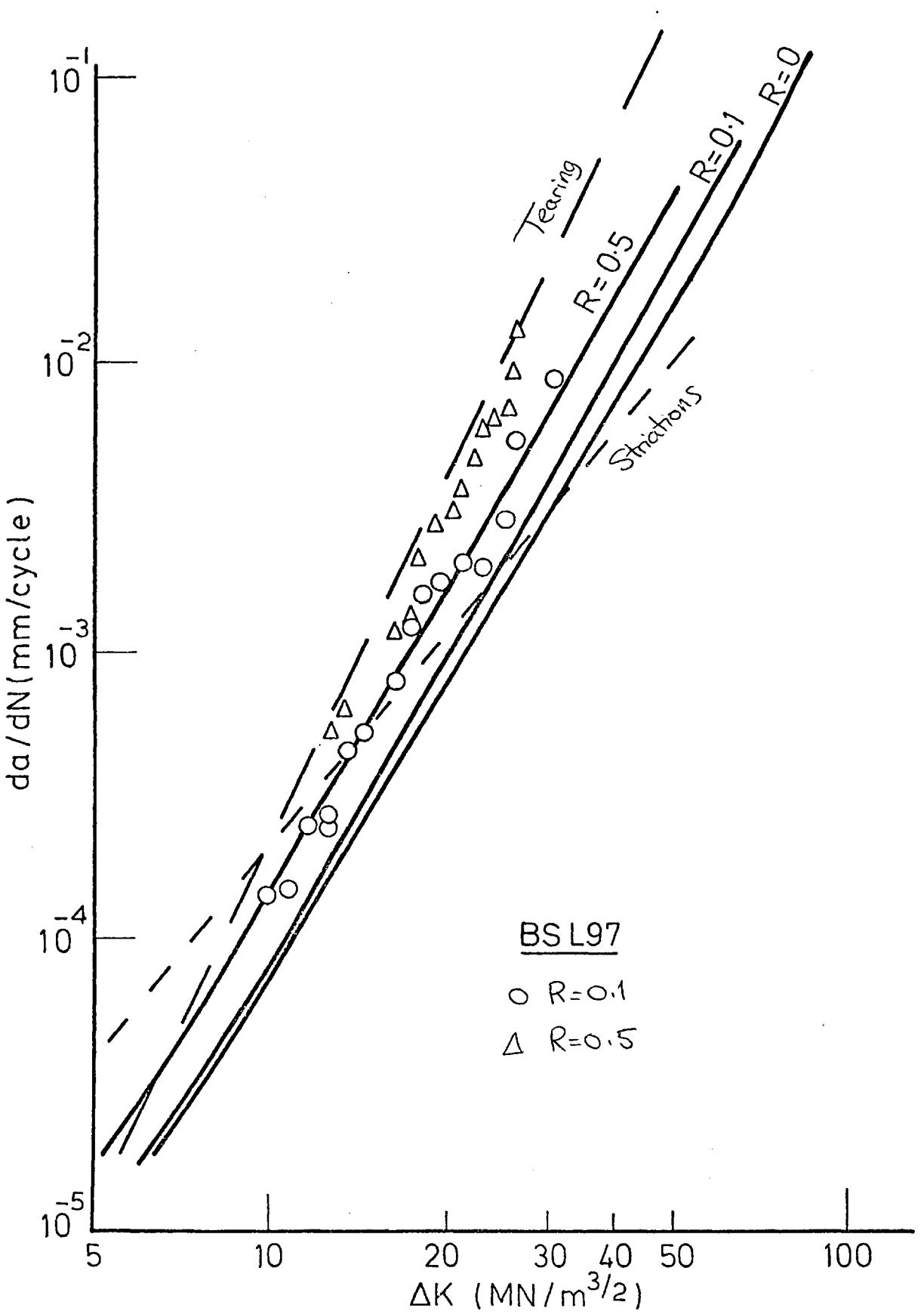


Figure 6.11: Crack resistance addition model for BS.L97

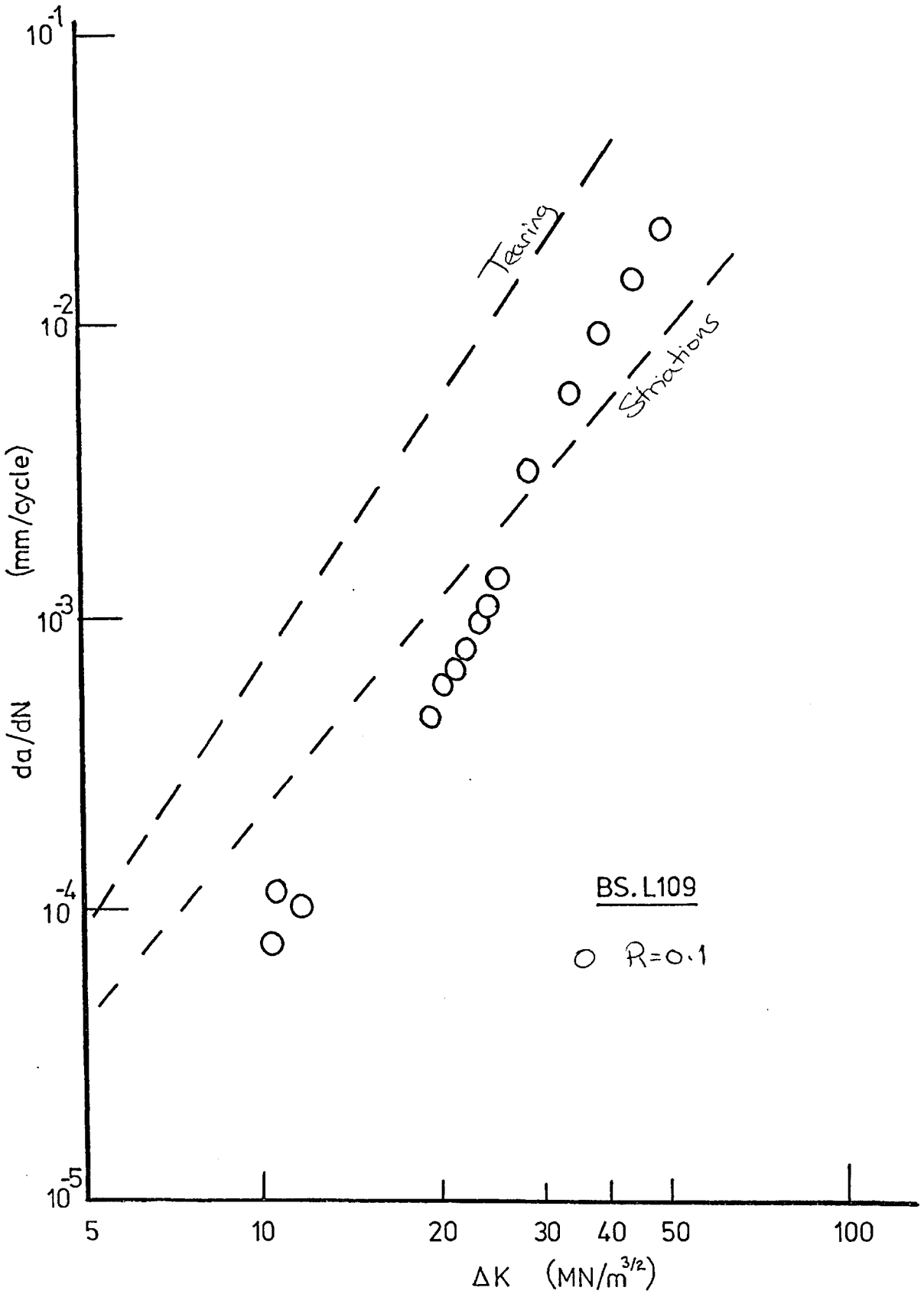


Figure 6.12: Crack resistance addition model for BS.L109

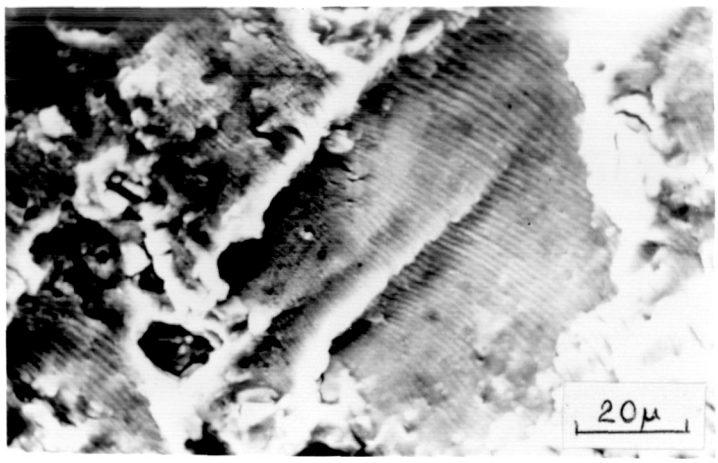


Figure 6.13: Striation markings on the surface of an L97 specimen fractured by fatigue crack growth at ΔK = 24 MN/m$^{3/2}$ and R = 0.1

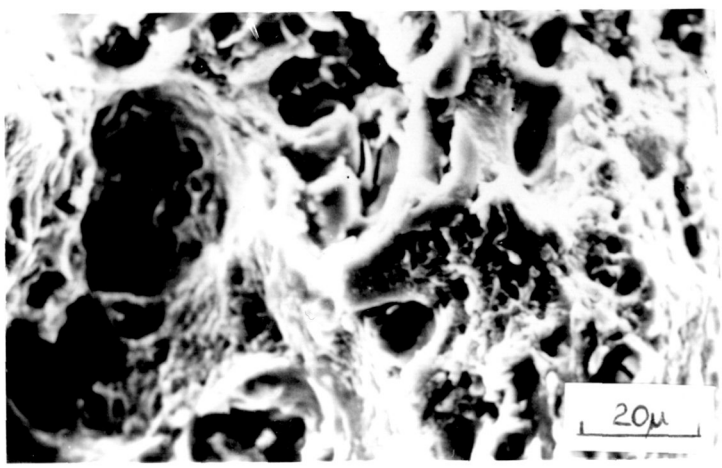


Figure 6.14: Dimple markings showing evidence of ductile tearing during fatigue crack growth in an L97 specimen at $\Delta K \simeq$ 35 MN/m$^{3/2}$ and R = 0.1

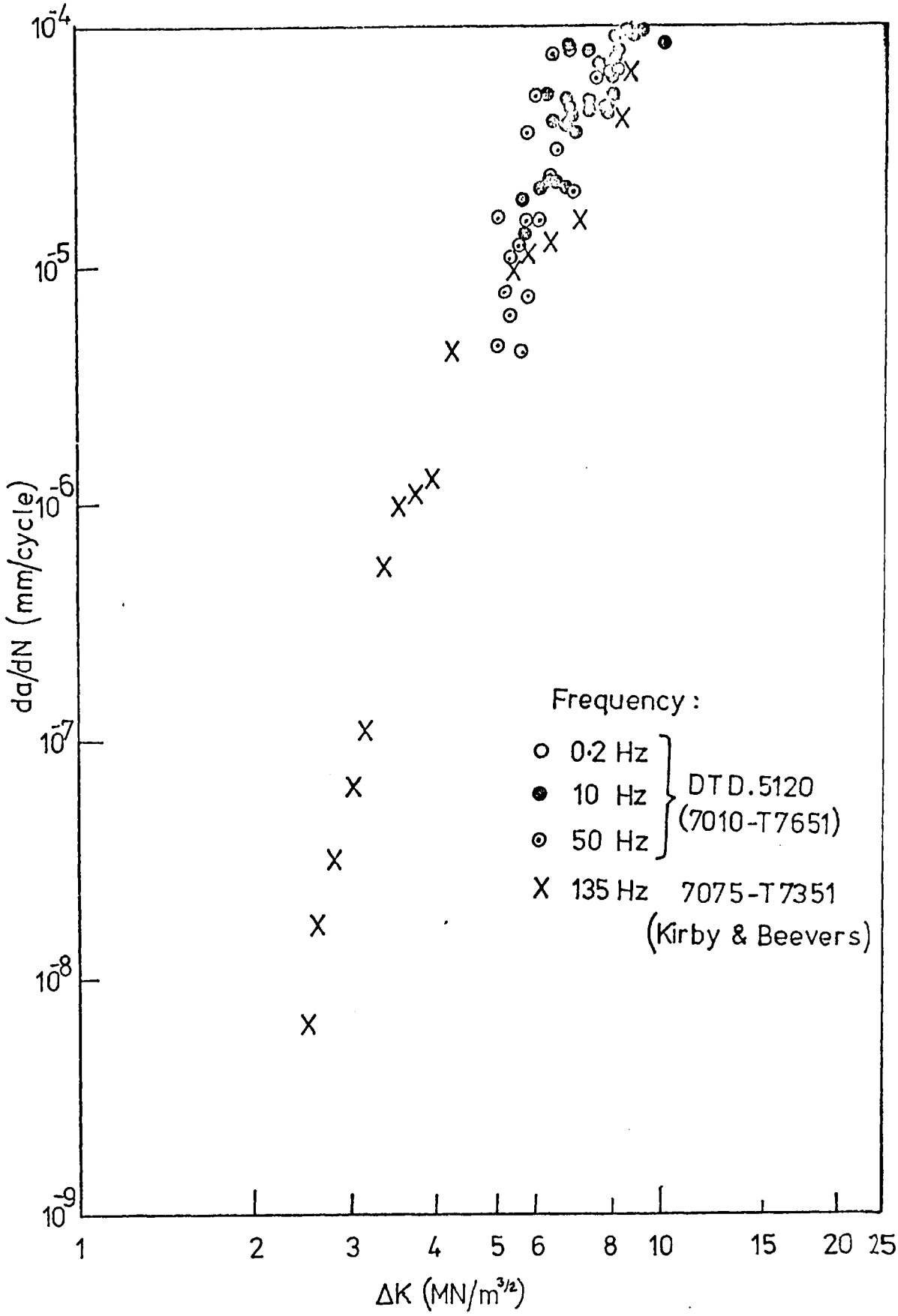


Figure 6.15: Near threshold crack growth data

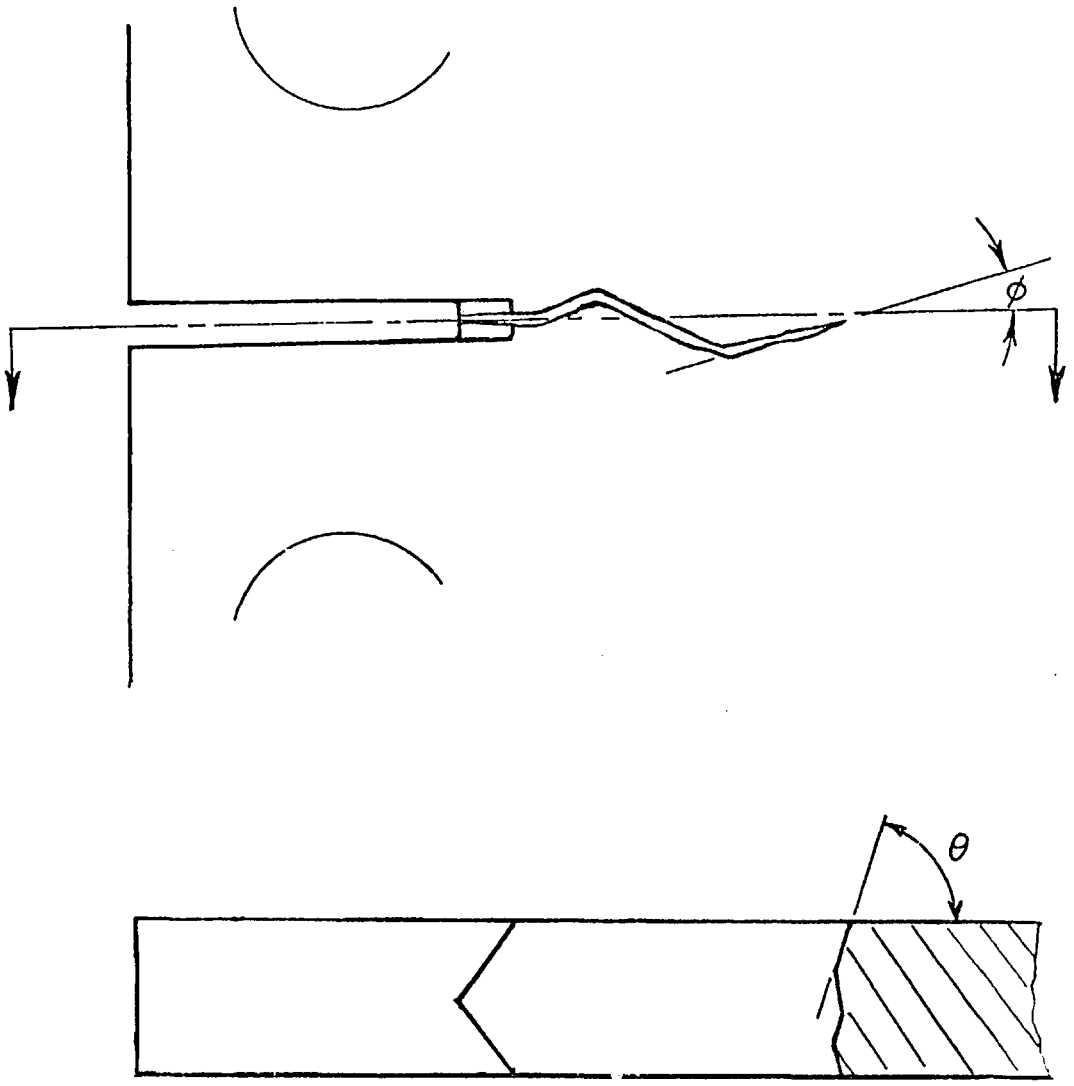


Figure 6.16: Deviations of crack tip orientation

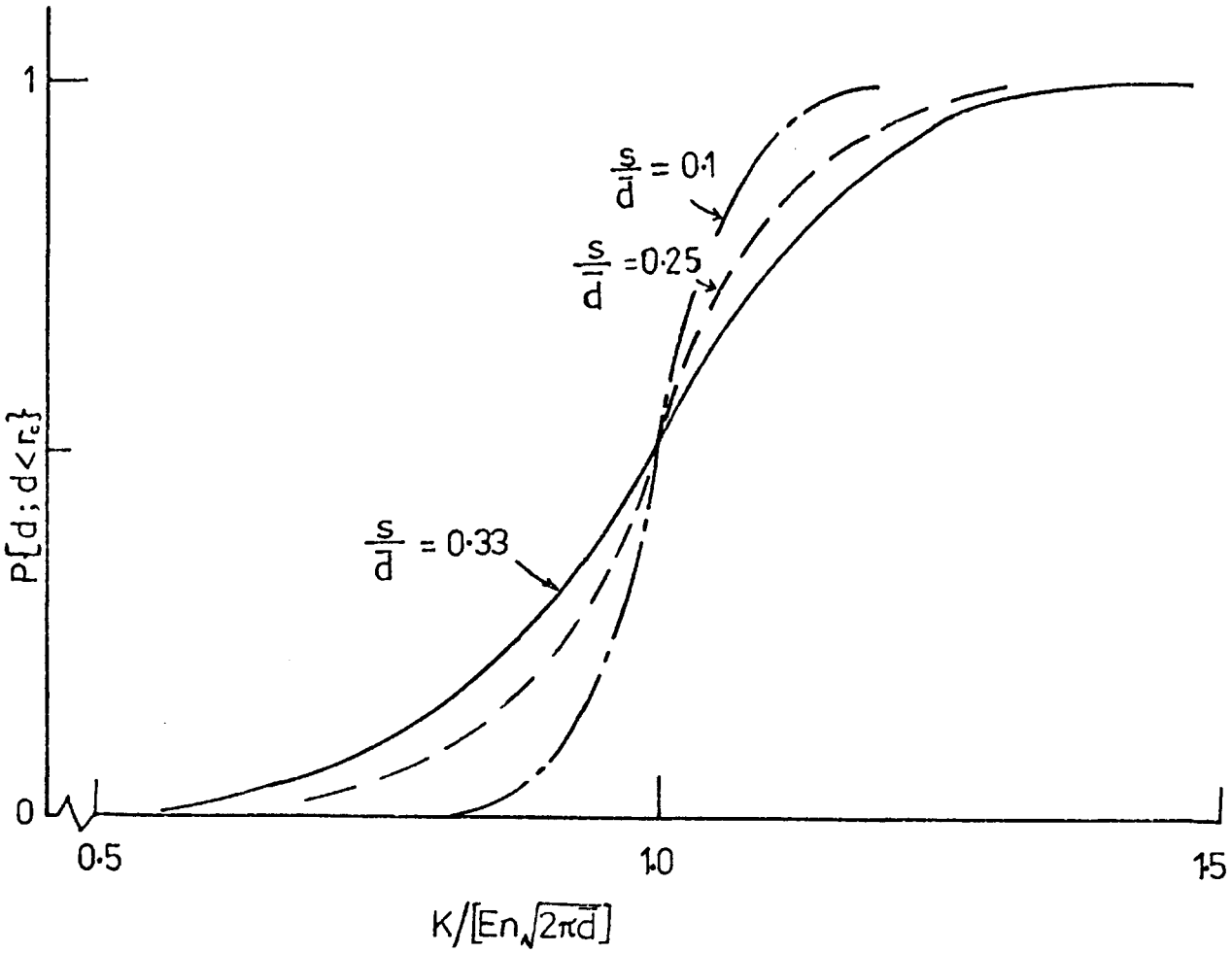


Figure 6.17: Probability of tearing under monotonic loading (normal distribution)

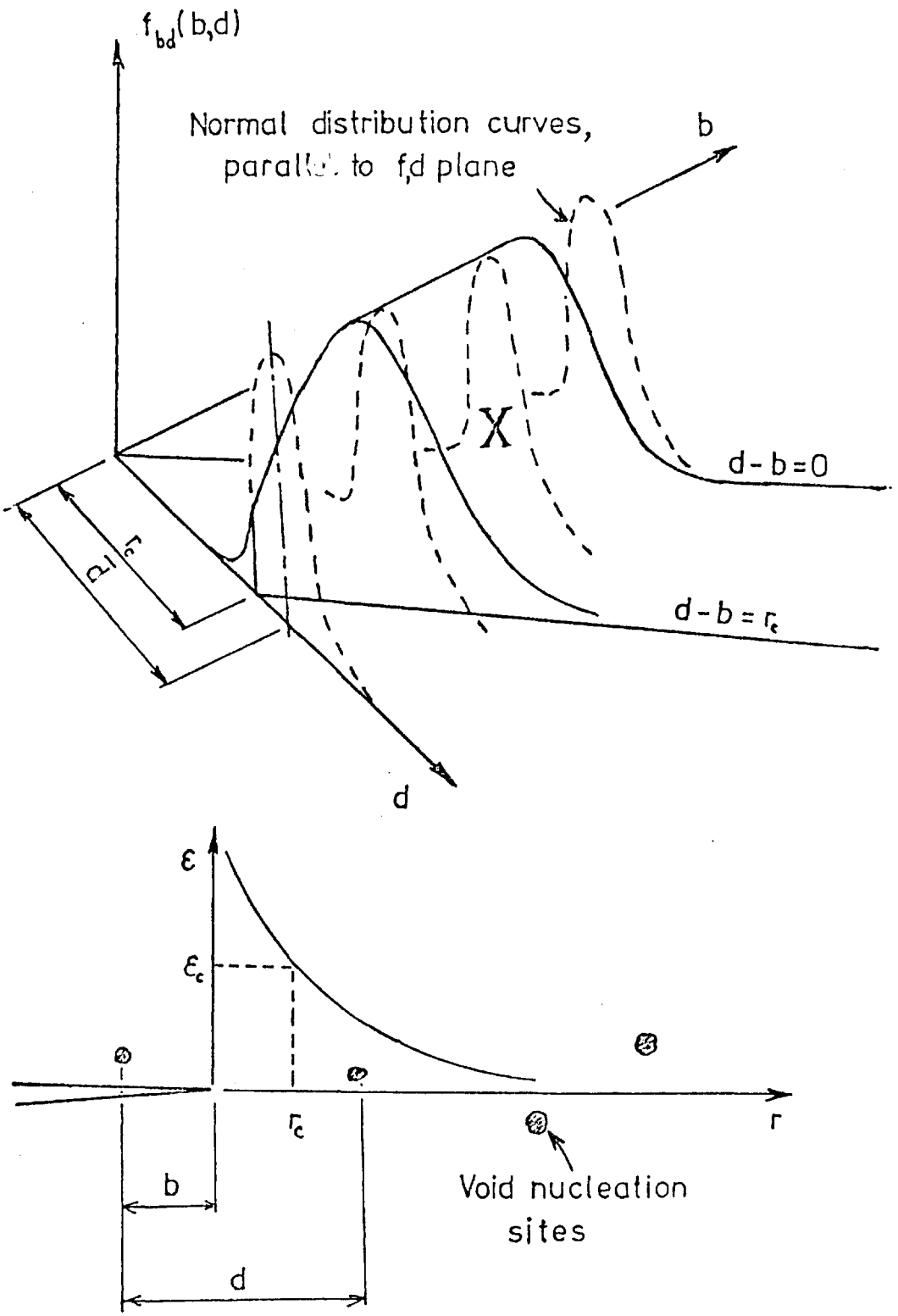


Figure 6.18: Probability density function for combined tearing and striation formation

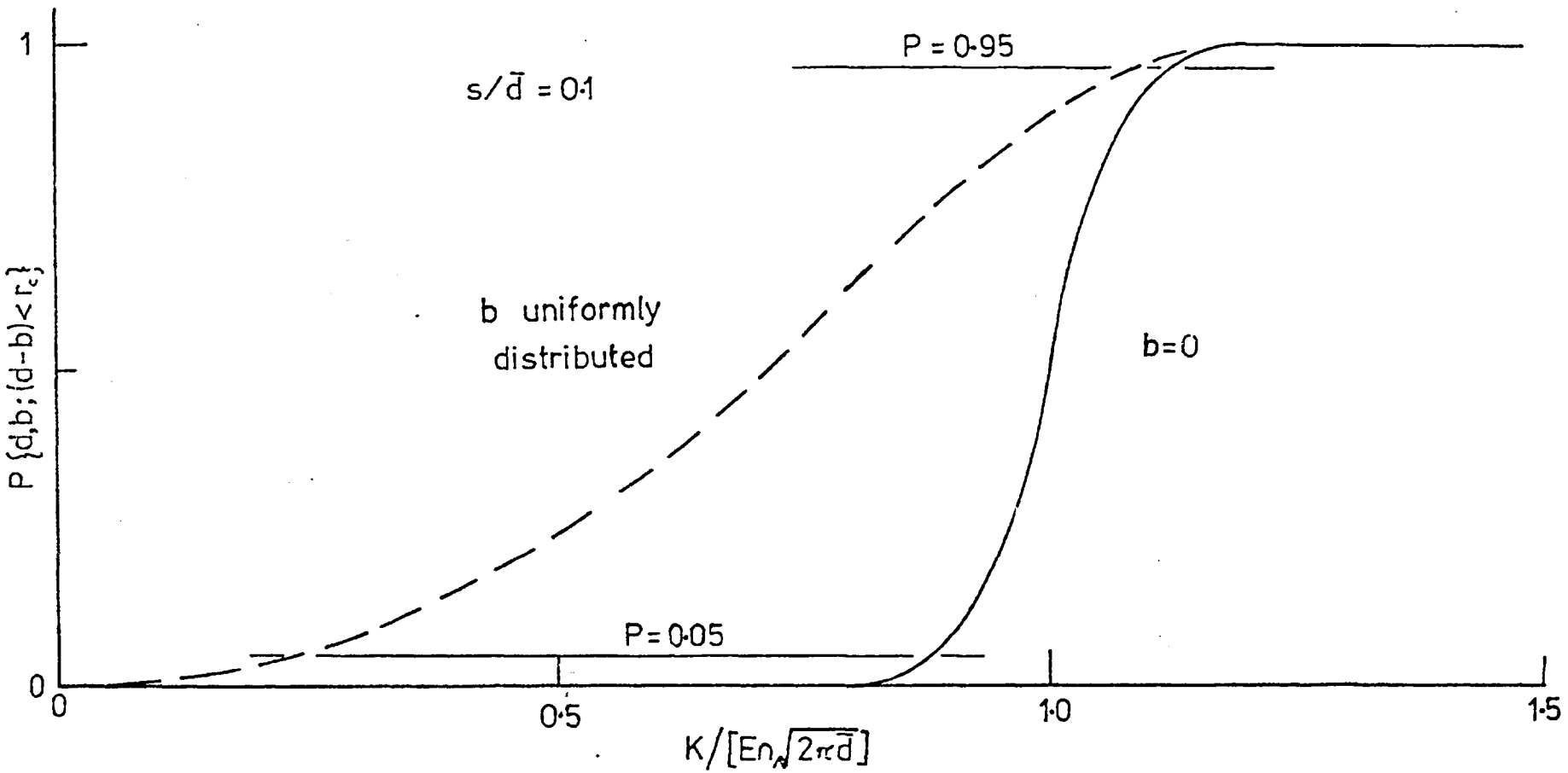


Figure 6.19: Probability of tearing under cyclic loading

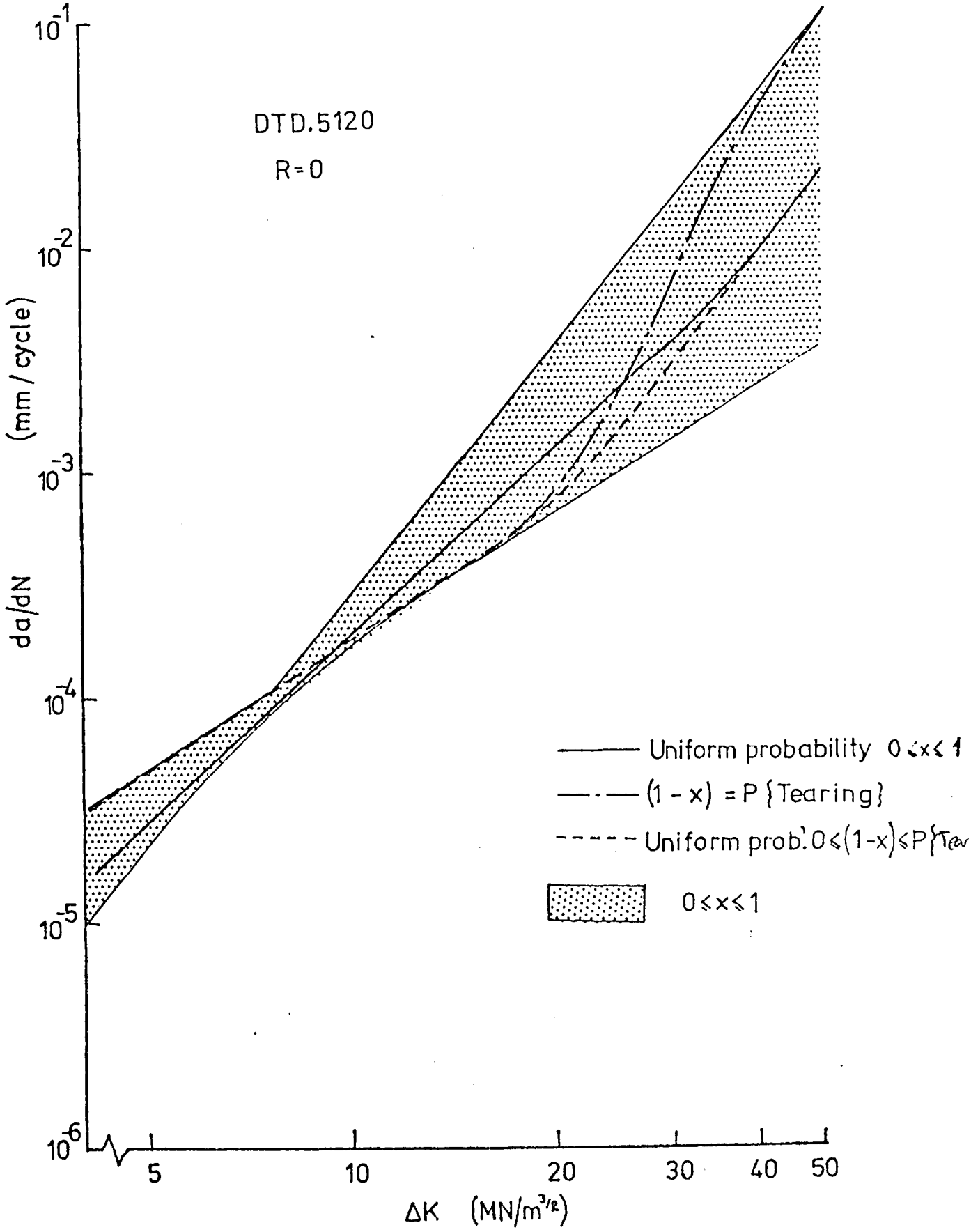


Figure 6.20: Crack resistance addition model for DTD.5120

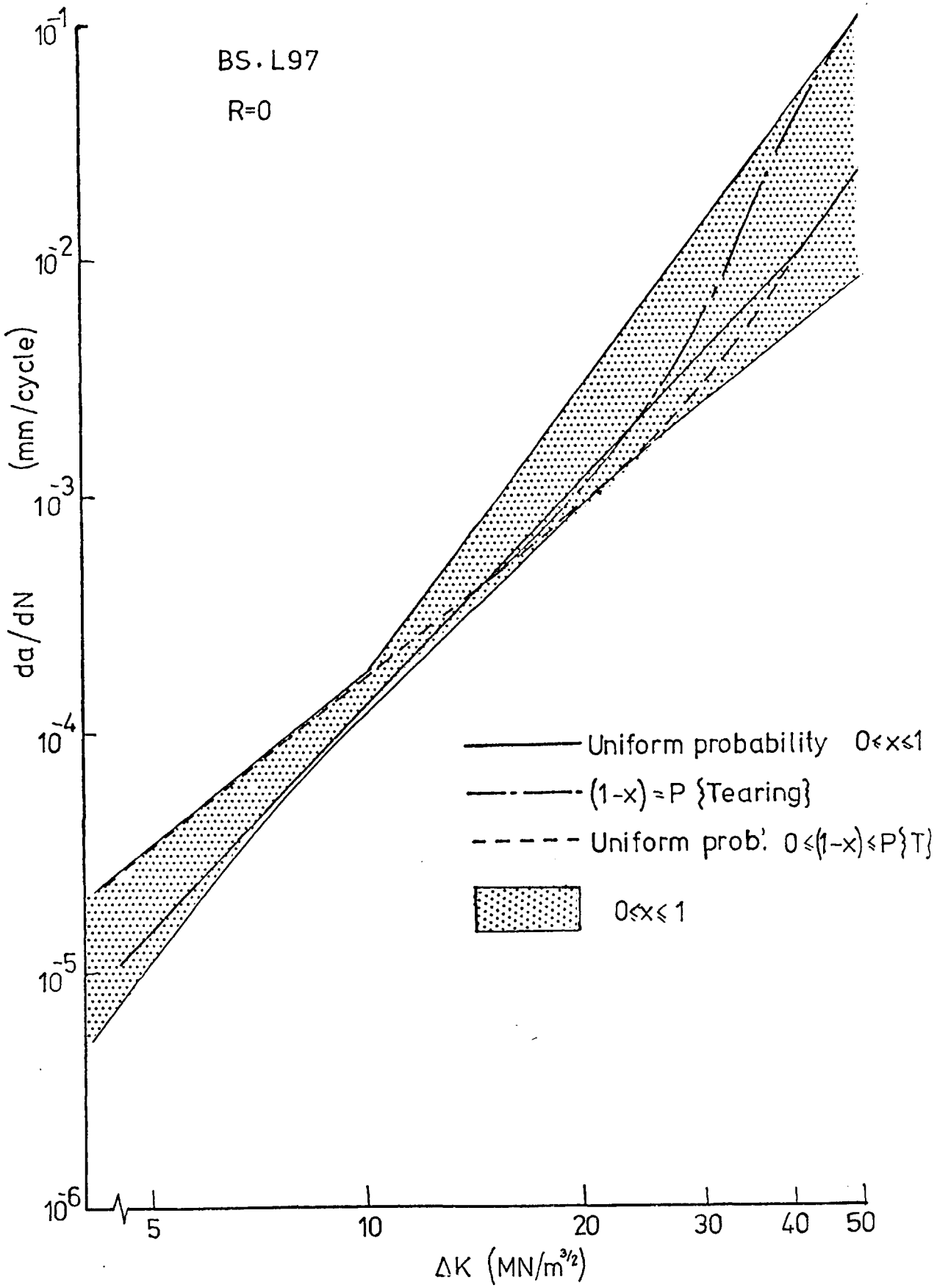


Figure 6.21: Crack resistance addition model for BS.L97

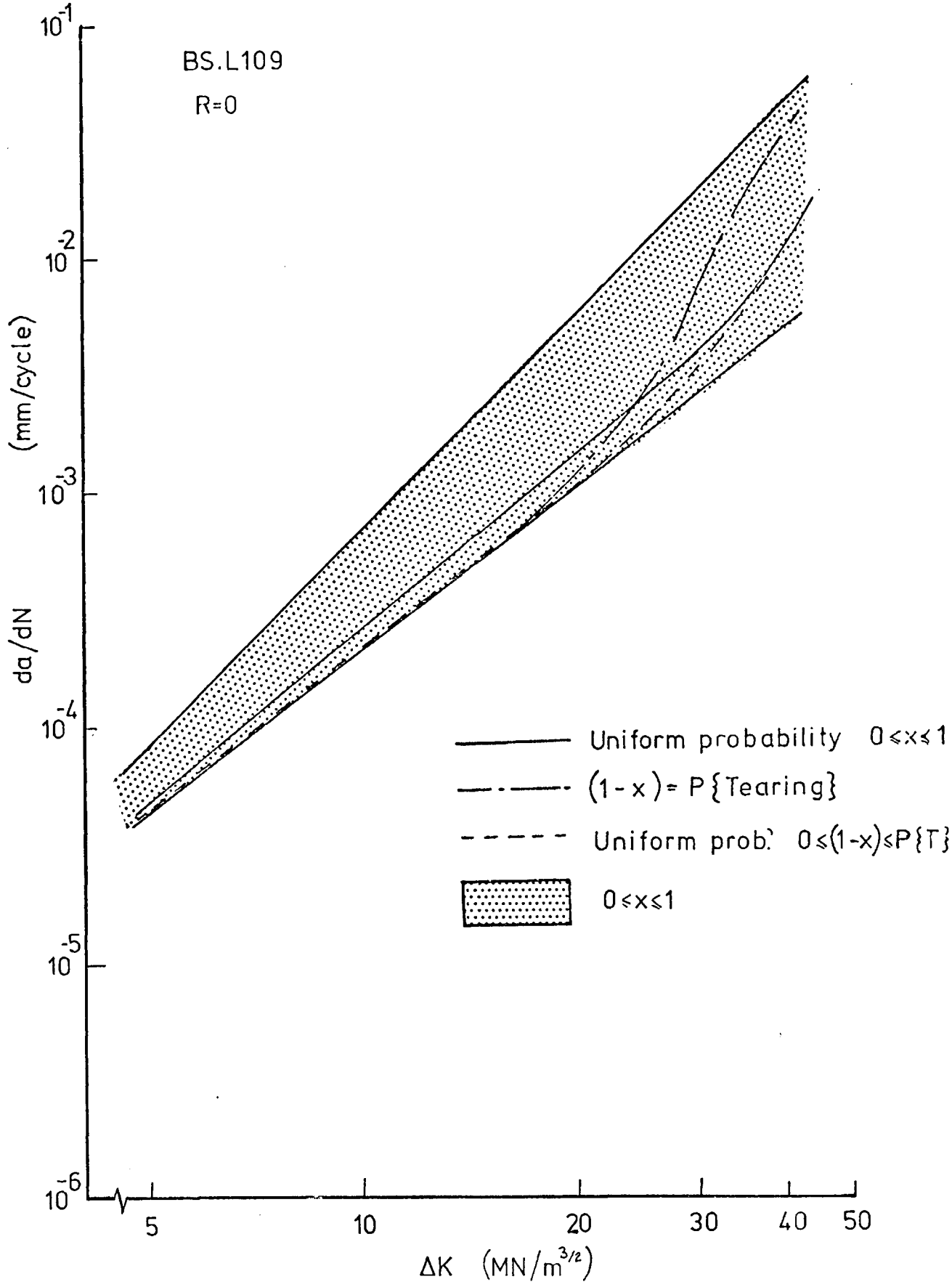


Figure 6.22: Crack resistance addition model for BS.L109

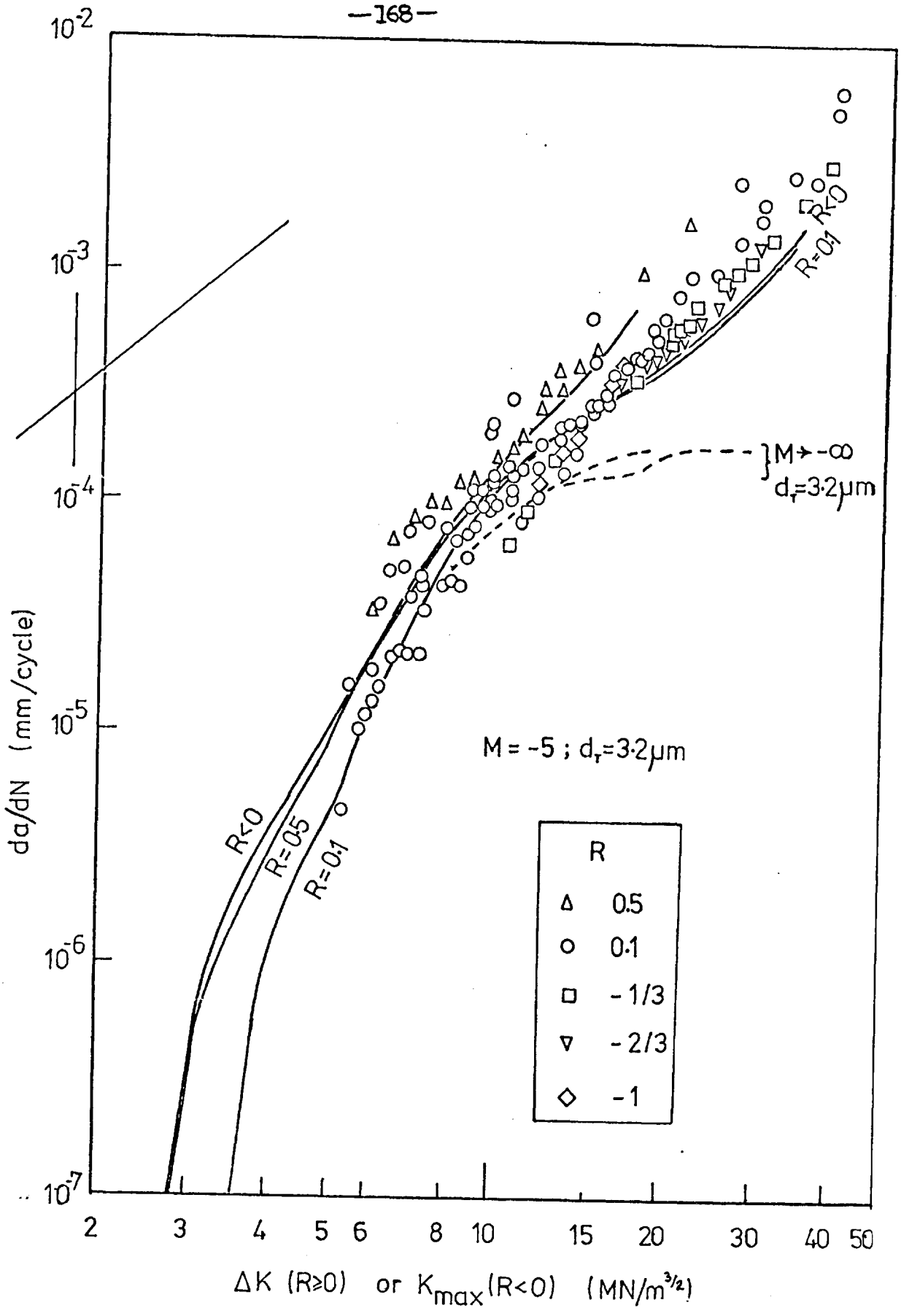


Figure 6.23: TLIM plot for DTD.5120 [107]

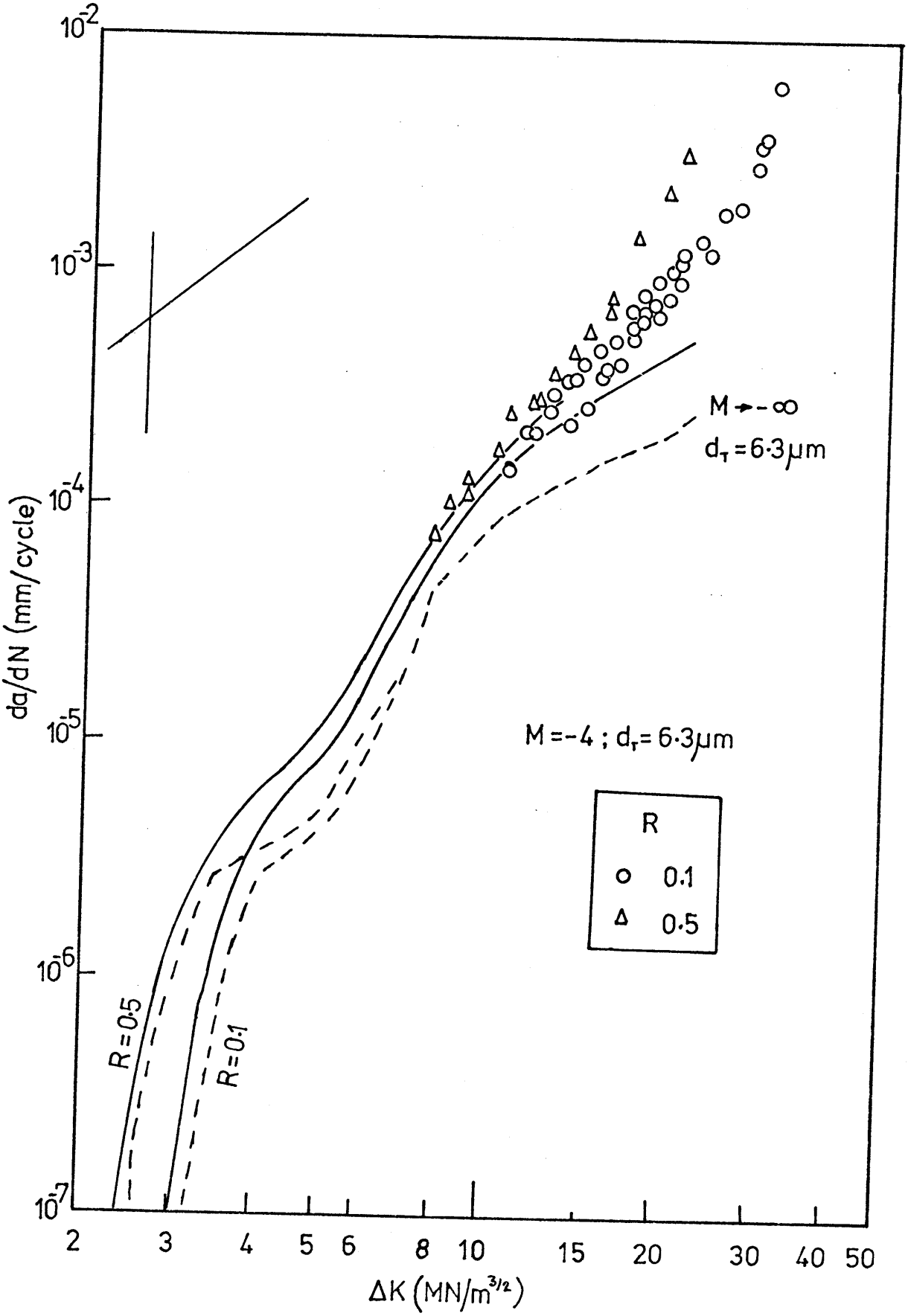


Figure 6.24: TLIM plot for BS.L97 [107]

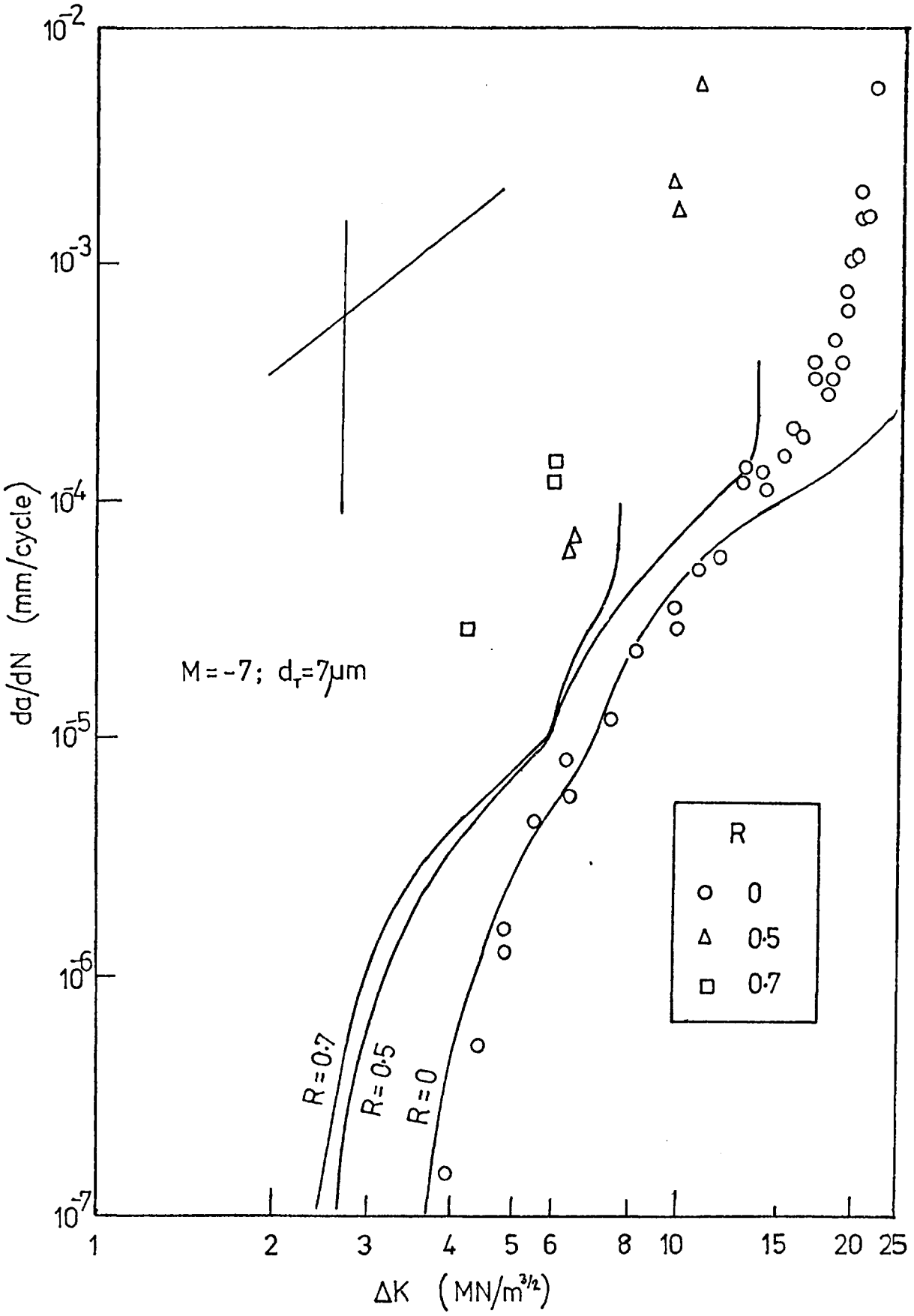


Figure 6.25: TLIM plot for RR58 [107]

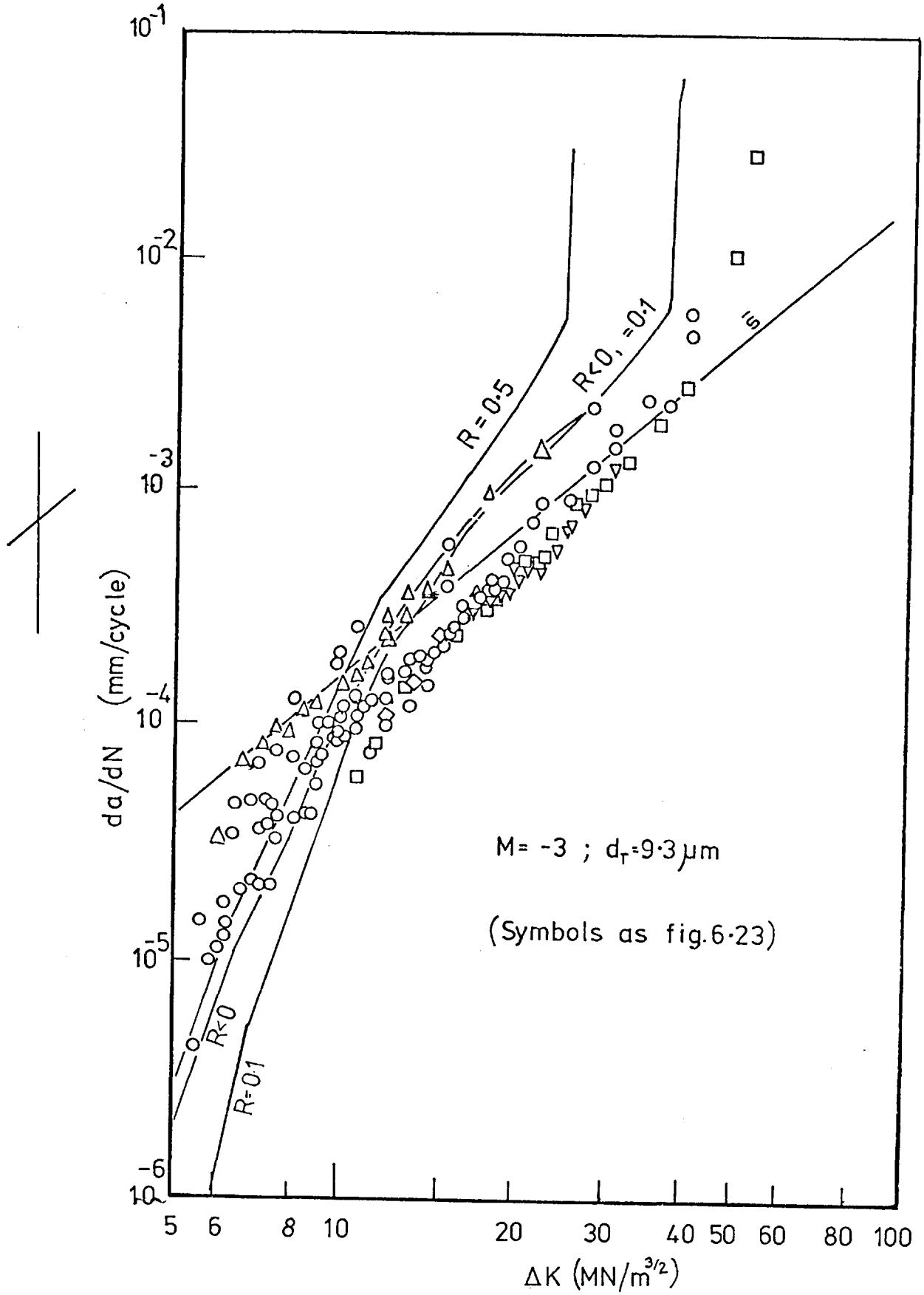


Figure 6.26: TLIM dual mechanism method for DTD.5120

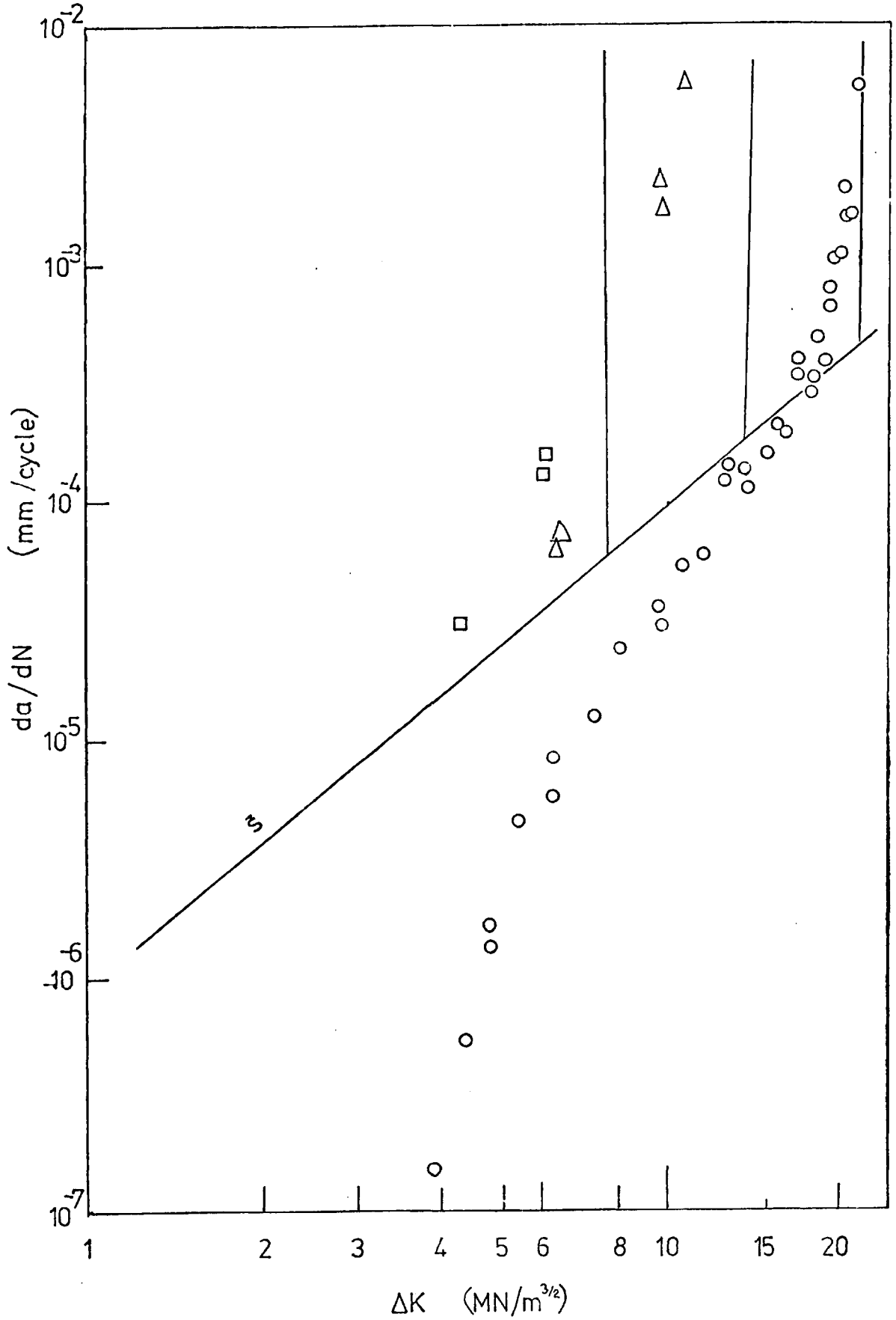


Figure 6.27: TLIM dual mechanism model for RR58

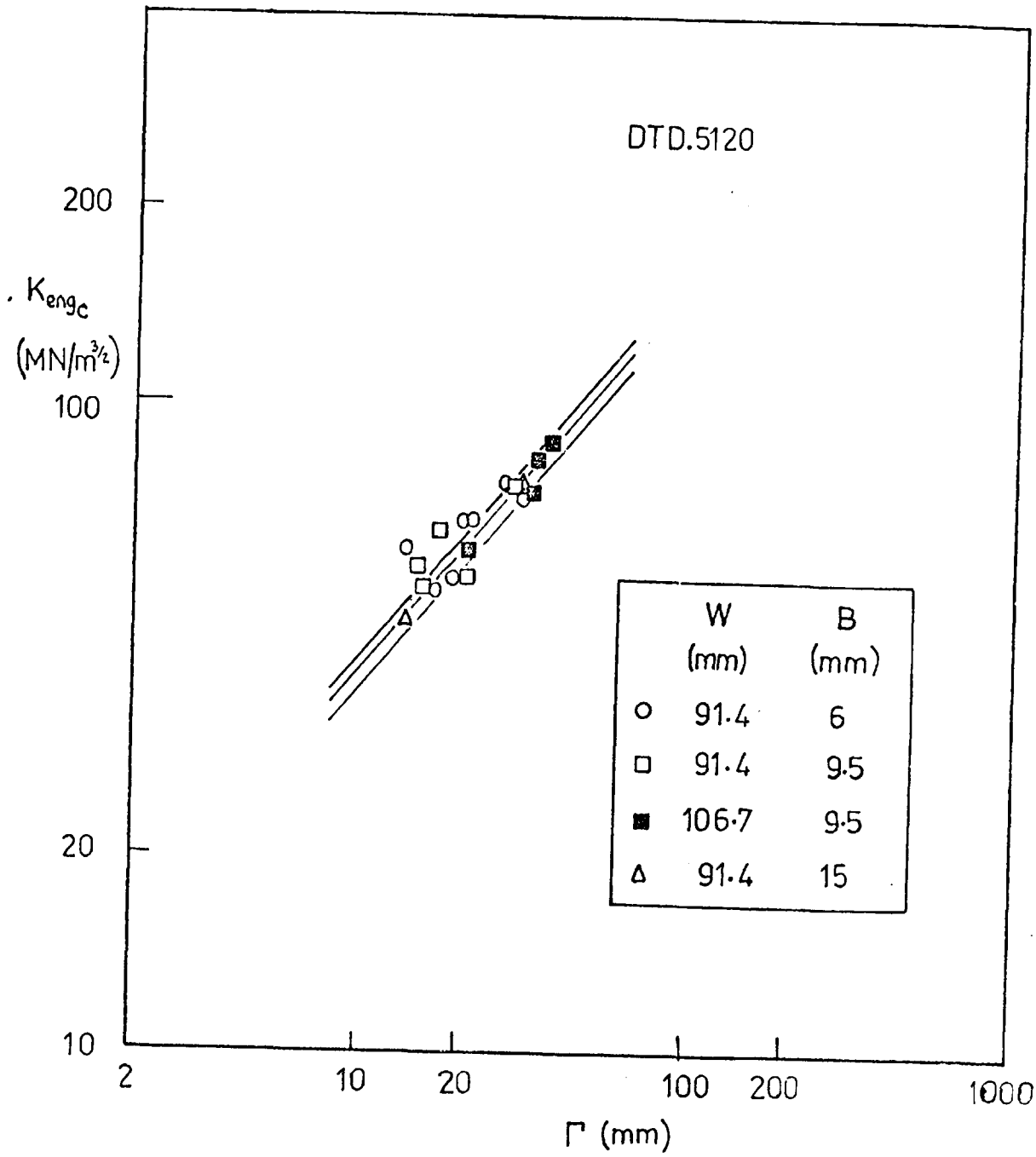


Figure 6.28a: Engineering toughness of DTD.5120

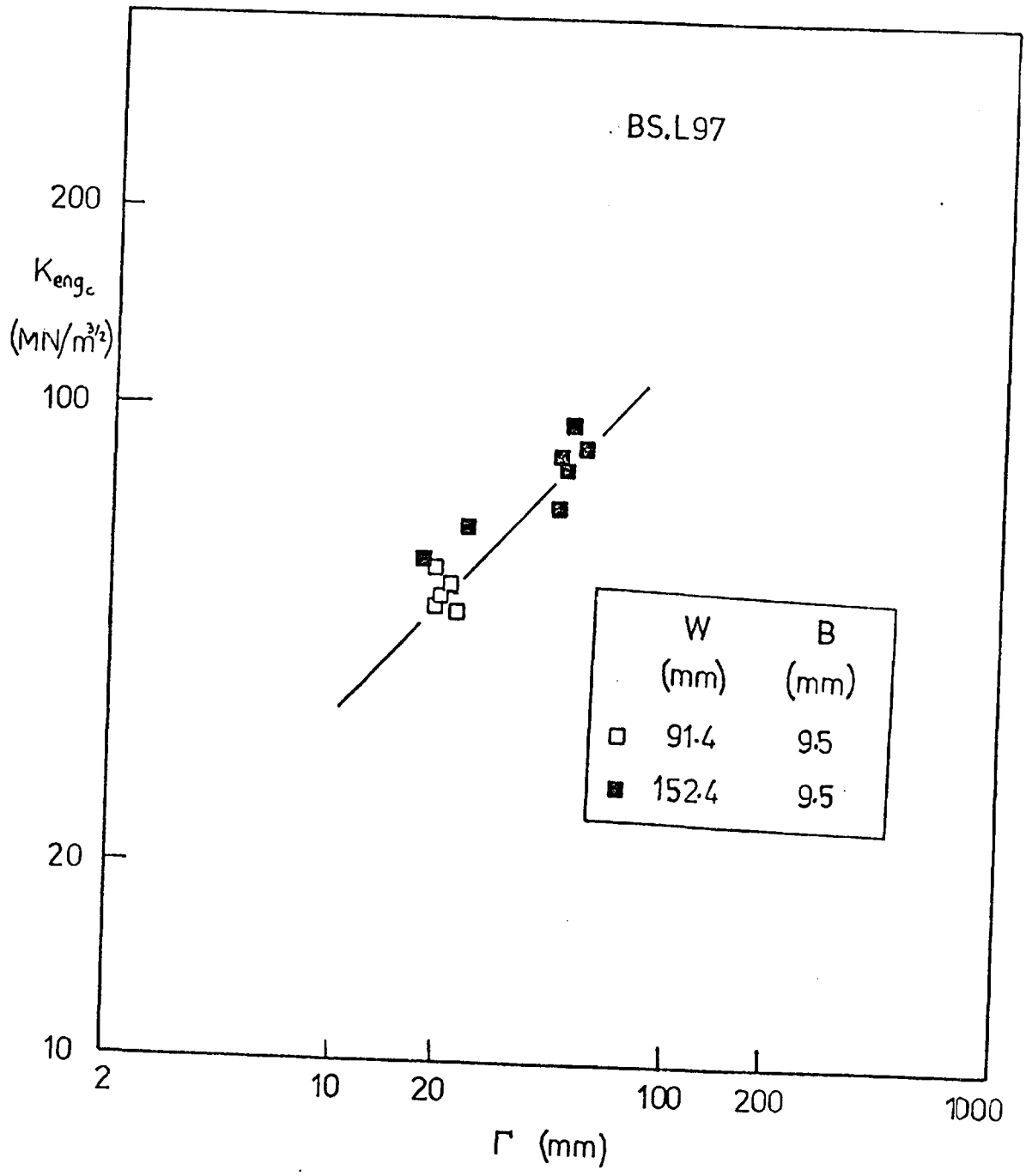


Figure 6.28b: Engineering toughness of BS.L97

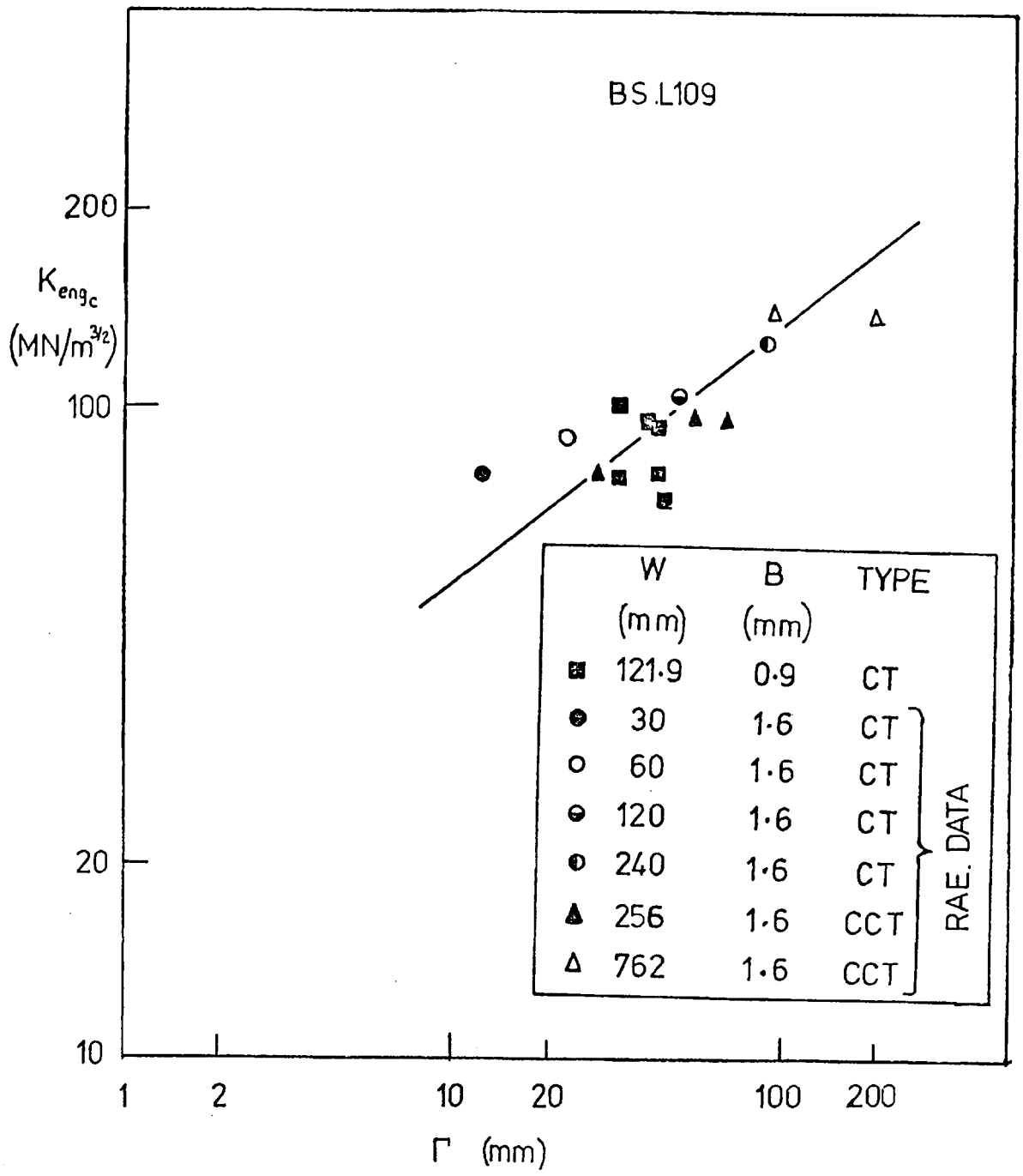


Figure 6.28c: Engineering toughness of BS.L109

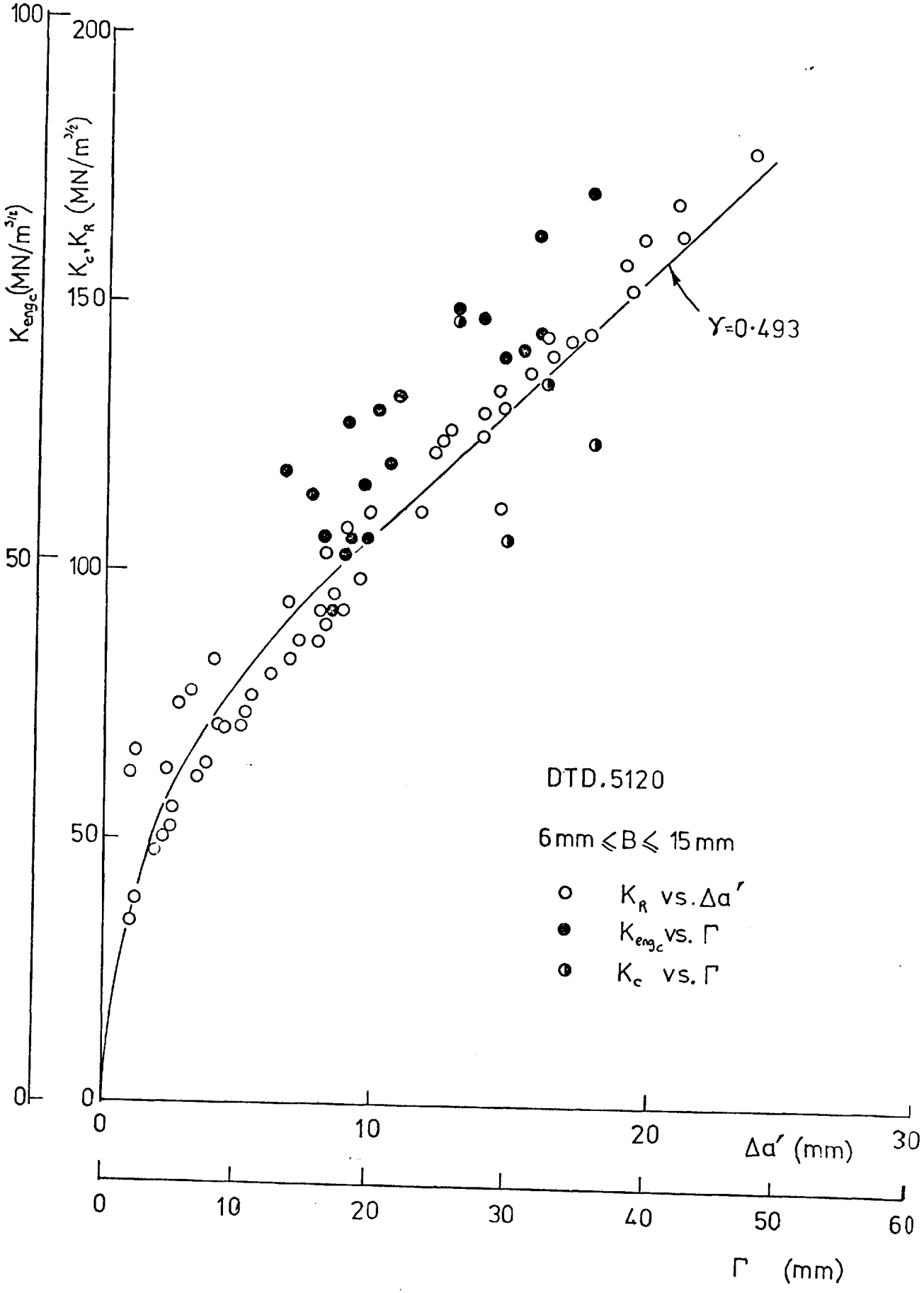


Figure 6.29a: Comparison of K_{eng_c} versus Γ with *R*-curve for DTD.5120

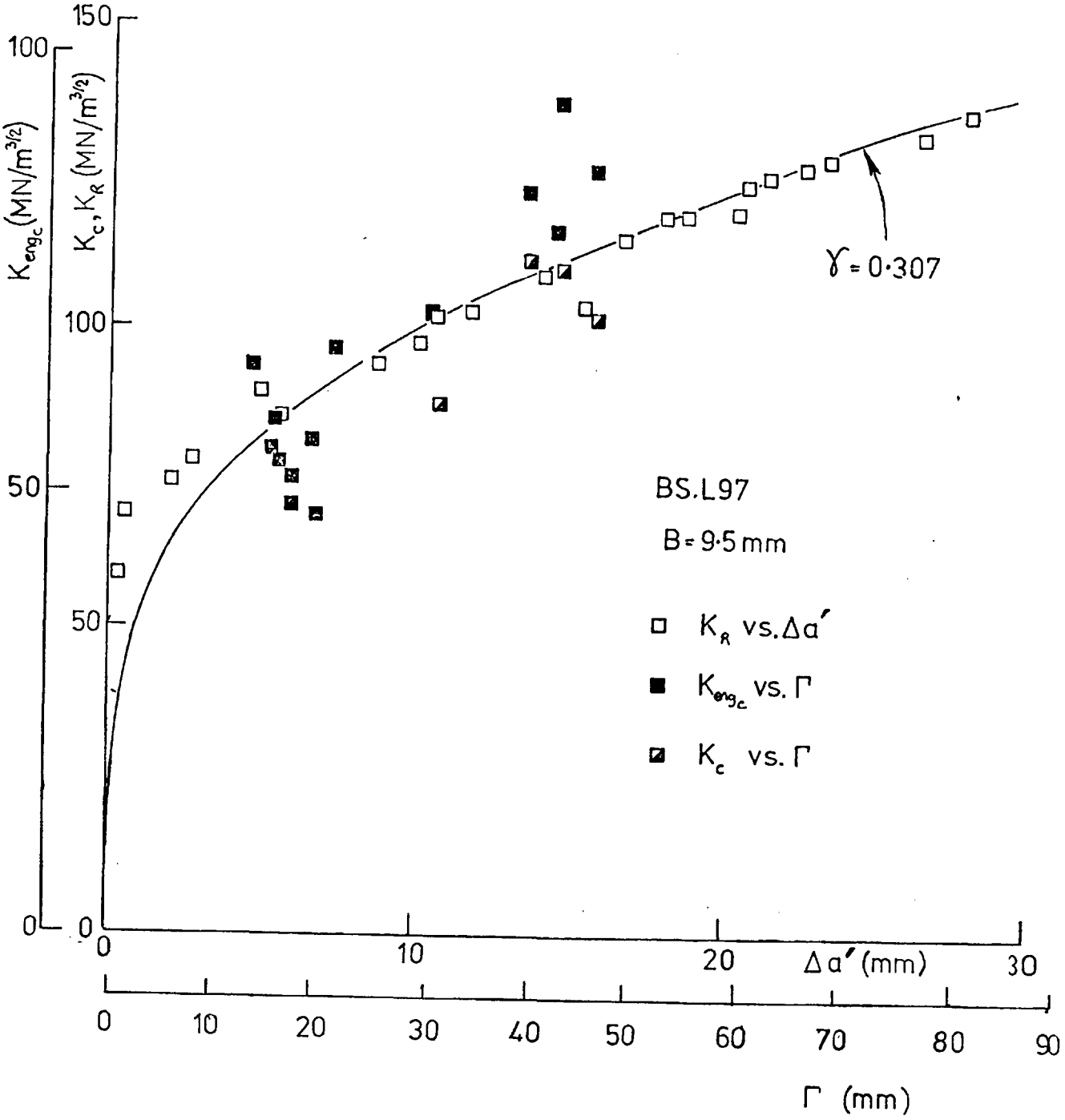


Figure 6.29b: Comparison of K_{eng_c} versus Γ with R-curve for BS.L97

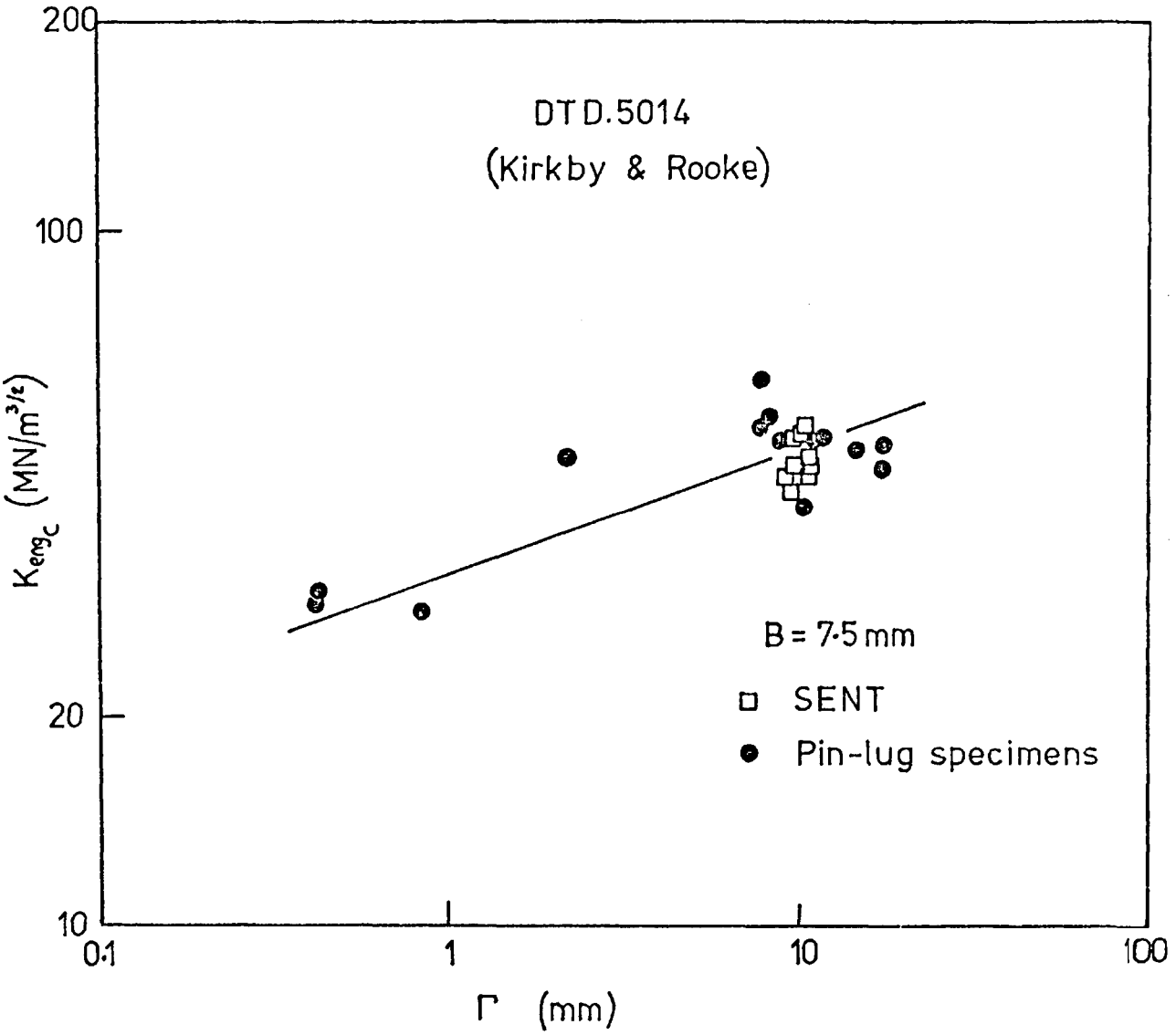


Figure 6.30: Engineering toughness of DTD.5014 [111]

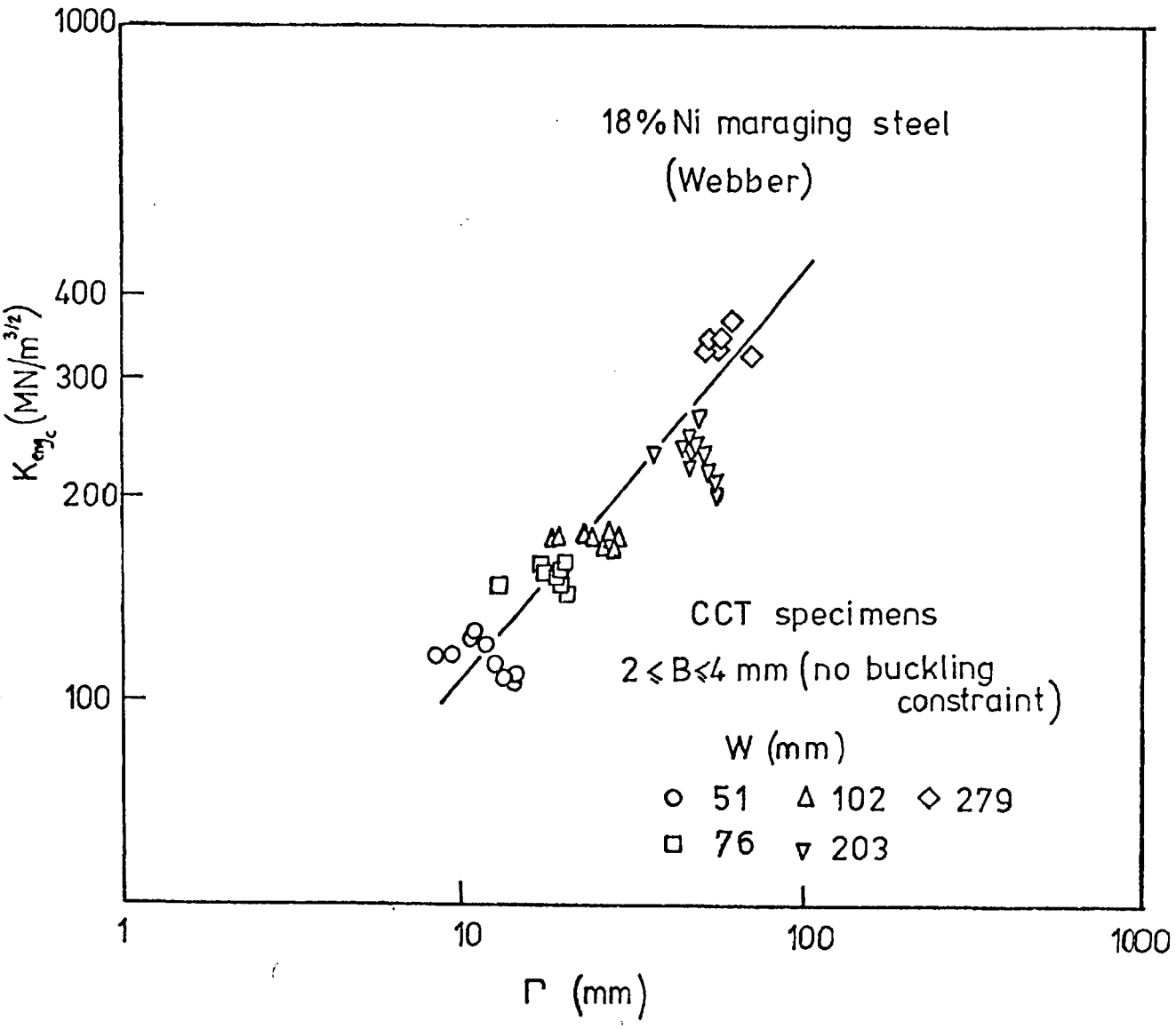


Figure 6.31: Engineering toughness of 18% Ni maraging steel [112]

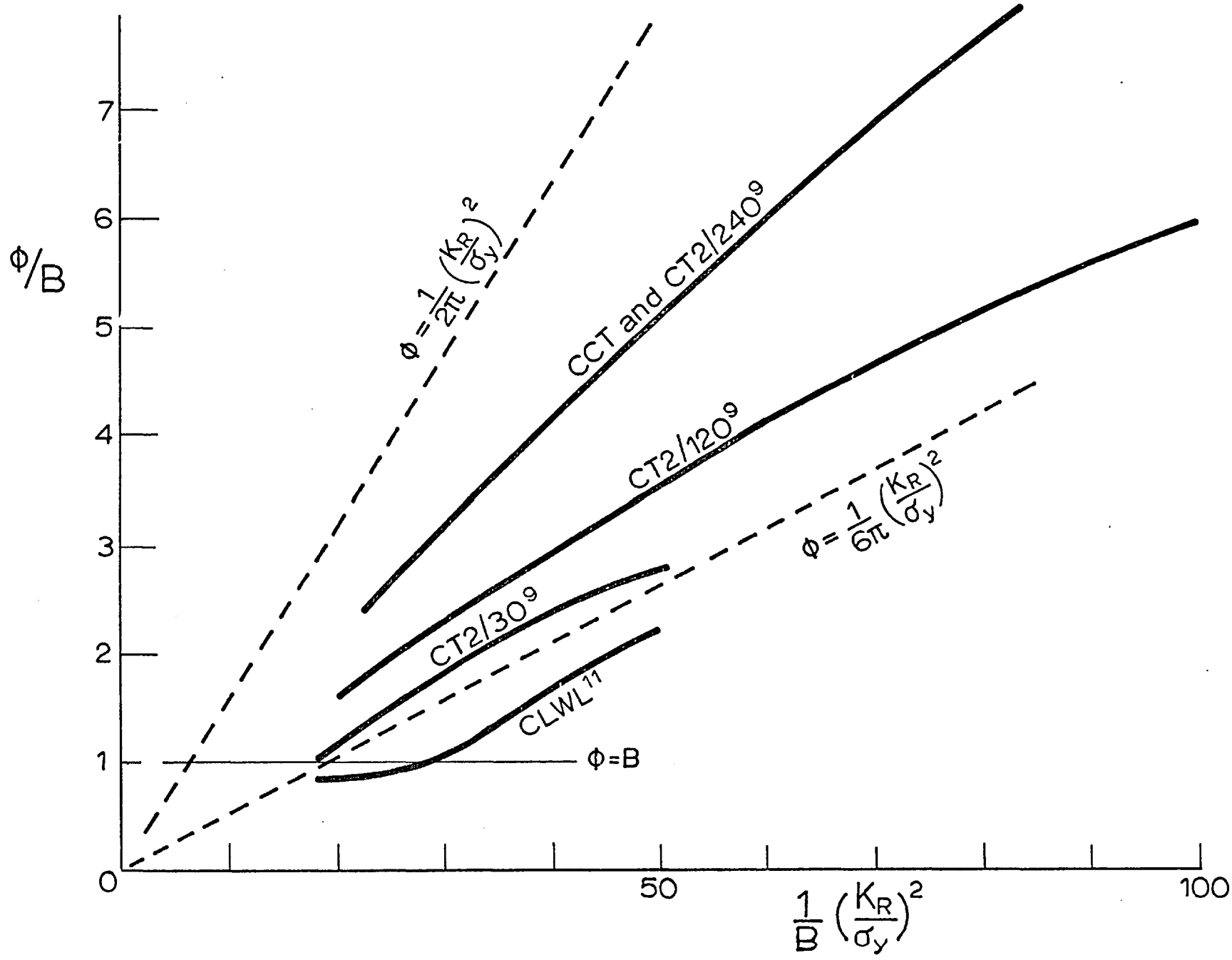


Figure 6.32a: Compliance of thin sheet Al-alloy specimens

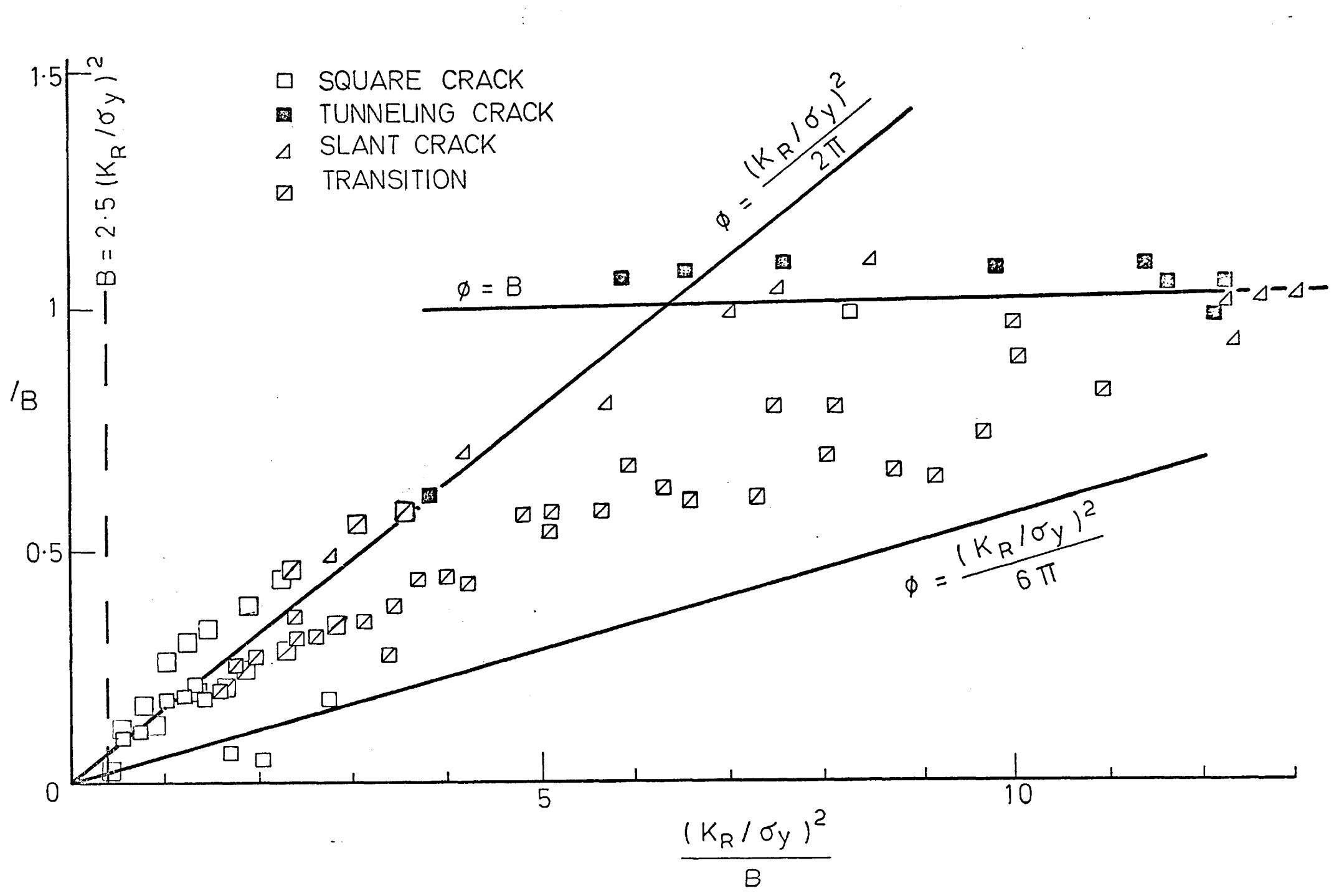


Figure 6.32b: Compliance of aluminium alloy specimens. Data include DTD.5120 (6 mm, 9.5 mm and 15 mm thick) and BS.L97 (9.5 mm thick)

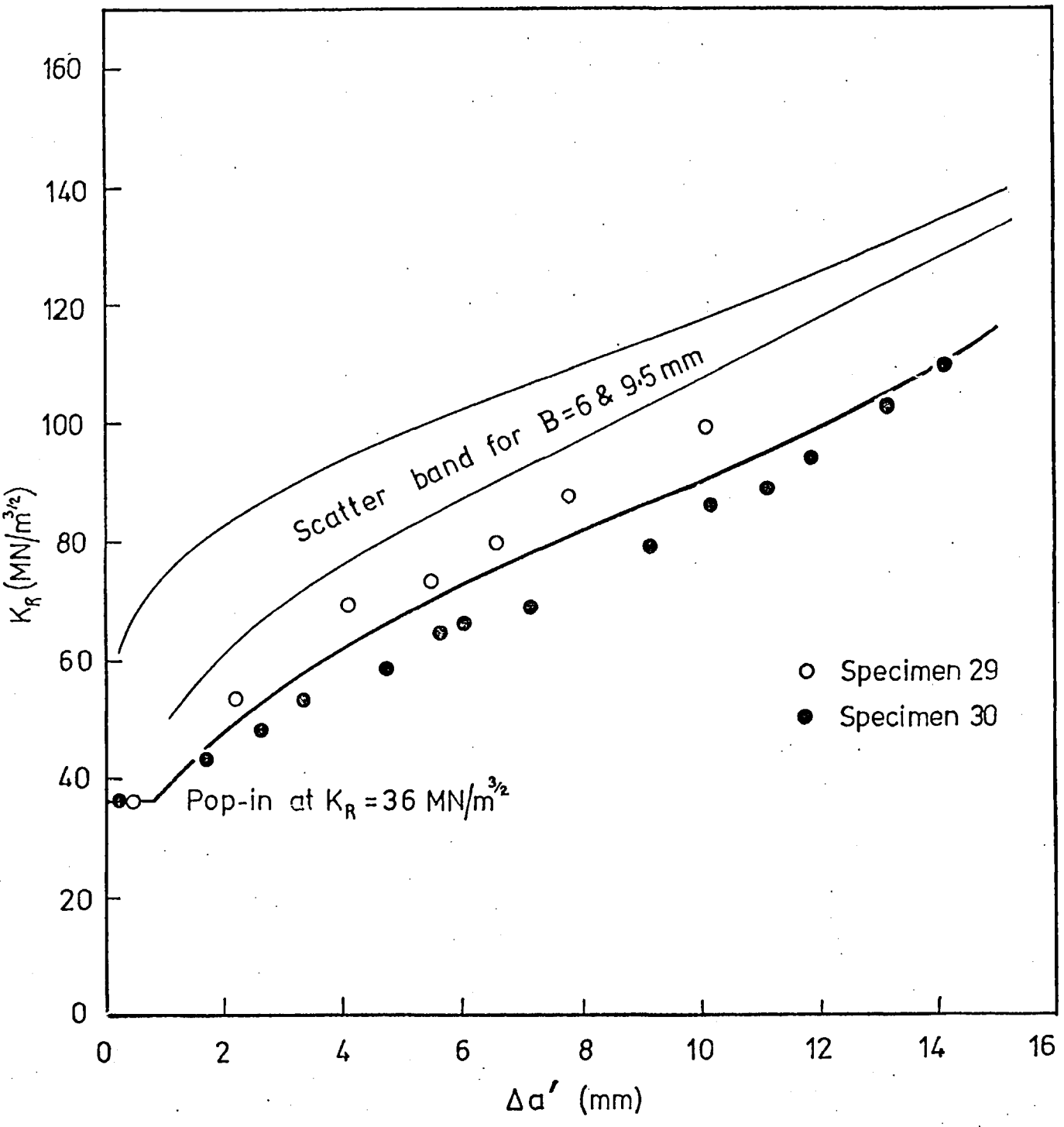


Figure 6.33: Effect of thickness on *R*-curve for DTD.5120

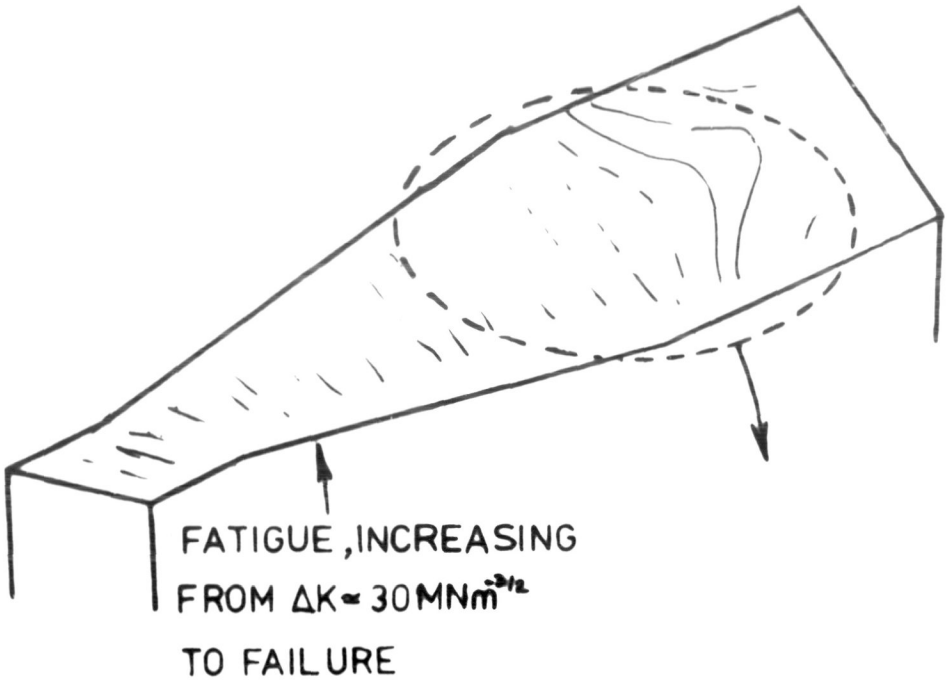
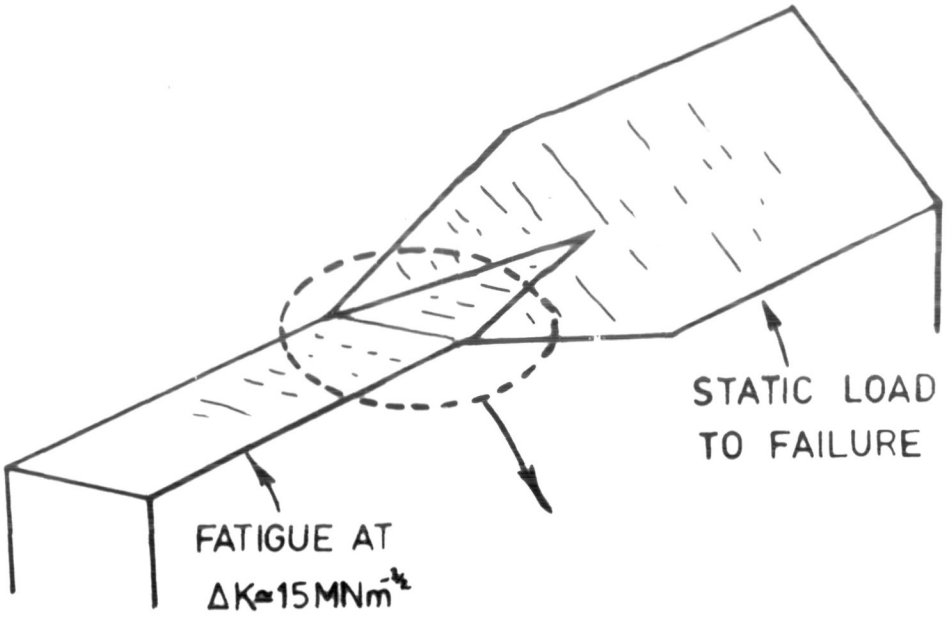




Figure 6.34a: Square-to-slant transition in 9.5 mm thick DTD.5120 under cyclic loading



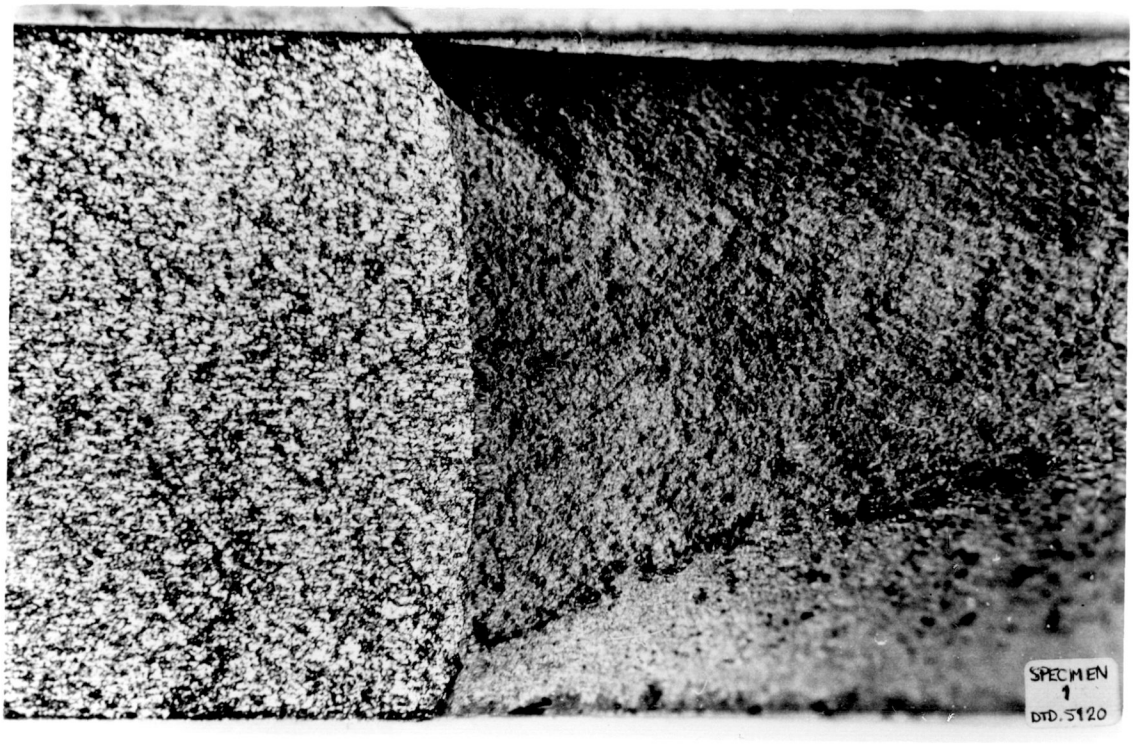


Figure 6.34b: **Square-to-slant transition in 9.5 mm thick** DTD.5120 under **monotonic loading**

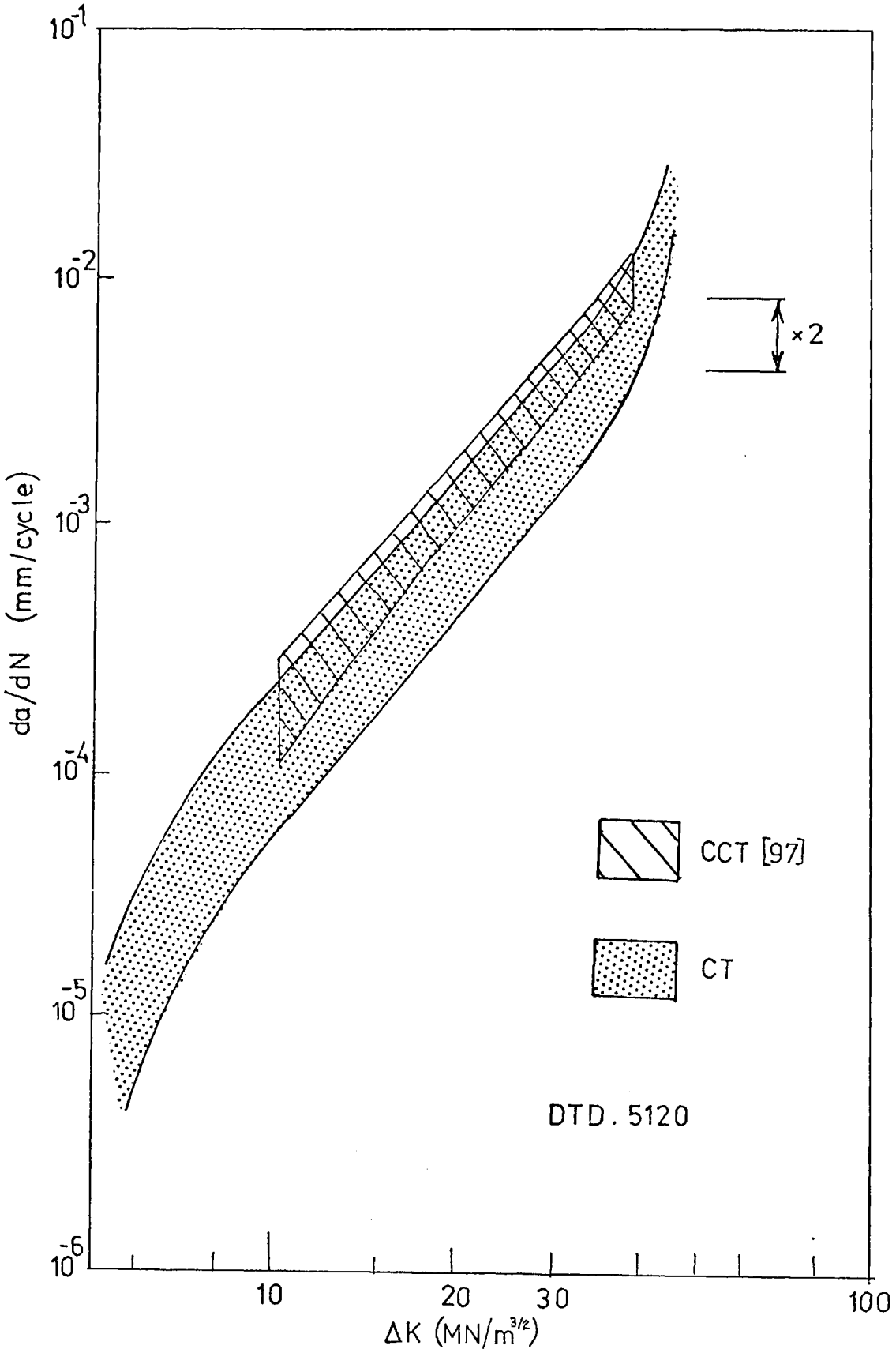


Figure 6.35: Comparison of CT and CCT test results for DTD.5120

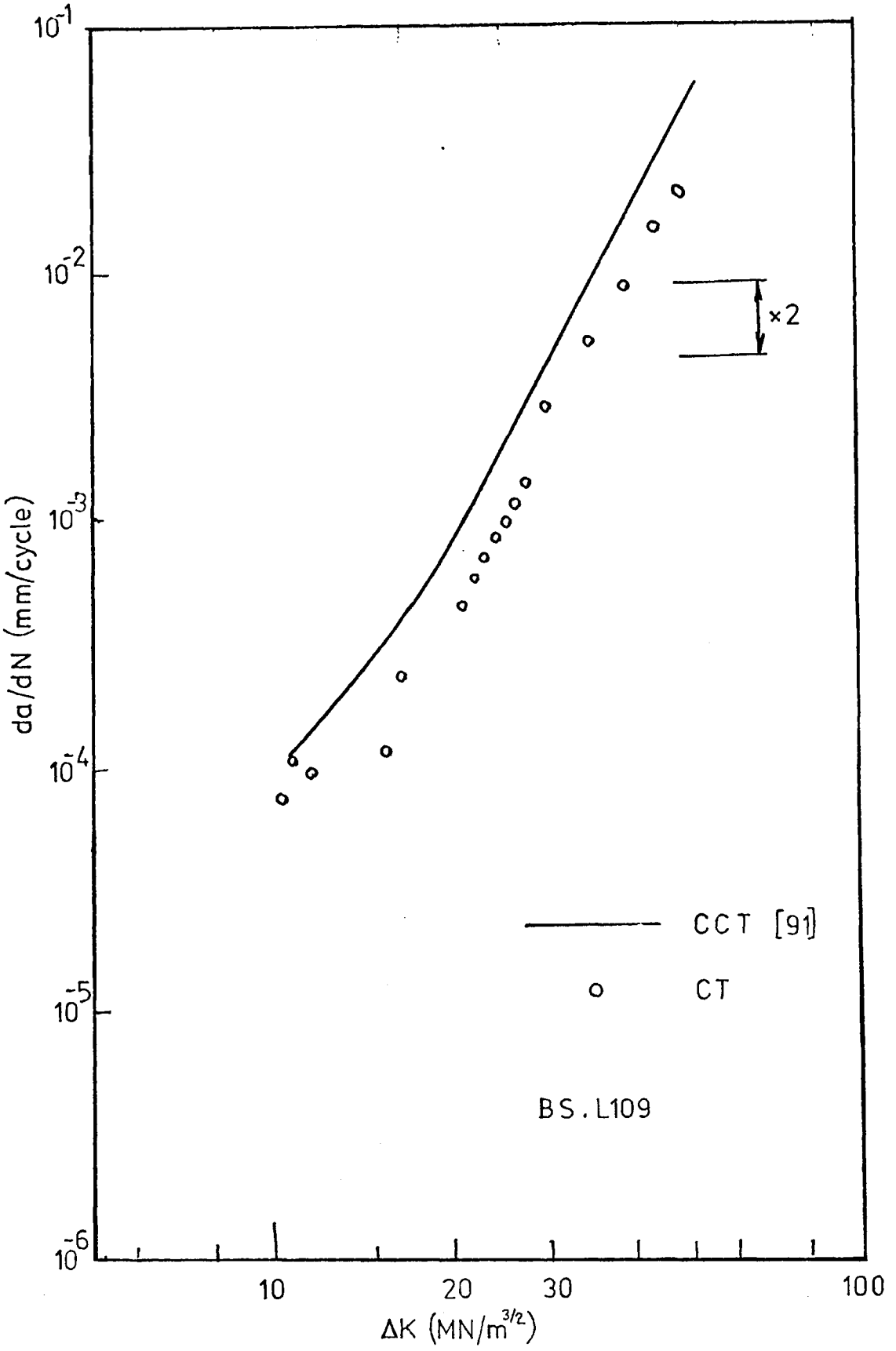


Figure 6.36: Comparison of CT and CCT test results for BS.L109

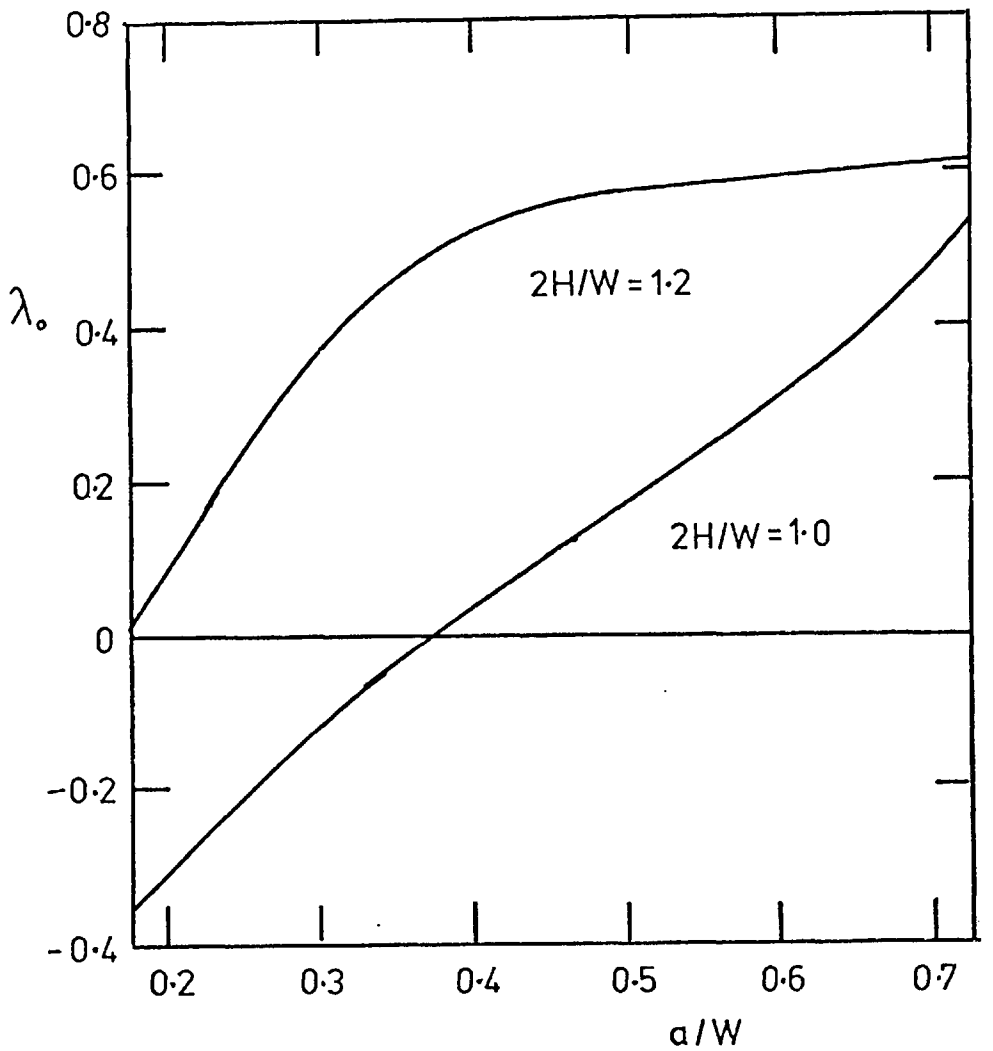


Figure 6.37a: Inherent biaxiality factor for CT specimens [122]

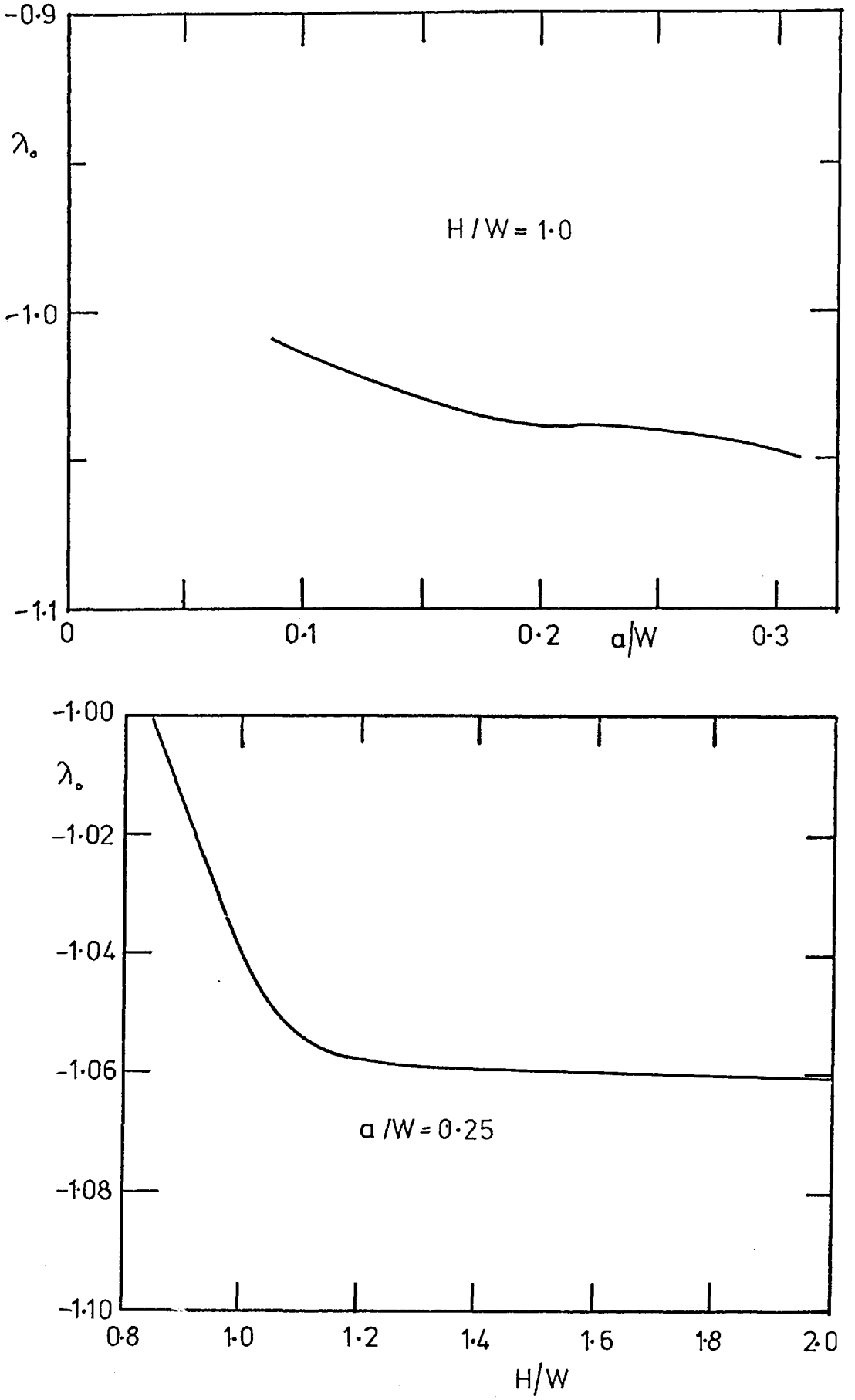


Figure 6.37b: Inherent biaxiality factor for CCT specimens [122]

CHAPTER 7

APPLICATIONS

7.1 COMBINED FATIGUE AND RESIDUAL STRENGTH DATA

Although the method of Section 6.2.2 provides a good correlation with test data, it is not in a form which may be applied conveniently in structural analysis. It may be used, however, as a basis for a semi-empirical crack growth equation.

In practice, the total crack growth rate is related to the stress intensity factor, ΔK, over a wide range of values by Paris' [13] equation - equation (2.14) - i.e.

$$\frac{da}{dN} = A\,(\Delta K)^n \tag{7.1}$$

If the stress ratio is altered at $\Delta K << K_c$ (or more specifically, when $da/dN << a$, c.f. equation (6.16)), then the curve is expected to translate with reference to the "$R = 0$" line in the same way as the total crack growth curves of Section 6.2.2.

Consider equations (6.36) and (6.37) which intersect at a point where:

$$\Delta K = \frac{C_2}{C_1}\left[\frac{(1-R^2)(1-R)^m}{(1-R)^2(1-R^m)}\right]^{1/(m-2)} \tag{7.2}$$

Thus, at any specified value of ΔK, one may derive a relationship between da/dN and R, such that the total curve moves back "down" the line $da/dN \propto (\Delta K)^2$. Thus:

$$\frac{da}{dN} = \left[\frac{(1-R)^2(1-R^m)}{(1-R^2)(1-R)^m}\right]^{(n-2)/(m-2)} A\,(\Delta K)^n \tag{7.3}$$

As the maximum stress intensity factor approaches K_c, equations such as (6.25) must be used to account for crack growth in a particular cycle.

Substituting equation (6.84) into equation (6.23) for $R = 0$ for zero stress ratio in the present notation:

$$\frac{da}{dN} = \frac{A\ (\Delta K)^n}{\left[1 - (\Delta K/K_{eng_c})^m\right]} \tag{7.4}$$

Adapting this form for non-zero stress ratios, in conjunction with equation (7.3), gives:

$$\frac{da}{dN} = \left[\frac{(1-R)^2(1-R^m)}{(1-R^2)(1-R)^m}\right]^{(n-2)/(m-2)} \left[1 - (\frac{K_{max}}{K_{eng_c}})^m\right]^{-1} A\ (\Delta K)^n \tag{7.5}$$

Further simplifications may be made: at modest stress ratios, the term $(1-R^m)/(1-R^2)$ is close to unity, and equation (7.5) reduces to:

$$\frac{da}{dN} = \frac{A\ (\Delta K)^n}{(1-R)^{n-2}\ \left[1 - (K_{max}/K_{eng_c})^m\right]} \tag{7.6}$$

This is considered to be a reasonable equation for practical applications. There are three empirical constants; A, n and m. A and n are from a conventional Paris equation fit at low stress intensities. The term, m, may be derived from the R-curve, or as $1/\gamma$ from equation (6.81).

It is informative to compare this equation with the empirical equations (2.16) to (2.18). The Forman/Pearson equations, (2.16), link the stress ratio dependence to the toughness, K_c. If R-curve methods are used, a geometry dependence is implied which may influence crack growth rate, even at low stress intensities. Alternatively, the "Region III" departure from the Paris equation may be ignored, as in equations (2.17) and (2.18). Referring to the form of these equations, represented in (2.19), typical values of $1 < r < 1.5$ are found for aluminium alloys [18]. This is in direct agreement with equation (7.6) when $K_{max} << K_{eng_c}$ and

$3 < n < 3.5$.

Figure 7.1 shows equation (7.6) applied to the 10 Hz results for DTD.5120 at $R = 0.1$ and 0.5. The constants used are $n = 2.8$ and $A = 1.15 \times 10^{-7}$ to give da/dN in mm/cycle with ΔK in $MN/m^{3/2}$. A value of $m = 2.04$ is taken from $m = 1/\gamma$ in Section 6.6.

For the corresponding data for L97, it is convenient to fit two Paris equation lines (Figure 7.2). The change in slope is not to be considered as anything but a convenient curve fit - any change in micro-mechanism, for example, should be viewed in the context of Section 6.2 and not at this point! The constants used are $n = 2.7$ and $A = 2.09 \times 10^{-7}$ for the lower part, and $n = 5.8$ and $A = 8.68 \times 10^{-12}$ for the upper part. Using $m = 1/\gamma$ from Section 6.6, once again $m = 3.26$ throughout.

In order to verify the power, $(n-2)$, as the stress ratio sensitivity, it is desirable to consider cases where n is not close to 3. Such data are available from Branco [44] who carried out some low frequency tests to provide reference data for corrosion fatigue research. The two alloys used were RR58 (2618-T651) tested in an S-L orientation, and a chill cast Al-17Si-4Cu alloy, BS.1490.LM30. In both cases, side-grooved DCB specimens were used and plane strain conditions achieved at failure. As no significant slow crack growth is expected during static loading, a value of $m = 20$ was used - equivalent to a very "steep" R-curve. Figures 7.3 and 7.4 show these results and indicate good correlation between equation (7.6) and experimental data. Note that for RR58 (S-L), $n = 6.64$ and $A = 1.37 \times 10^{-11}$, and for LM30, $n = 9.21$ and $A = 6.72 \times 10^{-14}$.

In order to account for the K_{eng_c} term, R-curve analysis may be used to derive a maximum load toughness value. Alternatively, K_{eng_c} versus Γ may be plotted, as in Section 6.6. For real geometries, close formed solutions for Γ may be available and some numerical solution is required.

If values of Y (= $K/\sigma\sqrt{\pi a}$, for example, [8]) are known as a function

of crack length, e.g. (Y_1, Y_2, Y_3, .., Y_i, etc.) at (a_1, a_2, a_3, .., a_i, etc.), then:

$$\Gamma_i = \frac{K}{(\partial K/\partial a)} \tag{7.7}$$

$$= Y_i \sigma \sqrt{\pi a_i} \left[\sigma \left(\frac{\partial Y}{\partial a}\right)_i \sqrt{\pi a_i} + \sigma \frac{Y_i}{2} \sqrt{\pi/a_i}\right]^{-1} \tag{7.8}$$

The differential term may be estimated by a crude finite difference method using points on either side of (a_i,Y_i), i.e.

$$\left(\frac{\partial Y}{\partial a}\right)_i = \frac{Y_{i+1} - Y_{i-1}}{a_{i+1} - a_{i-1}} \tag{7.9}$$

Subsituting (7.9) into (7.8) and simplifying the equation:

$$\Gamma_i = 2a_i Y_i \left[2a_i \frac{(Y_{i+1} - Y_{i-1})}{(a_{i+1} - a_{i-1})} + Y_i\right]^{-1} \tag{7.10}$$

7.2 ANALYSIS OF AN ENGINEERING COMPONENT

For fatigue life estimation purposes, joints in aircraft structures are classed as "highly loaded" (HLJ) or "lightly loaded" (LLJ) joints. In an HLJ, all of the load is carried from one component to the other through the joint. For test purposes, such a joint may be represented by a specimen, as indicated in Figure 7.5 ., in which three close tolerance clearance fit fasteners are used to transfer load in a double-shear arrangement. Loading well below the proportional limit and neglecting load transfer by friction, the distribution of the load may be estimated from elastic stress analysis [123] which predicts that the end bolts each carry a load:

$$P_e = 1.183 \frac{P}{3} \tag{7.11}$$

and the centre bolt carries a load:

$$P_c = 0.634 \frac{P}{3} \tag{7.12}$$

where P is the total applied load.

As the centre plate has less thickness than the total of the outer plates, failure is expected in the centre plate near to the end bolt. At this point, the stress distribution is defined by an end load in the plate, equal to the load transferred by the other two bolts, with a single "point" load of 1.183 $P/3$ superimposed.

Failure of one such test piece [91] manufactured from BS.L97 alloy occurred by propagation of a fatigue crack from an initiation site at the intersection of the bore of the hole and the centre plate surface (Figure 7.6). Several solutions exist for the stress intensity factor in such a configuration. The solution due to Broek et al. [124] was chosen as this allows a continuous curve of Y versus a for a corner crack which develops into a through-crack [125]. (The transition to a through-crack is dealt with similarly by Johnson [126], but with different integration limits for the shape function.) The solution is based on semi-elliptical surface crack analysis, with free surface corrections being applied to account for the hole and the finite plate thickness [127]. The plate width was taken into account using standard solutions [8] and a compounding method [22]. Finally, some account must be taken of the bolt loading effect. Hall et al. [129] have proposed a modification to Bowie's [129] method for predicting fastener loading effects. Although this is not strictly applicable to part-through cracks, a similar proportional increase in Y for a given fastener load gives an estimate of the solution for modest crack sizes. These modifications to the stress intensity solution are indicated in Figure 7.6.

By conventional methods, the critical gross stress for fracture, σ_{crit}, is given by:

$$\sigma_{crit} = \frac{K_c}{(Y \sqrt{\pi a})} \tag{7.13}$$

Taking a typical value of K_c = 72.5 MN/m$^{3/2}$ from Chapter 5, σ_{crit} may be plotted against the crack length, as shown in curve (a) of Figure 7.7. For linear elastic fracture mechanics to be valid, the net section stress must be below the 0.2% proof stress. Thus, the analysis is valid below the LEFM limit indicated in the figure. The test was, in fact, carried out with a maximum gross stress of 175 MN/m^2. This gives a critical crack length, $q_c(a)$, roughly equal to the hole diameter.

Using equation (7.10) and taking K_{eng_c} versus Γ data from Figure 6.28a, the curve of σ_{crit} may be modified to take into account the variation of K_{eng_c} with crack length in this geometry. As there is a severe stress concentration near to a free edge, Γ is very small - typically 7 mm < Γ < 9 mm - and K_{eng_c} varies between 49 MN/m$^{3/2}$ and 52 MN/m$^{3/2}$. The revised σ_{crit} values are shown in Figure 7.7, together with a reduced estimate for $q_c(b)$. This low toughness value is supported by the test result, and is similar to the pin-lug specimen of Figure 6.30.

The crack propagation rate may be estimated from striation spacing measurements taken from the specimen fracture surface, indicated by the open circles in Figure 7.8. The dashed line indicates the predicted growth rate using equation (7.6) with K_{eng_c} = 72.5 MN/m$^{3/2}$. The solid line is also based on equation (7.6), but with K_{eng_c} calculated via Γ. The solid circles are estimated macroscopic crack growth rates, taking into account the difference between da/dN and $\bar{s}$ observed at high growth rates (see Section 7.3).

At low growth rates, no difference is expected between da/dN and $\bar{s}$, and it appears that the stress intensity factor in this region is under-

estimated by about 30%. This is almost certainly due to errors in the bolt loading term in the stress intensity calculation. It is interesting to note that these striation measurements are in close agreement with those measured under pure fretting conditions [131] in 7075-T7351 aluminium alloy.

Integrating the curve (using the striation spacing for da/dN at $q < 4$ mm) gives a crack propagation life of 9200 cycles for 0.05 mm $< q <$ $q_c(b)$, compared with 11200 cycles for 0.05 mm $< q <$ $q_c(a)$ by conventional analysis. The total specimen life, including initiation of the crack, was 78400 cycles.

Tests on specimens of the type shown in Figure 7.5 are frequently used as a basis for fatigue and crack propagation life predictions in larger structures. If a similar failure were to occur at a fastener hole close to the edge of a large plate, crack propagation would not differ significantly from that in the test specimen as the crack grew from the hole to the edge of the plate. If, however, the crack then propagated from the other side of the hole into the plate, an edge crack would be formed and the geometry effect would make a considerable change to K_{eng_c}.

By conventional analysis, for a simple edge crack in a semi-infinite sheet:

$$K = 1.12\,\sigma\sqrt{\pi\,a} \tag{7.14}$$

therefore:

$$a_c = \frac{1}{\pi}\left(\frac{K_c}{1.12\,\sigma}\right)^2 \tag{7.15}$$

Once again, taking K_c = 72.5 MN/m$^{3/2}$ at σ = 175 MN/m^2:

$$a_c = 43.5 \text{ mm} \tag{7.16}$$

Alternatively, put:

$$\Gamma = \frac{K}{(\partial K/\partial a)} = 2a \tag{7.17}$$

For a crack 43 mm long, this gives K_{eng_c} in excess of 100 MN/m$^{3/2}$ so that failure would not occur. Figure 5.11 implies stable crack growth, $\Delta a'$, of about 30 mm in this case and a rigorous R-curve analysis would be required to predict failure.

7.3 APPLICATIONS OF FRACTOGRAPHY IN FAILURE ANALYSIS

It is confirmed by this study that the use of the scanning electron microscope (SEM) in failure analysis may be of vital importance. It may indicate fatigue crack growth mechanisms and growth rates, and thus indicate the prior load history of the component. Some caution is advised, however, on two counts:

1. Striation spacing may vary greatly, even at constant macroscopic growth rates. As many locations as possible should be studied in order to obtain useful results.
2. A surface which exhibits no striation markings may still be due to fatigue crack growth. At low growth rates, it may be difficult to resolve striation markings, and at high growth rates they may be obscured by local tearing which may not be distinguishable from the final fracture zone.

In all cases, measured striation spacings should be compared with those in test specimens in order to deduce crack growth rates. The comparison requires a knowledge of the stress ratio in the component (Figure 7.9).

7.4 STRESS RATIO AND RANDOM LOADING EFFECTS

The crack resistance addition model developed in Sections 6.2 to 6.4

and 7.1 predicts the effect of positive stress ratios on constant amplitude fatigue crack growth, but there has been no discussion of its application to random loading or other variable amplitude loading situations. There appears at first sight to be some disagreement between the proposed model and Elber's [68,72] crack closure model, discussed in Section 3.8, and it is necessary to make some detailed comparisons between these approaches.

The important experimental observation upon which Elber's theory is based is that the crack becomes closed at low stress intensities during the fatigue cycle. This observation is quite consistent with the plastic zone model discussed in Section 3.1.1, in which such closure is a necessary consequence of the plastic zone behaviour. It is this behaviour which gives rise to the different nature of the cyclic and total plastic zone sizes, represented in the crack resistance addition model by the term:

$$Q \frac{(1-R)^2}{(1-R^2)} \tag{7.18}$$

in equation (6.28), etc., and which correspondingly plays a major part in the stress ratio dependence predicted later. It is Elber's contention that the part of the cycle for which the crack is closed can do no damage as there is no singularity in the stress distribution in this case. This assumption cannot be made in the present analysis; in using the cyclic plastic zone size as calculated in Section 3.1.1, the analysis is dependent on the strain cycling behaviour ahead of the crack tip, and that part of the cycle for which the stress is compressive is included throughout. There is no difference in the experimental observations between Elber's work and the present study. There is, however, a difference in the philosophy:

Elber suggests that crack closure causes certain of the secondary effects observed in fatigue crack growth. The author prefers to consider

that both crack closure and crack growth are independent effects with a common cause, i.e. local plastic strain cycling behaviour.

As described in Section 3.8, Elber claims considerable success for the crack closure model in analysis of variable amplitude loading effects. No such tests have been carried out in this study, but it is possible to extend Rice's model [29] of the cyclic plastic zone size to deal with simple cases, such as that of a single overload during a constant amplitude fatigue sequence, in a qualitative sense. Figure 7.10 is a logical extension of Figure 3.2.

When the overload occurs, the total plastic zone size is increased to r_{ol}. During the next unloading event, a "cyclic plastic zone" is formed of size Δr_{ol}, which may be derived from equation (3.2), but substituting K_{ol} for K_{max}, giving $\Delta K = K_{ol} - K_{min}$. When constant amplitude cycling is resumed, fully reversed strain cycling continues only where the strain range exceeds twice the yield strain, and Δr_p is unchanged. However, in the region $\Delta r_p \leq r \leq \Delta r_{ol}$, elastic cycling occurs with $\sigma_{min} = \sigma_y$ in compression, whereas in the previous case $\sigma_{max} = \sigma_y$ in tension.

It is widely reported that overloads cause retardation of fatigue crack growth and that this effect is not instantaneous. The crack slows down over a number of cycles and then accelerates again. The argument above implies that this may be caused by the reduction in the mean stress for the (theoretically) elastic cycling of the material ahead of the cyclic plastic zone. This behaviour is identical to that expected at blunt notches, where overloads may increase high cycle fatigue initiation lives by the same mechanism [130]. There is, of course, a change in crack closure behaviour because $\Delta r_{ol} > \Delta r_p$, and it is this change which Elber uses in predicting variable amplitude loading effects.

In discussing crack closure phenomena, one further point must be made. Theories based on that of Elber have been used in evaluating the effect of

corrosion products which may hold the crack open in some environments (e.g. "oxide induced crack closure" [131] and the effects of calcarious deposits in seawater environments [132]). There is an important difference between this effect and crack closure under normal circumstances, in that the minimum strain is prevented from reaching zero, even under total unloading. In this case, a genuine increase in K_{min} does occur, so that the stress intensity range is effectively reduced.

7.5 CRACK PROPAGATION LIFE PREDICTIONS

Ultimately, crack propagation data are only of use if they may be used to obtain a reliable prediction of the crack propagation life of a component or structure. A standard computer program is used by British Aerospace, Hatfield, to carry out such a calculation [133]. In its basic form, the program evaluates the stress intensity factor for a specified crack length, a_o, and stress by interpolation within a table of values of $K/\sigma\sqrt{\pi a}$. The crack growth rate is then calculated using Forman's equation [15], i.e. equation (2.16). The increased crack length is calculated, following ΔN cycles at this rate, from:

$$a = a_o + \Delta N \left(\frac{da}{dN}\right) \tag{7.19}$$

ΔN is chosen as 10, 100, 1000, etc., such that $0.025 \text{ mm} \leq (a - a_o) < 0.25 \text{ mm}$. The new crack length is then re-substituted for a_o, and the calculation repeated until the maximum stress intensity exceeds K_c.

The program was modified [134] to use equation (7.6) in place of Forman's equation and to calculate K_{eng_c} at each step using equations (6.81) and (7.10). Coefficients were chosen for the crack growth equation to provide crack growth rates about 50% higher than the mean experimental data at $R = 0.1$. This is consistent with typical aircraft industry

practice in providing, for example, 90% confidence limit data as a design curve. An additional safety factor (normally between 1.5 and 2.5) would then be applied to give an operational crack propagation life which must provide for inaccuracies in load and stress intensity analyses, and difficulties in inspection, as well as variations in material properties. The program was used to "predict" the life of the specimens tested in the present study. Figure 7.11 is a summary of results for those specimens where a constant load amplitude was maintained for a large number of cycles. Where testing was carried out with $R < 0$, the calculation was run in two forms: (a) using the total range of load ($\Delta P > P_{max}$) and by substituting the negative value of R in equation (7.6); (b) using the positive load range ($\Delta P = P_{max}$) and substituting $R = 0$ in equation (7.6). The latter case provided the best correlation with test data. Of 26 specimens checked in this way, 19 calculations lay on the conservative side of the test result, increasing to 25 when a factor of 1.5 was applied to the calculated life.

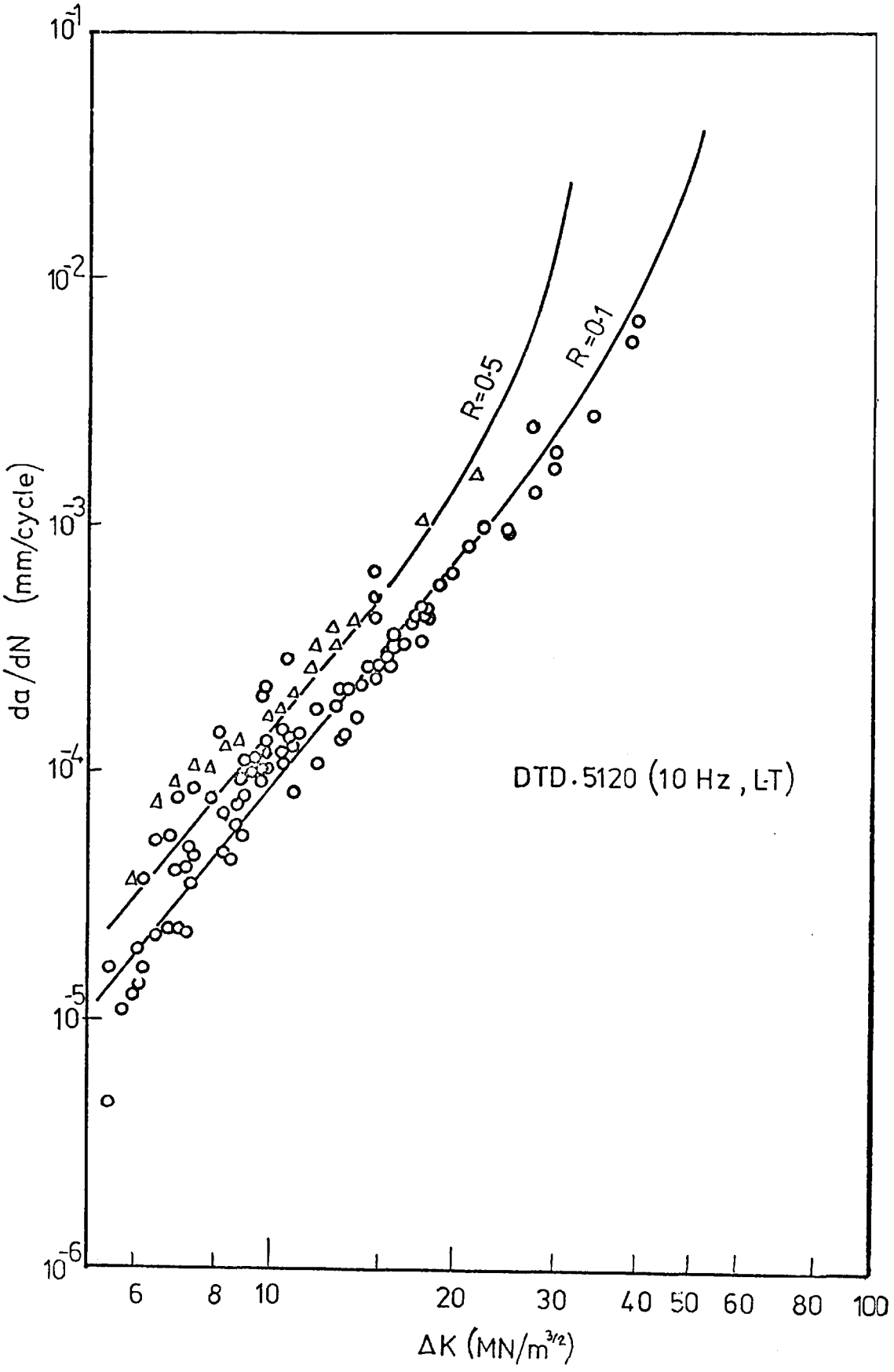


Figure 7.1: Fit of equation (7.6) to DTD.5120 data

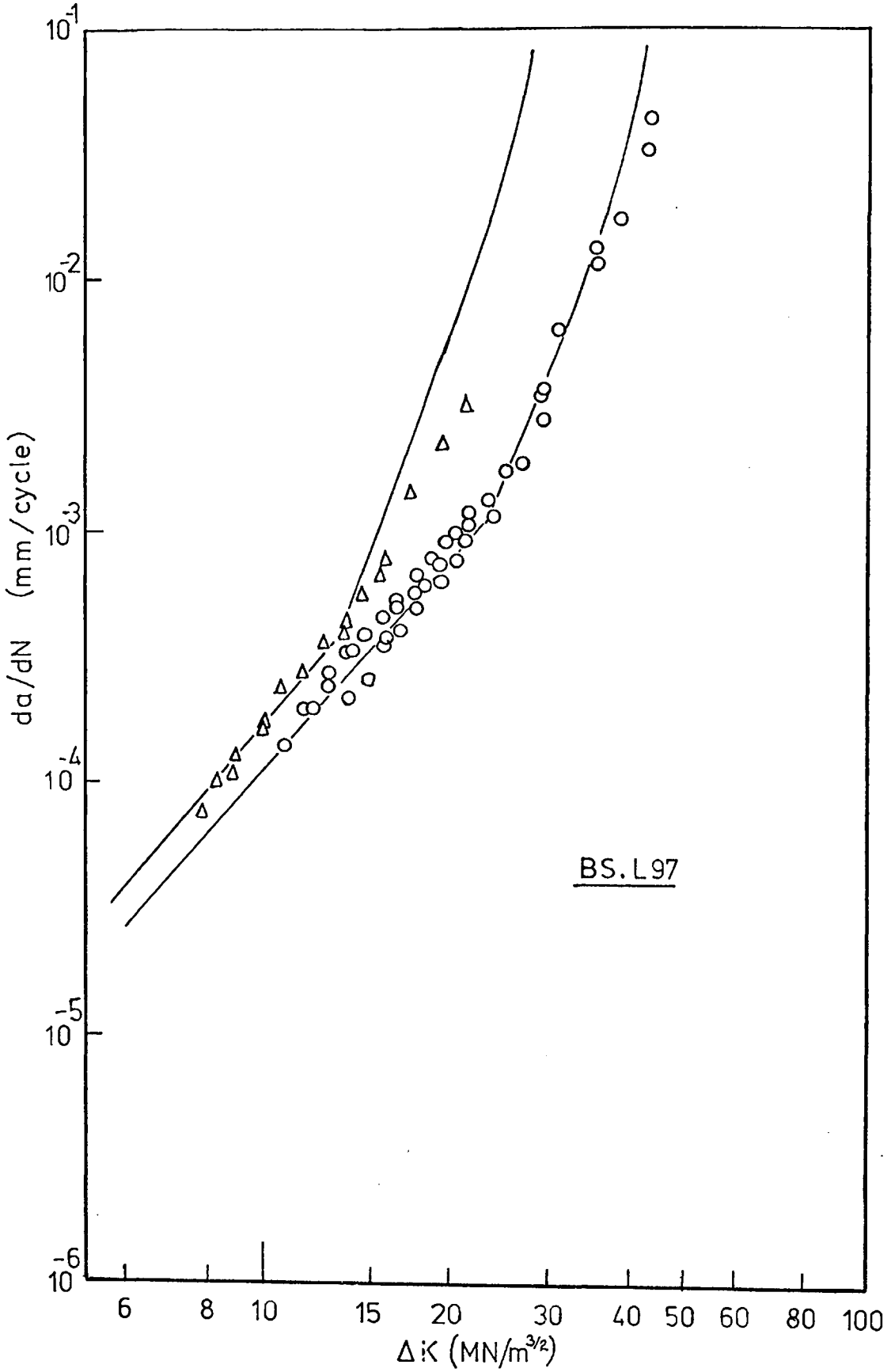


Figure 7.2: Fit of equation (7.6) to BS.L97 data

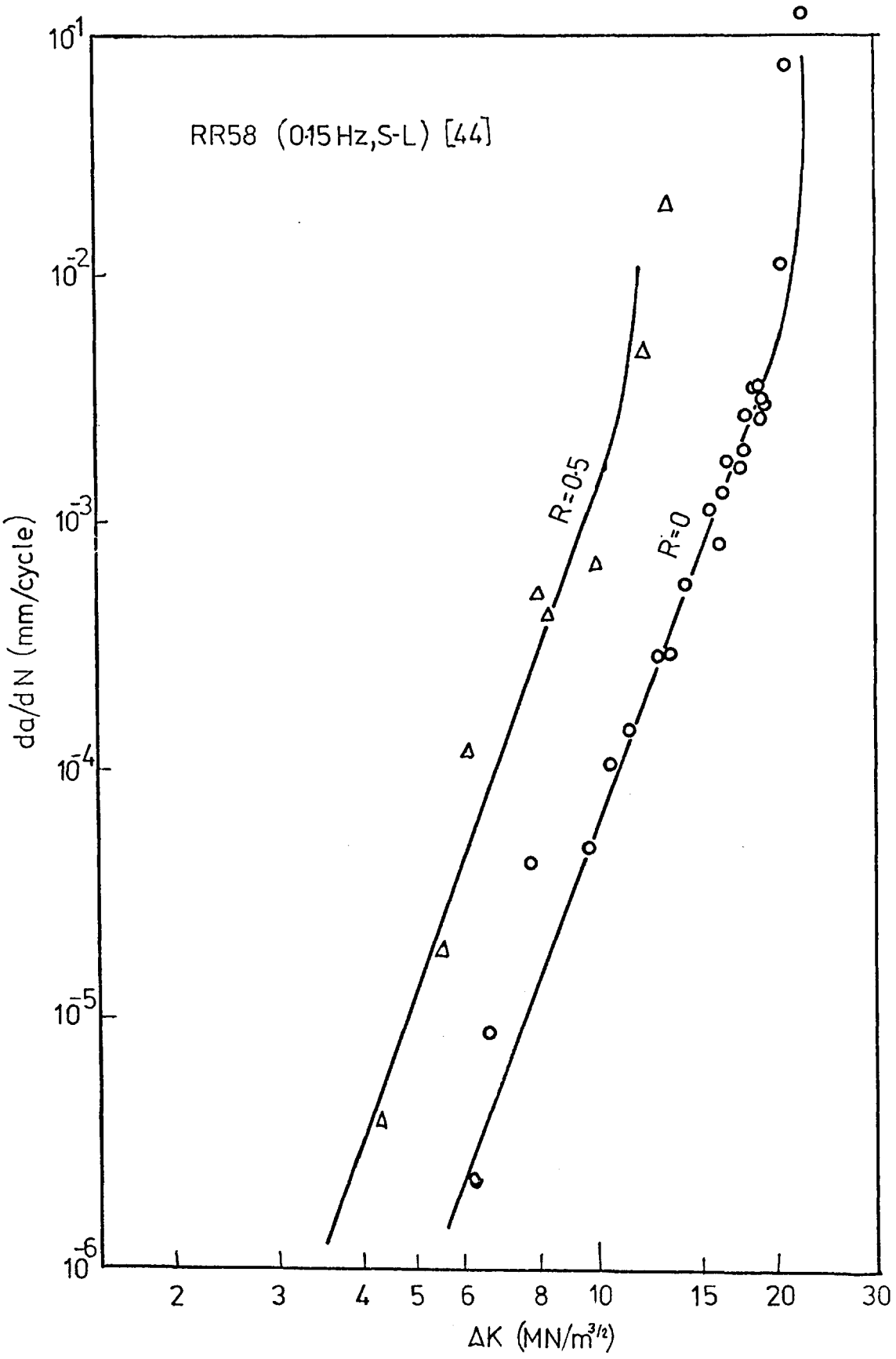


Figure 7.3: Fit of equation (7.6) to RR58 data

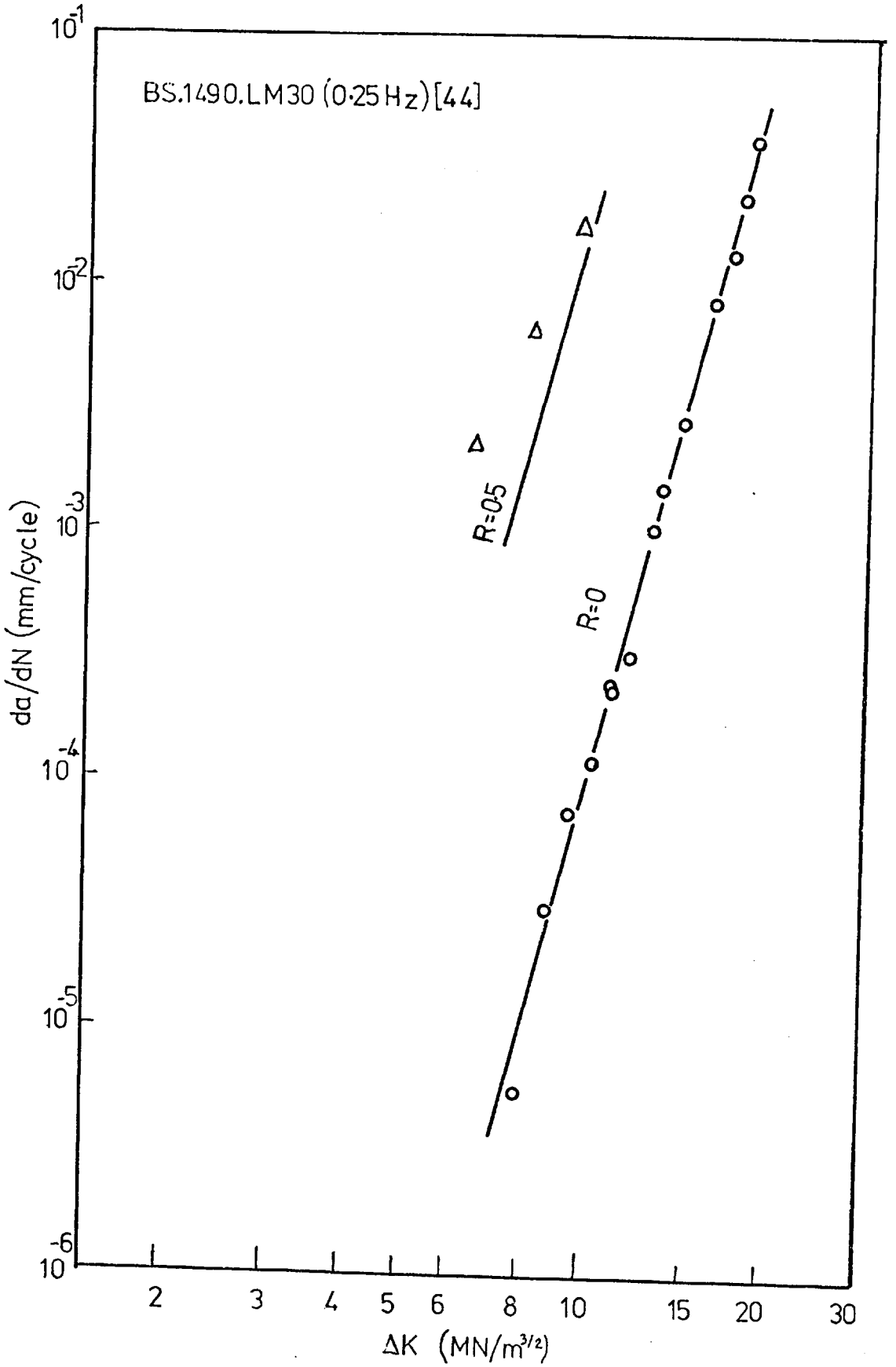


Figure 7.4: Fit of equation (7.6) to BS.1490.LM30 data

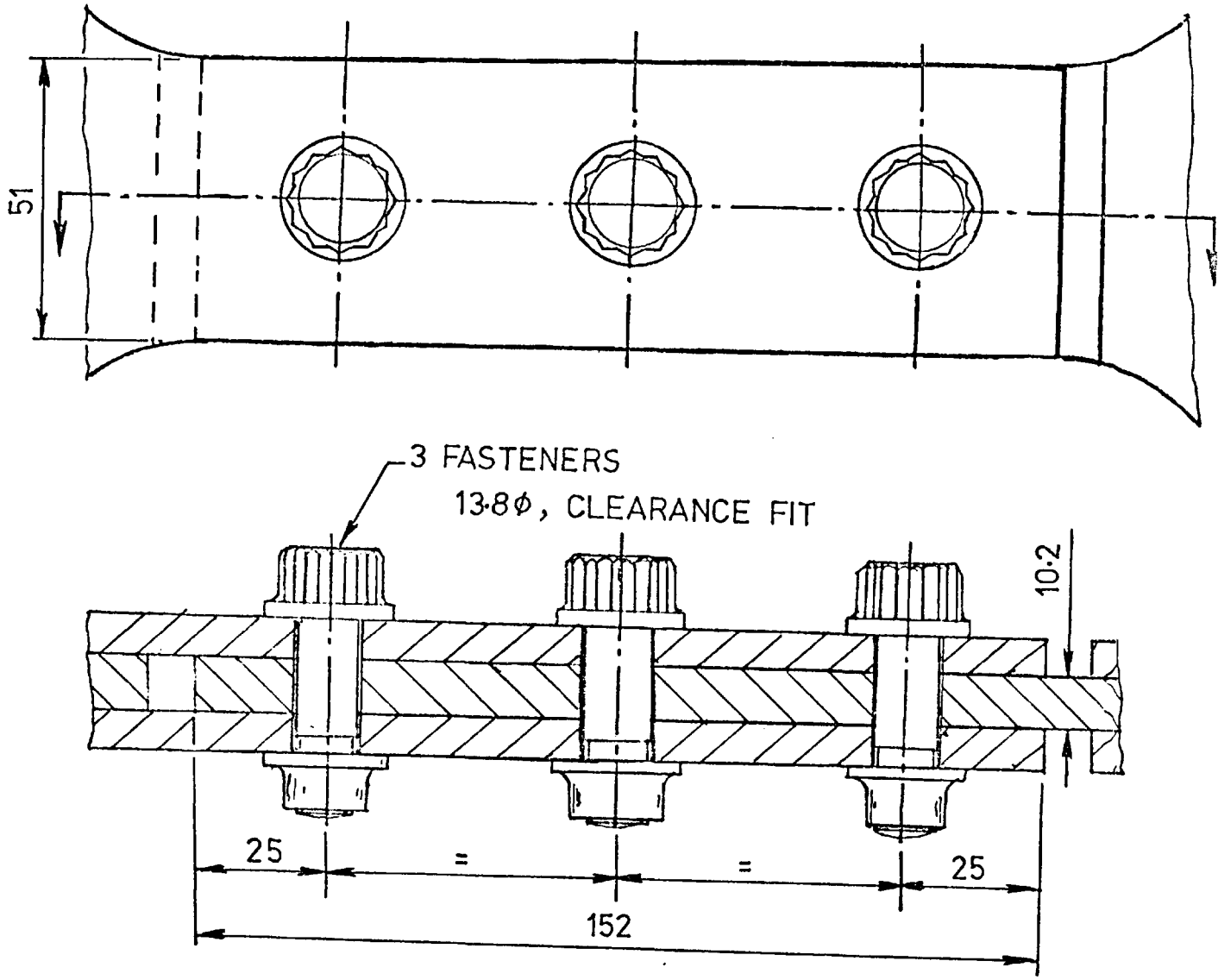


Figure 7.5: Fatigue test specimen for highly loaded joint

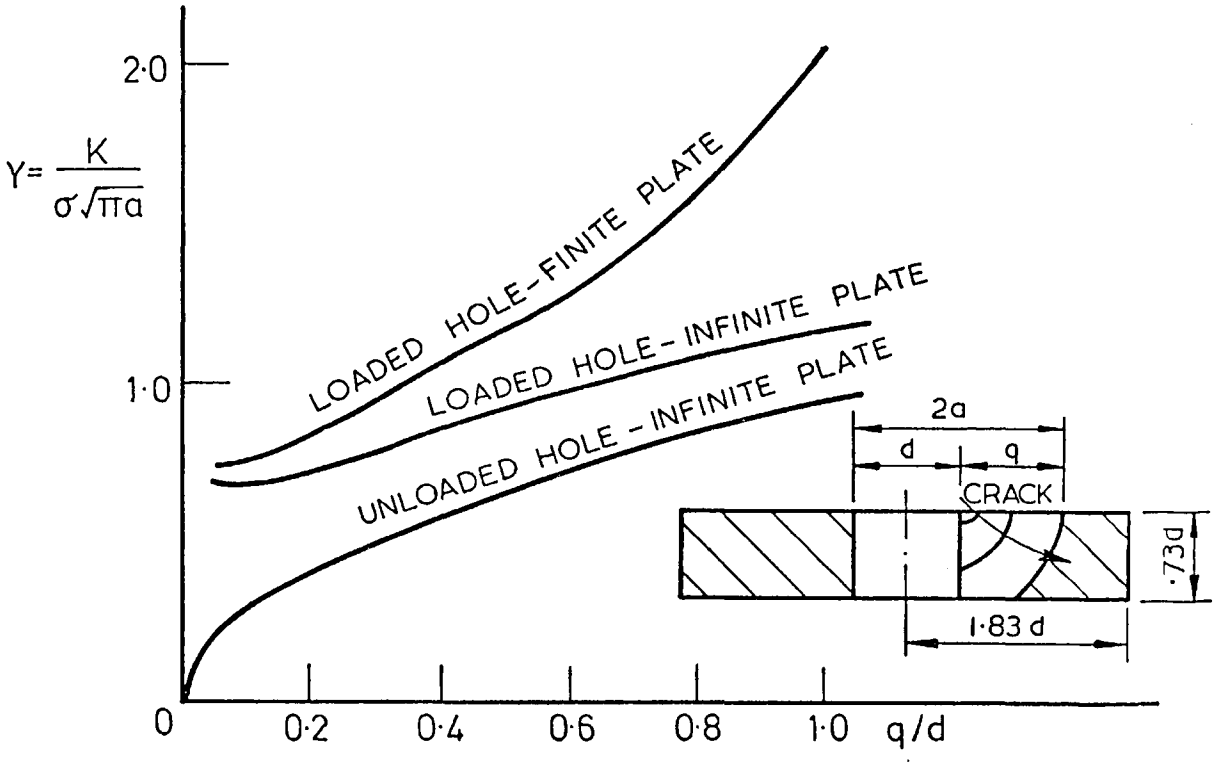


Figure 7.6: Stress intensity factor for HLJ specimen

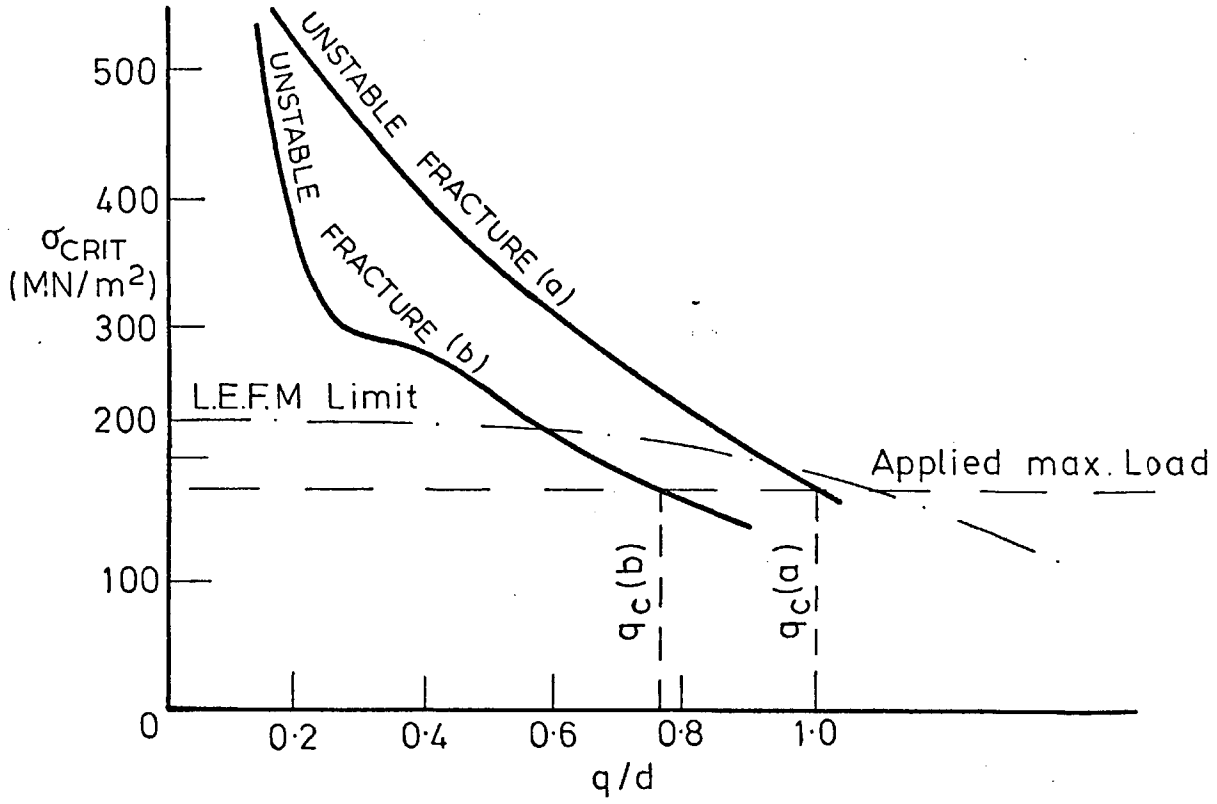


Figure 7.7: Fracture stress for HLJ specimen

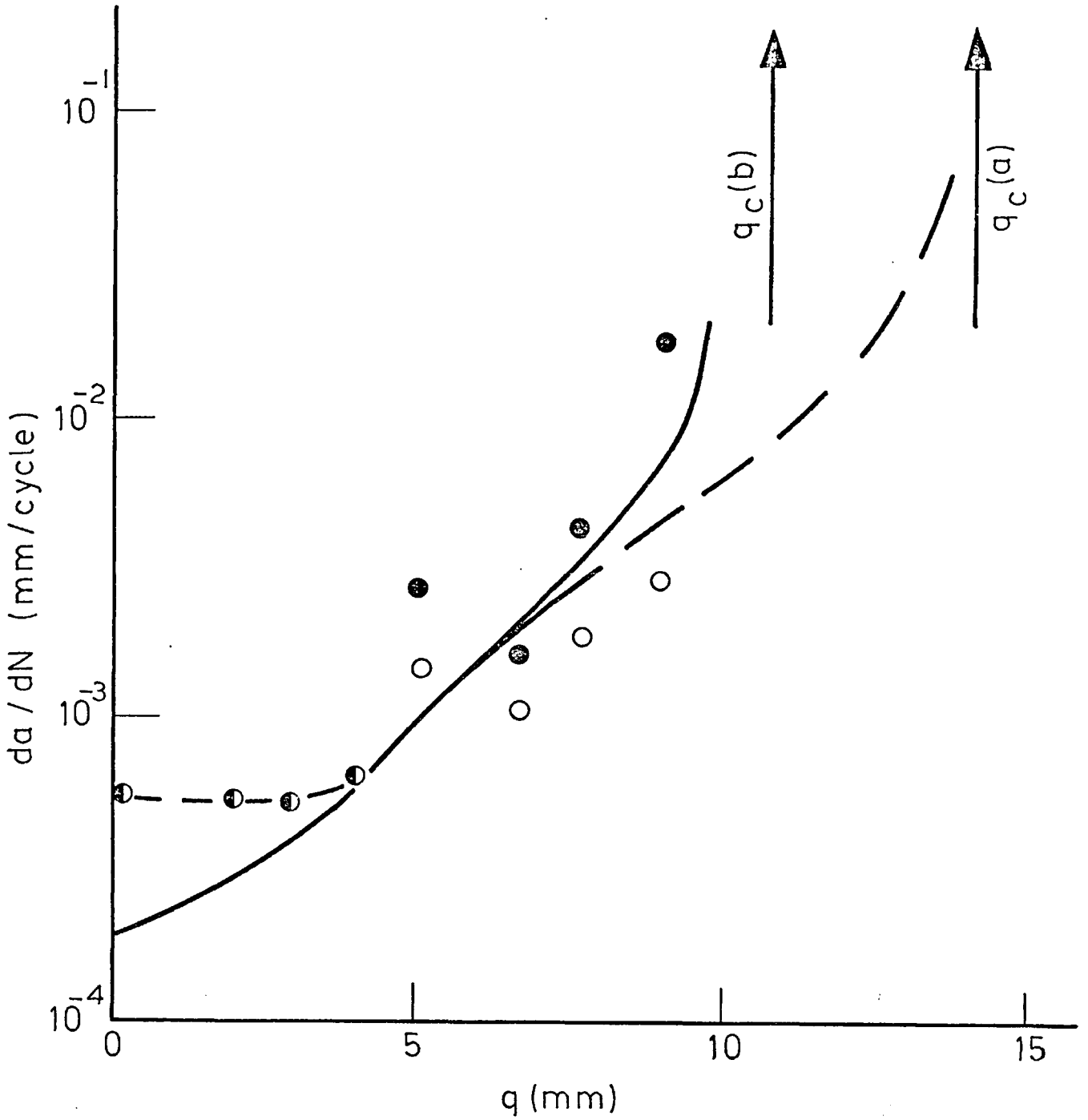


Figure 7.8: Crack growth rate in BS.L97 HLJ specimen

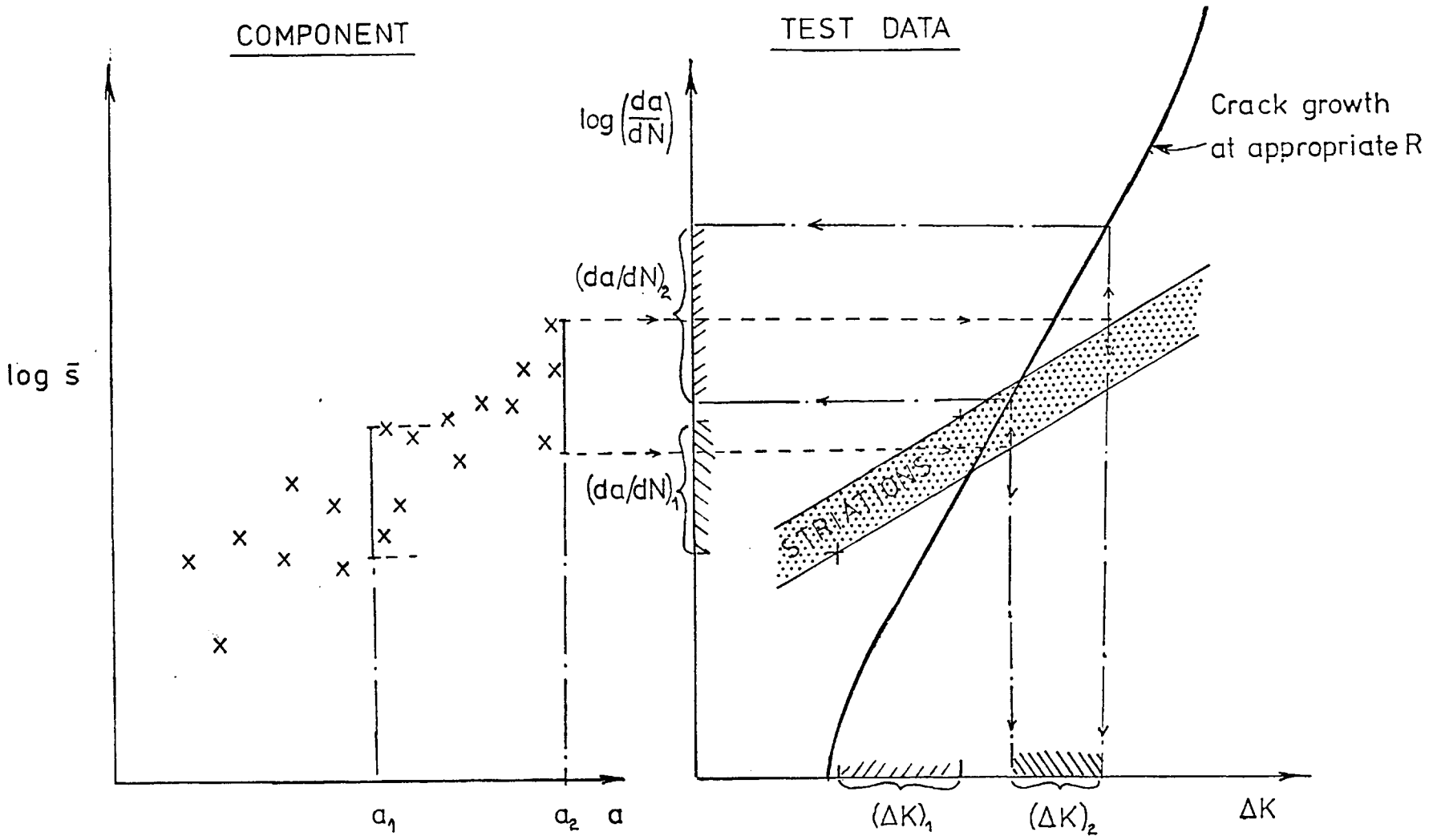
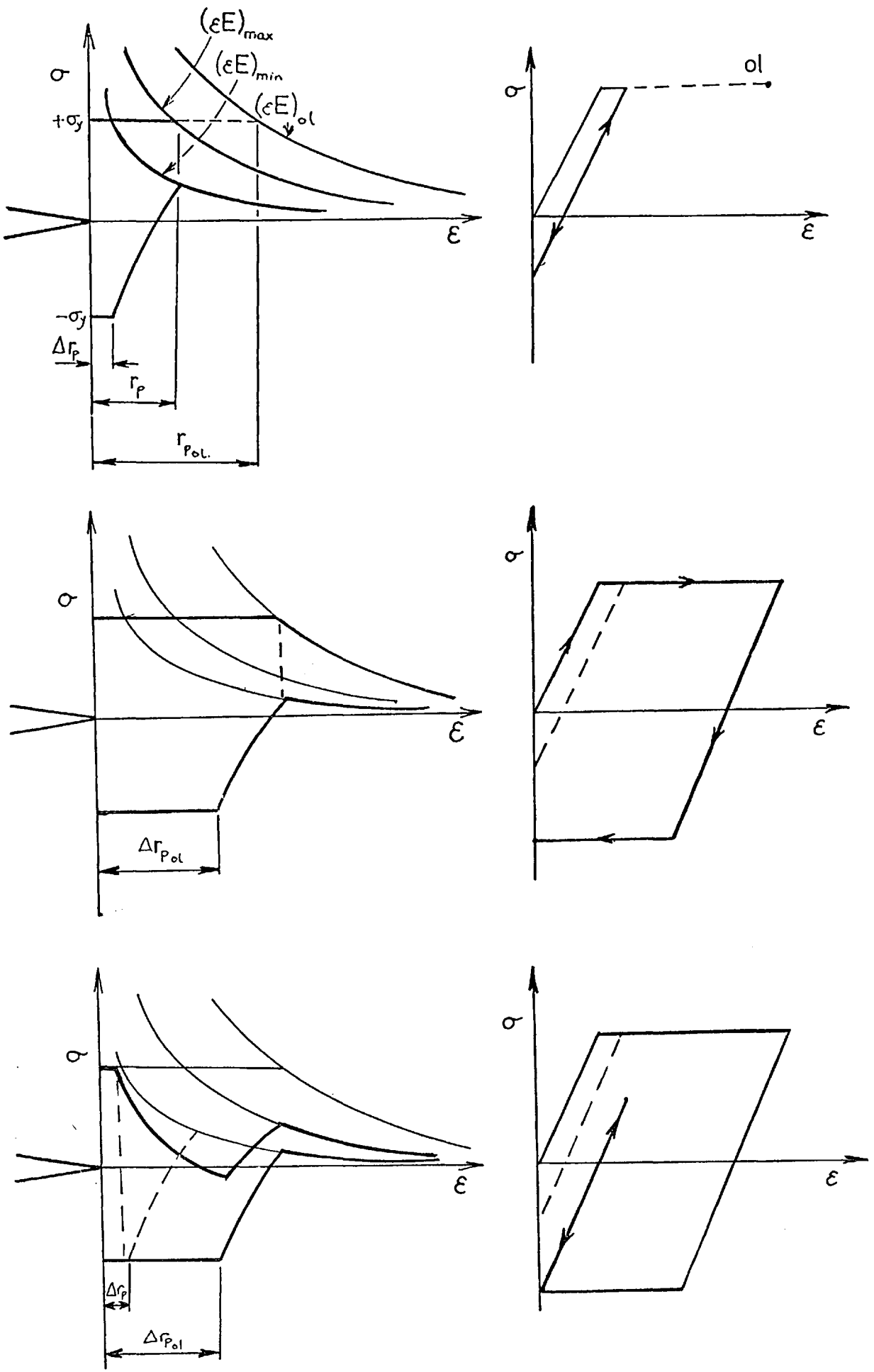
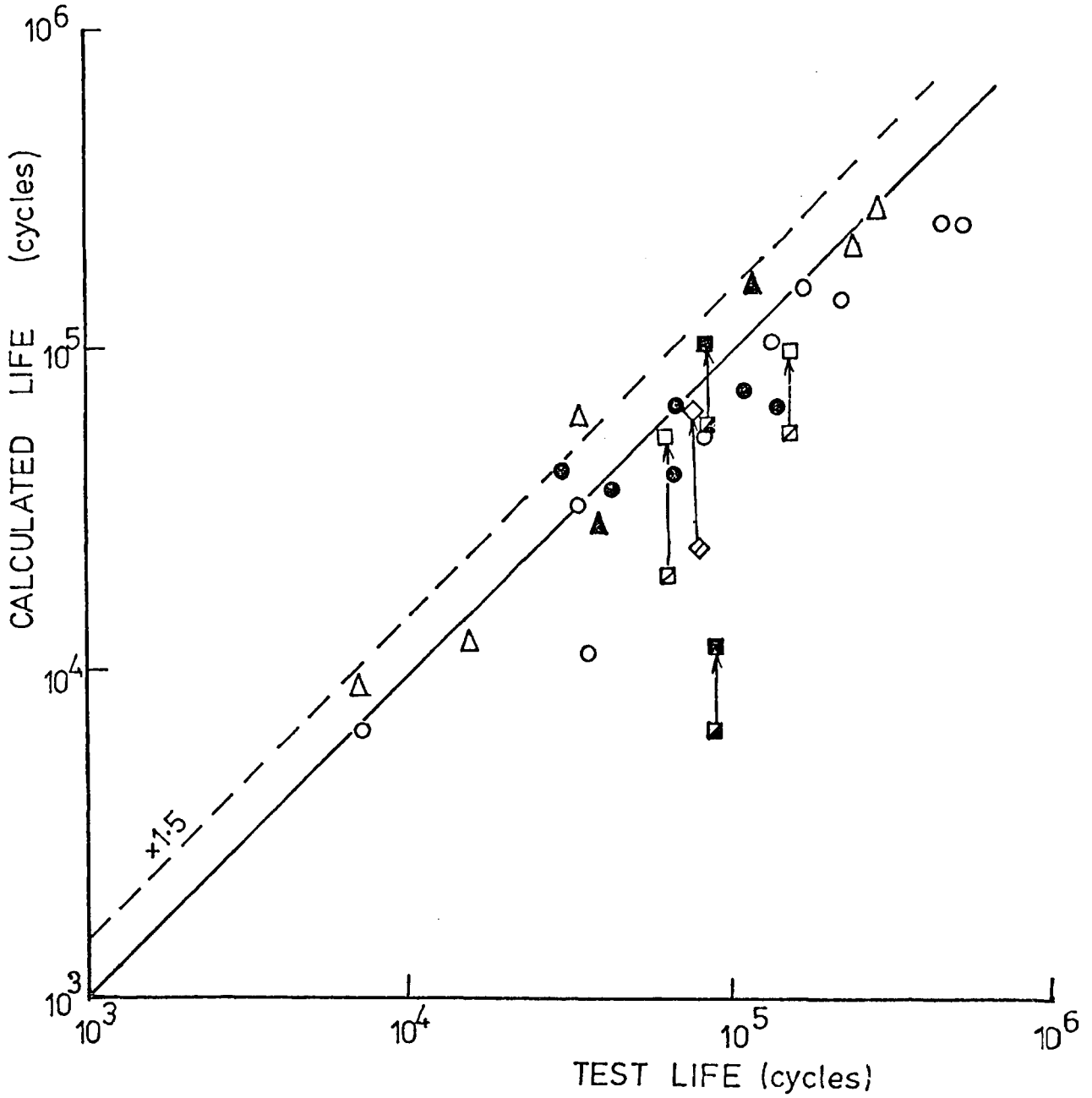


Figure 7.9: Use of striation data in assessing component failure



Fi-ure 7.10: Effect of overload on plastic zone size



R	DTD.5120 (a)	DTD.5120 (b)	BS.L97 (a)	BS.L97 (b)
0.5	△		▲	
0.1	○		●	
−1/3	▨	□	◪	■
−2/3	◈	◇		

(a) $\Delta P = P_{max} - P_{min}$

(b) $\Delta P = P_{max}$

Figure 7.11: Comparison of life predicted from equation (7.6) with test data

CHAPTER 8

CONCLUSIONS

i) It was demonstrated that small compact tension specimens may be used to generate fatigue, and stable crack growth data and fracture toughness data, provided that net section yielding does not occur. In assessing buckling effects, and in interpreting final data, the non-singular stress component parallel to the crack may be significant. In particular, this component is tensile in CT specimens but compressive in CCT specimens. This results in slightly lower fatigue crack growth rates in CT specimens at high stress intensities.

Some additional development work is required before reliable fatigue crack growth data may be obtained from very thin section CT specimens.

ii) DTD.5120 (7010-T7651) aluminium alloy was demonstrated to have similar crack propagation characteristics to BS.L97 (2024-T3) alloy, despite its substantially greater strength.

iii) Tests were carried out with both tensile and compressive minimum loads. Where the minimum load was compressive, considerable scatter occurred in crack growth rate measurements which could not be explained by analysis of the reversed plastic zone behaviour. It was confirmed that compressive loads may be detrimental, but that crack blunting and arrest could occur during prolonged tension-compression testing at constant load amplitude. This blunting behaviour was more evident in BS.L97 than in DTD.5120.

iv) Transition from square (mode I) to slant (mixed mode I/III) failure occurred during fatigue testing of all specimens. In DTD.5120, the

crack growth rate at which transition commenced was found to decrease as the thickness increased. In both materials, this growth rate was independent of frequency and stress ratio.

During monotonic loading, the transition occurred in DTD.5120 for all specimens (6 mm $\leqslant$ thickness $\leqslant$ 15 mm) and was accompanied by a steep rise in crack growth resistance. At high loading rates, the transition occurred over a shorter crack length. In BS.L97, crack tunnelling occurred and mode transition was not observed. During transition, the plastic zone size, derived from the compliance of the specimen, was less than the theoretical plane stress value and did not exceed the specimen thickness until transition was complete.

The effect of thickness on fatigue crack growth rate is accounted for, in full, by substitution of appropriate toughness data in the crack growth theory.

v) Fractography demonstrated that for crack growth rates above about 10^{-5} mm/cycle, fatigue crack growth in aluminium alloys is caused by a combination of ductile striation formation and micro-void coalescence. Methods were discussed whereby these two processes could be represented separately and then superimposed to predict total crack growth rates. A "crack resistance addition model" is proposed, developed from *R*-curve theory for monotonic loading, which expresses the total growth rate in terms of two mechanisms. The relative contributions of these mechanisms are considered in terms of both deterministic and probablistic approaches.

A semi-empirical method is used to develop an approximate crack growth equation from the crack resistance addition model, which may be useful for structural analysis:

$$\frac{da}{dN} = \frac{A\ (\Delta K)^n}{(1-R)^{n-2}\ \left[1 - (K_{max}/K_{eng_c})^m\right]}$$

in which ΔK and K_{max} are the range and maximum values of the stress intensity factor, and R is the stress ratio. The constants A and n are determined from constant stress ratio testing at modest stress intensities K_{eng_c} and m are derived from the monotonic R-curve for the material. An alternative derivation of K_{eng_c} enables it to be deduced from maximum load toughness data with a suitable geometry correction.

vi) The model developed is subject to the limitations of linear elastic fracture mechanics, and does not take "threshold" effects into account. Specifically, it is not expected to be valid when

a) The crack is very short (i.e. less than about 0.5 mm)

b) The stress intensity range is very low (i.e. less than about $6MN/m^{3/2}$)

c) The crack tip is in the close vicinity of a notch, or other stress concentration.

CHAPTER 9

RECOMMENDATIONS FOR FURTHER WORK

There are several aspects of this work which could be extended to provide additional useful information. Three aspects are recommended in particular:

9.1 Fatigue tests on very thin section CT specimens could provide useful data with very economical tests. Some improvement is required in the method of buckling constraint, and it is suggested that particular attention should be paid to the method of lubrication of anti-buckling plates. More detailed examination of the conditions for the onset of buckling would also be of interest.

9.2 The use of statistical methods in predicting the relative contributions of two mechanisms was discussed in some detail. This type of analysis could be pursued further and the method may also be adopted to analyse fatigue crack growth threshold behaviour.

9.3 The general method of crack resistance addition may apply to any form of multi-mechanism crack propagation. Its application to creep-fatigue, corrosion-fatigue or stress corrosion cracking may yield better quantitative analyses than present methods.

PUBLICATIONS

1. RHODES, D., & RADON, J.C.

"Fracture analysis of exfoliation in an aluminium alloy",

Engineering Fracture Mechanics, 10 (1978) 843-853.

2. RHODES, D., & RADON, J.C.

"A dual mechanism model for environmental crack propagation",

International Journal of Fracture, 15 (1979) R65-R67.

3. RHODES, D., & RADON, J.C.

"Environmental effects on crack propagation in aluminium alloys",

Fatigue of Engineering Materials and Structures, 1 (1979) 383-393.

* 4. RHODES, D., RADON, J.C., & CULVER, L.E.

"Cyclic and monotonic crack propagation in a high toughness aluminium alloy",

International Journal of Fatigue, 2 (1980) 61-67.

* 5. RHODES, D., & RADON, J.C.

"The geometry dependence of K_c - a request for data",

International Journal of Fracture, 16 (1980) R169-R170.

* 6. RHODES, D., CULVER, L.E., & RADON, J.C.

"The influence of fracture mode transition on the compliance of thin section fracture specimens",

Proc. 3rd European Colloquium on Fracture (ECF3), (ed. J.C. Radon), Pergamon Press (1980).

* 7. RHODES, D., CULVER, L.E., & RADON, J.C.

"Application of combined static and fatigue crack growth data in structural assessment",

Proc. Conf. "Fatigue '81", (eds. J. Sturgeon & F. Sherratt), IPC Business Press (1981).

* 8. RHODES, D., RADON, J.C., & CULVER, L.E.

"The effect of secondary test variables on fatigue crack growth",

To be presented at ASTM Symposium, Los Angeles (1981).

* 9. RHODES, D., RADON, J.C., & CULVER, L.E.

"Analysis of combined static and fatigue crack growth data",

To be published in *Fatigue of Engineering Materials & Structures*.

10. RHODES, D.

"Fracture of multiple load path structures",

To be presented at the Institute of Physics, London (1981).

11. RHODES, D., & RADON, J.C.

"The influence of crack tip morphology on crack growth rates in corrosive environments",

Corrosion Science, 21 (1981) 381-389.

12. RADON, J.C., RHODES, D., & MUSUVA, J.K.

"The significance of stress corrosion cracking in corrosion fatigue crack growth",

To be published in *Engineering Fracture Mechanics*.

---

* Papers related directly to this project.

BIBLIOGRAPHY

[1] PAYNE, A.O. (1976)
The fatigue of aircraft structures,
Engineering Fracture Mechanics, 8, 157-203.

[2] RAMSDEN, J.M. (1978)
Help for the aged airliner,
Flight International, 8 July 1978, 87-90.

[3] LAMBERT, J.A.B., & TROUGHTON, A.J. (1967)
The importance of service inspection in aircraft fatigue,
Proc. 5th ICAF Symposium, Melbourne (ed. Mann & Milligan),
Aircraft Fatigue, Pergamon Press.

[4] RAMSDEN, J.M. (1980)
The inspectable aeroplane,
Proc. Convention on Long Life Aircraft Structures, Royal
Aeronautical Society, London.

[5] BROEK, D. (1974)
Elementary Engineering Fracture Mechanics, Noordhof Publishing.

[6] KNOTT, J.F. (1973)
Fundamentals of Fracture Mechanics, Butterworths.

[7] TURNER, C.E. (1975)
Yielding fracture mechanics,
J. Strain Analysis, 10, 207-216.

[8] ROOKE, D.P., & CARTWRIGHT, D.J. (1976)
A Compendium of Stress Intensity Factors, HMSO, London.

[9] HEYER, R.H. (1973)
Crack growth resistance curves (R-curves) - literature review,
ASTM STP 527, 3-16.

[10] KRAFFT, J.M., SULLIVAN, A.M., & BOYLE, R.W. (1961)
Proc. Symposium on Crack Propagation, Cranfield, 1, 8-26.

[11] BROEK, D. (1966)
The effect of finite specimen width on the residual strength of light alloy sheet,
NLR TRM2152, National Aerospace Laboratory, Amsterdam.

[12] SCHWALBE, K.H., & SETZ, W. (1980)
R-curves evaluation for centre-cracked panels,
Proc. 3rd European Colloquium on Fracture (ECF3), London (ed. Radon), Fracture and Fatigue, Pergamon Press, 277-285.

[13] PARIS, P.C., & ERDOGAN, F. (1963)
Critical analysis of crack propagation laws,
Trans. ASME, J. Basic Engineering, 85, 528-534.

[14] FROST, N.E., & DUGDALE, D.S. (1958)
The propagation of fatigue cracks in sheet specimens,
J. Mechanics & Physics of Solids, 6, 92-

[15] FORMAN, R.G., KEARNEY, V.E., & ENGLE, R.M. (1967)
Numerical analysis of crack propagation in cyclic-loaded structures,
Trans. ASME, J. Basic Engineering, 89, 459-464.

[16] PEARSON, S. (1969)
The effect of mean stress on fatigue crack propagation in half inch (12.7 mm) thick specimens,
TR68297 and TR69195, Royal Aircraft Establishment, Farnborough.

[17] WALKER, K. (1970)
The effect of stress ratio during crack propagation and fatigue in 2024-T3 and 7075-T6 aluminium,
ASTM STP 462, 1-14.

[18] CRAIG, L.E., & GORANSON, U.G. (1979)
Airworthiness assessment of Boeing jet transport structures,
10th ICAF Symposium, Brussels.

[19] WILHEM, D.P. (1970)
Fracture mechanics guidelines for aircraft structural applications, AFFDL-TR-111.

[20] LIEBOWITZ, H. (ed.) (1974)
Fracture mechanics in aircraft structures,
AGARDograph AG-176.

[21] ESDU (1980)
Estimation of fatigue crack growth rates and residual strength of components using linear elastic fracture mechanics,
Data Item 80036, Engineering Sciences Data Unit, London.

[22] CARTWRIGHT, D.J., & ROOKE, D.P. (1974)
Approximate stress intensity factors compounded from known solutions,
Engineering Fracture Mechanics, 6, 563-571.

[23] RHODES, D. (1981)
Paper to be presented at Institute of Physics meeting, London.

[24] FORSYTH, P.J.E. (1963)
Fatigue damage and crack growth in aluminium alloys,
Acta Metallurgica, 11, 703-715.

[25] BROEK, D. (1974)
Some contributions of electron fractography to the theory of fracture,
Int. Met. Reviews, 19, 135-182 (Review No. 185).

[26] NIX, K.J. (1980)
PhD Thesis, Department of Metallurgy & Materials Science, Imperial College, University of London.

[27] McEVILY, A.J., & BOETTNER, R.C. (1963)
On fatigue crack propagation in FCC metals,
Acta Metallurgica, 11, 725-743.

[28] SCHWALBE, K.H. (1979)
Some properties of stable crack growth,
Engineering Fracture Mechanics, 11, 331-342.

[29] RICE, J.R. (1966)
Mechanics of crack tip deformation and extension by fatigue,
ASTM STP 415, 247-309.

[30] LAIRD, C., & SMITH, G.C. (1962)
Crack propagation in high-stress fatigue,
Phil. Mag., 7, 847-857.

[31] TOMKINS, B. (1980)
Micromechanisms of fatigue crack growth at high stress,
Proc. Conference on Micromechanisms of Crack Extension, Metals Society, Cambridge.

[32] KIRBY, B.R., & BEEVERS, C.J. (1979)
Slow fatigue crack growth and threshold behaviour in air and vacuum of commercial aluminium alloys,
J. Fatigue of Engineering Materials & Structures, 1, 203-215.

[33] YOKOBORI, T., & SATO, K. (1976)
The effect of frequency on fatigue crack propagation rate and striation spacing on 2024-T3 aluminium alloy and SM-50 steel,
Engineering Fracture Mechanics, 8, 81-88.

[34] HERTZBERG, R.W. (1979)
On the relationship between fatigue striation spacing and stretch zone width,
Int. J. Fracture, 15, R69-R72.

[35] e.g. PASCOE, K.J. (1972)
in An Introduction to the Properties of Engineering Materials,
2nd edition, Chapter 10, Van Nostrand Reinhold, London.

[36] TIPPER, C.F. (1949)
The fracture of metals,
Metallurgia, 39, 133-137.

[37] PUTTICK, K.E. (1959)
Ductile fracture of metals,
Phil. Mag., 4, 964-969.

[38] GURLAND, J., & PLATEAU, J. (1963)
The mechanism of ductile rupture of metals containing inclusions,
Trans. American Society of Metals, 56, 442-454.

[39] KRAFFT, J.M. (1963)
Applied Materials Research, 3, 88.

[40] HERTZBERG, R.W., & MILLS, W.J. (1976)
Character of fatigue fracture surface micro-morphology in the ultra-low growth rate régime,
ASTM STP 600.

[41] NIX, K.J., & FLOWER, H.M. (1981)
The use of electron optical techniques in the study of fatigue in the high strength aluminium alloy, 7010.
Proc. Conference "Fatigue '81", Society of Environmental Engineers, IPC Press, 117-121.

[42] VOSIKOVSKY, O. (1975)
Fatigue crack growth in an X-65 line pipe steel at low cyclic frequencies in aqueous environments,
Trans. ASME, J. Engineering Materials, 95, 298-304.

[43] RHODES, D., & RADON, J.C. (1979)
Environmental effects on crack propagation in aluminium alloys,
J. Fatigue of Engineering Materials & Structures, 1, 383-393.

[44] BRANCO, C.M. (1976)
PhD Thesis, Department of Mechanical Engineering, Imperial College, University of London.

[45] BRADSHAW, F.J., & WHEELER, C. (1969)
The influence of gaseous environments and fatigue frequency on the growth of cracks in some aluminium alloys,
Int. J. Fracture Mechanics, 5, 255-268.

[46] HARTMAN, A., & SCHIJVE, J. (1970)
The effects of the environment and load frequency on the crack propagation law for macro-fatigue crack growth,
Engineering Fracture Mechanics, 1, 615-631.

[47] BORODACHEV, N.M., & MALASHENKOV, S.P. (1977)
The effect of loading frequency on the growth rate of fatigue cracks,
Russian Engineering J., 7, 24-26 (*Trans. Vestnik Mashinostroeniya*, 57, 33-36).

[48] VARLEY, P.C. (1970)
The Technology of Aluminium and Its Alloys, Newnes-Butterworths Publishers, London.

[49] WOODWARD, A.R. (1980)
Future uses of aluminium alloys,
Proc. I. Mech. E., 194, No. 14.

[50] BUCCI, R.J. (1979)
Selecting aluminium alloys to resist failure by fracture mechanisms,
Engineering Fracture Mechanics, 12, 407-441.

[51] STALEY, J.T. (1976)
Microstructure and toughness of high strength aluminium alloys,
ASTM STP 605, 71-96.

[52] REYNOLDS, M.A., FITZSIMMONS, P.E., & HARRIS, J.G. (1976)
Presentation of properties of a new, high strength aluminium alloy, designated 7010,
Proc. Symposium on Aluminium Alloys for the Aircraft Industry, Turin Publications: Technicopy, London.

[53] WELLS, R.R. (1975)
New alloys for advanced fighter wing structures,
AIAA J. of Aircraft, 12, 586-592.

[54] SPEIDEL, M.O., & HYATT, M.V. (1972)
Stress corrosion cracking of high strength aluminium alloys,
in Advances in Corrosion Science and Technology, 2 (eds. Fontana & Staehle), Plenum, New York.

[55] QUIST, W.E., HYATT, M.V., & ANDERSON, W.E. (1976)
Discussion of reference [51],
ASTM STP 605, 96-103.

[56] VAN ORDEN, J.M., KRUPP, W.E., WALDEN, E., & RYDER, J.T. (1979)
Effects of purity on fatigue and fracture of 7XXX-T76511 aluminium extrusion,
AIAA J. of Aircraft, 16, 327-333.

[57] SCHULTE, K., TRAUTMANN, K.-H., & NOWACK, H. (1980)
Influence of microstructure of high strength aluminium alloys on fatigue crack propagation under variable amplitude loading,
Proc. Conference on Analytical and Experimental Fracture Mechanics, Rome.

[58] WANHILL, R.J.H., T'HART, W.G.J., & SCHRA, L. (1979)
Flight simulation fatigue crack propagation in 7010 and 7075 aluminium plate,
Int. J. Fatigue, 1, 205-209.

[59] WANHILL, R.J.H.

Private communication (NLR, Amsterdam).

[60] FU-SHIONG LIN & STARKE, E.A., Jr. (1980)

The effect of copper content and re-crystallisation on the fatigue resistance of 7XXX type aluminium alloys,

Mat. Sci. & Engineering, 43, 65-76.

[61] KRAFFT, J.M., & CULLEN, W.H., Jr. (1979)

Organisational scheme for corrosion fatigue crack propagation,

Engineering Fracture Mechanics, 10, 609-650.

[62] KRAFFT, J.M. (1980)

Case studies of fatigue crack growth, using an improved micro-ligament instability model,

NRL Memorandum Report No. 4161, Naval Research Laboratory, Washington, D.C.

[63] DUGGAN, T.V. (1974)

A theory for fatigue crack propagation,

Symposium on Mechanical Behaviour of Materials, Kyoto, Japan.

[64] NEUBER, H. (1961)

Theory of stress concentration for shear strained prismatical bodies with arbitrary, non-linear stress-strain law,

J. Applied Mechanics, 28, 544-550.

[65] COFFIN, L.F. (1963)

Low cycle fatigue,

Metals Eng. Quarterly, 3, 15-24.

[66] KANNINEN, M.F., & ATKINSON, C. (1980)

Application of an inclined strip yield crack tip plasticity model to predict constant amplitude fatigue crack growth,

Int. J. Fracture, 16, 53-69.

[67] TURNER, C.E. (1978)
Internal memorandum, Imperial College, London.

[68] ELBER, W. (1971)
The significance of crack closure,
ASTM STP 486, 230-242.

[69] VAZQUEZ, J.A., MORRONE, A., & ERNST, H. (1979)
Experimental results on fatigue crack closure for two aluminium alloys,
Engineering Fracture Mechanics, 12, 231-240.

[70] BROWN, R.D., & WEERTMAN, J. (1978)
Mean stress effects on crack propagation rate and crack closure in 7050-T76 aluminium alloy,
Engineering Fracture Mechanics, 10, 757-771.

[71] CLERIVET, A., & BATHIAS, C. (1979)
Study of crack tip opening under cyclic loading, taking into account the environment and R ratio,
Engineering Fracture Mechanics, 12, 599-611.

[72] ELBER, W. (1976)
Equivalent amplitude concept for crack growth under spectrum loading,
ASTM STP 595, 236-250.

[73] SCHIJVE, J. (1976)
Observations on the prediction of fatigue crack propagation under variable amplitude loading,
ASTM STP 595, 3-26.

[74] BATHIAS, C., & VANCON, M. (1978)
Mechanisms of overload effect on fatigue crack propagation in aluminium alloys,
Engineering Fracture Mechanics, 10, 409-418.

[75] B S I (1977)

Methods for plane strain fracture toughness of metallic materials, *BS.5447.*

[76] A S T M (1978)

Standard test method for plane strain fracture toughness of metallic materials,

Std. E399-78a.

[77] A S T M (1978)

Standard practice for plane strain fracture toughness of aluminium alloys,

Std. B645-78.

[78] B S I (1979)

Procedures for crack opening displacement (COD) testing,

BS.5762.

[79] A S T M (1978)

Tentative recommended practice for R-curve determination,

Std. E561-78T.

[80] A S T M (1978)

Standard practice for fracture toughness testing of aluminium alloys,

Std. B646-78.

[81] A S T M (1978)

Tentative test method for constant amplitude fatigue crack growth rates above 10^{8} m/cycle,

Std. E647-78T.

[82] GREEN, G., & WILLOUGHBY, A. (1980)

Resistance to ductile tearing of structural steel in three- and four-point bending,

Proc. 3rd European Colloquium on Fracture (ECF3), London (ed. Radon), Fracture and Fatigue, Pergamon Press.

[83] RADON, J.C. (1980)
Fatigue crack growth in polymers,
Int. J. Fracture, 16, 533-552.

[84] MOSTOVOY, S., CROSLEY, P.B., & RIPLING, E.J. (1967)
Use of crack line loaded specimens for measuring plane strain fracture toughness,
J. Materials, 2, 661-681.

[85] KENYON, J.M. (1976)
PhD Thesis, Department of Mechanical Engineering, Imperial College, University of London.

[86] COTTRELL, B. (1970)
On fracture path stability in the compact tension test,
Int. J. Fracture Mechanics, 6, 189-192.

[87] DIXON, J.R., & STRANNIGAN, J.S. (1969)
Stress distribution and buckling in thin sheets with central slits,
in Fracture 1969, Chapman & Hall, 105-108.

[88] FREED, C.N., & KRAFFT, J.M. (1966)
Effect of side-grooving on measurements of plane strain fracture toughness,
J. Materials, 1, 770-790.

[89] BRADSHAW, F.J., & WHEELER, C. (1974)
The crack resistance of some aluminium alloys and the prediction of thin section failure,
Technical Report TR73191, Royal Aircraft Establishment, Farnborough.

[90] WHEELER, C.
Private communication, Royal Aircraft Establishment, Farnborough.

[91] LAMBERT, J.A.B.
Private communication, British Aerospace, Hatfield.

[92] BROWN, W.F., & SRAWLEY, J.E. (1966)
Plane strain crack toughness testing of high strength metallic materials,
ASTM STP 410.

[93] TURNER, C.E. (1980)
Use of the *R*-curve for design with contained yield,
Proc. 3rd European Colloquium on Fracture (ECF3), London (ed. Radon), Fracture and Fatigue, Pergamon Press.

[94] MUSUVA, J.K. (1980)
PhD Thesis, Department of Mechanical Engineering, Imperial College, University of London.

[95] TIMOSHENKO, S.P., & GERE, J.M. (1961)
Theory of Elastic Stability, Chapter 9, McGraw-Hill, New York.

[96] OBERPARLEITER, W., & KURTH, U. (1980)
Some experience in *R*-curve technique,
Proc. 3rd European Colloquium on Fracture (ECF3), London (ed. Radon), Fracture and Fatigue, Pergamon Press.

[97] SIMPSON, A. (1976)
Evaluation of material properties of aluminium alloy X166 (DTD.5120) in sheet and plate form,
Report No. HSA-MSM-R-GEN-0291, Hawker Siddeley Aviation Limited, Manchester.

[98] RHODES, D. (1976)
BSc Special Task Report, Department of Mechanical Engineering, Imperial College, University of London.

[99] DRUCE, S.G., BEEVERS, C.J., & WALKER, E.F. (1979)
Fatigue crack growth retardation following load reduction in a plain C-Mn steel,
Engineering Fracture Mechanics, 11, 385-395.

[100] SANDOR, B.I. (1972)
Fundamentals of Cyclic Stress and Strain, University of Wisconsin Press.

[101] LOW, K.B. (198)
BSc Special Task Report, Department of Mechanical Engineering, Imperial College, University of London.

[102] MANSON, S.S. (1965)
Fatigue - a complex subject - some simple approximations, *Experimental Mechanics*, 5, 193-226.

[103] CRUICKSHANKS-BOYD, D.W. (1976)
A comparison of fatigue crack growth rates as determined by striation measurement and by observations of crack length on the specimen surface during test,
Technical Report No. TR76012, Royal Aircraft Establishment, Farnborough.

[104] ALBERTIN, L., & HUDAK, S.J. (1980)
The effect of compressive loading on fatigue crack growth rate and striation spacing in 2219-T851 aluminium alloy,
Westinghouse Report.

[105] FORD, F.P. (1979)
Corrosion fatigue crack propagation in aluminium-7% magnesium alloy, *Trans. NACE, Corrosion*,

[106] MACKAY, T.L. (1979)
Fatigue crack propagation at low ΔK of two aluminium alloy sheets, 2024-T3 and 7075-T6,
Engineering Fracture Mechanics, 11, 753-761.

[107] KRAFFT, J.M. (1980)
Private communication, Naval Research Laboratory, Washington, D.C.

[108] ORANGE, T.W. (1980)
On the equivalence between semi-empirical fracture analyses and R-curves,
ASTM STP 700, 478-499.

[109] ORANGE, T.W. (1980)
A relation between semi-empirical fracture analyses and R-curves,
NASA Technical Paper 1600.

[110] ORANGE, T.W. (1980)
Method for estimating crack extension resistance curve from residual strength data,
NASA Technical Paper 1753.

[111] KIRKBY, W.T., & ROOKE, D.P. (1977)
A fracture mechanics study of the residual strength of pin-lug specimens,
Proc. Conference on Fracture Mechanics in Engineering Practice,
Institute of Physics (ed. Stanley), Applied Science Publishers.

[112] WEBBER, D. (1977)
Damage tolerance of military bridges,
Proc. Conference on Fracture Mechanics in Engineering Practice,
Institute of Physics (ed. Stanley), Applied Science Publishers.

[113] SULLIVAN, A.M., & STOOP, J. (1974)
Further aspects of fracture resistance measurement,
ASTM STP 559, 99-110.

[114] SULLIVAN, A.M., & FREED, C.N. (1971)
The influence of geometric variables on K_c values for two thin sheet aluminium alloys,
NRL Report 7270, Naval Research Laboratory, Washington, D.C.

[115] KAUFMANN, J.G. (1967)
Fracture toughness of 7075-T6 and -T651 sheet, plate and multi-layered adhesive-bonded panels,
Trans. ASME, J. Basic Engineering, 89, 503-507.

[116] WHEELER, C., WOOD, R.A., & BRADSHAW, F.J. (1974)
Some crack resistance curves for thin sheet compact tension specimens of aluminium alloys,
Technical Report No. TR74086, Royal Aircraft Establishment, Farnborough.

[117] HEYER, R.H., & McCABE, D.E. (1972)
Plane stress fracture toughness testing, using a crack line loaded specimen,
Engineering Fracture Mechanics, 4, 393-412.

[118] BROEK, D., & SCHIJVE, J. (1963)
The influence of mean stress on the propagation of fatigue cracks in aluminium alloy sheet,
NLR-TR-M2111, National Aerospace Laboratory, NLR, Amsterdam.

[119] ANSTEE, R.F.W., & MORROW, SARAH M. (1979)
The effects of biaxial loading on the propagation of cracks in integrally stiffened panels,
Proc. 10th ICAF Symposium, Brussels.

[120] HOPPER, C.D., & MILLER, K.J. (1977)
Fatigue crack propagation in biaxial stress fields,
J. Strain Analysis, 12, 23-28.

[121] KITAGAWA, H., YUUKI, R., & TOHGO, K. (1980)
A fracture mechanics approach to high-cycle fatigue crack growth under in-plane biaxial loads,
J. Fatigue of Engineering Materials & Structures, 2, 195-206.

[122] LEEVERS, P.S. (1979)
PhD Thesis, Department of Mechanical Engineering, Imperial College, University of London.

[123] FRANCIS, A.J. (1953)
The behaviour of Al-alloy rivetted joints,
Aluminium Development Association Research Report No. 15.

[124] BROEK, D., NEDEVEEN, A., & MEULMAN, A. (1971)
Applicability of fracture toughness data to surface flaws and to corner cracks at holes,
NLR-TR-71033U, National Aerospace Laboratory, NLR, Amsterdam.

[125] RHODES, D. (1977)
Report No. HST-N-GEN-510084, Hawker Siddeley Aviation Limited, Hatfield (Company Internal Document).

[126] JOHNSON, W.S. (1979)
Prediction of constant amplitude fatigue crack propagation with surface flaws,
ASTM STP 687, 143-155.

[127] SHAH, R.C., & KOBAYASHI, A.S. (1972)
Stress intensity factor for an elliptical crack approaching the surface of a plate in bending,
ASTM STP 513, 3-21.

[128] HALL, L.R., SHAH, R.C., & ENGSTROM, W.L. (1974)
Fracture and fatigue crack growth behaviour of surface flaws originating at fastener holes,
AFFDL-TR-74-47, Air Force Flight Dynamics Laboratory, Wright Patterson AFB, Ohio.

[129] BOWIE, O.L. (1956)
J. Mathematical Physics, 35, 60.

[130] E S D U (1977)

Fatigue life estimation under variable amplitude loading,

Data Item 77004, Engineering Sciences Data Unit, London.

[131] RITCHIE, R.O. (1981)

Discussion at SEE Conference, "Fatigue '81", Warwick University.

[132] SCOTT, P.M. (1980)

Discussion at UKOSRP meeting, Harwell.

[133] RHODES, D. (1978)

in Stress Office File SO/COMP/623, British Aerospace, Hatfield.

[134] RHODES, D. (1981)

in Stress Office (Fatigue Section) File V34, British Aerospace, Hatfield.

[135] SRAWLEY, J.E. (1976)

Wide range stress intensity factor expressions for ASTM method E399 standard specimens,

Int. J. Fracture, 12, 475-476.

[136] SAXENA, A., & HUDAK, S.J. (1978)

Review and extension of compliance information for common crack growth specimens,

Int. J. Fracture, 14, 453-468.

[137] ISIDA, M. (1971)

Effect of width and length on stress intensity factors of internally cracked plates,

Int. J. Fracture Mechanics, 7, 301-316.

[138] BRITISH AEROSPACE (1973)

Fatigue Data Sheet HFS/N3, British Aerospace, Hatfield.

[139] E S D U (1969)

Elastic stress concentration factors: geometric discontinuities in flat bars or strips,

Data Item No. 69020, Engineering Sciences Data Unit, London.

APPENDIX I

STRESS INTENSITY AND COMPLIANCE RELATIONSHIPS FOR CT AND CCT TEST SPECIMENS

I.1 COMPACT TENSION SPECIMENS

Calculations for CT'A' compact tension specimens are based on Srawley's [135] wide range formula, as quoted in ASTM Standard E647 [81], i.e.

$$\Delta K = \frac{\Delta P}{B\sqrt{W}} \frac{(2+a/W)}{(1-a/W)^{1\cdot5}} \left[0.886 + 4.64 \left(\frac{a}{W}\right) - 13.32 \left(\frac{a}{W}\right)^2 + 14.72 \left(\frac{a}{W}\right)^3 - 5.6 \left(\frac{a}{W}\right)^4\right]$$

$$\text{for } a/W \geq 0.2$$

In calculating the geometry characteristic Γ, as defined in Section 6.6, this equation is differentiated as follows. Writing $\Delta K = \Delta L\, f(a)$, in which $\Delta L = \Delta P/B$:

$$f'(a) = W^{-1\cdot5} \left\{\left[\frac{1}{(1-a/W)^{1\cdot5}} + \frac{3}{2} \frac{(2+a/W)}{(1-a/W)^{2\cdot5}}\right] (0.886 + \ldots, \text{ etc.}) \right.$$

$$\left. + \frac{(2+a/W)}{(1-a/W)^{1\cdot5}} \left[4.64 - 26.64 \left(\frac{a}{W}\right) + 44.16 \left(\frac{a}{W}\right)^2 - 22.4 \left(\frac{a}{W}\right)^3\right]\right\}$$

Then $\Gamma/W = f(a)/f'(a)$, as shown in Figure I.1.

For the CT'B' specimen, which does not meet ASTM standards, a curve may be fitted through Bradshaw & Wheeler's [89] experimental data, i.e.

$$\Delta K = \frac{\Delta P}{B\sqrt{W}} \frac{(2+a/W)}{(1-a/W)^{1\cdot5}} \left[0.918 + 2.16 \left(\frac{a}{W}\right) - 4.05 \left(\frac{a}{W}\right)^2 + 1.73 \left(\frac{a}{W}\right)^3 + 1.21 \left(\frac{a}{W}\right)^4\right]$$

This gives values within 1.5% of the experimental data, within the range $0.2 \leq a/W \leq 0.6$. The geometry characteristic is determined in the same way as for the CT'A' specimen:

$$f'(a) = W^{-1\cdot5}\left\{\left[\frac{1}{(1-a/W)^{1\cdot5}} + \frac{3}{2}\frac{(2+a/W)}{(1-a/W)^{2\cdot5}}\right](0.918 + \ldots, \text{ etc.}) + \frac{(2+a/W)}{(1-a/W)^{1\cdot5}}\left[2.16 - 8.10\left(\frac{a}{W}\right) + 5.19\left(\frac{a}{W}\right)^2 + 4.84\left(\frac{a}{W}\right)^3\right]\right\}$$

For the *R*-curve testing, a relationship is required between specimen compliance, C_s, and crack length for an ideal linear elastic case. Saxena & Hudak [136] give such data for the CT'A' specimen, i.e. for long cracks:

$$EBC_s = \frac{16}{(1-a/W)} - \frac{24}{(1-a/W)} - 4.5\ ln\ (1-a/W) + 18.71$$

This is shown compared with measured values in Figure I.2.

Correspondingly:

$$\frac{a}{W} = 1.0002 - 4.0632\,u + 11.242\,u^2 - 106.04\,u^3 + 463.33\,u^4 - 650.68\,u^5$$

where:
$$u = \frac{1}{(1 + \sqrt{EBC_s})}$$

I.2 CENTRE-CRACKED TENSION SPECIMENS

Much of the data available in the literature are derived for centre-cracked tension (CCT) specimens, and a variety of formulae have been used in deriving these. To be consistent, any such data which have been used have been re-calculated (if possible) using Isida's [137] equation, i.e.

$$\Delta K = \Delta\sigma\sqrt{a\ F(2a/W)}$$

where: $F(2a/W) = 1.77\ [1 - 0.1\ (2a/W) + (2a/W)^2]$

Thus:

$$\frac{\Gamma}{W} = \frac{1.77\ [(a/W)^{0.5} - 0.1\ (2a/W)^{1.5} + (2a/W)^{2.5}]}{0.885\ (a/W)^{-0.5} - 0.751\ (a/W)^{0.5} + 24.03\ (a/W)^{1.5}}$$

This is shown in Figure I.3.

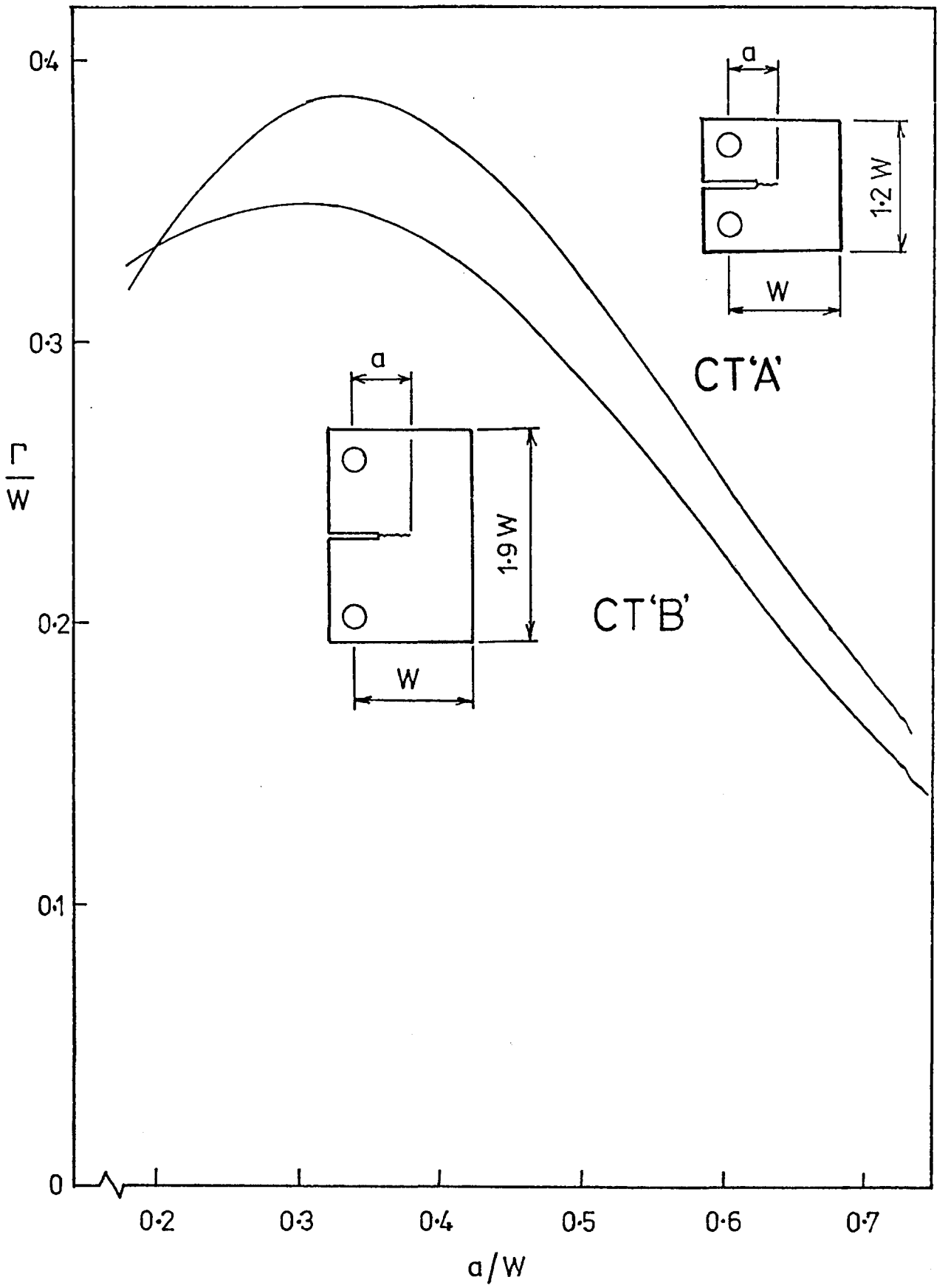


Figure I.1: Geometry characteristic for CT specimens

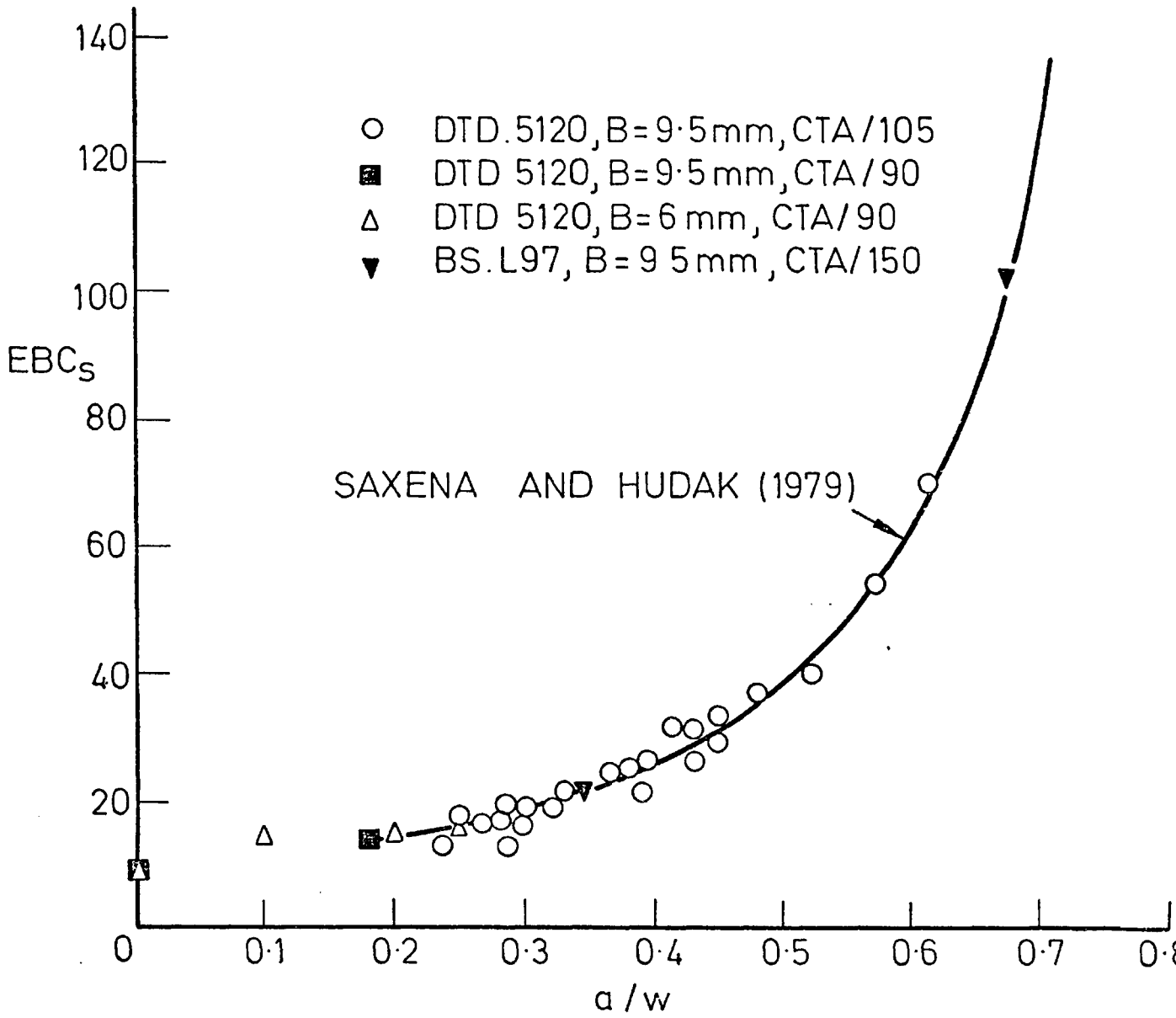


Figure I.2: Compliance of CT specimens

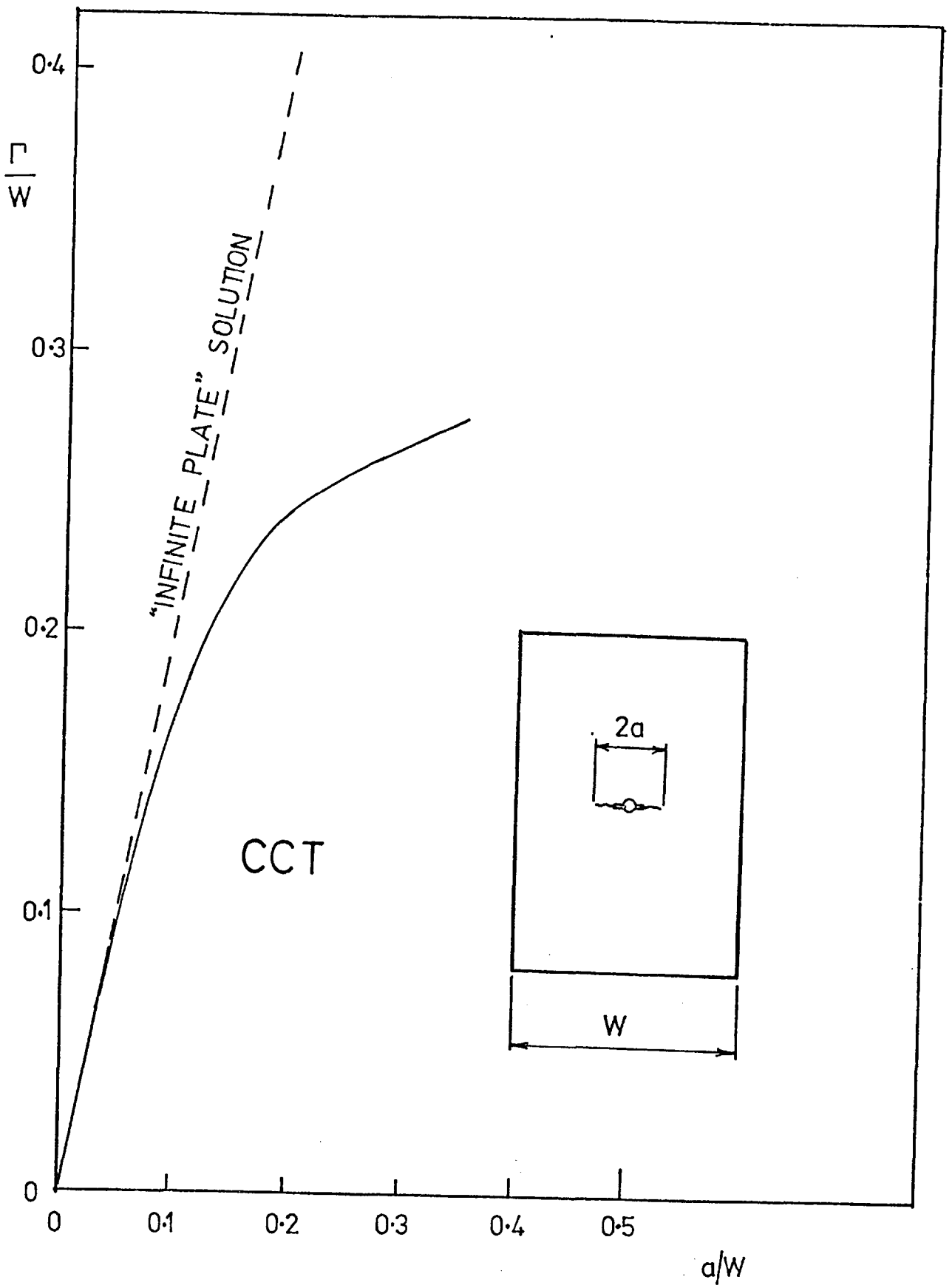


Figure I.3: Geometry characteristic for CCT specimen

APPENDIX II

NOMINAL STRESS DISTRIBUTION FOR CT SPECIMENS IN TENSION AND COMPRESSION

For the purposes of evaluating the validity of linear elastic fracture mechanics and for estimates of crack path stability, the nominal stress distribution in a specimen must be known. In tension-compression fatigue tests, this nominal distribution may be used to relate the crack tip stress ratio to the overall load ratio.

The nominal stress was estimated by using the simple beam approximation of Figures II.1 and II.2. This is expected to overestimate the peak stress, which is given by:

$$\sigma_{nom} = \frac{P}{A} + \frac{My}{I} \tag{II.1}$$

where the cross-sectional area, $A = B(W-a)$

the bending moment, $M = P\{a + (W-a)/2\}$

the second moment of area, $I = B(W-a)^3/12$

Thus, at the crack tip, where $y = (W-a)/2$

$$\sigma_{nom} = \frac{P}{B(W-a)} + \frac{P\{a+(W-a)/2\}(W-a)/2}{B(W-a)^3/12} \tag{II.2}$$

$$= \frac{P}{B}\frac{1}{(W-a)}\left[1 + \frac{3(W+a)}{(W-a)}\right] \tag{II.3}$$

$$\sigma_{nom} = \frac{2P(2W+a)}{B(W-a)^2} \tag{II.4}$$

When loaded in compression, the crack faces can support a load, and the stress distribution is determined by the notch length, a_o, rather than

the crack length, a. The crack tip now lies at $y = (W-a_o)/2-a$.

Equation (II.2) becomes:

$$\sigma_{nom} = \frac{P}{B(W-a_o)} + \frac{P\{a_o + (W-a_o)/2\}\{(W-a_o)/2-a\}}{B(W-a_o)^3/12} \qquad (II.5)$$

$$= \frac{P}{B}\frac{1}{(W-a_o)}\left[1 + \frac{3(W+a_o)(W-a_o-2a)}{(W-a_o)^2}\right] \qquad (II.6)$$

During tension-compression testing, the stress ratio, R, at the crack tip is given by:

$$R = \frac{\sigma_{nom}(min)}{\sigma_{nom}(max)} \qquad (II.7)$$

where $\sigma_{nom}(min)$ is calculated from P_{min} in equation (II.6) and $\sigma_{nom}(max)$ from P_{max} in equation (II.4). If the load ratio, R_p, is given by:

$$R_p \equiv \frac{P_{min}}{P_{max}} \qquad (II.8)$$

and the crack lengths are normalised against specimen width, W, then for all values of R and $R_p \leq 0$:

$$\frac{R}{R_p} = \frac{1+3(1-a_o/W)(1+a_o/W-2a/W)(1-a_o/W)^{-2}}{1+3(1+a_o/W)(1-a_o/W)^{-1}} \qquad (II.9)$$

For R, $R_p \geq 0$, of course, $R/R_p = 1$. Equation (II.9) is evaluated in Figure II.3 for a range of values, a_o/W.

Note that equation (II.9) becomes invalid if the crack tip stress is tensile under compressive loading. This occurs when:

$$\frac{\sigma_{nom}}{P} < 0 \qquad (II.10)$$

From (II.6), it may be shown that this occurs when:

$$\frac{a}{W} > \frac{2}{3}\left[\frac{1 + (a_o/W) + (a_o/W)^2}{1 + (a_o/W)}\right] \qquad \text{(II.11)}$$

and: $P < 0$

Typical values for the maximum permissible crack length under tension-compression loading are given in Table II.1.

TABLE II.1

Notch Length, a_o/W	Maximum Crack Length, a/W
0.2	0.689
0.3	0.712
0.4	0.743
0.5	0.778
0.6	0.817
0.7	0.859

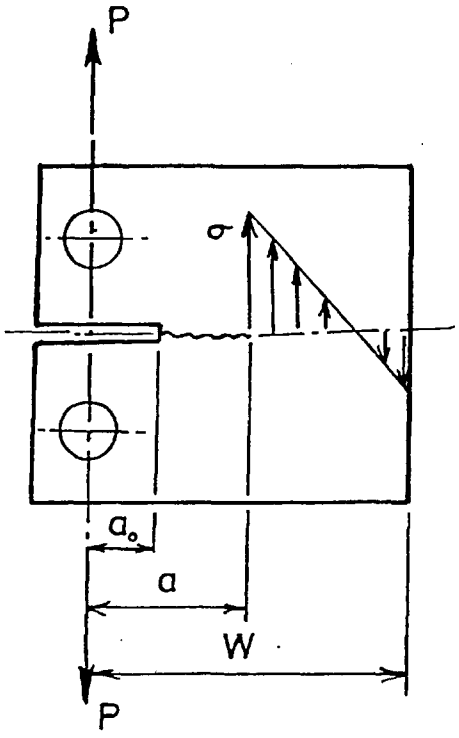


Figure II.1: Bending stresses in CT specimen

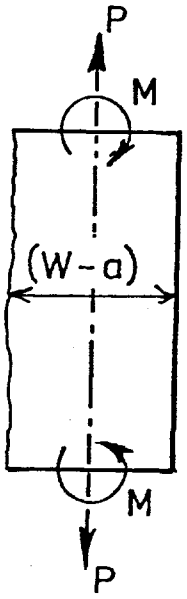


Figure II.2: Idealisation of back edge of specimen

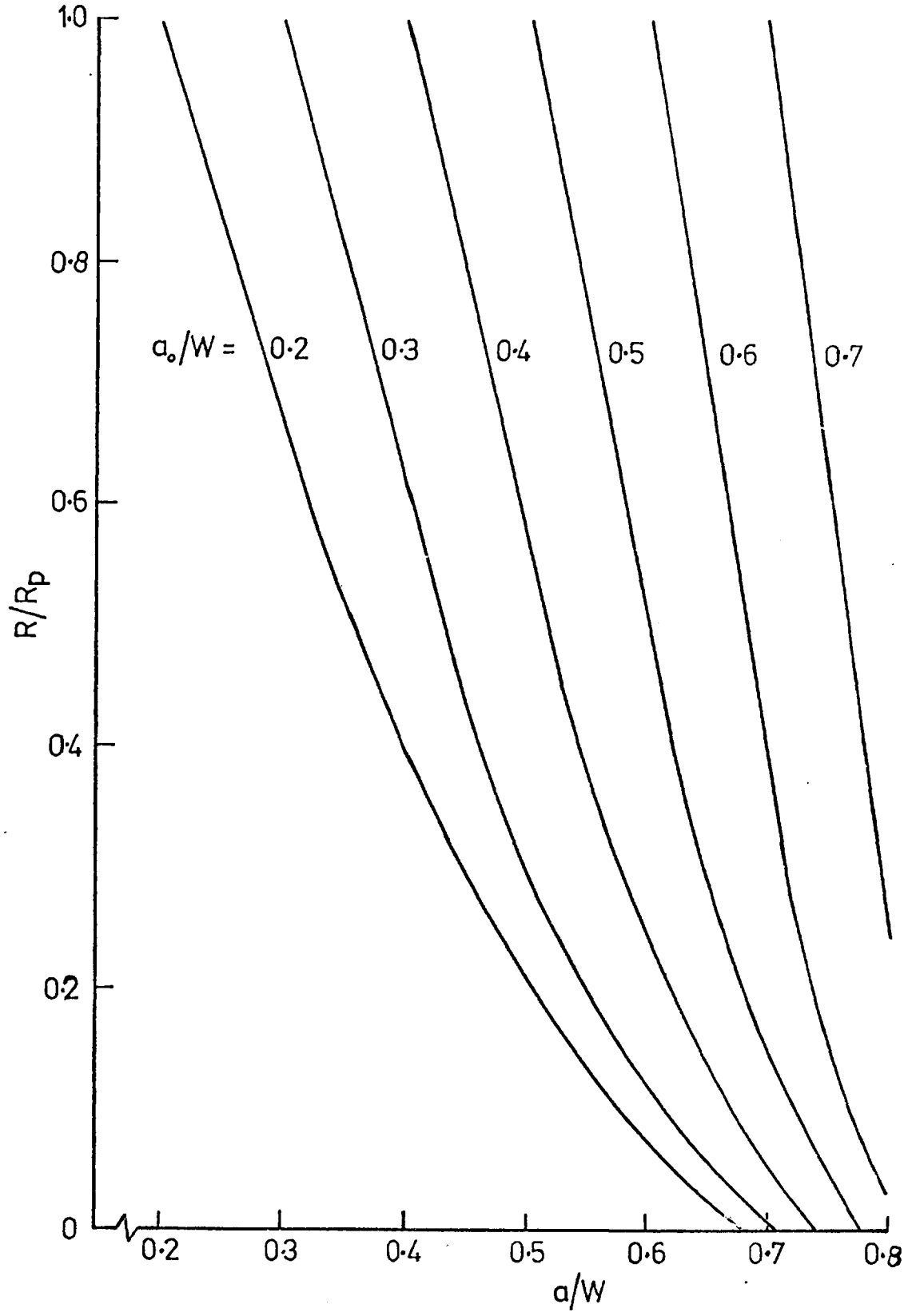


Figure II.3: Relationship between stress ratio and load ratio ($R < 0$) for CT specimens

APPENDIX III

PRE-CRACKING AND "STEPPING DOWN" IN FATIGUE TEST SPECIMENS

During fatigue pre-cracking and for a number of cycles after a reduction in load in a fatigue test, no useful data are obtained and it is desirable to minimise the time spent under these conditions. Care must be taken, however, to ensure that the subsequent crack growth behaviour is not affected.

Cracks in compact tension specimens were initiated at chevron saw-cuts, as described in Chapter 4. The notch is finished with a 'rough' cut using a junior hacksaw with a ground blade. Measurement of pre-cracking times is rather subjective, but they could be recorded as the time from the start of the test until a fatigue crack existed, suitable for taking crack growth readings. This time is shown in the form of an S-N curve in Figure III.1. Rather than the notch stress, which is not readily determined, the vertical axis is measured in terms of the maximum stress intensity at the end of the pre-cracking time.

There does not appear to be any significant variation in pre-cracking time with frequency or between materials. There is considerable scatter, which is partly attributable to the variation in notch geometry. Working back from the pre-cracking times and nominal stresses calculated from Appendix II, in conjunction with notched specimen S-N data [138], there is an implied elastic stress concentration factor in the range $10 \lesssim K_t \lesssim 20$. The corresponding figure for a machined notch [139] would be in the range $5 \leqslant K_t \leqslant 10$.

There is no effect on crack growth behaviour during the crack propagation test, provided that the maximum stress intensity factor during pre-cracking does not exceed that during the subsequent test. The minimum

pre-cracking time is thus achieved at the minimum possible load ratio. Some attempt was made to pre-crack specimens at R = -1, and it appears that this reduces the number of cycles required. The advantage is offset, however, by difficulties in running negative R tests at high frequencies.

Where it became necessary to reduce the maximum load during a test, efforts were made to avoid any loading history effects. Firstly, the reduction in maximum load was limited to a 10% step down. Secondly, crack growth immediately after the step was ignored for the purpose of the analysis. Two methods were used in order to estimate the point at which readings became valid:

i) The crack growth rate was calculated by extrapolating known data and readings were ignored until two successive readings were taken which were close to this value.

ii) The crack growth rate was considered invalid until a clear crack extension was observed ahead of the calculated total plastic zone size, r_p.

In practice, at low stress intensities, these two methods are both controlled by the resolution of the crack length measurement technique. With the travelling microscope, this is about 0.03 mm, which is equal to the total (plane strain) plastic zone at K_{max} = 11.4 MN/m$^{3/2}$.

Typical step-down times were of the order 10,000 cycles, with a tendency to longer times at lower stress intensities with the 10% step maintained.

As an example, one may ignore the crack growth during each step-down and assume 10,000 cycles per step. The pre-cracking time may be taken from the solid line in Figure III.1:

$$N, \text{ total time} = N_{pre\text{-}crack} + \sum_{o}^{X} N_{step\text{-}down} \qquad \text{(III.1)}$$

If the stress intensity at pre-cracking is K_{pc} and that at the beginning of the crack growth test is K, then for 10% a step-down:

$$(0.9)^X = \frac{K}{K_{pc}} \qquad \text{(III.2)}$$

i.e.
$$X = 22 \log \left(\frac{K_{pc}}{K}\right) \qquad \text{(III.3)}$$

Now, equation (III.1) becomes:

$$N = N_{pc} + 220000 \log \left(\frac{K_{pc}}{K}\right) \qquad \text{(III.4)}$$

This is plotted in Figure III.2, which shows that the minimum time is achieved with $K_{pc} \simeq 14$ MN/m$^{3/2}$. In practice, a figure of $K_{pc} \simeq 12$ MN/m$^{3/2}$ was used successfully for many tests.

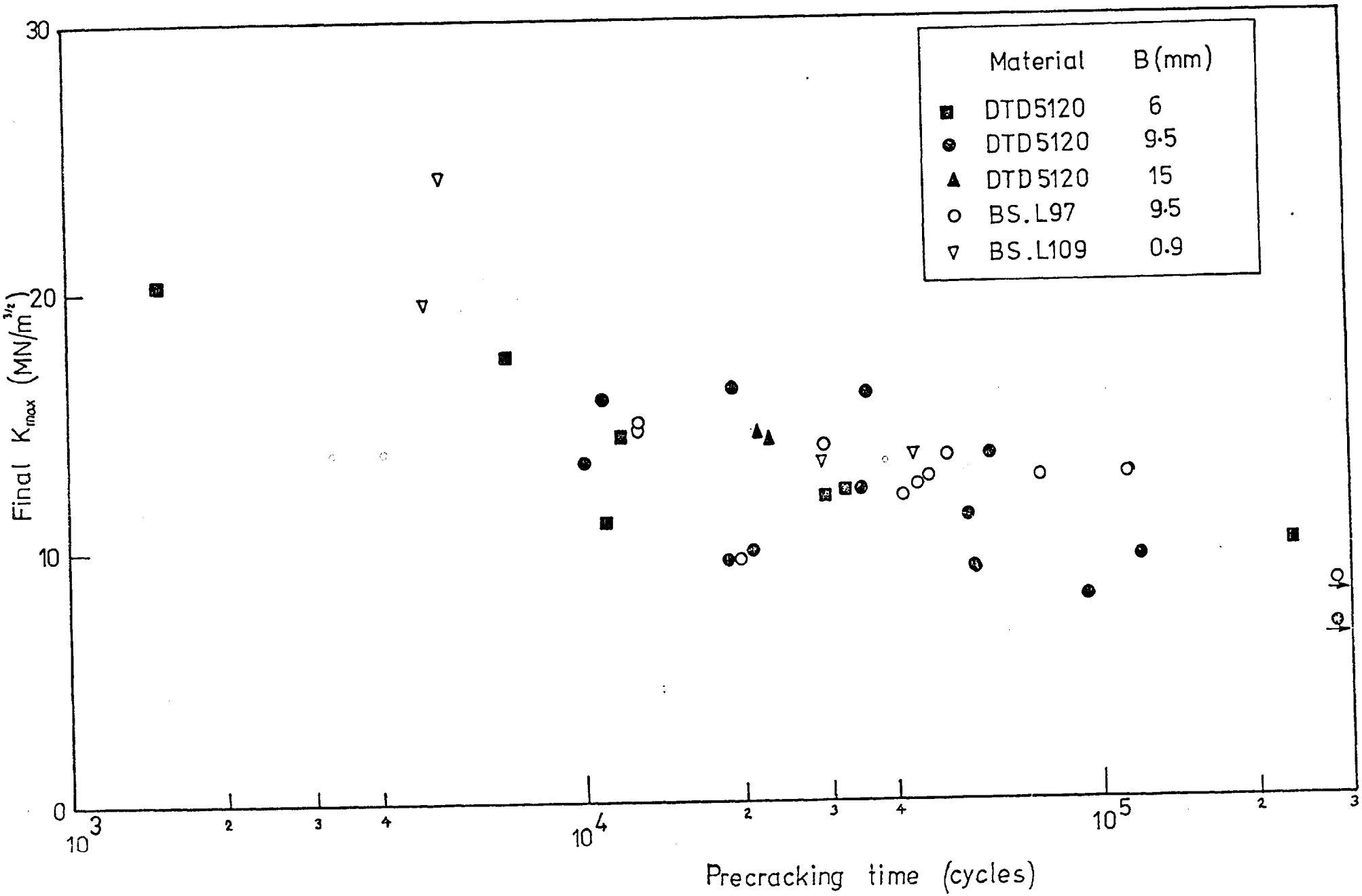


Figure III.1: Pre-cracking times

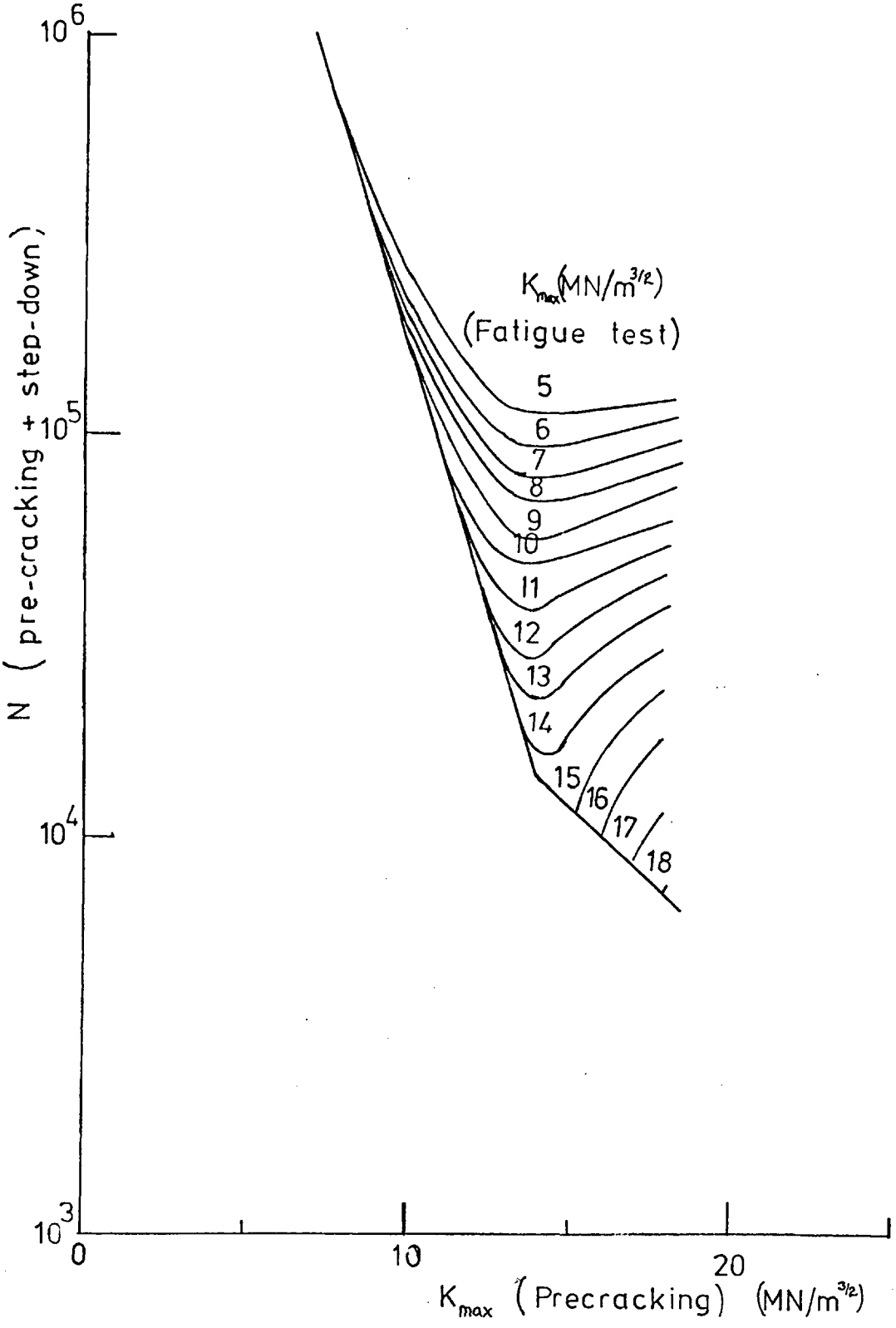


Figure III.2: Pre-cracking and step-down times

APPENDIX IV

CRACK RESISTANCE MODEL - NUMERICAL EVALUATION

The relationship between crack growth rate and stress intensity range is given by equation (6.41). For cyclic cases, using $Q.\Delta a = da/dN$:

$$(\Delta K)^2 = \left[\frac{x\ Q.\Delta a}{C_1}\right]^{2/m_1} + \left[\frac{(1-x)\ Q.\Delta a}{C_2}\right]^{2/m_2} \qquad \text{(IV.1)}$$

Initially, (ΔK) is tabulated for a range of values of $Q.\Delta a$ and x for each material. A logarithmic interpolation procedure is used to extract values of $(Q.\Delta a)$ for a range of ΔK and x from that table.

Final values of (da/dN) are estimated by each of the three methods of Section 6.4.

The crack growth rate is given by the mean value of $Q.\Delta a$ for all values of x at each value of ΔK, using a "trapezium rule" method. The percentage of the surface area over which striation markings are expected, $\%s$, is given by:

$$\%s = \frac{\text{mean value of } (x\ Q.\Delta a)}{\text{mean value of } (Q.\Delta a)} \qquad \text{(IV.2)}$$

Stress ratio effects were calculated as in Section 6.2.2.

All calculations were carried out on a Texas Instruments TI57 programmable calculator.

IV.1 DTD.5120 ALUMINIUM ALLOY AT 0.2 Hz

$$\text{Striation spacing} \quad , \quad \bar{s} = C_1\ (\Delta K)^{m_1}$$

For best fit through data of Section 5.2:

$$\bar{s} \simeq 10^{-4} \text{ mm} \quad \text{at} \quad \Delta K = 7.45 \text{ MN/m}^{3/2}$$

$$\bar{s} \simeq 10^{-3} \text{ mm} \quad \text{at} \quad \Delta K = 25.9 \text{ MN/m}^{3/2}$$

Hence, $C_1 = 2.44 \times 10^{-6}$, and $m_1 = 1.85$.

From the early (square fracture) part of the R-curve, using crack extension data from Section 5.3:

$$\Delta a = 0.185 \text{ mm} \quad \text{at} \quad K_R = 48.4 \text{ MN/m}^{3/2}$$

$$\Delta a = 1.85 \text{ mm} \quad \text{at} \quad K_R = 91.0 \text{ MN/m}^{3/2}$$

Hence, $C_2/Q = 1.25 \times 10^{-7}$, and $m_2 = 3.65$.

From Section 5.7:

$$Q = \frac{2^{n'+1}}{4} \left(\frac{\sigma_y}{\sigma'_y}\right) = 0.475$$

Therefore: $$C_2 = 5.94 \times 10^{-8}$$

These values of C_1, C_2, m_1 and m_2 are used to calculate data in Tables IV.1, IV.2 and IV.3.

For stress ratio effects, using equation (6.49) from Section 6.2.2, and $m_1 = 1.85$, $m_2 = 3.65$:

$$\eta = \frac{(1-R)^{2-m}\,(1-R^m)}{(1-R^2)} \qquad \text{(IV.3)}$$

Values of η are tabulated in Table IV.4.

IV.2 BS.L97 ALUMINIUM ALLOY AT 0.2 Hz

$$\text{Striation spacing} \quad , \quad \bar{s} = C_1 (\Delta K)^{m_1}$$

For best fit through data in Section 5.2:

$$\bar{s} \simeq 10^{-4} \text{ mm} \quad \text{at} \quad \Delta K = 7.94 \text{ MN/m}^{3/2}$$
$$\bar{s} \simeq 10^{-3} \text{ mm} \quad \text{at} \quad \Delta K = 20.89 \text{ MN/m}^{3/2}$$

Hence, $C_1 = 7.19 \times 10^{-7}$, and $m_1 = 2.38$.

From early part of R-curve (with negligible tunnelling):

$$\Delta a \simeq 0.185 \text{ mm} \quad \text{at} \quad K_R = 47.0 \text{ MN/m}^{3/2}$$
$$\Delta a \simeq 1.85 \text{ mm} \quad \text{at} \quad K_R = 84.3 \text{ MN/m}^{3/2}$$

Hence, $C_2/Q = 4.83 \times 10^{-8}$, and $m_2 = 3.94$.

From Section 5.7:

$$Q = \frac{2^{n'+1}}{4} \left(\frac{\sigma_y}{\sigma_y'}\right) = 0.403$$

Therefore: $$C_2 = 1.95 \times 10^{-8}$$

These values of C_1, C_2, m_1 and m_2 are used to evaluate Tables IV.5, IV.6 and IV.7.

Once again, stress ratio effect is from equation (IV.3) with $m_1 = 2.38$ and $m_2 = 3.94$, listed in Table IV.8.

IV.3 BS.L109 ALUMINIUM ALLOY AT 1 Hz

Striation spacing: there is no significant difference between striation spacing measurements in the BS.L97 and BS.L109 2024-T3 alloys. Thus, as for L97, $C_1 = 7.19 \times 10^{-7}$, and $m_1 = 2.38$.

There are no R-curve data for 0.9 mm thickness 2024-T3, but as the K_{eng_c} data are close to that obtained by Bradshaw & Wheeler [89] for 1.6 mm thick material, their R-curve data will be used. This gives:

$$\Delta a \simeq 0.9 \text{ mm} \quad \text{at} \quad K_R = 77 \text{ MN/m}^{3/2}$$
$$\Delta a \simeq 1.7 \text{ mm} \quad \text{at} \quad K_R = 100 \text{ MN/m}^{3/2}$$

(These data relate to slant fracture but, as much of the fatigue data are on a slant, this is relevant.) Thus, $C_2/Q = 1.98 \times 10^{-5}$, and $m_2 = 2.48$.

Using the same value for Q as for L97:

$$C_2 = 7.62 \times 10^{-6}$$

These values of C_1, C_2, m_1 and m_2 are used to evaluate data in Tables IV.9, IV.10 and IV.11.

Stress ratio effects are calculated from equation (IV.3) with $m_1 = 2.38$ and $m_2 = 2.48$, listed in Table IV.12.

TABLE IV.1

ΔK, K_R Values for DTD.5120

$Q.\Delta a$ \ x	0 (Tearing)	0.2	0.4	0.6	0.8	1.0 (Striations)
10^{-6}	2.17	2.05	1.92	1.75	1.50	0.617
3×10^{-6}	2.93	2.79	2.63	2.43	2.13	1.12
10^{-5}	4.07	3.93	3.77	3.56	3.24	2.14
3×10^{-5}	5.50	5.43	5.33	5.20	4.94	3.88
10^{-4}	7.65	7.85	8.05	8.21	8.23	7.45
3×10^{-4}	10.3	11.2	12.2	13.0	13.7	13.5
10^{-3}	14.4	17.3	20.1	22.6	24.7	25.9
3×10^{-3}	19.4	26.8	33.1	38.5	43.3	46.9
10^{-2}	27.0	45.4	59.5	71.2	81.4	90.0
3×10^{-2}	36.5	76.2	104.0	126.0	146.0	163.0
10^{-1}	50.8	139.0	195.0	239.0	278.0	313.0
3×10^{-1}	68.6	245.0	349.0	431.0	502.0	567.0
10^{0}	95.4	462.0	664.0	823.0	960.0	
3×10^{0}	129.0	829.0				
10^{1}	179.0					
3×10^{1}	242.0					

TABLE IV.2

$Q.\Delta\alpha$ Values for DTD.5120

ΔK \ x	0	0.2	0.4	0.6	0.8	1.0
3	3.27×10^{-6}	3.87×10^{-6}	4.66×10^{-6}	5.83×10^{-6}	8.02×10^{-6}	1.86×10^{-5}
5	2.12×10^{-5}	2.27×10^{-5}	2.45×10^{-5}	2.68×10^{-5}	3.09×10^{-5}	4.79×10^{-5}
10	2.69×10^{-4}	2.11×10^{-4}	1.77×10^{-4}	1.60×10^{-4}	1.52×10^{-4}	1.72×10^{-4}
20	3.35×10^{-3}	1.44×10^{-3}	9.88×10^{-4}	7.66×10^{-4}	6.50×10^{-4}	6.20×10^{-4}
30	1.47×10^{-3}	3.88×10^{-3}	2.41×10^{-3}	1.79×10^{-3}	1.46×10^{-3}	1.31×10^{-3}
40	4.19×10^{-2}	7.49×10^{-3}	4.42×10^{-3}	3.23×10^{-3}	2.57×10^{-3}	2.23×10^{-3}
50	9.44×10^{-2}	3.75×10^{-2}	6.50×10^{-3}	5.00×10^{-3}	3.95×10^{-3}	3.37×10^{-3}

TABLE IV.3

Crack Growth Rate and % Striated Surface for DTD.5120 at $R = 0$

ΔK	$\frac{\Delta K}{E\ n\ \sqrt{2\pi\ d}}$	$P\{Tear\}$	Uniform P, $0 \leqslant x \leqslant 1$		Uniform P, $0 \leqslant (1-x) \leqslant P\{T\}$		$x = P\{Tear\}$	
			da/dN	%s	da/dN	%s	da/dN	%s
3	0.091	≈0	6.66×10^{-6}	66	1.86×10^{-5}	100	1.86×10^{-5}	100
5	0.152	0.01	2.79×10^{-5}	57	4.79×10^{-5}	≈100	4.79×10^{-5}	99
10	0.305	0.08	1.84×10^{-4}	45	1.68×10^{-4}	95	1.65×10^{-4}	92
20	0.610	0.36	1.16×10^{-3}	34	6.70×10^{-4}	79	7.43×10^{-4}	64
30	0.915	0.79	3.46×10^{-3}	27	3.77×10^{-3}	51	7.34×10^{-3}	21
40	1.22	≈1	7.97×10^{-3}	21	7.97×10^{-3}	21	4.19×10^{-2}	≈0
50	1.52	≈1	2.04×10^{-3}	18	2.04×10^{-2}	18	9.44×10^{-2}	0

TABLE IV.4

Stress Ratio Effects in DTD.5120

R	η_1	η_2
0	1.000	1.000
0.1	0.980	1.202
0.2	0.956	1.501
0.3	0.929	1.955
0.4	0.900	2.688
0.5	0.868	3.851
0.6	0.833	5.988
0.7	0.791	10.41
0.8	0.738	22.03

TABLE IV.5

ΔK, K_R Values for BS.L97

$Q.\Delta a$ \ x	0 (Tearing)	0.2	0.4	0.6	0.8	1.0 (Striations)
10^{-6}	2.72	2.63	2.51	2.34	2.09	1.14
3×10^{-6}	3.59	3.52	3.38	3.20	2.91	1.82
10^{-5}	4.87	4.85	4.75	4.57	4.25	3.02
3×10^{-5}	6.44	6.56	6.53	6.40	6.11	4.79
10^{-4}	8.74	9.20	9.39	9.44	9.28	7.94
3×10^{-4}	11.5	12.7	13.3	13.7	13.8	12.6
10^{-3}	15.7	18.2	19.8	20.9	21.7	20.9
3×10^{-3}	20.7	25.8	29.0	31.4	33.2	33.1
10^{-2}	28.1	38.6	44.9	49.7	53.5	54.9
3×10^{-2}	37.2	56.6	67.8	76.4	83.3	87.2
10^{-1}	50.5	87.8	108.0	123.0	136.0	145.0
3×10^{-1}	66.7	133.0	167.0	193.0	214.0	229.0
10^{0}	90.5	212.0	271.0	316.0	352.0	381.0
3×10^{0}	120.0	328.0	425.0	497.0	556.0	603.0
10^{1}	162.0	533.0	697.0	819.0	920.0	
3×10^{1}	214.0	834.0				

TABLE IV.6

$Q.\Delta a$ Values for BS.L97

ΔK \ x	0	0.2	0.4	0.6	0.8	1.0
3	1.47×10^{-6}	1.64×10^{-6}	1.93×10^{-6}	2.39×10^{-6}	3.30×10^{-6}	9.84×10^{-6}
5	1.11×10^{-5}	1.12×10^{-5}	1.19×10^{-5}	1.34×10^{-5}	1.63×10^{-5}	3.32×10^{-5}
10	1.71×10^{-4}	1.33×10^{-4}	1.22×10^{-4}	1.18×10^{-4}	1.23×10^{-4}	1.73×10^{-4}
20	2.62×10^{-3}	1.34×10^{-3}	1.03×10^{-3}	8.82×10^{-4}	8.05×10^{-4}	9.00×10^{-4}
30	1.29×10^{-2}	4.71×10^{-3}	3.29×10^{-3}	2.65×10^{-3}	2.31×10^{-3}	2.37×10^{-3}
40	3.99×10^{-2}	1.11×10^{-2}	7.27×10^{-3}	5.66×10^{-3}	4.80×10^{-3}	4.71×10^{-3}
50	9.61×10^{-2}	2.10×10^{-2}	1.33×10^{-2}	1.01×10^{-2}	8.43×10^{-3}	8.00×10^{-3}

TABLE IV.7

Crack Growth Rate and % Striated Surface for BS.L97 at $R = 0$

ΔK	$\frac{\Delta K}{E\ n\ \sqrt{2\pi\ \overline{d}}}$	$P\{Tear\}$	Uniform P, $0 \leqslant x \leqslant 1$		Uniform P, $0 \leqslant (1-x) \leqslant P\{T\}$		$x = P\{Tear\}$	
			da/dN	%s	da/dN	%s	da/dN	%s
3	0.098	≈0	2.98×10^{-6}	68	9.84×10^{-6}	100	9.84×10^{-6}	100
5	0.163	0.04	1.50×10^{-5}	60	3.30×10^{-5}	≈99	2.98×10^{-5}	96
10	0.326	0.09	1.34×10^{-4}	50	1.62×10^{-4}	≈95	1.50×10^{-4}	91
20	0.652	0.40	1.16×10^{-3}	38	8.48×10^{-4}	80	8.82×10^{-4}	60
30	0.980	0.86	4.01×10^{-3}	32	3.54×10^{-3}	45	7.17×10^{-3}	14
40	1.304	≈1	9.98×10^{-3}	27	9.98×10^{-3}	27	3.99×10^{-2}	0
50	1.63	≈1	2.05×10^{-2}	23	2.05×10^{-2}	23	9.61×10^{-2}	0

TABLE IV.8

Stress Ratio Effects in BS.L97

R	η_1	η_2
0	1.000	1.000
0.1	1.047	1.239
0.2	1.109	1.603
0.3	1.187	2.176
0.4	1.282	3.120
0.5	1.402	4.783
0.6	1.557	8.008
0.7	1.772	15.297
0.8	2.110	36.88

TABLE IV.9

ΔK, K_R Values for BS.L109

$Q.\Delta a$ \ x	0 (Tearing)	0.2	0.4	0.6	0.8	1.0 (Striations)
10^{-6}	2.96	2.77	2.54	2.25	1.87	1.15
3×10^{-6}	4.62	4.32	3.96	3.51	2.93	1.82
10^{-5}	7.50	7.03	6.44	5.73	4.79	3.02
3×10^{-5}	11.7	10.9	10.0	8.95	7.51	4.79
10^{-4}	18.9	17.8	16.4	14.6	12.3	7.94
3×10^{-4}	29.6	27.8	25.5	22.8	19.2	12.6
10^{-3}	48.0	45.2	41.6	37.2	31.5	20.9
3×10^{-3}	74.8	70.4	65.0	58.2	49.4	33.1
10^{-2}	122.0	115.0	106.0	95.1	80.9	54.9
3×10^{-2}	189.0	179.0	165.0	148.0	127.0	87.2
10^{-1}	308.0	291.0	269.0	243.0	208.0	145.0
3×10^{-1}	479.0	453.0	420.0	380.0	326.0	229.0
10^{0}	779.0	738.0	685.0	620.0	535.0	381.0
3×10^{0}				970.0	840.0	603.0

TABLE IV.10

$Q.\Delta a$ Values for BS.L109

ΔK \ x	0	0.2	0.4	0.6	0.8	1.0
3	1.00×10^{-6}	1.22×10^{-6}	1.51×10^{-6}	2.03×10^{-6}	3.18×10^{-6}	9.84×10^{-6}
5	3.65×10^{-6}	4.31×10^{-6}	5.34×10^{-6}	7.15×10^{-6}	1.11×10^{-5}	3.32×10^{-5}
10	2.04×10^{-5}	2.42×10^{-5}	3.00×10^{-5}	3.94×10^{-5}	6.03×10^{-5}	1.73×10^{-4}
20	1.15×10^{-4}	1.33×10^{-4}	1.64×10^{-4}	2.17×10^{-4}	3.31×10^{-4}	9.00×10^{-4}
30	3.10×10^{-4}	3.62×10^{-4}	4.47×10^{-4}	5.89×10^{-4}	8.88×10^{-4}	2.37×10^{-3}
40	6.35×10^{-4}	7.38×10^{-4}	9.20×10^{-4}	1.19×10^{-3}	1.79×10^{-3}	4.71×10^{-3}
50	1.11×10^{-3}	1.28×10^{-3}	1.57×10^{-3}	2.07×10^{-3}	2.92×10^{-3}	8.00×10^{-3}

TABLE IV.11

Crack Growth Rate and % Striated Surface for BS.L109 at $R = 0$

ΔK	$\frac{\Delta K}{E\ n\ \sqrt{2\pi\ d}}$	$P\{Tear\}$	Uniform P, $0 \leqslant x \leqslant 1$		Uniform P, $0 \leqslant (1-x) \leqslant P\{T\}$		$x = P\{Tear\}$	
			da/dN	$\%s$	da/dN	$\%s$	da/dN	$\%s$
3	0.098	≈0	2.67×10^{-6}	71	9.84×10^{-6}	100	9.84×10^{-6}	100
5	0.163	0.04	9.26×10^{-6}	70	3.30×10^{-5}	≈99	2.88×10^{-5}	96
10	0.326	0.09	5.01×10^{-5}	70	1.62×10^{-4}	≈95	1.22×10^{-4}	91
20	0.652	0.40	2.71×10^{-4}	69	4.45×10^{-4}	88	2.17×10^{-4}	60
30	0.980	0.86	7.25×10^{-4}	69	8.22×10^{-4}	75	3.46×10^{-4}	14
40	1.304	≈1	1.46×10^{-3}	69	1.46×10^{-3}	69	6.35×10^{-4}	0
50	1.63	≈1	2.48×10^{-3}	68	2.48×10^{-3}	68	1.11×10^{-3}	0

TABLE IV.12

Stress Ratio Effects in BS.L109

R	n_1	n_2
0	1.000	1.000
0.1	1.047	1.059
0.2	1.109	1.138
0.3	1.187	1.238
0.4	1.282	1.364
0.5	1.402	1.526
0.6	1.557	1.742
0.7	1.772	2.052
0.8	2.110	2.556